

---

Doctoral Dissertations

Student Theses and Dissertations

---

2009

## Electrodeposition of inorganic materials with tailored shapes and chiral morphologies

Elizabeth A. Kulp

Follow this and additional works at: [https://scholarsmine.mst.edu/doctoral\\_dissertations](https://scholarsmine.mst.edu/doctoral_dissertations)

 Part of the [Chemistry Commons](#)

Department: Chemistry

---

### Recommended Citation

Kulp, Elizabeth A., "Electrodeposition of inorganic materials with tailored shapes and chiral morphologies" (2009). *Doctoral Dissertations*. 29.

[https://scholarsmine.mst.edu/doctoral\\_dissertations/29](https://scholarsmine.mst.edu/doctoral_dissertations/29)

This thesis is brought to you by Scholars' Mine, a service of the Missouri S&T Library and Learning Resources. This work is protected by U. S. Copyright Law. Unauthorized use including reproduction for redistribution requires the permission of the copyright holder. For more information, please contact [scholarsmine@mst.edu](mailto:scholarsmine@mst.edu).

ELECTRODEPOSITION OF INORGANIC MATERIALS WITH TAILORED SHAPES  
AND CHIRAL MORPHOLOGIES

by

ELIZABETH ANN KULP

A DISSERTATION

Presented to the Faculty of the Graduate School of the  
MISSOURI UNIVERSITY OF SCIENCE AND TECHNOLOGY

In Partial Fulfillment of the Requirements for the Degree

DOCTOR OF PHILOSOPHY

in

CHEMISTRY

2009

Approved by:

Jay A. Switzer, Advisor  
Frank Blum  
Nicholas Leventis  
Ekkehard Sinn  
F. Scott Miller



## PUBLICATION DISSERTATION OPTION

This dissertation has been prepared in the format used by *Solid State Ionics*, *Chemistry of Materials*, *Science*, and *the Journal of the American Chemical Society*. This dissertation consists of the three articles that have been published and two articles intended for submission. Paper I found on pages 87-114 is published in *Solid State Ionics*. Paper II is written for submission to *Chemistry of Materials* (pages 115-149). Paper III on pages 150-163 is prepared for publication in the *Science*. Paper IV is published in *Chemistry of Materials* (pages 164-208) while Paper V is published in the *Journal of the American Chemical Society* (pages 209-217). The appendices include discussions on growth morphology, x-ray diffraction characterization, and electrochemical biomineralization. It also includes the supporting information published with Paper V.

## ABSTRACT

This dissertation investigates the electrodeposition of metal oxide films and biomaterial deposits on polycrystalline and single crystal substrates. Paper I describes the mechanisms and the characterization of an electrodeposited polycrystalline insulator, ceria ( $\text{CeO}_2$ ), on Hastelloy substrates produced by the electrochemical oxidation of Ce(III) acetate complexes. In Paper II, epitaxial films of magnetite ( $\text{Fe}_3\text{O}_4$ ) and ferrihydrite ( $\text{Fe}_{10}\text{O}_{14}(\text{OH})_2$ ) are deposited on gold single crystals. Paper III reports the electrodeposition of epitaxial  $\text{Fe}_3\text{O}_4$  and zinc ferrite ( $\text{ZnFe}_2\text{O}_4$ ) periodic nanostructures known as superlattices by pulsing between two potentials. Papers IV and V describe chiral electrodeposition. In Paper IV, epitaxial, chiral orientations of cupric oxide ( $\text{CuO}$ ) are electrodeposited on Au(001) single crystals. In Paper V, chiral morphologies of the biomaterial calcite ( $\text{CaCO}_3$ ) are electrochemically deposited on stainless steel substrates. In both chiral electrodeposition studies, the chirality of these materials is controlled by the enantiomer in solution.

The first two appendices of this dissertation cover morphology and x-ray diffraction characterization. The third appendix has supplementary information from the calcite paper (Paper V) followed by unpublished biomineralization results.

## ACKNOWLEDGEMENTS

I would like to thank my advisor, Jay A. Switzer, for his knowledge, encouragement, guidance, and patience throughout my graduate studies. His time and effort will always be appreciated. Likewise, I would like to thank Professors Frank Blum, Nicholas Leventis, F. Scott Miller, and Ekk Sinn for agreeing to be part of my committee and educating me in the fundamentals of science throughout my years at Missouri University of Science and Technology (formerly the University of Missouri-Rolla). Similarly, I would like to thank all my professors and teachers for their words of wisdom and their time spent educating my cohorts and me.

Along with this gratitude is the appreciation of the scientific discussions, basic knowledge, and many friendships gained from being part of the Switzer group, the Chemistry department, and the Materials Research Center. Special thanks go to Eric Bohannan, Hiten Kothari, Run Liu, Steven Limmer, and Rakesh Gudavarthy. I would like to thank Jeanine Bruening for editing my introduction. I would also like to thank my family for their constant encouragement and support during the course of my studies at this university. In addition, I would like to express my appreciation for all the laughs and tears my undergraduate and graduate friends have shared and shed with me over the years.

Last but not least, I would like to acknowledge the financial support of the National Science Foundation, AstraZeneca Corp, the Foundation for Chemical Research, Department of Energy, and my Chancellor's Fellowship from the University of Missouri-Rolla.

## TABLE OF CONTENTS

	Page
PUBLICATION THESIS OPTION.....	iii
ABSTRACT.....	iv
ACKNOWLEDGEMENTS.....	v
LIST OF ILLUSTRATIONS.....	ix
LIST OF TABLES.....	xvi
SECTION	
1. INTRODUCTION.....	1
1.1 FILM DEPOSITION AND CHARACTERIZATION.....	3
1.1.1 Electrodeposition by an Oxidation State Change.....	4
1.1.2 Electrodeposition by pH Change.....	5
1.1.3 Thermodynamics of Electrochemical Cells .....	6
1.1.4 Electrochemical Characterization.....	9
1.1.4.1 Modes of Mass Transfer.....	9
1.1.4.2 Cyclic Voltammetry. ....	10
1.1.4.3 Linear Sweep Voltammetry.....	13
1.1.4.4 Chronopotentiometry and Chronoamperometry .....	16
1.1.5 X-ray Diffraction Characterization of Films.....	18
1.1.6 Other Film Characterization Techniques .....	30
1.2 CERIA .....	31
1.3 IRON COMPOUNDS .....	36
1.3.1 Magnetite.....	36
1.3.2 Ferrihydrite.....	42
1.3.3 Zinc Ferrite.....	45
1.4 SUPERLATTICES.....	49
1.5 CHIRALITY OF COPPER(II) OXIDE .....	53
1.6 ELECTROCHEMICAL BIOMINERALIZATION.....	69
REFERENCES.....	75

## PAPER

I. Electrodeposition of Nanometer-Thick Ceria Films by Oxidation of Cerium(III)-Acetate .....	87
ABSTRACT .....	87
INTRODUCTION.....	88
EXPERIMENTAL SECTION .....	89
RESULTS AND DISCUSSION .....	90
CONCLUSION .....	101
ACKNOWLEDGEMENTS .....	102
REFERENCES.....	103
II. Electrodeposition of Magnetite Films and Ferrihydrite Nanoribbons on Single-Crystal Gold .....	115
ABSTRACT .....	115
INTRODUCTION.....	116
EXPERIMENTAL SECTION .....	118
RESULTS AND DISCUSSION .....	120
CONCLUSION .....	132
ACKNOWLEDGEMENT.....	133
FOOTNOTES.....	133
III. Epitaxial Electrodeposition of Ferrite Superlattices on Au(111).....	150
REFERENCES .....	157
IV. Enantiospecific Electrodeposition of Chiral CuO Films from Copper(II) Complexes of Tartaric and Amino Acids on Single-Crystal Au(001) .....	164
ABSTRACT .....	164
INTRODUCTION.....	165
EXPERIMENTAL SECTION .....	167
Case 1: Deposition using Tartaric Acid .....	167
Case 2: Deposition using Amino Acids.....	168
X-ray Diffraction Measurements .....	168
Electrochemical Selectivity .....	169
RESULTS AND DISCUSSION .....	169
Deposition from Tartaric Acid.....	170

Deposition from Amino Acids.....	181
CONCLUSIONS.....	186
ACKNOWLEDGEMENTS .....	187
REFERENCES.....	188
V. Electrochemical Biomineralization: the Deposition of Calcite with Chiral Morphologies .....	209
ACKNOWLEDGEMENT.....	213
REFERENCES.....	214
APPENDICES	
A. MORPHOLOGY CHARACTERIZATION .....	218
B. X-RAY DIFFRACTION CHARACTERIZATION.....	225
C. ELECTROCHEMICAL BIOMINERALIZATION .....	251
VITA .....	261

## LIST OF ILLUSTRATIONS

Figure	Page
INTRODUCTION	
1.1 A CV of alkaline Fe(III)-TEA bath at 80°C at a scan rate of 50 mV/s.....	12
1.2 The linear sweep voltammograms of an alkaline TEA solution (blue squares) and Fe(TEA) solution (black line) at 80°C scanned at 50 mV/s at a rotation of 100 rpm on a gold rotating disk electrode.....	14
1.3 A plot of ratio of current to limiting current versus the applied potential based on the LSV of Figure 2.....	16
1.4 Illustrations and X-ray diffraction patterns of A) a polycrystalline magnetite film on stainless steel and B) a (111) oriented magnetite film on Au(111) single crystal.....	21
1.5 An illustration of the method to produce a (311) magnetite pole figure of a (111) oriented magnetite film (top) and (311) azimuthal scans of a (111) oriented magnetite film on Au(111) (bottom).....	23
1.6 Illustrations of the cubic material magnetite (Fe <sub>3</sub> O <sub>4</sub> ) as A) a polycrystalline film on stainless steel, B) a (111) fiber-textured film on stainless steel, and C) a (111) epitaxial film on Au(111). (311) Fe <sub>3</sub> O <sub>4</sub> pole figures of a D) polycrystalline, E) (111) fiber-textured, and F) (111) epitaxial films.....	25
1.7 Illustrations of the cubic material magnetite (Fe <sub>3</sub> O <sub>4</sub> ) as a (111) epitaxial film on Au(111) with A) one domain, B) two domains, and C) four domains.....	26
1.8 Mosaic spreads and rocking curves of two films.....	28
1.9 X-ray diffraction patterns for the [111] oriented A) magnetite and B) magnetite superlattice on Au(111). The (444) peak of the C) magnetite and D) superlattice....	30
1.10 The crystal structure of ceria.....	32
1.11 A) The calculated speciation distribution for a 0.1 M cerium(III) nitrate and 0.1 M ammonium acetate solution. B) The cyclic voltammogram on Pt for 0.1 M cerium(III) nitrate and 0.1M ammonium acetate solution.....	34
1.12 SEM micrographs of ceria films grown at A) 0.5 V and B) 1.1 V vs. Ag/AgCl.....	35
1.13 Crystal structure of magnetite.....	37

1.14 Plot of the concentrations of Fe(III) (red line) and Fe(II) (black line) at the electrode surface as a function of potential.....	39
1.15 The (311) pole figures of A) epitaxial (111)magnetite on Au(111) deposited at -1.01 V vs. Ag/AgCl and B) Au(111).....	42
1.16 A polyhedral representation of the crystal structure of 2-line ferrihydrite.....	43
1.17 SEM images of films deposited on Au(110) from an alkaline Fe(III)-TEA bath at A) -1.10 V and B) -1.20 V vs. AgCl.....	44
1.18 The polyhedral representation of zinc ferrite.....	47
1.19 A) The (444) X-ray diffraction peaks of magnetite superlattices with a range of modulation wavelengths. Magnetite superlattices were produced by pulsing between -1.01 V and -1.05 V vs. Ag/AgCl in an alkaline Fe(III)-TEA bath with modulation wavelength of 20.7 (top) and 9.5 nm (bottom). B) The (444) X-ray diffraction peaks of zinc ferrite superlattices with a range of modulation wavelengths. Zinc ferrite superlattices were electrodeposited using -0.99 V and -1.05 V vs. Ag/AgCl from an alkaline Zn(II)-Fe(III)-TEA deposition bath with modulation wavelengths of 29.2 (top), 16.8 (middle), and 12.5 nm (bottom). The main Bragg peak is indicated with a "0".....	52
1.20 Chiral structures exist if they contain only proper symmetry operators such as A) a two-fold rotation (2), B) a translation, and C) a screw rotation (2 <sub>1</sub> ).....	55
1.21 Achiral structures exist if they contain improper symmetry operators such as A) inversion (i), B) a mirror plane (m), C) a rotation inversion ( $\bar{4}$ ), or D) a glide plane (c).....	56
1.22 The crystal structure of copper(II) oxide.....	58
1.23 Stereographic projections of the A) (001) and B) (00 $\bar{1}$ ) orientations of CuO. These two orientations are superimposable mirror images of each other; they are achiral. The radial grid lines on the stereographic projections correspond to 30° increments of the tilt angle, $\chi$ . C) The interface model of (00 $\bar{1}$ ) CuO (front, blue Cu atoms) on (001)CuO (back, brown Cu atoms) with a common [010] direction. These two orientations are superimposed onto each other, indicating that they are achiral.....	63

- 1.24 Stereographic projections of A) (111) and B)  $(\bar{1}\bar{1}\bar{1})$  orientations of CuO. These two orientations are nonsuperimposable mirror images of each other; they are chiral. The radial grid lines on the stereographic projections correspond to  $30^\circ$  increments of the tilt angle,  $\chi$ . C) The interface model of  $(\bar{1}\bar{1}\bar{1})$  CuO (red oxygen atoms) on (111)CuO (violet oxygen atoms) with a common  $[1\bar{1}0]$  direction. These two surfaces are nonsuperimposable; therefore, they are chiral.....64
- 1.25 The stereographic projections of A) CuO( $1\bar{1}\bar{1}$ ) and B) CuO( $\bar{1}11$ ), indicating the positions where the {111} and {100} reflections occur. The CuO(111) pole figures for CuO films on Au(001) grown from C) L-tartaric and D) D-tartaric acid.....68
- 1.26 The crystal structure of calcite.....72
- 1.27 Achiral and chiral facets of calcite.....74

## PAPER I

1. Calculated species distribution for 0.1 M  $\text{Ce}^{3+}$  and 0.1 M acetate at  $25^\circ\text{C}$ .....106
2. (A) E-pH diagrams for  $\text{CeO}_2(\text{s})/\text{Ce}^{3+}$  and  $\text{CeO}_2(\text{s})/\text{Ce}(\text{OAc})_i^{3-i}$  species and (B) E-pH diagrams for  $\text{Ce}(\text{OH})_4(\text{aq})/\text{Ce}^{3+}$  and  $\text{Ce}(\text{OH})_4(\text{aq})/\text{Ce}(\text{OAc})_i^{3-i}$  species assuming unit activity at  $25^\circ\text{C}$ .....106
3. Cyclic voltammetry at 100 mV/s in the deposition solution on a Pt electrode, showing an oxidation peak at about 0.5 V vs. Ag/AgCl in the initial scan, which disappears upon successive scans. Also shown is a scan of a ceria film on Pt in 0.1 M acetate at a pH of about 6.1, demonstrating a current increase presumably due to oxygen evolution at potentials above about 1.0 V vs. Ag/AgCl.....107
4. Chronoamperometry of deposition on Hastelloy substrates at +0.5 and +1.1 V vs. Ag/AgCl and  $65^\circ\text{C}$ , showing the rapid decay in current at low potential, compared to the consistently larger currents at higher potential..... 107
5. SEM micrographs of ceria films grown for 1000 s at +0.5 V vs. Ag/AgCl and  $65^\circ\text{C}$ , at both lower (A) and higher (B) magnifications.....108
6. X-ray diffraction pattern of a ceria film grown for 1000 s at +0.5 V vs. Ag/AgCl and  $65^\circ\text{C}$ , showing the presence of ceria with no other phases observed.....108
7. (A) X-ray reflectivity of a ceria film grown for 1000 s at +0.5 V vs. Ag/AgCl and  $65^\circ\text{C}$ , showing a number of interference fringes. (B) Least-squares fit of the fringe numbers to determine film thickness (39 nm) and critical angle ( $\theta_c = 5 \times 10^{-3}$  rad, or  $2\theta_c = 0.573^\circ$ ) for this sample.....109

8. Film thickness as a function of time, as determined by ellipsometry.....	109
9. SEM micrograph of ceria film grown for 6000 s at +1.1 V and 65 °C, showing the cracked morphology of such films.....	110
10. Ce 3d XPS spectrum of a CeO <sub>2</sub> film electrodeposited at +1.1 V vs. Ag/AgCl for 1000 s.....	110
11. (A) Powder x-ray diffraction pattern of ceria nanopowders precipitated from the growth solution by bubbling with O <sub>2</sub> at 65 °C. (B) Williamson-Hall analysis of the powders, showing that the particle size is ~7 nm, with a residual strain of about 0.5%.....	111
12. X-ray diffraction pattern of a ceria film deposited on a glass slide during growth at +1.1 V and 65 °C, showing that ceria is formed away from the electrodes at this potential.....	111

#### Scheme

1. Anodic deposition of ceria films at a low potential. For clarity, ligands on the cerium ions have been omitted.....	114
2. Possible route for ceria formation at a higher potential. For clarity, ligands on the cerium ions have been omitted.....	114

#### PAPER II

1. The linear sweep voltammograms of an alkaline TEA solution (blue squares) and Fe(III)-TEA solution (black solid line) at 80 °C scanned at 50 mV/s at a rotation of 100 rpm on a gold rotating disk electrode.....	138
2. A plot of the surface concentrations of Fe(III) (red) and Fe(II) (black) as a function of potential based on the linear sweep voltammogram of the alkaline Fe(III)-TEA bath in Figure 1.....	138
3. Symmetric X-ray diffraction patterns of magnetite films deposited on 430 stainless steel substrates at a potential of A) -1.01 V, B) -1.05 V, and C) -1.1 V vs. Ag/AgCl until 1 C/cm <sup>2</sup> was passed at 80 °C.....	139
4. Lattice parameters from Rietveld analysis of XRD patterns of magnetite films deposited as a function of potential.....	140
5. SEM images of magnetite films deposited on stainless steel at A) -1.01 V, B) -1.05 V, and C) -1.1 V vs. Ag/AgCl.....	141

6. Room temperature Mössbauer spectra of magnetite deposited on HOPG at A) -1.01 V, B) -1.05 V, C) -1.10 V and D) -1.20 vs. Ag/AgCl.....142
7. X-ray diffraction patterns of magnetite deposited on A) Au(111), B) Au(001), and C) Au(110) for 300 s at -1.01 V vs. Ag/AgCl at 80°C.....143
8. (311) pole figures of magnetite films deposited on A) Au(111), B) Au(001), and C) Au(110) for 300 s at -1.01 V vs. Ag/AgCl at 80 °C. ....144
9. SEM images of magnetite deposited on A) Au(111), B) Au(001), and C) Au(110) for 300 s at -1.01 V vs. Ag/AgCl at 80 °C.....145
10. (311) azimuthal scans of magnetite and gold for magnetite films deposited on A) Au(111), B) Au(001), and C) Au(110). ....146
11. X-ray diffraction patterns of magnetite and ferrihydrite electrodeposited at A) -1.10 V and B) -1.20 V vs. Ag/AgCl on Au(110). ....147
12. SEM images of a film deposited at -1.1 V vs. Ag/AgCl at 80 °C on Au(110). A) A SEM image of the overall view of the surface of the film showing two distinct morphologies. The ribbon-like morphology of ferrihydrite (B) on underlying nonstoichiometric magnetite (C) is shown.....148
13. (311) magnetite pole figures of  $(11\bar{2}0)$  ferrihydrite on (110) magnetite on Au(110) electrodeposited at A) -1.10 V and B) -1.20 V vs. Ag/AgCl are shown. The (311) magnetite pole figure is actually probing three planes: (311) magnetite,  $(11\bar{2}0)$  ferrihydrite, and (111) Au due to their similar d-spacings. Figure C is a (111) Au pole figure of the Au(110) substrate. The radial grid lines on the pole figure correspond to 30° increments of the tilt angle,  $\chi$ .....149

### PAPER III

1. (A) Linear sweep voltammogram of the alkaline Fe(III)—TEA deposition solution at 80°C scanned at 50 mV/s on a gold rotating disk electrode at 100 rpm. (B) Plot of the concentrations of Fe(III) and Fe(II) at the electrode surface as a function of potential. (C) Plot of the lattice parameters of the magnetite as a function of applied potential.....160
2. (A) X-ray diffraction pattern for the {111} oriented magnetite superlattice on Au(111). (B) (311) pole figures of magnetite superlattice (left) and Au (right). (444) peaks of magnetite (C) superlattices from the x-ray diffraction patterns with a range of modulation wavelengths. Magnetite superlattices (C) were produced by pulsing between -1.01 V and -1.05 V vs. Ag/AgCl in an alkaline Fe(III)-TEA bath with modulation wavelength of 20.7 (top) and 9.5 nm (bottom)..161

3. (A) Plot of the lattice parameters of the zinc ferrite as a function of potential. (B) Zinc ferrite superlattices were electrodeposited by pulsing between -0.99 V and -1.05 V vs. Ag/AgCl from an alkaline Zn(II)—Fe(III)—TEA deposition bath with modulation wavelengths of 29.2 (top), 16.8 (middle), and 12.5 nm (bottom). (C) FIB image of a zinc ferrite superlattice showing a modulation wavelength of 78 nm.....162

#### PAPER IV

1. Structure of monoclinic CuO with space group  $C2/c$ . .....194
2. X-ray diffraction  $\theta$ - $2\theta$  scan for a 300 nm thick CuO film deposited on Au(001) from a solution of L-tartaric acid.....195
3. Stereographic projections for (a)  $(1\bar{1}\bar{1})$  and (b)  $(\bar{1}11)$  orientations indicating the positions where the (111)-type and the (100)-type reflections should be observed in the pole figures.....196
4. CuO(111) pole figures for films of CuO on Au(001) grown from a solution of (a) L-tartaric acid, (b) D-tartaric acid and (C) DL-tartaric acid.....197
5. Azimuthal scans probing the  $\{111\}$  reflections at  $\chi = 63^\circ$  for films of CuO on Au(001) grown from a solution of (a) L-tartaric acid, (b) D-tartaric acid and (C) DL-tartaric acid.....198
6. Polyhedra models for the  $(1\bar{1}\bar{1})$  and  $(\bar{1}11)$  orientations with the faces aligned parallel with the plane of the paper. ....199
7. SEM images of CuO films on Au(100) grown from solutions of (a) L-tartaric acid, (b) D-tartaric acid and (c) DL-tartaric acid.....200
8. CuO(111) pole figures for films deposited from (a) L-tartaric acid before switching to D-tartaric acid, and (b) D-tartaric acid before switching to L-tartaric acid.....201
9. Chiral recognition of tartaric acid by chiral CuO. Cyclic voltammograms were run at room temperature in solutions of 5 mM L-tartaric acid (solid line) or 5 mM D-tartaric acid (dash) in 0.1 M NaOH (dot) for CuO films grown in (a) L-tartaric acid, (b) D-tartaric acid and (c) DL-tartaric acid solutions.....202
10. X-ray diffraction  $\theta$ - $2\theta$  scan of a CuO film on Au(001) from L-alanine solution...203

11. Stereographic projections for (a) $(\bar{1}11)$ , (b) $(1\bar{1}\bar{1})$ , (c) $(\bar{1}\bar{1}\bar{1})$ and (d) $(111)$ orientations indicating the positions where the $(111)$ -type and $(100)$ -type reflections should be observed in the pole figures.....	204
12. Stereographic projections for the (a) $(\bar{1}11)$ , (b) $(1\bar{1}\bar{1})$ , (c) $(\bar{1}\bar{1}\bar{1})$ and (d) $(111)$ orientations indicating the positions where the $(10\bar{1})$ -type reflections should be observed in the pole figures.....	205
13. Pole figures probing the in-plane orientation for a CuO film on Au(001) grown from a solution of L-alanine using (a) $(111)$ reflections and (b) $(20\bar{2})$ reflections..	206
14. Expected $(111)$ pole figure obtained by overlaying the stereographic projections...	207
15. CuO $(20\bar{2})$ pole figures for various CuO films grown from solutions of (a) L-alanine, (b) D-alanine, (c) DL-alanine, (d) L-valine, (e) D-valine and (f) DL-valine.....	208

## PAPER V

1. Deposition of calcite and aragonite by the electrochemical generation of base.....	216
2. Electrodeposition of calcite with chiral facets.....	217

## LIST OF TABLES

Table	Page
INTRODUCTION	
1.1 Comparison of compositions of zinc ferrite films as a function of applied potential measured from energy dispersive spectroscopy and calculated from the linear sweep voltammetry.....	48
1.2 Symmetry of the planes of a point group.....	59
PAPER I	
1. The water ionization constant, acid dissociation constant for acetic acid, and formation constants of cerium(III) complexes with hydroxide and acetate ions at 25°C.....	112
2. The standard Gibbs free energy of formation of selected substances.....	113
3. Calculated formal potentials for the equilibria at pH values of 0, 6.1, and 14 at 25°C assuming unit activity.....	113
PAPER II	
1. Potentials and constants used to calculate the reduction potential of $\text{Fe}(\text{OH})_4\text{TEA}_2^-$ to $\text{Fe}_3\text{O}_4$ .....	136
2. The Mössbauer spectral parameters at 25 °C obtained from the spectra in Figure 6 of films deposited from four different potentials vs. Ag/AgCl. The isomer shifts are given relative to the $\alpha$ -Fe foil at 25°C.....	137
PAPER III	
1. Comparison of compositions of zinc ferrite films as a function of applied potential measured from energy dispersive spectroscopy and calculated from the linear sweep voltammetry.....	163
PAPER IV	
1. List of planes having identical d-spacing for monoclinic CuO.....	191
2. Calculated interplanar angles, $\chi$ , between the observed orientation in the $\theta$ -2 $\theta$ X-ray diffraction scans and the CuO reflections probed in the pole figure.....	191

3. Calculated interplanar angles between the observed orientation in the  $\theta$ - $2\theta$  X-ray diffraction scans and the CuO reflections being probed in the pole figure.....192
4. Enantiomeric excesses for CuO films grown from various solution precursors determined from the (111)-type reflections.....193

#### PAPER V

1. Selection rules for chirality of the calcite crystal system.....215

## 1. INTRODUCTION

Electrodeposition is a low temperature processing method by which films are deposited from solution precursors at an electrode surface. A major focus in the Switzer group has been the use of the deposition solution (temperature, pH, and complexing agents) and potential to control the shape, orientation, and chirality of epitaxial metal oxide films. This dissertation includes a study on the electrodeposition of polycrystalline ceria, as well as studies of epitaxial magnetite and ferrihydrite, superlattices of magnetite and zinc ferrite, chiral cupric oxide, and calcite with chiral morphologies.

Paper I reports experiments in which thin films of ceria ( $\text{CeO}_2$ ) were electrodeposited onto Hastelloy substrates by the electrochemical oxidation of Ce(III) acetate complexes. The mode of deposition was dependent on the applied potential. At a potential of +0.5 V vs. Ag/AgCl, the deposition proceeded by direct oxidation of Ce(III) to  $\text{CeO}_2$ . At a higher potential of +1.1 V vs. Ag/AgCl, the films grew by an indirect mechanism in which the electrochemical oxidation of water formed  $\text{O}_2$ , which then reacted with Ce(III) to form  $\text{CeO}_2$  nanoparticles in the growth solution. Consistent with this mechanism, nanometer-scale  $\text{CeO}_2$  powder was produced by bubbling the solution with molecular oxygen.

Paper II describes the cathodic electrodeposition of magnetite ( $\text{Fe}_3\text{O}_4$ ) and ferrihydrite ( $\text{Fe}_{10}\text{O}_{14}(\text{OH})_2$ ) films from an alkaline Fe(III)-triethanolamine solution. The concentration of Fe(III) and Fe(II) at the electrode surface was controlled by the applied potential. Determined from X-ray diffraction patterns, the lattice parameter of the magnetite decreased as the overpotential increased. Ribbon-like morphologies of ferrihydrite were deposited in the mass-transport limited region. Verified by X-ray pole

figures, epitaxial films of magnetite and ferrihydrite were electrodeposited on the low-index gold surfaces.

Paper III reports that the exploitation of the electrochemical-chemical (EC) nature of the reaction permitted the deposition of magnetite superlattices by pulsing the applied potential. The EC mechanism also allowed for the incorporation of electrochemically inactive cations into the system to produce other ferrite superlattices. The addition of  $\text{Zn}^{2+}$  to the magnetite deposition bath allowed for the electrodeposition of zinc ferrite ( $\text{ZnFe}_2\text{O}_4$ ). By increasing the overpotential, the concentration of zinc and lattice parameter of the film decrease. This work demonstrates by X-ray diffraction and cross-sectional FIB images that compositional superlattices based on zinc ferrite were deposited by varying the applied potential.

A chiral surface lacks mirror or glide plane symmetry. An approach to produce chiral surfaces is to electrodeposit a low symmetry material with possible chiral orientations on achiral substrates. Paper IV describes work in which copper(II) oxide ( $\text{CuO}$ ), which is intrinsically achiral, was electrodeposited onto single-crystal Au. The chiral orientations of these films were produced using an enantiomer of tartaric acid or the amino acids alanine and valine to control the handedness of the electrodeposited films. Electrochemical chiral recognition experiments showed that the chiral orientations also expose chiral surfaces.

Paper V addresses the deposition of chiral structures of calcite by electrochemical biomineralization. Calcite deposits that exhibit chiral facets were grown in the presence of an enantiomer of tartaric, malic, or aspartic acid. Symmetric calcite facets were produced in the presence of a racemic mixture of malic acid or achiral succinic acid.

In addition, two appendices cover morphology and X-ray diffraction characterization. A third appendix provides supplementary information on the work described in Paper V, followed by unpublished biomineralization results.

## 1.1 FILM DEPOSITION AND CHARACTERIZATION

Electrodeposition is the process of producing a film on a conductive substrate by applying an electrical current. The simplicity of this method has certain advantages and disadvantages when compared to other deposition processes.<sup>1,2</sup> Whereas other methods often require a high vacuum, high temperature, pure gases, or pure solid-state targets, electrodeposition is a low cost process using electrically conductive aqueous, organic, or fused salt solutions. Electrodeposition is not a line-of-sight method; therefore, complex shapes can be coated. Another advantage of electrodeposition is its ability to control the deposition rate by varying the applied current or overpotential. Electrodeposition also offers the ability to tune the characteristics of the film by varying factors such as the electrolyte composition, the additives, the pH and temperature of the electrolyte, and the applied overpotential or current density.<sup>3-14</sup>

Electrodeposition does, however, have its drawbacks. The process requires an electrically conductive substrate on which to deposit a film. The resistivity of the deposited material can limit the thickness of the film. Impure films can result from undesirable electrochemical and chemical side reactions during deposition, dissolution of the film, and incorporation of electrolyte components. Furthermore, competing electrochemical reactions can inhibit film deposition such as the generation of gas bubbles at the electrode surface, which produces pinholes in the film. Nonetheless, the

advantages of electrodeposition outweigh the difficulties, making it a valuable method for film deposition.

**1.1.1 Electrodeposition by an Oxidation State Change.** Electrodeposition is a versatile method for depositing metals, metal oxides, semiconductors, and biomaterials. The most familiar method to electrodeposit a film involves electrochemically oxidizing or reducing the cation in the electrolyte at the electrode surface. For metal deposition, the cation is directly reduced to the metal at the electrode surface. Both oxidation (anodic) and reduction (cathodic) reactions are used for metal oxides. The electrochemically produced species reacts with water or hydroxide ions to form a metal oxide on the electrode. Equation 1 offers a simple example in which  $\text{Ce}^{3+}$  is stable in the aqueous solution and then electrochemically oxidized to produce  $\text{CeO}_2$ .<sup>15-17</sup>

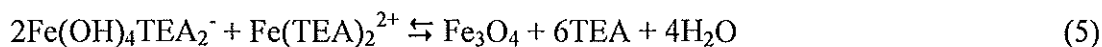


A more complex example of electrodeposition is iron(II,III) oxide, known as magnetite ( $\text{Fe}_3\text{O}_4$ ). Magnetite can be deposited by electrochemically oxidizing  $\text{Fe(II)}$ <sup>18-26</sup> or reducing  $\text{Fe(III)}$ <sup>27-29</sup> in solution and then eliciting a chemical reaction between the generated species and the original cation to produce a film. This type of reaction is called an electrochemical-chemical (EC) reaction. The oxidation of  $\text{Fe}^{2+}$  (Eq. 2) and the chemical reaction (Eq. 3) that produce magnetite occur as follows:



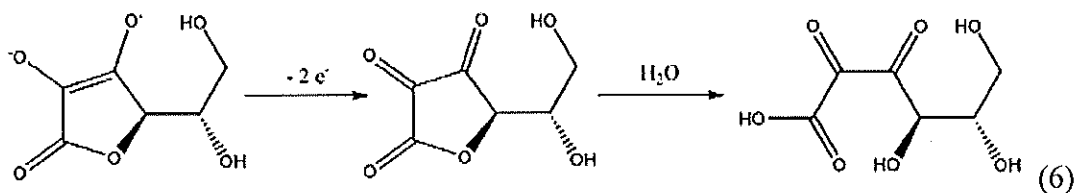
The reduction and chemical reaction to produce magnetite can be represented in Equations 4 and 5:





where TEA is triethanolamine, an iron(III) complexing agent.<sup>29</sup> The Switzer group has used electrochemical reduction and oxidation of metal cations to produce materials such as  $\text{Cu}_2\text{O}$ ,<sup>3-7,13,14,30,31</sup>  $\text{Fe}_3\text{O}_4$ ,<sup>19,27-29</sup>  $\text{Tl}_2\text{O}_3$ ,<sup>32,33</sup>  $\text{AgO}$ ,<sup>34</sup>  $\text{Bi}_2\text{O}_3$ ,<sup>35,36</sup>  $\text{PbO}_2$ ,<sup>37</sup> and metal oxide superlattices.<sup>38-43</sup> This dissertation describes the use of this method to produce  $\text{CeO}_2$ ,<sup>15</sup>  $\text{Fe}_3\text{O}_4$ , and  $\text{ZnFe}_2\text{O}_4$ .

**1.1.2 Electrodeposition by pH Change.** A second method to produce films such as metal oxides and biomaterials is to electrochemically change the pH of the electrolyte at the electrode surface. Initially, the cation in solution is stable and in its appropriate oxidation state for the film. Because the solubility of any material is dependent on pH, the pH can be electrochemically changed at the electrode surface, thus lowering the solubility of the material and resulting in the precipitation of the material only on the electrode surface. The pH can be decreased by electrochemically oxidizing water, ascorbate, hydroquinone, and other organics to produce materials like zinc oxide. ZnO nanospears have been deposited from an alkaline solution by oxidizing ascorbate, which lowered the pH at the electrode surface.<sup>44</sup> This ZnO deposition occurs as follows:



Likewise, the pH can be electrochemically increased by reducing water, molecular oxygen, nitrate, peroxide, or organic molecules such as quinones to produce

biomaterials and films such as zinc oxide. For instance, biominerals such as calcium carbonates can be produced by the following EC reactions:<sup>45</sup>



The Switzer group has produced ZnO,<sup>44</sup> CeO<sub>2</sub>,<sup>46,47</sup> ZrO<sub>2</sub>,<sup>48</sup> and various biomaterials<sup>45</sup> by electrochemically changing the pH.

**1.1.3 Thermodynamics of Electrochemical Cells.** Whereas a galvanic cell produces current when a reaction proceeds spontaneously, an electrolytic cell uses electrical energy to produce chemical change by an otherwise nonspontaneous reaction. All cells are a combination of two half reactions, each of which is associated with a characteristic electrode potential. One of the half reactions involves oxidation, while the other involves reduction. In electrodeposition, the electrode at which oxidation occurs is called the anode; the electrode at which reduction occurs is called the cathode.

Each half reaction is written, by convention, as a reduction reaction, as seen in Equation 10:



where the oxidized ions are designated as ox, the reduced ions as red, and the number of electrons (e<sup>-</sup>) as n. The formal potential of each reversible half-cell reaction can be calculated by means of the Nernst equation:

$$E = E^\circ + \frac{RT}{nF} \ln \frac{[\text{ox}]}{[\text{red}]} = E^\circ + 2.303 \frac{RT}{nF} \log \frac{[\text{ox}]}{[\text{red}]} \quad (11)$$

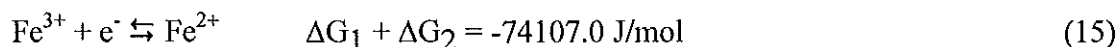
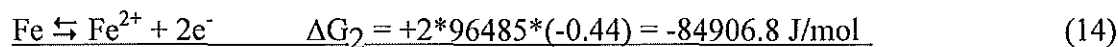
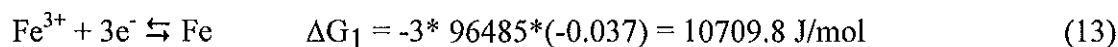
where E is the formal potential (V vs. reference electrode), E<sup>o</sup> is the standard reduction potential (V vs. reference electrode), R is the gas constant (8.314 mol<sup>-1</sup>K<sup>-1</sup>), T is temperature (K), n is the number of electrons in the reaction, and F is the Faraday's

constant ( $96485 \text{ C mol}^{-1}$ ). The standard reduction potential ( $E^\circ$ ) is equal to the formal potential ( $E$ ) when the reaction is at equilibrium and both the oxidized and reduced species are at unit activity. When the concentrations of these species are not at equilibrium, the formal potential ( $E$ ) for the reaction can be calculated using the Nernst equation. For instance, the formal potential moves toward more positive potentials when the concentration of the oxidized species is larger than that of the reduced species.

Standard reduction potentials are known for numerous half-reactions. Many have been determined directly from voltage measurements of cells. However, it is possible to calculate  $E^\circ$  values from thermodynamic values. The standard reduction potential ( $E^\circ$ ) for a half-cell can be calculated by Equation 12:

$$\Delta G^\circ = -nFE^\circ \quad (12)$$

where  $\Delta G^\circ$  is the Gibbs free energy,  $n$  is the number of electrons, and  $F$  is Faraday's constant ( $96485 \text{ C mol}^{-1}$ ). Using Equation 12, the two reduction reactions of  $\text{Fe}^{3+}/\text{Fe}$  ( $E^\circ = -0.037 \text{ V vs. NHE}$ )<sup>49</sup> and  $\text{Fe}^{2+}/\text{Fe}$  ( $E^\circ = -0.44 \text{ V vs. NHE}$ )<sup>49</sup> can be used to calculate the  $E^\circ$  for the reduction of  $\text{Fe}^{3+}$  to  $\text{Fe}^{2+}$  as follows:



Because the reaction in Equation 14 is written as an oxidation reaction, the sign changes. Therefore,  $E^\circ = -\Delta G_{\text{total}}/(nF) = -74107/(-1)/96485 = 0.77 \text{ V vs. NHE}$ . This value is consistent with the reported  $E^\circ = 0.771 \text{ V vs. NHE}$ .<sup>49</sup>

Many anions and molecules form complexes with metal cations. These metal complexes are normally more stable than the uncomplexed cations, and their increased stability can shift the potential. Based on thermodynamics, the equilibrium constant,  $K$ , is associated with free energy ( $\Delta G^\circ$ ) by Equation 16:

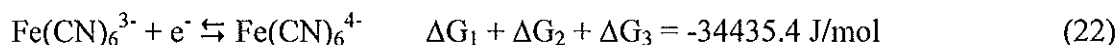
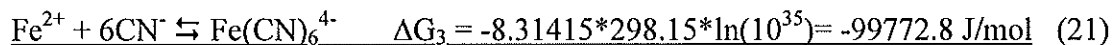
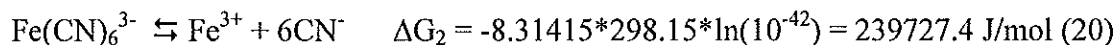
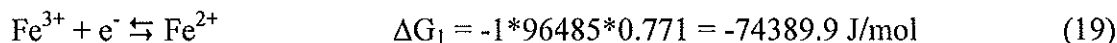
$$\Delta G^\circ = -RT \ln K \quad (16)$$

where  $R$  is the molar gas constant ( $8.314 \text{ mol}^{-1}\text{K}^{-1}$ ) and  $T$  is the absolute temperature (K). Using the equilibrium constant for the formation of the complex, the standard potential can also be calculated.

The  $E^\circ$  for a reaction can be calculated for any system with Equations 12 and 16 using known equilibrium constants and standard potentials. For example, the formation of  $\text{Fe}(\text{CN})_6^{3-}$  shown in Equation 17 has a  $K$  value of  $1 \times 10^{42}$ , whereas the formation of  $\text{Fe}(\text{CN})_6^{4-}$  has a  $K$  value of  $1 \times 10^{32}$  (Eq. 18).<sup>50</sup>



The  $E^\circ$  for the reduction of  $\text{Fe}(\text{CN})_6^{3-}$  can be calculated from the  $E^\circ$  for  $\text{Fe}^{3+}/\text{Fe}^{2+}$  (0.771 V vs. NHE)<sup>49</sup> and the iron cyanide  $K$  as shown below:



A sign change in the  $K$  value occurs in Equation 20 because the reaction is written as a dissolution reaction instead of a formation reaction such as that in equation 17. So,  $E^\circ = -\Delta G_{\text{total}}/(nF) = -34435.4/(-1)/96485 = 0.36 \text{ V vs. NHE}$ . This value is consistent with the

reported value of  $E^{\circ} = 0.356$  V vs. NHE.<sup>49</sup> Comparison of the reported values of the  $E^{\circ}$  of  $\text{Fe}^{3+}/\text{Fe}^{2+}$  to the  $E^{\circ}$  of  $\text{Fe}(\text{CN})_6^{3-}/\text{Fe}(\text{CN})_6^{4-}$  indicates that the reduction potential shifts to a more negative value by 0.415 V vs. NHE by complexing the  $\text{Fe}^{3+}$  and  $\text{Fe}^{2+}$  with cyanide, assuming the species involved are at unit activity.

**1.1.4 Electrochemical Characterization.**<sup>51-54</sup> Calculated potentials only indicate the possibility of a reaction. To characterize the electrochemical reactions occurring in solution, cyclic voltammetry, linear sweep voltammetry, chronoamperometry, and chronopotentiometry are used.<sup>51-54</sup> Cyclic and linear sweep voltammetry are used in electrodeposition to classify the electrochemical reactions in solution, to study the effect of additives on the system, and to determine the conditions necessary to deposit a film. The range of potentials that can be used in aqueous solutions depends upon the electrode material and the composition of the electrolyte. Chronopotentiometry and chronoamperometry are used to determine the kinetics of a system and to monitor the electrochemical reactions. In all the electrochemical plots in this dissertation, cathodic currents are always negative values whereas anodic currents are positive.

**1.1.4.1 Modes of Mass Transfer.**<sup>51-54</sup> A main component of electrochemical reactions is the movement of the reactant to the electrode surface. The reactant is carried to the surface of the electrode by three modes of mass transfer: migration, convection, and diffusion. Migration is the movement of ions under the influence of an electric field. Convection is movement of a volume of solution by hydrodynamic or mechanical stirring. In diffusion, the movement is due to the concentration differences between the solution at the electrode surface and the bulk solution. Electrochemical experiments can be designed to minimize the effect of one or more modes of mass transfer. Although

diffusion cannot be eliminated in electrolysis, convection can be avoided by preventing stirring or vibrations in the solution. The effect of migration can be minimized by the addition of a supporting electrolyte. An excess of an inactive supporting electrolyte is added normally to the deposition solution to increase its conductivity. This addition also reduces the resistance between the working electrode and the counter electrode to help maintain a uniform current and potential distribution. Finally, it reduces the resistance between the working electrode and the reference electrode to minimize potential error. When the concentration of the supporting electrolyte is normally 100 times greater than that of the electrochemically active species, the majority of the current is carried by the supporting electrolyte. As a result, the rate of migration of the active species towards the electrode of opposite charge is not dependent on the applied potential.

**1.1.4.2 Cyclic Voltammetry.**<sup>51-54</sup> In cyclic voltammetry (CV), the potential is varied at a constant scan rate (the rate of change of the potential), and the resulting current response is plotted versus the applied potential. A cyclic voltammogram is run in quiescent solutions, diminishing convection. Migration is also minimized by adding a supporting electrolyte to the deposition bath. Therefore, diffusion is the primary means to transfer the reactant to the electrode surface in cyclic voltammetry.

The potential separation between the anodic and cathodic peak indicates the reversibility of the reaction. By running CVs at different scan rates, the anodic and cathodic peaks can be characterized. For example, if the peak current increases linearly as the scan rate increases, then a *surface* species is being oxidized or reduced. If the peak current increases linearly with the square root of the scan rate, then the reaction is limited by diffusion of the *solution* species.

Figure 1 shows a CV of the alkaline Fe(III)-TEA bath at 80°C; this bath is described in Papers II and III. The working electrode was a stationary gold rotating disk electrode ( $A = 0.196 \text{ cm}^2$ ), and the scan rate was 50 mV/s. A CV generally starts at the open circuit potential of the system, at which the current is zero. Normally in these scans, the positive potential is limited by the large currents that develop due to the oxidation of water to molecular oxygen. The negative potential limitation is due to the reduction of water to hydrogen gas. In this CV, the potential was varied from -0.43 V to -1.25 V vs. Ag/AgCl, at which point the potential was returned to -0.43 V vs. Ag/AgCl. Initially, no significant current was observed between -0.43 V to -0.95 V vs. Ag/AgCl because the Fe(III) is not reduced at these potentials. As the potential became more negative, the beginning of the reduction peak was at -0.95 V vs. Ag/AgCl where the Fe(III) began to be reduced to Fe(II). With a further decrease in potential, the thickness of the diffusion layer increased as more Fe(III) was reduced to Fe(II). At the cathodic peak potential of -1.15 V vs. Ag/AgCl, all of the Fe(III) at the electrode surface was immediately reduced to Fe(II). The amount of Fe(III) arriving at the electrode surface decreased as the diffusion layer continued to increase. This species limitation caused the current to decrease, resulting in a peak in the CV. Black films of magnetite ( $\text{Fe}_x\text{O}_y$ ) were deposited at potentials between -1.00 V and -1.08 V vs. Ag/AgCl. These films were produced through the EC reactions of Equations 4 and 5. The cathodic peak current density increased linearly with square root dependence as the scan rate was increased. This rate dependence suggests that this reaction is diffusion limited.

The potential was switched at -1.25 V vs. Ag/AgCl. The current was still cathodic even though the scan was moving towards more positive potentials. Potentials between

-1.25 V to -1.1 V vs. Ag/AgCl were still negative enough to reduce the Fe(III). Once the potential was positive enough that it no longer reduced the Fe(III), the current went to zero, and beyond this point, an anodic current was detected. If this reaction were reversible, these anodic currents would be attributed to Fe(II) being oxidized to Fe(III). This current would then decrease as the generated Fe(II) is depleted by the oxidation process. However, the anodic peak current density increased linearly as the scan rate increased. Therefore, the anodic peak is assumed to be due to the oxidation of a surface species, magnetite, to an iron(III) oxide or hydroxide.

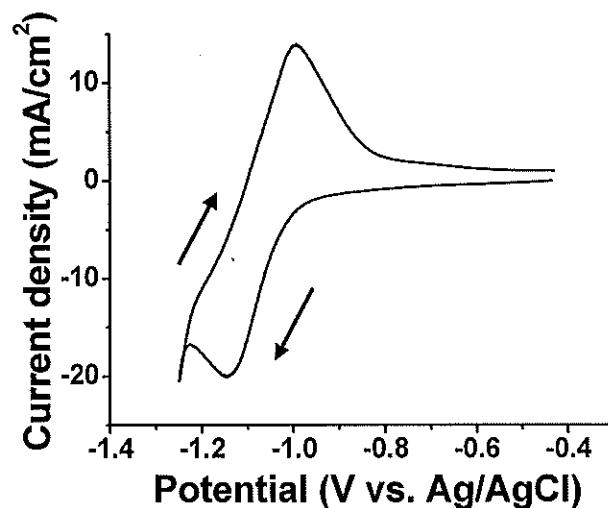


Figure 1. A CV of an alkaline Fe(III)-TEA bath at 80°C at a scan rate of 50 mV/s.

**1.1.4.3 Linear Sweep Voltammetry.**<sup>51-54</sup> A linear sweep voltammogram (LSV) consists of only the forward sweep of a CV. Typically, CVs are run in quiescent solutions, whereas LSVs can be run in quiescent or stirred solutions. Like CVs, when the solution is

not stirred, a peak occurs in the scan. This peak is due to the diffusion layer continuing to increase at potentials where the electroactive species is reduced or oxidized. In a stirred solution, no peak occurs; instead, the scan plateaus because the thickness of the diffusion layer remains relatively constant. The transport of electroactive species to the electrode surface is convection controlled. For stirred solutions, a rotating disc electrode is normally used. This allows for reproducible rotation speeds, which result in reproducible limiting currents. Similar to CV, LSV is used in electrodeposition to classify the electrochemical reactions in solution. It is also used to study the effect of additives on the system and to determine the conditions necessary to deposit a film. To determine the appropriate contribution to the limiting current, a LSV of the deposition solution without the electroactive species is run for comparison. (citations)

An example of this procedure is described in Papers II and III. Figure 2 shows the results of LSV of the alkaline Fe(III)-TEA bath (black line) and of an alkaline TEA solution (blue squares) at 80°C, both run at a scan rate of 50 mV/s. For the working electrode, a rotating gold disc electrode was revolved at 100 rpm for the LSV. The first wave was the (A) reduction of Fe(III) to Fe(II), and the second wave was the (C) reduction of Fe(II) to Fe. The constant current densities (B and D) beyond the steep declines are called the limiting current densities. They arise from the limitation in the rate at which the reactant is brought to the surface of the electrode by the mass-transport processes. The limiting current density (B), where all of the Fe(III) is reduced to Fe(II), was  $-14.7 \text{ mA/cm}^2$ . The limiting current density (D), where the Fe(II) is reduced to Fe, was  $-56.5 \text{ mA/cm}^2$ . The height of the second wave (C) was roughly twice that of the first wave (A) because the second wave was a two-electron process, whereas the first was a

one-electron process. Based on the LSV of the base electrolyte (blue squares), the excess current density of the second wave can be credited to the competing reaction of water reduction. An additional contribution to this current difference may be attributable to the change in electrode material and area due to magnetite deposition.

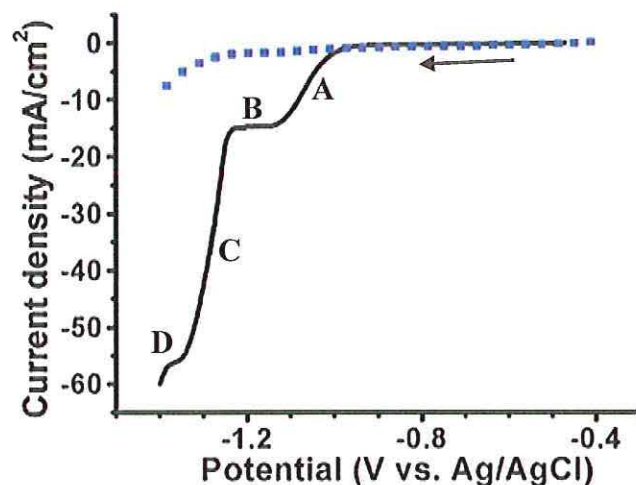


Figure 2. The linear sweep voltammograms of an alkaline TEA solution (blue squares) and Fe(III)-TEA solution (black solid line) at 80°C scanned at 50 mV/s at a rotation of 100 rpm on a gold rotating disk electrode. The alkaline TEA solution consisted of 0.1 M TEA in 2 M NaOH. The alkaline Fe(III)-TEA solution consisted of 43 mM Fe<sub>2</sub>SO<sub>4</sub>, 0.1 M TEA, and 2 M NaOH.

The surface concentration of Fe(III) is dependent on the departure from equilibrium, which is controlled through the applied potential. Assuming convective control, the surface concentration can be calculated from Equation 23:

$$\frac{i}{i_l} = \frac{C_{\text{Fe(III)}}(\text{bulk}) - C_{\text{Fe(III)}}(\text{surface})}{C_{\text{Fe(III)}}(\text{bulk})} \quad (23)$$

where  $i$  is the measured current,  $i_l$  is the limiting current,  $C_{\text{Fe(III)}}(\text{bulk})$  is the bulk concentration of Fe(III) in solution, and  $C_{\text{Fe(III)}}(\text{surface})$  is the concentration of Fe(III) at the electrode surface.<sup>51</sup> At the open circuit potential, the surface concentration of Fe(III) was equal to the bulk concentration of Fe(III), making the numerator of Equation 24 equal to 0. Therefore, the ratio of the measured current to the limiting current would be equal to 0, as seen in Equation 24.

$$\frac{i}{i_l} = \frac{[C_{\text{Fe(III)}}(\text{bulk}) - C_{\text{Fe(III)}}(\text{bulk})]}{C_{\text{Fe(III)}}(\text{bulk})} = \frac{0}{C_{\text{Fe(III)}}(\text{bulk})} = 0 \quad (24)$$

As the potential became more negative, the current increased, and more Fe(III) is reduced to Fe(II). At the plateau in LSV, where the current was mass-transport limited, all the Fe(III) was reduced to Fe(II). Therefore, the surface concentration of Fe(III) at the electrode surface is 0. As seen in Equation 25, this ratio would be equal to 1.

$$\frac{i}{i_{lc}} = \frac{[C_{\text{Fe(III)}}(\text{bulk}) - 0]}{C_{\text{Fe(III)}}(\text{bulk})} = \frac{C_{\text{Fe(III)}}(\text{bulk})}{C_{\text{Fe(III)}}(\text{bulk})} = 1 \quad (25)$$

For stoichiometric magnetite, 2/3 of the iron is Fe<sup>3+</sup> and 1/3 is Fe<sup>2+</sup>. To produce stoichiometric magnetite, therefore, the Fe(III) surface concentration must equal 2/3 of the bulk concentration of Fe(III) or where the current ratio is equal to 1/3:

$$\frac{i}{i_{lc}} = \frac{[C_{\text{Fe(III)}}(\text{bulk}) - \frac{2}{3}C_{\text{Fe(III)}}(\text{bulk})]}{C_{\text{Fe(III)}}(\text{bulk})} = \frac{\frac{1}{3}C_{\text{Fe(III)}}(\text{bulk})}{C_{\text{Fe(III)}}(\text{bulk})} = \frac{1}{3} \quad (26)$$

Figure 3 shows the plot of the ratio of current to the limiting current versus the applied potential. Stoichiometric magnetite would be deposited at approximately -1.045 V vs. Ag/AgCl, when 1/3 of the total concentration of Fe(III) would be reduced to Fe(II). Any

potential positive of this value should produce magnetite with excess Fe(III), whereas potentials more negative than -1.045 V should produce magnetite with excess Fe(II).

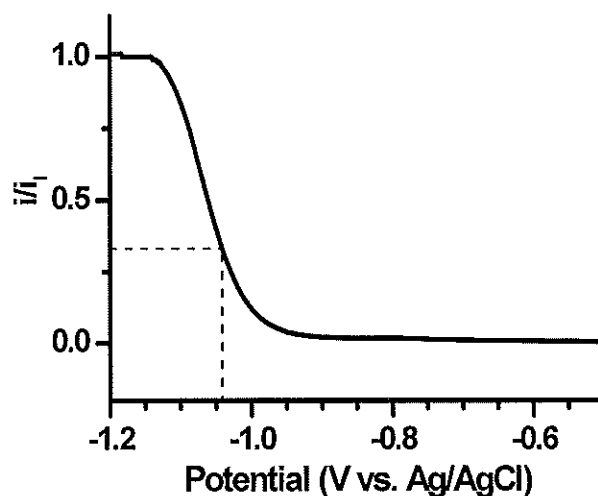


Figure 3. A plot of ratio of current to limiting current versus the applied potential based on the LSV of Figure 2. Based on this plot, stoichiometric magnetite should be produced where 1/3 of the Fe(III) has been reduced to Fe(II) at a potential of -1.045 V vs. Ag/AgCl as indicated by the dashed line.

**1.1.4.4 Chronopotentiometry and Chronoamperometry.**<sup>51-55</sup> Two additional electrochemical methods to monitor the electrochemical reactions are chronopotentiometry and chronoamperometry. In the former procedure, a constant current is applied while the potential is monitored and plotted versus time. In the latter, a potential is applied to the working electrode, and the resulting measured current is plotted versus time. These transients can indicate the nucleation and growth mechanism of the films.

The thickness of electrodeposited material can be controlled electrochemically by varying the deposition time in chronoamperometry or by varying the current density and

time in chronopotentiometry. Faraday's law (Equation 27) can be used to determine the theoretical film thickness:

$$T_{\text{theor}} = \frac{Q * MW}{n * F * A * \rho} \quad (27)$$

where  $T_{\text{theor}}$  is the theoretical film thickness calculated in cm,  $Q$  is charge passed in coulombs,  $t$  is time in seconds,  $MW$  is the molecular weight of the deposited material in g/mol,  $n$  is the number of electrons,  $F$  is Faraday's constant of 96485 C/mol,  $A$  is area in  $\text{cm}^2$ , and  $\rho$  is the density of the deposited material in  $\text{g}/\text{cm}^3$ . This calculation assumes that the reactions are 100% efficient and that the films are 100% dense. As stated above, side reactions can occur during the deposition process that can decrease the Faradaic efficiency. A more precise film thickness can be calculated if this efficiency is known.

The deposition efficiency can be determined using the electrochemical quartz crystal microbalance (EQCM).<sup>55</sup> This technique uses a mass-sensitive detector that measures frequency changes of an oscillating quartz wafer coated with a metal such as Au or Pt. As the mass of the crystal increases due to film deposition or adsorption, the frequency decreases. To determine the change in mass, the Sauerbrey equation can be used. The Sauerbrey equation is:

$$\Delta m = \frac{\Delta f * A * (\rho_{\text{quartz}} * \mu_{\text{quartz}})^{1/2}}{-2 * f_o^2} \quad (28)$$

where  $\Delta m$  is the change in mass in g,  $\Delta f$  is the change in measured frequency in Hz,  $A$  is the piezoelectrically active area in  $\text{cm}^2$ ,  $\rho_{\text{quartz}}$  is the density of quartz ( $2.648 \text{ g}/\text{cm}^3$ ),  $\mu_{\text{quartz}}$  is the shear modulus of quartz ( $2.947 \times 10^{11} \text{ dyn}/\text{cm}^2$ ), and  $f_o$  is the frequency of the

quartz crystal prior to a mass change in Hz. The theoretical mass can be calculated from the Faraday's Law:

$$m_{\text{theor}} = \frac{Q * MW}{n * F} \quad (29)$$

where  $m_{\text{theor}}$  is the theoretical mass in g,  $Q$  is the charge passed in C,  $MW$  is the molecular weight of the deposited material in g/mol,  $n$  is the number of electrons, and  $F$  is Faraday's constant of 96485 C/mol. The current efficiency of the deposition is the ratio of  $\Delta m$  divided by  $m_{\text{theor}}$ .

**1.1.5. X-ray Diffraction Characterization of Films.**<sup>56-59</sup> One of the most useful methods to characterize electrodeposited films is the nondestructive technique known as X-ray diffraction (XRD).<sup>56-59</sup> In a crystalline material, the atoms are arranged in a regular pattern. Diffraction occurs when the atomic plane of the crystal causes X-rays of the incident beam to interfere constructively. This interaction creates a diffracted X-ray beam, related to the interplanar spacing in the crystal by Bragg's law:

$$n\lambda = 2d_{hkl}\sin\theta \quad (30)$$

where  $n$  is an integer 1, 2, 3, etc. normally designated as 1,  $\lambda$  is the wavelength in angstroms which is dependent on the source ( $\text{Cu}_{k\alpha}$  is 1.54 angstroms),  $d_{hkl}$  (d-spacing) is the distance between atomic layers known as the interplaner spacing (not the spacing between the atoms on a single plane) in the crystal measured in angstroms, and  $\theta$  is the diffraction angle in degrees.<sup>56-59</sup> Therefore, diffraction occurs when Bragg's law is met.

Traditionally, X-ray diffraction patterns are a plot of intensity versus  $2\theta$ . Each of the incident and diffracted X-rays makes an angle,  $\theta$ , with the atomic plane. From the reflection of the plane, the angle from the incident beam to the diffracted beam is  $2\theta$ .

Therefore, the possible  $2\theta$  values are determined by the unit cell parameters of the material. The intensities of the reflections are determined by the distribution of the electrons in the unit cell. The highest electron density is found around atoms. Therefore, the intensities depend on the type of atoms and their location in the unit cell. Planes with high electron density will reflect x-rays strongly; planes with low electron density will reflect x-rays weakly.

Different planes of atoms produce different diffraction peaks, which contains information about the atomic arrangement within the crystal. Therefore, every crystalline material has a unique X-ray diffraction pattern. This pattern can be used to determine the crystallinity and phase of the deposited material. The lattice parameters of a material can be calculated from the peaks by properly assigning Miller indices (hkl) and accurately measuring the d-spacings. Additionally, broad peaks found in some diffraction patterns can be used to determine both the particle size and any residual strain of the sample by Williamson-Hall analysis. Because multiple peaks in the X-ray patterns improve material recognition and characterization of particle size, strain, and lattice parameter values, X-ray patterns of powders or polycrystalline films grown on polycrystalline substrates are used for identification and characterization.

Besides polycrystalline substrates, single crystalline substrates are used in electrodeposition. Usually, low-index single crystals such as Au(001), Au(111), Si(111), and InP(110) are used. Single crystals eliminate the presence of grains of various orientations, which may have different film growth rates (see Appendix A for further information). Films electrodeposited on these substrates tend to be epitaxial. If a

crystalline film grows with an out-of-plane and in-plane orientation that is dependent on the orientation of the substrate, the film is said to be epitaxial.

The properties of epitaxial films depend on the substrate. The film will have better crystalline quality and more uniform morphology when fewer defects are present on the substrate. Generally, an epitaxial film will deposit with an orientation providing the lowest lattice mismatch with the substrate. In some cases, the film will become strained or will rotate to obtain this low mismatch. Thus, different substrates will produce different orientations of the film. Since properties of a material can be dependent on the orientation, this control over selection of orientation permits optimization of the properties of a deposited material. Epitaxial films are useful in device applications, since the intrinsic properties of the material can be exploited rather than its grain boundaries.

Characterization of epitaxial films involves X-ray characterization such as diffraction patterns, pole figures, azimuthal scans, and rocking curves. For example, the diffraction pattern of a polycrystalline film is different than that of an epitaxial film. Whereas a polycrystalline film has all possible planes, resulting in multiple peaks in the pattern, an epitaxial film will normally grow with one orientation and show only a family of planes in the pattern. In Figure 4, magnetite films are deposited on (A) a stainless steel polycrystalline substrate and (B) a (111) gold single crystal. The sample is stationary and the X-ray source and the detector are moved simultaneously over an angular range. The X-ray diffraction patterns are plots of intensity as a function of  $2\theta$ . In Figure 4A, three of the peaks are due to the iron substrate; these are indicated with SS. Comparison of the locations and intensities of the remaining peaks to the JCPDS #19-0629 for magnetite in this range indicates that all the peaks of magnetite are present and the film has no

preferred orientation. No other peaks are present; no other crystalline material is present in the film. In Figure 4B, a magnetite film electrodeposited on Au(111) has only the (111) family peaks of magnetite. Peaks related to the substrate are labeled with Au.

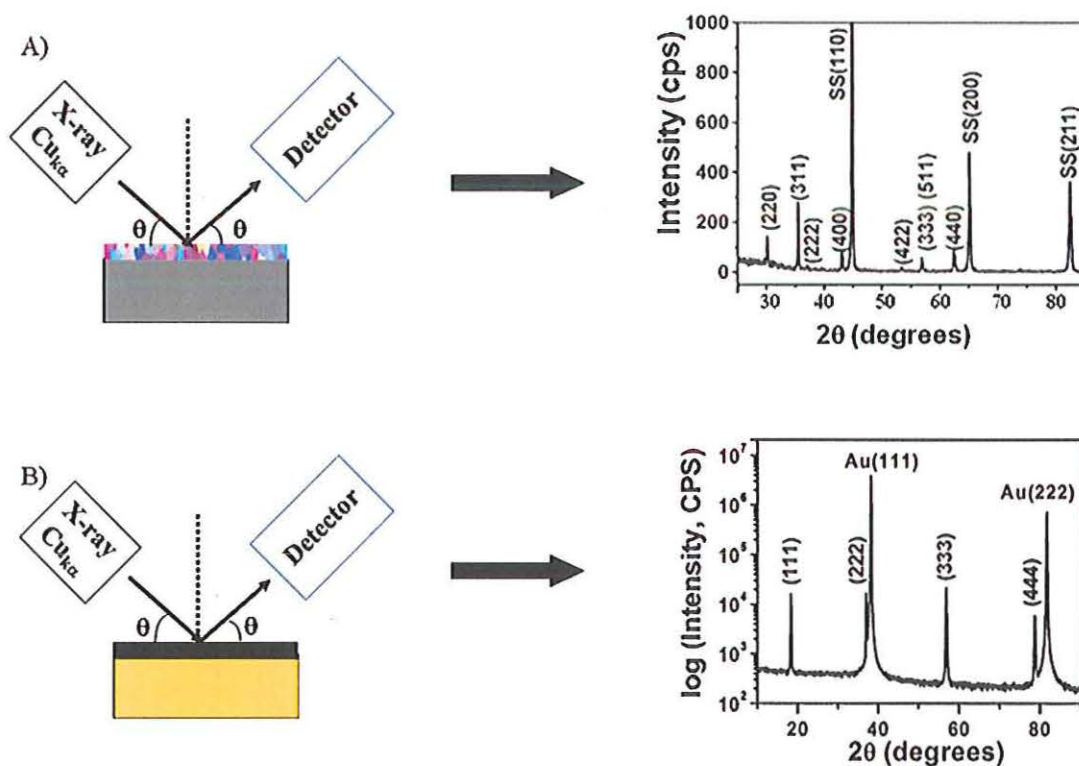


Figure 4. Illustrations and X-ray diffraction patterns of A) a polycrystalline magnetite film on stainless steel and B) a (111) oriented magnetite film on a Au(111) single crystal. The films were deposited from an alkaline Fe(III)-TEA bath at 80°C by applying a constant potential of -1.01 V vs. Ag/AgCl for 100 s.

However, this strong out-of-plane texture does not provide proof of an epitaxial film. An epitaxial film has both out-of-plane and in-plane orientation. To determine the

in-plane orientation distribution of the grains of the film, X-ray pole figures and azimuthal scans are run. A pole figure probes reflections of planes that are oriented in-plane with respect to the sample normal while measuring the diffracted intensity as a function of sample tilt ( $\chi$ ) and rotation ( $\phi$ ). As illustrated in Figure 5 (top), to perform the pole figure analysis, the  $2\theta$  is set to the angle of the plane (reflection) of interest, normally the orientation with the highest intensity of a randomly oriented powder diffraction pattern of the material. The  $2\theta$  value is held constant. For the magnetite pole figure, the  $2\theta$  is set to  $35.45^\circ$  of the (311) reflection. The  $2\theta$  of the (311) pole figure of the Au(111) substrate is set to  $77.62^\circ$ . The sample is moved through a sequence of tilt angles,  $\chi$ , from  $0^\circ$  to  $90^\circ$ , and at each  $\chi$ , the sample is rotated azimuthally,  $\phi$ , from  $0^\circ$  to  $360^\circ$ . A peak results when Bragg's condition is met. In Figure 5 (bottom), an azimuthal scan can be considered a cross-section of a pole figure. Such a scan is obtained when the measurement is carried out at a specific  $2\theta$  for only one specific tilt angle,  $\chi$ , and rotated azimuthally,  $\phi$ , from  $0^\circ$  to  $360^\circ$ . Again, a peak results when Bragg's condition is met. For the azimuthal scans in the lower image of Figure 5, the  $2\theta$  values are the same as those used in the pole figures. The specific tilt angle is  $28.5^\circ$ . Pole figures and azimuthal scans are performed on the film and substrate to determine the alignment of the film on the substrate and the number of domains of the film.

As shown in Figure 5 (bottom), two domains of magnetite are aligned on the one domain of the gold substrate. The two alignments of this magnetite film on Au(111), known as the epitaxial relationships, can be expressed as  $\text{Fe}_3\text{O}_4(111)[01\bar{1}]//\text{Au}(111)[0\bar{1}1]$  for the antiparallel domain and

$\text{Fe}_3\text{O}_4(111)[0\bar{1}1] // \text{Au}(111)[0\bar{1}1]$  for the parallel domain. That is, for the dominate domain (antiparallel), the  $\text{Fe}_3\text{O}_4(111)$  and  $\text{Au}(111)$  planes are parallel, and the  $\text{Fe}_3\text{O}_4[01\bar{1}]$  and  $\text{Au}[0\bar{1}1]$  in-plane directions are coincident. Similarly, for the parallel domain, the  $\text{Fe}_3\text{O}_4(111)$  and  $\text{Au}(111)$  planes are parallel but the  $\text{Fe}_3\text{O}_4[0\bar{1}1]$  and  $\text{Au}[0\bar{1}1]$  in-plane directions are coincident.

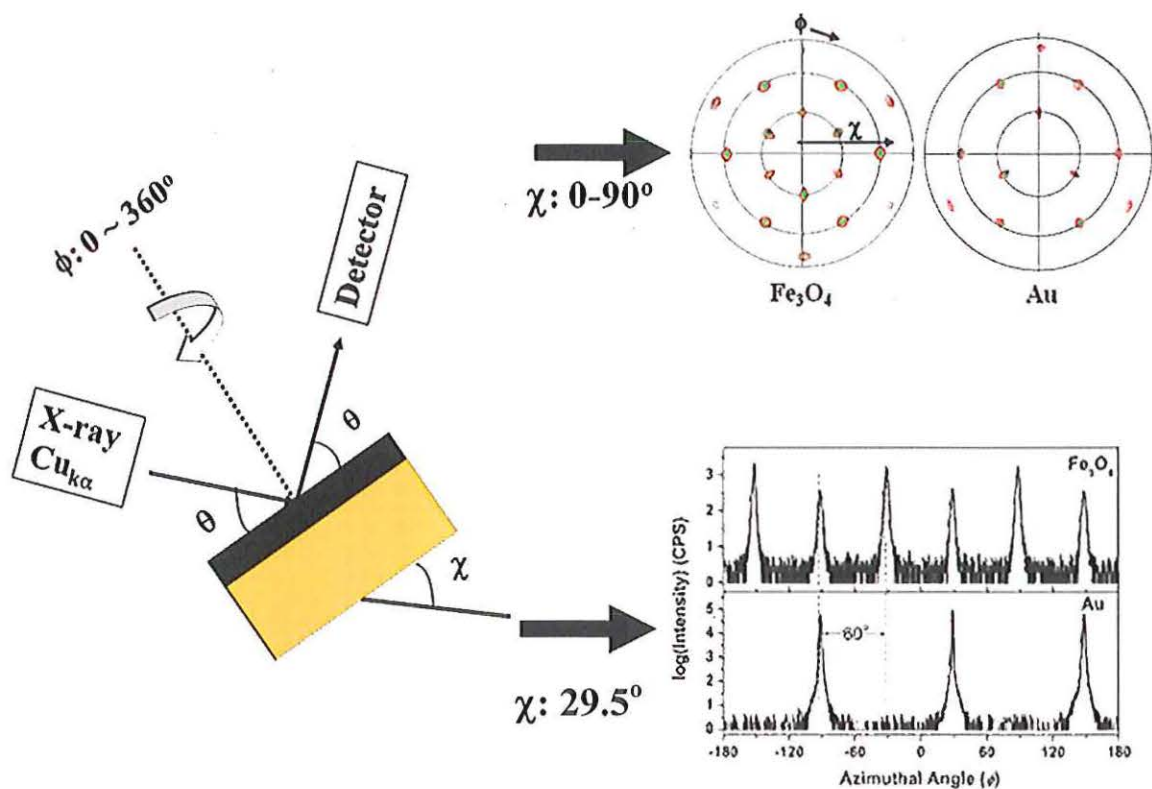


Figure 5. An illustration of the method to produce a (311) magnetite pole figure of a (111) oriented magnetite film (top) and (311) azimuthal scans of a (111) oriented magnetite film on  $\text{Au}(111)$  (bottom). The radial grid lines on the pole figures correspond to  $30^\circ$  increments of the tilt angle,  $\chi$ .

To further clarify the pole figure analysis, Figure 6 shows the morphologies and (311) pole figure results of three different depositions of a cubic material such as magnetite on a substrate. As seen in Figure 6A, a polycrystalline film has no out-of-plane or in-plane orientation. Therefore, a pole figure on this sample would have uniform intensity at all tilt and azimuthal angles (Figure 6D). Figures 6B and 6C show films with (111) out-of-plane orientation. The deposits of Figure 6B have multiple in-plane orientations known as a fiber texture, whereas the deposits of Figure 6C are aligned in one in-plane orientation, an example of epitaxial growth. A (111) fiber-textured film has a ring pattern pole figure at azimuthal angles,  $\chi$ , equal to  $29.5^\circ$ ,  $58.5^\circ$ , and  $80^\circ$  as seen in Figure 6E, whereas the (111) epitaxial film with one domain has a pole figure with three peaks at  $\chi = 29.5^\circ$  and  $\chi = 80^\circ$  and six peaks at  $\chi = 58.5^\circ$  as seen in Figure 6F. The ring pattern in Figure 6E can be understood with reference to Figure 6F. Since the deposits in Figure 6B are rotated azimuthally with respect to one another, each aligned set would produce three peaks at  $\chi = 29.5^\circ$  and  $\chi = 80^\circ$  and six peaks at  $\chi = 58.5^\circ$ . These sets of peaks are slightly rotated azimuthally from each other. Therefore, a pole figure of a fiber-textured film is a product of multiple sets of peaks rotating azimuthally and converging to form a ring.

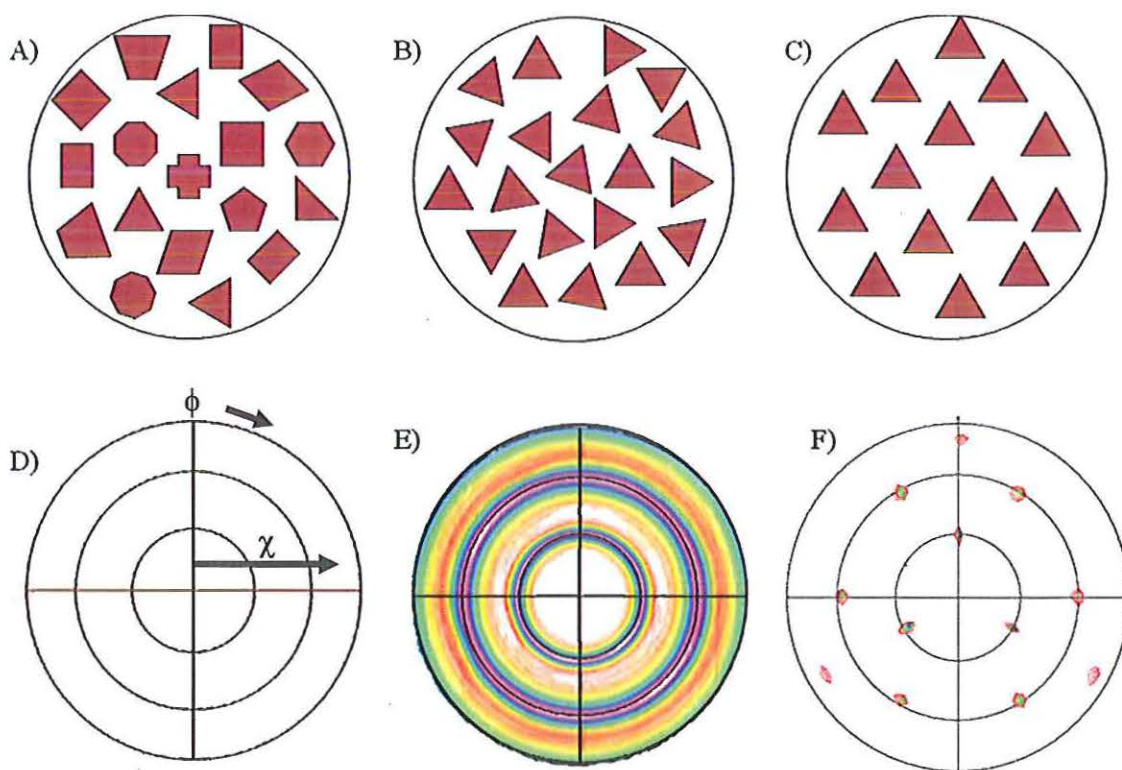


Figure 6: Illustrations of the cubic material magnetite ( $\text{Fe}_3\text{O}_4$ ) as A) a polycrystalline film on stainless steel, B) a (111) fiber-textured film on stainless steel, and C) a (111) epitaxial film on Au(111). (311)  $\text{Fe}_3\text{O}_4$  pole figures of a D) polycrystalline, E) (111) fiber-textured, and F) (111) epitaxial films. A polycrystalline film has no out-of-plane or in-plane orientation. Therefore, this sample would have uniform intensity in a pole figure. A randomly ordered film known as a fiber texture has a pole figure with a ring pattern whereas an epitaxial film has a pole figure with separated peaks. The radial grid lines on the pole figures correspond to  $30^\circ$  increments of the tilt angle,  $\chi$ .

Pole figures can also be used to determine the number of domains in the film. For example, Figure 7 shows (111) oriented films with A) one domain, B) two domains, and C) four domains. Below each illustration is the corresponding (311) pole figure of a (111) oriented cubic material. The number of domains can be determined from number of peaks at  $\chi = 29.5^\circ$  in the pole figure. For a (111) oriented film with one domain, the pole

figure has three peaks at  $\chi = 29.5^\circ$  as seen in Figure 7D. A film with two domains will have six peaks, or two sets of three peaks, (Figure 7E) at  $\chi = 29.5^\circ$ , whereas a film with four domains will have twelve peaks, or four sets of three peaks (Figure 7F).

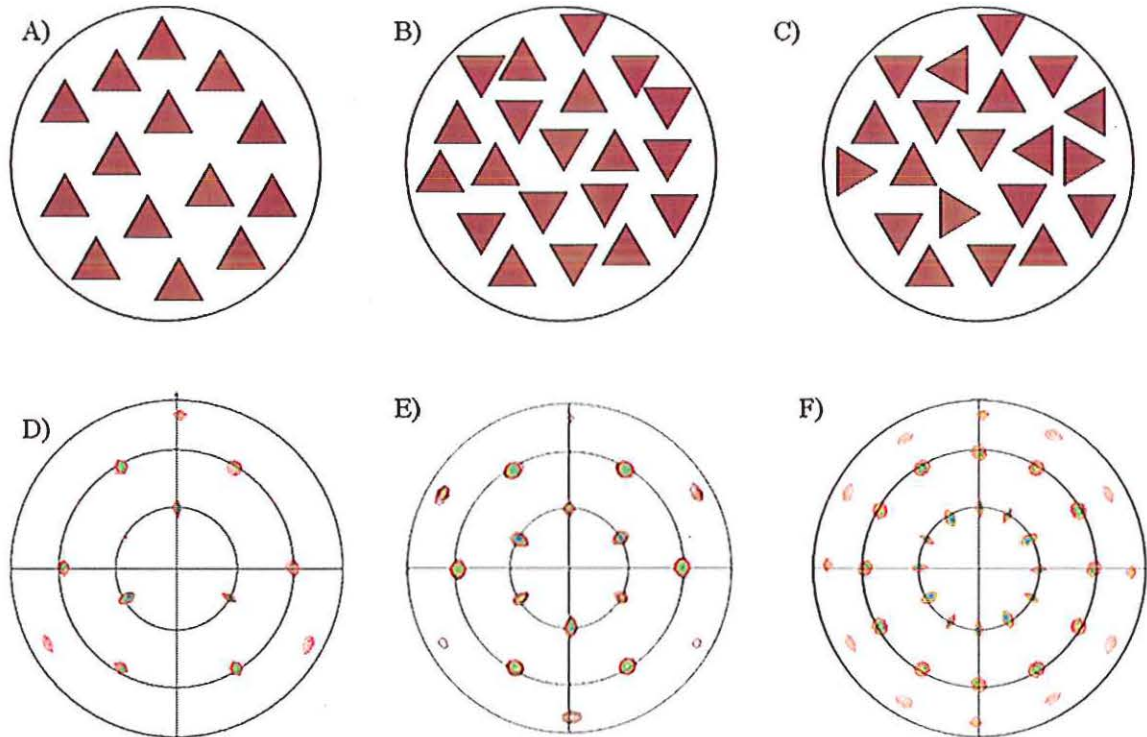


Figure 7: Illustrations of the cubic material magnetite ( $\text{Fe}_3\text{O}_4$ ) as a (111) epitaxial film on Au(111) with A) one domain, B) two domains, and C) four domains. (311)  $\text{Fe}_3\text{O}_4$  pole figures of (111) epitaxial films with D) one domain, E) two domains, and F) four domains. The radial grid lines on the pole figures correspond to  $30^\circ$  increments of the tilt angle,  $\chi$ .

Azimuthal scans produce results similar to those given by pole figures. If the sample has an in-plane orientation, the azimuthal scan will show separated peaks at a specific tilt, as shown in Figure 5 (bottom). If the sample has a fiber texture, the

azimuthal scan will show equal intensity rather than peaks, higher than the baseline at a specific tilt. For a polycrystalline film, the azimuthal scan will show a plot with baseline intensity at any tilt. Azimuthal scans are also used to determine the number of domains, the alignment of the domains on the substrate, and the relative percentage of one domain over the others.

Once an epitaxial film is produced, other X-ray diffraction analyses are performed on the film and substrate. Specifically, X-ray rocking curves are run indicating the mosaic spread of the films relative to the substrate. The larger the mosaic spread, the larger the full width at half maximum. These curves measure the crystallographic quality (i.e., the mosaic spread) of the films relative to the substrate. Mosaic spread is the misorientation of domains. In a perfect crystal, all domains are aligned and no atomic dislocations are present; there is no mosaic spread. A large mosaic spread means poor crystal quality. For a rocking curve (Figure 8), the  $2\theta$  is set to a single diffraction peak, one of the family orientations present in the X-ray pattern of the epitaxial film. A rocking curve is performed by "rocking" the sample, or the source and detector, bringing each grain into Bragg's condition. The width of the rocking curve is a direct measurement of the range of orientation of the sample.<sup>56</sup> As seen in Figure 8A, when the film is highly ordered, the full width at half maximum (FWHM) of the rocking curve peak is small. Rocking curves with broader peaks (greater FWHM) have larger mosaic spreads (Figure 8B). The rocking curves of the film and of the substrate are performed for mosaic spread comparison. These mosaic spreads of the film and the substrate are also seen in pole figures. The peaks in the pole figure become sharper and more intense when the film is more ordered.

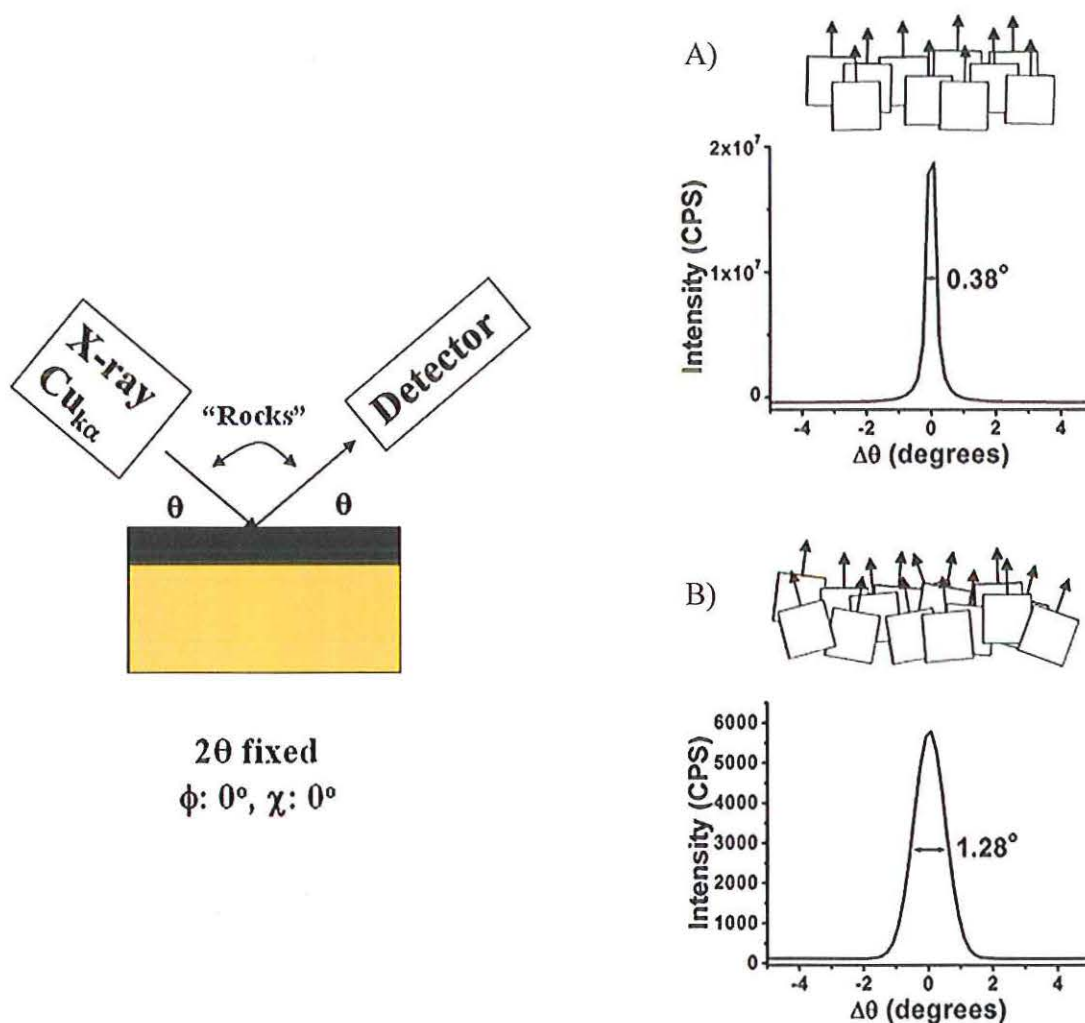


Figure 8. Mosaic spreads and rocking curves of two films. A) A film with a small mosaic spread will have a sharp rocking curve with a low full width at half maximum (FWHM). B) A film with a large mosaic spread will have a broad rocking curve with a big FWHM.

A superlattice is a periodic structure with alternating layers of crystalline materials.<sup>2</sup> Superlattices are characterized by XRD patterns since the periodicity appears as satellites around the main Bragg peak. The fundamental reflection, or main Bragg peak, is the "0" peak. The satellite peaks toward higher angles, to the right of the main

Bragg peak, are labeled +1, +2, and so on, whereas satellites are labeled -1, -2, etc. toward smaller angles. The modulation wavelength ( $\Lambda$ ), the bilayer thickness of two alternating materials, can be calculated from the satellite spacing using Equation 27:

$$\Lambda = \frac{\lambda(L_1 - L_2)}{2(\sin \theta_1 - \sin \theta_2)} \quad (27)$$

Here,  $\lambda$  is the wavelength of the X-ray source (Cu  $K_{\alpha}$  1.5401 Å) used,  $L$  is the order of the reflection, and  $\theta$  is the diffraction angle of the reflection. As the  $\Lambda$  increases, the satellites move closer to the main Bragg peak. Eventually, no satellites are seen and two separate peaks exist, one for each material of the bilayer. Ultimately, no satellites are seen as the  $\Lambda$  decreases. The intensity of the satellites decreases as they move farther from the main peak and disappear into the background intensity.

Magnetite and zinc ferrite superlattices (Paper III) are produced by electrodeposition. A comparison between an epitaxial magnetite film and a magnetite superlattice on Au(111) is shown in Figure 8. In both cases, films deposit with a [111] orientation as seen in Figures 9A and 9B. However, the difference in the two scans is visible around the (333) and (444) peaks of films. The (444) peaks for magnetite and the magnetite superlattice are shown in Figures 9C and 9D, respectively. Whereas the magnetite film shows a single peak, the superlattice with 100 layers shows one main peak flanked by a smaller peak on each side. Using Equation 27, the modulation wavelength of this superlattice was calculated to be 20.7 nm.

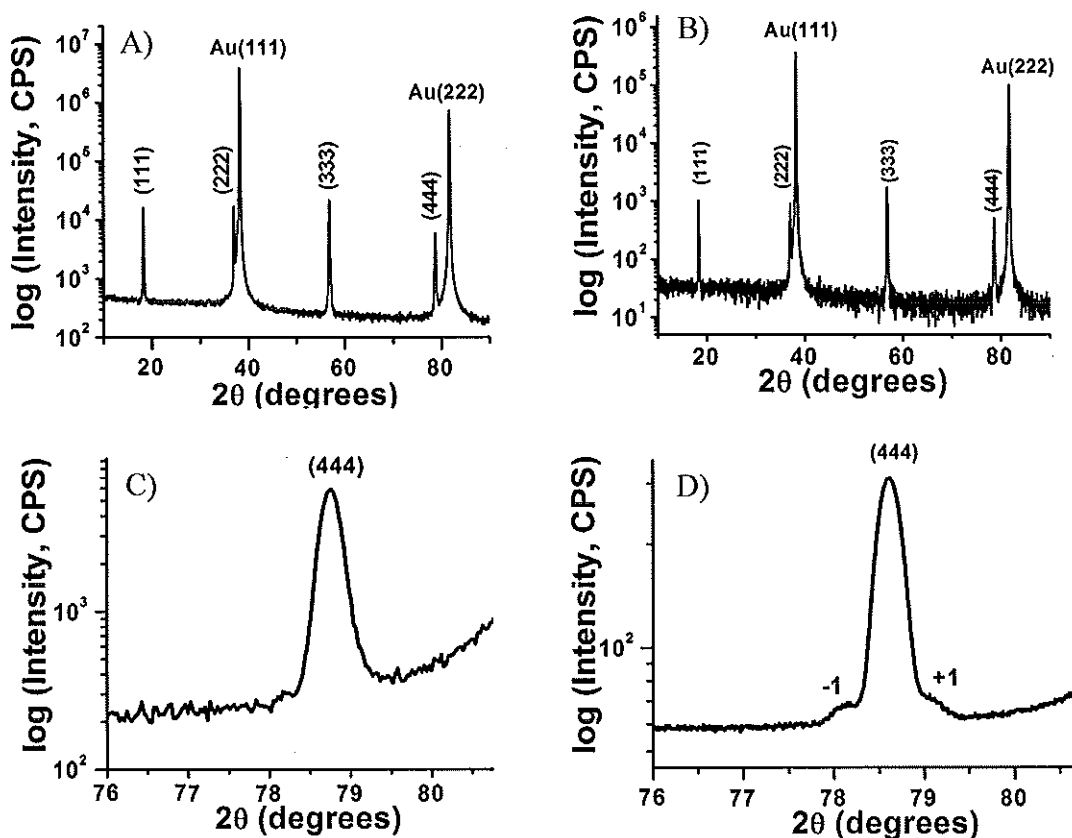


Figure 9. X-ray diffraction patterns for the [111] oriented A) magnetite and B) magnetite superlattice on Au(111). The (444) peak of the C) magnetite and D) superlattice. In D, satellite peaks are present. The modulation wavelength of the magnetite superlattice is 20.7 nm. The films were deposited from an alkaline Fe(III)-TEA bath at 80°C. A potential of -1.01 V vs. Ag/AgCl was applied for the magnetite film. For the superlattice, the potential was pulsed 100 times between -1.01 V vs. Ag/AgCl for 3s and -1.05 V vs. Ag/AgCl for 1s.

**1.1.6 Other Film Characterization Techniques.** Many other techniques are used to characterize an electrodeposited film. In this dissertation, the film morphology, particle size, and cross-sectional film thickness is examined by scanning electron microscopy (SEM).<sup>60</sup> Coupled with an SEM, an energy-dispersive spectroscopy (EDS)

system is used to detect characteristic X-rays of elements produced by the electrons of the SEM source interacting with the sample. The energy of the peak is characteristic of an element and the intensity of the peak indicates the amount of the element present in the sample. To measure film thickness and particle size as well as film morphology, atomic force microscopy (AFM) is used.<sup>61</sup> In addition, X-ray photoelectron spectroscopy (XPS) is used to determine the elemental and chemical composition of the film. Auger electron spectroscopy (AES) is used to characterize the elemental composition and to perform depth profiling.<sup>62</sup> Mössbauer spectroscopy, routinely used for iron compounds, provides information about the chemical and structural properties of a sample.<sup>63</sup> In this dissertation, electrochemical techniques, XRD, and SEM are used for characterizing all of the films. The other techniques mentioned above may be used depending on the chemical composition and physical properties of the deposited material.

## 1.2 CERIA

Paper I involves a discussion of the mechanism for electrodepositing a polycrystalline insulator, ceria ( $\text{CeO}_2$ ), onto Hastelloy substrates, and the characterization of these deposits. The crystal structure of ceria is shown in Figure 10. Ceria is a cubic material, space group  $Fm\bar{3}m$ , with a lattice parameter of  $a = 0.5411$  nm. It has the calcium fluorite structure consisting of four cerium and eight oxygen atoms per unit cell. Due to its insulating behavior,  $\text{CeO}_2$  films are researched for numerous applications such as buffer layers for superconducting<sup>64,65</sup> and ferroelectric films.<sup>66-68</sup> Ceria and doped-ceria have been used for every component of solid oxide fuel cells.<sup>69-84</sup> Ceria-based materials are also used in gas desulfurization and automotive exhaust gas conversion due

to their ability to acquire and release oxygen under oxidizing and reducing conditions.<sup>85,86</sup> Although many vacuum based methods have been used to produce ceria, electrodeposition is an attractive option due to its low cost and low processing temperatures. Ceria films have been electrochemically prepared by cathodic<sup>46,47,87-89</sup> and anodic<sup>15-17</sup> deposition. Previously, during the oxidation of Ce(III) to ceria, the films became highly cracked, exhibiting a dried mud morphology.<sup>15-17</sup> Paper I describes the production of films by anodic deposition, in which the mechanism of ceria deposition depends on the applied potential. A film deposited at +0.5 V vs. Ag/AgCl has a smooth surface from the direct oxidation of Ce(III) to nanocrystalline CeO<sub>2</sub> at the electrode surface. A film deposited at +1.1 V vs. Ag/AgCl has a cracked surface. At this potential, molecular oxygen is generated at the electrode surface resulting in the indirect oxidation of Ce(III) to nanocrystalline CeO<sub>2</sub> in the bulk solution.

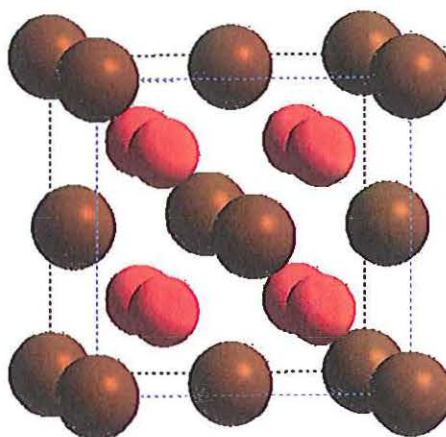


Figure 10. The crystal structure of ceria. Ceria is a face-centered cubic material, space group Fm3m, with a lattice parameter of 0.5411 nm. The brown atoms represent cerium and the smaller red atoms are oxygens.

This paper reports the use of acetate ions to form a complex with the  $\text{Ce}^{3+}$  in the ceria deposition solution. The deposition bath was formed by first dissolving the mass equivalent of 0.1 M ammonium acetate in deionized water. This solution was bubbled with Ar for at least 1 hour to remove  $\text{O}_2$ , and then the mass equivalent of 0.1 M  $\text{Ce}(\text{NO}_3)_3$  was added. The final pH of the solution was 6.1. If the solution were not bubbled with Ar to remove dissolved oxygen gas, a colloidal suspension of ceria powder would form. The deposition solution was heated to  $65^\circ\text{C}$  in an argon atmosphere. An applied potential of +0.5 V or +1.1 V vs. Ag/AgCl was used to deposit the ceria films.

The speciation distribution of the 0.1 M cerium(III) nitrate and 0.1 M ammonium acetate solution is shown in Figure 11A. At the deposition bath pH of 6.1, the solution consists of 39.75%  $\text{Ce}^{3+}$ , 0.02%  $\text{CeOH}^{2+}$ , 47.33%  $\text{CeOAc}^{2+}$ , 12.05 %  $\text{Ce}(\text{OAc})_2^+$ , 0.83%  $\text{Ce}(\text{OAc})_3$ , and 0.02%  $\text{Ce}(\text{OAc})_4^-$ . In the pH region studied, Ce(III) species can be directly oxidized to ceria. Calculated potentials for oxidizing the three major Ce(III) ions to  $\text{CeO}_2$  (s) in solution are -0.3856 V vs. Ag/AgCl for  $\text{CeO}_2/\text{Ce}^{3+}$ , -0.2866 V vs. Ag/AgCl for  $\text{CeO}_2/\text{CeOAc}^{2+}$ , and -0.2266 V vs. Ag/AgCl for  $\text{CeO}_2/\text{Ce}(\text{OAc})_2^+$ . For the oxidation of Ce(III) species to  $\text{Ce}(\text{OH})_4$  (aq), the calculated potentials are +0.3424 V vs. Ag/AgCl for  $\text{Ce}(\text{OH})_4/\text{Ce}^{3+}$ , +0.4413 V vs. Ag/AgCl for  $\text{Ce}(\text{OH})_4/\text{CeOAc}^{2+}$ , and +0.5014 V vs. Ag/AgCl for  $\text{Ce}(\text{OH})_4/\text{Ce}(\text{OAc})_2^+$ .

In Figure 11B, the CV of a 0.1 M cerium(III) nitrate and 0.1 M ammonium acetate solution shows a peak at 0.5 V vs. Ag/AgCl and 0.8 V vs. Ag/AgCl. Oxygen evolution occurs at potentials above 1.0 V vs. Ag/AgCl. Based on the CV of the deposition solution and the calculated potentials,  $\text{Ce}^{3+}$  is oxidized to  $\text{Ce}(\text{OH})_4$ (aq) followed by the oxidation of Ce(III) acetate species to  $\text{Ce}(\text{OH})_4$ (aq). The

electrochemically produced  $\text{Ce}(\text{OH})_4$  (aq) will spontaneously dehydrate to produce  $\text{CeO}_2$  (s) as follows:

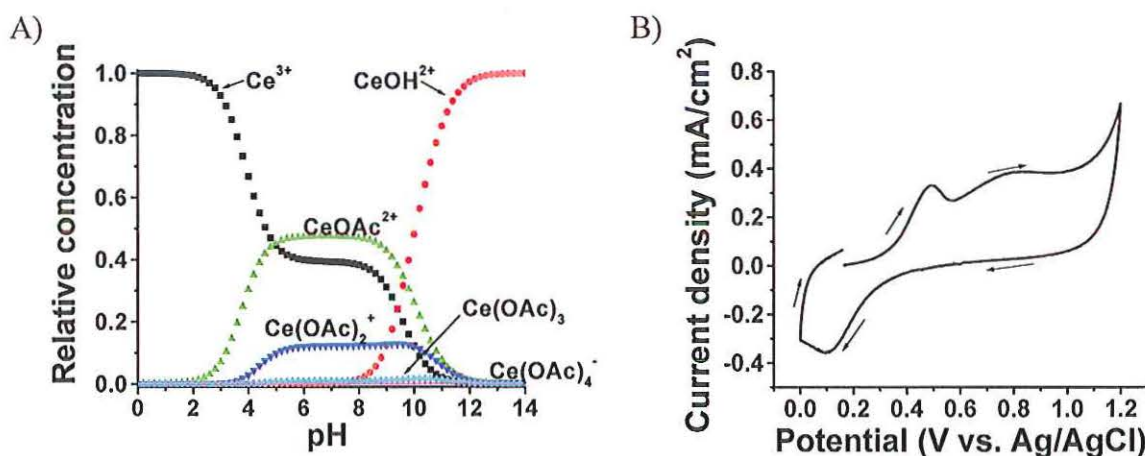
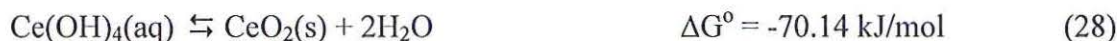


Figure 11. A) The calculated speciation distribution for a 0.1 M cerium(III) nitrate and 0.1 M ammonium acetate solution. At the deposition bath pH of 6.1, the solution consists of 39.75%  $\text{Ce}^{3+}$ , 0.02%  $\text{CeOH}^{2+}$ , 47.33%  $\text{CeOAc}^{2+}$ , 12.05%  $\text{Ce}(\text{OAc})_2^+$ , 0.83%  $\text{Ce}(\text{OAc})_3$ , and 0.02%  $\text{Ce}(\text{OAc})_4^-$ . B) The cyclic voltammogram on Pt for 0.1 M cerium(III) nitrate and 0.1 M ammonium acetate solution. The CV at 100 mV/s in the deposition solution on a Pt electrode shows oxidation peaks at about 0.5 V and 0.8 V vs. Ag/AgCl and oxygen evolution above 1.0 V vs. Ag/AgCl.

At a potential of +1.1 V vs. Ag/AgCl, oxygen is electrochemically produced at the electrode surface. During this reaction, ceria is deposited on the electrode surface. To verify this, the deposition solution was bubbled with oxygen gas. The bubbling of oxygen gas in the deposition solution chemically precipitated ceria with a particle size of 7 nm. Using either the electrochemical or chemical conditions, films are deposited on all

surfaces in the bulk solution. Therefore, an applied potential of +1.1 V vs. Ag/AgCl indirectly oxidizes Ce(III) to CeO<sub>2</sub> by electrochemically-generating oxygen gas.

To characterize these films, XPS, XRD, and SEM were used. The tetravalent state of the cerium was verified by XPS. The XRD patterns verified that the films were crystalline CeO<sub>2</sub> films with no other phases or materials present at either potential. Based on the low angle X-ray reflectance data, a ceria film deposited at +0.5 v vs. Ag/AgCl for 1000 s was 39 nm thick and had a density of 4.48 g/cm<sup>2</sup> (61% of the bulk density). These values were consistent with ellipsometry results. Films deposited at +1.1 V vs. Ag/AgCl were not smooth enough for X-ray reflectance or ellipsometry measurements. The SEM micrographs in Figure 12 show the morphology of the deposited films. Smooth, crack-free ceria films were deposited at +0.5 V vs. Ag/AgCl (Figure 12A), whereas rougher, cracked ceria films were deposited at +1.1 V vs. Ag/AgCl (Figure 12B). The rougher, cracked morphology is consistent with a film produced by solution-formed nanoparticles adhering to a substrate.

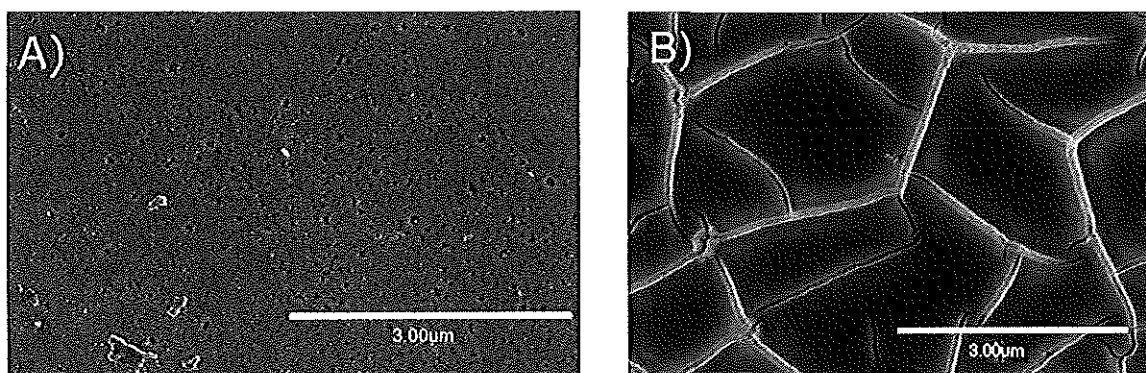


Figure 12. SEM micrographs of ceria films grown at A) 0.5 V and B) 1.1 V vs. Ag/AgCl.

The film characterization indicates that the deposition of ceria films proceeds by one of two mechanisms, depending on the applied potential. Smooth films are deposited when Ce(III) is directly oxidized to CeO<sub>2</sub> at +0.5 V vs. Ag/AgCl. Cracked films are deposited at the more positive potential of +1.1 V vs. Ag/AgCl because the Ce(III) is indirectly oxidized by electrochemically generated O<sub>2</sub>, which forms CeO<sub>2</sub> in the bulk solution.

### 1.3 IRON COMPOUNDS

Iron oxides, including iron hydroxides and iron (oxy)hydroxides, are abundant in nature.<sup>90</sup> These materials are used as catalysts, pigments, filters, and magnetic coatings for recording devices due to their chemical and physical properties.<sup>90,91</sup> Although various methods are used to produce these iron oxides,<sup>90,91</sup> this dissertation addresses the use of electrodeposition to produce magnetite, ferrihydrite, and zinc ferrite films.

**1.3.1 Magnetite.** Magnetite, Fe<sub>3</sub>O<sub>4</sub>, is a mixed-valence metal oxide with an inverse spinel structure (space group, Fd $\bar{3}$ m) and a lattice parameter of 0.8397 nm. The crystal structure of Fe<sub>3</sub>O<sub>4</sub> is shown in Figure 13. Magnetite exhibits ferrimagnetism below the Curie temperature of 860K.<sup>90</sup> Calculations have also indicated that the electrons are 100% spin-polarized at the Fermi level in this ferrimagnetic phase.<sup>92,93</sup> The Fe<sup>3+</sup> ions are in the tetrahedral sites (Figure 13B) while the Fe<sup>2+</sup> and Fe<sup>3+</sup> ions are in the octahedral sites (Figure 13C). In the ideal case of stoichiometric magnetite, the moments of the Fe<sup>3+</sup> ions are antiferromagnetically coupled, and the resulting magnetic moment is due to the Fe<sup>2+</sup> in the cell. The hopping of the charge carriers between the di- and trivalent iron ions create the electrical conduction of this material.<sup>94,95</sup> As the temperature

drops below 120K, the electron hopping for  $\text{Fe}_3\text{O}_4$  decreases (and conductivity decreases) resulting in a metal-insulator transition known as the Verwey transition.<sup>96</sup> This charge-ordered insulator has a magnetoelectronic effect, becoming ferroelectric below this Verwey temperature.<sup>97-100</sup> The characteristics of magnetite make it a candidate for magnetic recording, magnetoreceptors, and spintronic devices.<sup>101-112</sup>

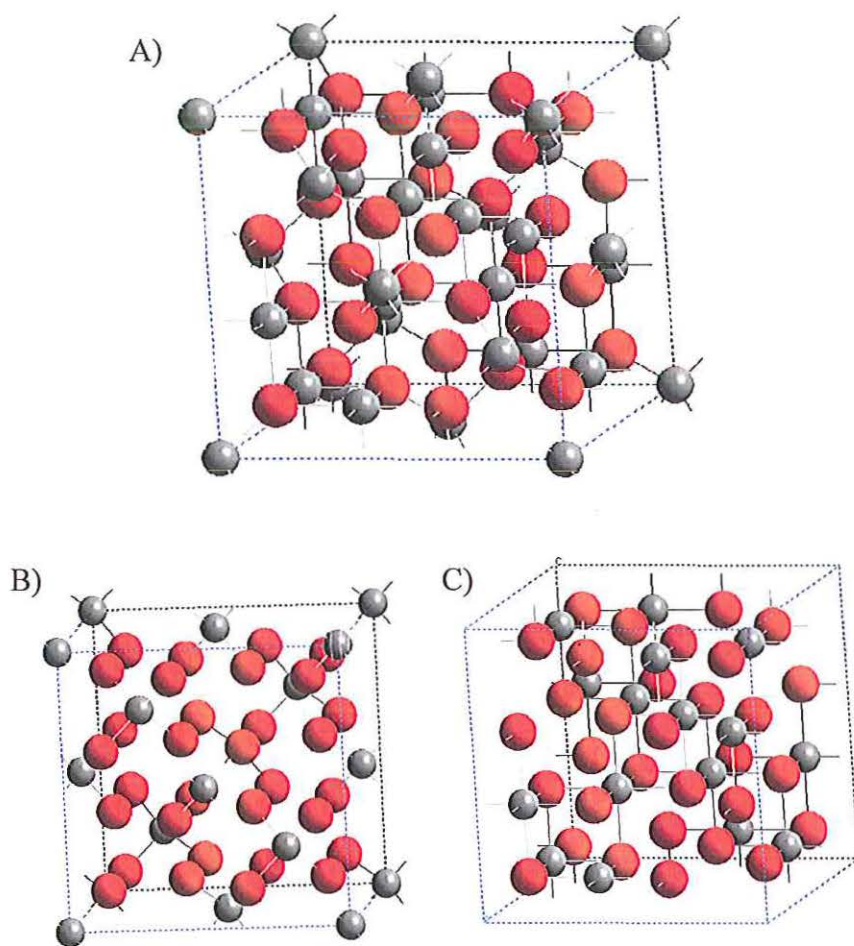


Figure 13. Crystal structure of magnetite. A) Magnetite is an inverse spinel structure (space group,  $Fd\bar{3}m$ ) with a lattice parameter of 0.8397 nm. In the crystal structure of magnetite, the iron and oxygen atoms are represented in gray and red, respectively. B) A representation of magnetite showing the  $\text{Fe}^{3+}$  in tetrahedral sites. C) A representation of magnetite showing the  $\text{Fe}^{2+}$  and  $\text{Fe}^{3+}$  cations in octahedral sites.

Magnetite has been deposited by electrochemically oxidizing Fe(II)<sup>18-26</sup> or reducing Fe(III)<sup>27-29</sup> in solution, followed by a chemical reaction between the generated species and the original cation to produce a film. Sapieszko and Matijevic initially found that Fe<sub>3</sub>O<sub>4</sub> powder was produced from Fe(III)-triethanolamine solutions using reducing agents and thermal decomposition at 250K.<sup>113</sup> The Switzer group has shown that films of magnetite can be electrodeposited from a similar bath at temperatures ranging from 60 to 90°C by electrochemically reducing this complex to produce Fe<sup>2+</sup>, which reacts chemically with the complex in solution.<sup>27-29</sup> In this previous work, the films were deposited on polycrystalline stainless steel electrodes at a constant cathodic current deposition of 2 mA/cm<sup>2</sup>.<sup>27</sup> Since the report on this work was published, the group's research has progressed to the deposition of epitaxial films and to the use of constant potential deposition to deposit magnetite.

The deposition bath was prepared by dissolving 2.6 grams of iron(III) sulfate hydrate in 15 ml of 1 M triethanolamine (TEA), resulting in a deep red colored solution. This solution was diluted with 50 ml of distilled, deionized water. It was then added to a second solution of 12.0 g of NaOH pellets in 85 ml of distilled, deionized water. The resulting gray-green solution was heated to 80°C. The final concentration of the solution is 86 mM Fe(III), 100 mM TEA, and 2 M NaOH. Magnetite films on the stainless steel substrates are produced by applying a potential between -1.01 V and -1.08 V vs. Ag/AgCl until 1 C/cm<sup>2</sup> was passed. Magnetite films were deposited on the gold single crystal at a constant potential of -1.01 V vs. Ag/AgCl for 100 seconds.

Papers II and III report that the surface concentrations of Fe(III) and Fe(II) are dependent on the applied potential. At low overpotentials, the Fe(III) surface

concentration is nearly the same as the bulk concentration (low concentration of Fe(II)), whereas at high overpotentials, at which the current becomes mass-transport controlled, the surface concentration of Fe(III) approaches zero (high concentration of Fe(II)). Using the ratio of the measured current to the limiting current, the concentration of Fe(III) and Fe(II) at the electrode surface is determined at each potential (Figure 14). Thus, stoichiometric magnetite would be deposited at approximately  $-1.045$  V vs. Ag/AgCl where  $1/3$  of the total concentration of Fe(III) has been reduced to Fe(II). Theoretically, any potential more positive than this value should produce magnetite with excess Fe(III), whereas potentials more negative than  $-1.045$  V vs. Ag/AgCl should produce magnetite with excess Fe(II).

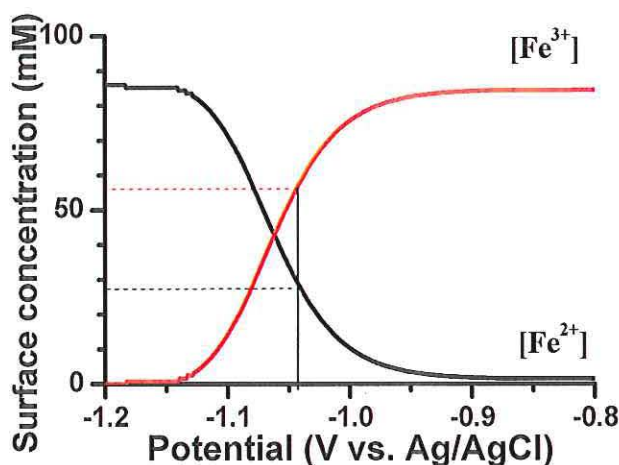


Figure 14. Plot of the concentrations of Fe(III) (red line) and Fe(II) (black line) at the electrode surface as a function of potential. Stoichiometric magnetite is produced when  $1/3$  of the  $\text{Fe}^{3+}$  has been reduced to  $\text{Fe}^{2+}$ . The potential where  $28.6$  mM of  $\text{Fe}^{2+}$  (black dashed line) and  $57.4$  mM of  $\text{Fe}^{3+}$  (red dashed line) exist at the electrode surface is  $-1.045$  V vs. Ag/AgCl

Papers II and III report that magnetite films are deposited between -1.01 V and -1.08 V vs. Ag/AgCl. As the overpotential increases, the lattice parameter of the film decreases. Paper II notes that magnetite films deposited at -1.01 V vs. Ag/AgCl have a lattice parameter of 0.8415 nm. Films deposited at -1.05 V vs. Ag/AgCl have a lattice parameter of 0.8394 nm, comparable to the value of 0.8397 nm reported in JCPDS #19-0629. The Mössbauer spectra indicate that films deposited at -1.05 V vs. Ag/AgCl are closer to stoichiometric magnetite than films deposited at -1.01 V vs. Ag/AgCl. These results are consistent with the analysis of the linear sweep data.

Previously, the Switzer group has demonstrated that epitaxial magnetite films can be electrodeposited on single-crystal Au from a Fe(II)-acetate bath.<sup>19</sup> Paper II reports the epitaxial electrodeposition of magnetite thin films on Au single crystals using the electrochemical reduction of Fe(III). Magnetite films on both Au(100) and Au(111) grew initially with a [111] orientation. As these films grew thicker, the magnetite films grew with [111] and [511] orientations. The [511] orientation is the result of twinning on the {111} planes. On Au(110), magnetite grew with a [110] orientation that aligned with the underlying Au(110) substrate.

Pole figure analysis indicated that magnetite films deposited on these substrates were epitaxial. Known as epitaxial relationships, the alignments of the films on the single crystals were determined from the pole figures in conjunction with stereographic projections. Figure 15 shows the (311) pole figures of A) the Fe<sub>3</sub>O<sub>4</sub>(111) film and B) the Au(111) substrate. For a (311) pole figure of a (111) oriented cubic material, one domain will have three peaks at  $\chi = 29.5^\circ$  separated  $\Delta\phi = 120^\circ$ , six peaks at  $\chi = 58.5^\circ$  separated  $\Delta\phi = 60^\circ$ , and three peaks at  $\chi = 80^\circ$  separated  $\Delta\phi = 120^\circ$ . Figure 15 shows that two

domains of magnetite are oriented on one domain of gold. In addition, the magnetite peaks antiparallel to the gold peaks were more intense than those aligned parallel with the gold peak. For the two domains of magnetite on Au(111), the epitaxial relationships can be expressed as  $\text{Fe}_3\text{O}_4(111)[01\bar{1}]//\text{Au}(111)[0\bar{1}1]$  for the antiparallel domain and  $\text{Fe}_3\text{O}_4(111)[0\bar{1}1]//\text{Au}(111)[0\bar{1}1]$  for the parallel domain. That is, for the dominate domain (antiparallel), the  $\text{Fe}_3\text{O}_4(111)$  and Au(111) planes are parallel, and the  $\text{Fe}_3\text{O}_4[01\bar{1}]$  and Au $[0\bar{1}1]$  in-plane directions are coincident. Similarly, for the parallel domain, the  $\text{Fe}_3\text{O}_4(111)$  and Au(111) planes are parallel but the  $\text{Fe}_3\text{O}_4[0\bar{1}1]$  and Au $[0\bar{1}1]$  in-plane directions are coincident. Pole figure analysis was also used for the magnetite films on Au(001) and Au(110). The epitaxial relationships for the four equivalent  $\text{Fe}_3\text{O}_4$  domains on Au(001) are  $\text{Fe}_3\text{O}_4(111)[0\bar{1}1]//\text{Au}(001)[110]$ ,  $\text{Fe}_3\text{O}_4(111)[0\bar{1}1]//\text{Au}(001)[\bar{1}\bar{1}0]$ ,  $\text{Fe}_3\text{O}_4(111)[0\bar{1}1]//\text{Au}(001)[\bar{1}\bar{1}0]$ , and  $\text{Fe}_3\text{O}_4(111)[0\bar{1}1]//\text{Au}(001)[\bar{1}\bar{1}0]$ . The presence of  $[511]$  orientations is common due to the twinning of the  $\{111\}$  planes. For each of these four relationships on Au(001), three arrangements exist due to the  $(511)$ :  $(511)[\bar{2}55]$ ,  $(511)[\bar{1}14]$ , and  $(511)[\bar{1}41]$ . The epitaxial relationship for the (110) magnetite films on Au(110) is  $\text{Fe}_3\text{O}_4(110)[001]//\text{Au}(110)[001]$ .

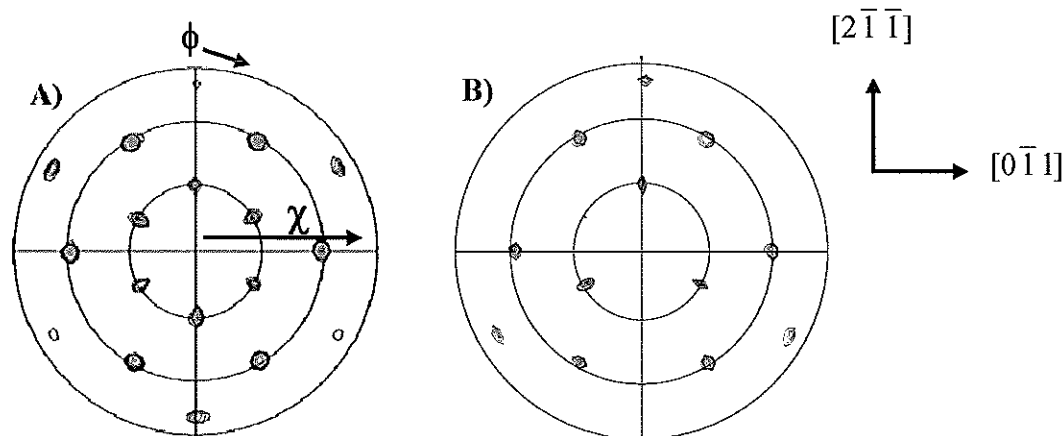


Figure 15. The (311) pole figures of A) epitaxial (111)magnetite on Au(111) deposited at -1.01 V vs. Ag/AgCl and B) Au(111). In both cases, peaks are observed at azimuthal angles,  $\chi$ , at  $29.5^\circ$ ,  $58.5^\circ$ , and  $80^\circ$ . Comparing the two pole figures at  $\chi = 29.5^\circ$ , two domains of magnetite are evident. In addition, the magnetite peaks antiparallel to the gold peaks are more intense than those that align parallel with the gold peak. The radial grid lines on the pole figures correspond to  $30^\circ$  increments of the tilt angle,  $\chi$ .

**1.3.2 Ferrihydrite.** Another iron compound is ferrihydrite, a poorly crystalline material labeled as 2-line or 6-line ferrihydrite based on the number of observed peaks in the XRD pattern. Due to its poor crystallinity, various chemical structures have been determined for this material.<sup>90,114</sup> Examples of the chemical formulas include  $5\text{Fe}_2\text{O}_3 \cdot 9\text{H}_2\text{O}$ ,  $\text{Fe}_5\text{HO}_8 \cdot 4\text{H}_2\text{O}$ , and  $\text{Fe}_2\text{O}_3 \cdot 2\text{FeOOH} \cdot 2.6\text{H}_2\text{O}$ .<sup>114,115</sup> Recently, a new ferrihydrite model (space group,  $P6_3mc$ ) using synchrotron data was determined with a proposed ideal chemical formula of  $\text{Fe}_{10}\text{O}_{14}(\text{OH})_2$  with  $1/5$  of the  $\text{Fe}^{3+}$  in tetrahedral sites and  $4/5$  in octahedral sites.<sup>115</sup> A polyhedral model of this structure is shown in Figure 16. Ferrihydrite is superparamagnetic at room temperature and show magnetic ordering at 4.2K.<sup>90,114</sup> Ferrihydrite is observed in the corrosion of iron and steel, in mining waste, and in soil and sediments.<sup>114</sup> Due to its natural adsorption of cations, anions, and

organics in soil, ferrihydrite has been studied for the removal of heavy metals in water treatment.<sup>114</sup> Used as a precursor for the production of goethite and hematite, this material is made synthetically by rapid oxidation of Fe(II) or by hydrolysis of Fe(III) salts.<sup>90,91,114</sup>

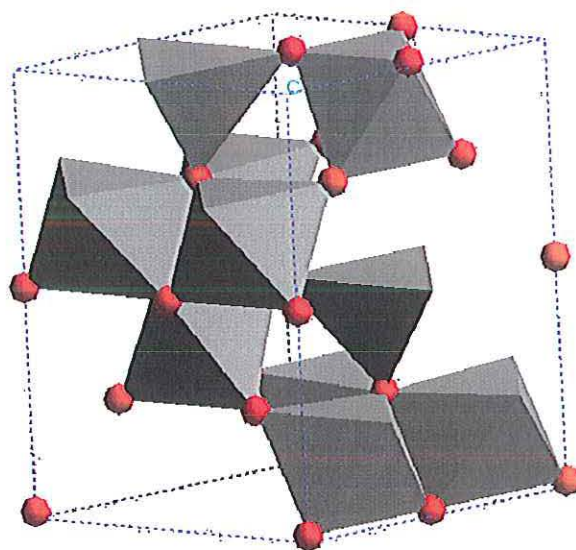


Figure 16. A polyhedral representation of the crystal structure of 2-line ferrihydrite, with an ideal formula of  $\text{Fe}_{10}\text{O}_{14}(\text{OH})_2$ , (space group,  $P6_3mc$ ). The lattice parameters are  $a = 0.5958$  nm and  $c = 0.8965$  nm. In this structure, 1/5 of the  $\text{Fe}^{3+}$  are in tetrahedral sites and 4/5 are in octahedral sites.<sup>115</sup>

Paper II describes the electrodeposition of ferrihydrite nanoribbons from the same alkaline Fe(III)-TEA bath as the magnetite, but deposited at potentials more negative than  $-1.09$  V vs. Ag/AgCl. The SEM images of the nanoribbon material deposited at two different potentials are shown in Figure 17. Based on the XRD patterns and Mössbauer spectra, these nanoribbon films are ferrihydrite. During the electrodeposition, magnetite is initially deposited below the ferrihydrite. The underlying magnetite film is visible in

Figure 17A of the film deposited at -1.1 V vs. Ag/AgCl. The production of ferrihydrite, an Fe(III) compound, in a Fe(II) rich condition is consistent with the aerial oxidation of an electrodeposited green rust film in basic conditions.<sup>116</sup> Based on pole figure analysis, the ferrihydrite films are epitaxial. On Au(110), the epitaxial relationship for the two films on Au(110) is  $\text{Fe}_{10}\text{O}_{14}(\text{OH})_2(11\bar{2}0)[0001]//\text{Fe}_3\text{O}_4(110)[001]//\text{Au}(110)[001]$ . On Au(001),  $\text{Fe}_{10}\text{O}_{14}(\text{OH})_2(11\bar{2}0)[0001]//\text{Fe}_3\text{O}_4(001)[110]//\text{Au}(001)[110]$  and  $\text{Fe}_{10}\text{O}_{14}(\text{OH})_2(11\bar{2}0)[\bar{1}100]//\text{Fe}_3\text{O}_4(001)[110]//\text{Au}(001)[110]$  are the epitaxial relationships. On Au(111), the epitaxial relationship is  $\text{Fe}_{10}\text{O}_{14}(\text{OH})_2(11\bar{2}0)[\bar{1}100]//\text{Fe}_3\text{O}_4(111)[01\bar{1}]//\text{Au}(111)[01\bar{1}]$ .

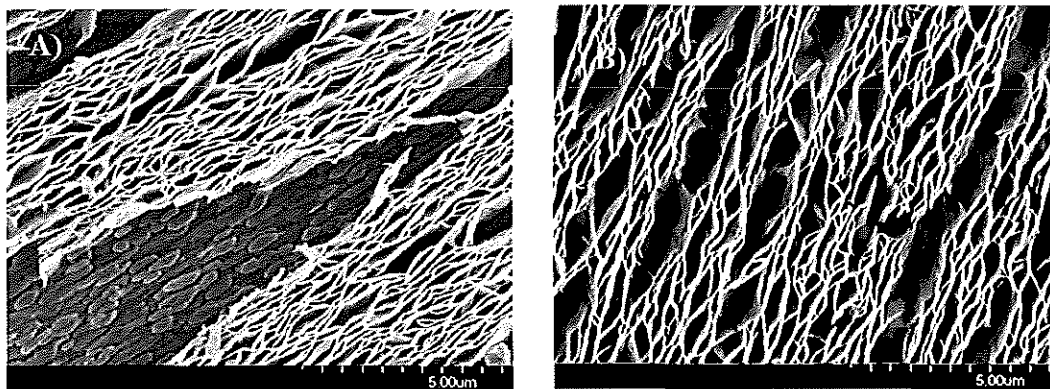


Figure 17. SEM images of films deposited on Au(110) from an alkaline Fe(III)-TEA bath at A) -1.10 V and B) -1.20 V vs. AgCl. A film deposited at -1.10 V vs. Ag/AgCl has two morphologies present in the SEM image. The ribbon-like morphology is attributed to ferrihydrite and the lower layer morphology is consistent with magnetite. A film deposited at -1.20 V vs. Ag/AgCl is predominately ferrihydrite.

**1.3.3 Zinc Ferrite.** In addition to magnetite, a wide range of ferrites can be produced in which divalent and trivalent ions substitute for the  $\text{Fe}^{2+}$  and  $\text{Fe}^{3+}$ . Based on the mineral spinel ( $\text{MgAl}_2\text{O}_4$ ), the general chemical formula for these ferrites is  $[\text{M}_{1-x}\text{Fe}_x]_{\text{A}}[\text{M}_x\text{Fe}_{2-x}]_{\text{B}}\text{O}_4$  where the Fe is trivalent and the M is generally a divalent cation such as  $\text{Mn}^{2+}$ ,  $\text{Zn}^{2+}$ ,  $\text{Fe}^{2+}$ ,  $\text{Co}^{2+}$ ,  $\text{Ni}^{2+}$ , or a mixture of these, which occupies either tetrahedral (A) or octahedral (B) sites. Spinel is characterized as either normal or inverse. In spinels, eight formula units are present per unit cell. The spinel is normal if M only occupies the tetrahedral sites ( $x = 0$ ). In this structure, 32  $\text{O}^{2-}$  are present with eight  $\text{M}^{2+}$  ions in the tetrahedral sites and 16  $\text{Fe}^{3+}$  ions in the octahedral sites. If M only occupies the octahedral sites, then the spinel is inverse ( $x = 1$ ). Here, the eight  $\text{Fe}^{3+}$  ions exist in the tetrahedral sites, and eight  $\text{M}^{2+}$  and eight  $\text{Fe}^{3+}$  are distributed in the octahedral sites.

The site preference of divalent and trivalent ions is based on the size of the ions and the interstitial sites, on bonding, and on their crystal field stabilization energies (CFSE).<sup>59</sup> The resulting magnetism of these materials is due to the interaction of the ions in the tetrahedral and octahedral sites. For example, magnetite is an example of an inverse spinel. The  $\text{Fe}^{2+}$  ions are larger than the  $\text{Fe}^{3+}$  ions. The octahedral sites are larger than the tetrahedral sites. The  $\text{Fe}^{3+}$  ion ( $d^5$ ) has zero CFSE in an octahedral or tetrahedral site; the  $\text{Fe}^{2+}$  ion ( $d^6$ ) has a larger octahedral CFSE than its tetrahedral CFSE. Therefore,  $\text{Fe}^{2+}$  ions go preferentially into the octahedral sites ( $(\text{Fe}^{3+})_{\text{A}}(\text{Fe}^{2+}\text{Fe}^{3+})_{\text{B}}\text{O}_4$ ). Due to this inverse formation, the moments of the  $\text{Fe}^{3+}$  ions in the tetrahedral sites are antiferromagnetically coupled with the  $\text{Fe}^{3+}$  ions in the octahedral sites, resulting in a net magnetic moment due to the  $\text{Fe}^{2+}$  in the octahedral sites. Therefore, magnetite is

ferrimagnetic material, making it useful in magnetic recording, magnetoreceptors, and spintronic devices.<sup>100-112</sup>

Whereas magnetite is an inverse spinel, zinc ferrite ( $\text{ZnFe}_2\text{O}_4$ ) is a normal spinel. In this material, both  $\text{Zn}^{2+}$  and  $\text{Fe}^{3+}$  have zero CFSE. However, the electronic configuration of  $\text{Zn}^{2+}$  favors tetrahedral ( $\text{sp}^3$ ) bonding to the oxygen ions instead of octahedral ( $\text{d}^2\text{sp}^3$ ) bonding.<sup>117</sup> This affinity of  $\text{Zn}^{2+}$  for tetrahedral sites results in a normal spinel structure ( $(\text{Zn}^{2+})_A(\text{Fe}^{3+})_2\text{B}\text{O}_4$ ) (Figure 18). Stoichiometric  $\text{ZnFe}_2\text{O}_4$  is paramagnetic at room temperature because  $\text{Zn}^{2+}$  has no magnetic moment and the  $\text{Fe}^{3+}$  ions on the octahedral sites are randomly oriented. At the Néel temperature of 10.5K, zinc ferrite becomes antiferromagnetic since the  $\text{Fe}^{3+}$  ions become antiferromagnetically coupled. Nanocrystalline zinc ferrite has shown ferrimagnetism due to a change in the Zn and Fe distribution, resulting in a mixed spinel.<sup>118-124</sup> Zinc ferrite is used as an anticorrosion pigment in paint and a tan pigment for plastic bags and roof shingles.<sup>90</sup> This material is also being investigated as a  $\text{H}_2\text{S}$  gas sensor and an absorbent for detoxification of hot coal gas.<sup>125-129</sup> In mixed zinc ferrites,  $\text{Zn}^{2+}$  replaces some of the divalent ions in the tetrahedral sites in inverse spinels such as nickel ferrite and manganese ferrite. These show higher magnetic moments than the pure ferrites and are used in telecommunications, electromagnetic interference suppression, and power and microwave applications.<sup>117,118</sup>

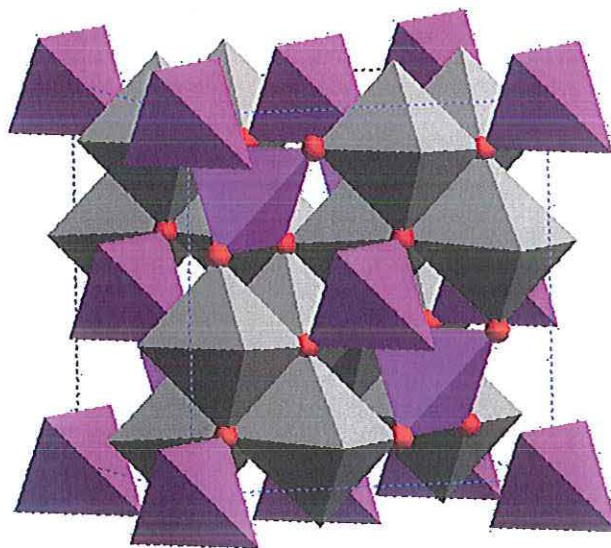


Figure 18. The polyhedral representation of zinc ferrite. Zinc ferrite is a normal spinel structure (space group,  $Fd\bar{3}m$ ) with a lattice parameter of 0.8446 nm. The zinc atoms are in tetrahedral sites (purple), and the iron atoms are in octahedral sites (dark gray). Oxygen atoms are represented in red.

Zinc ferrite is produced by various methods such as sintering,<sup>118,127</sup> sol-gel processing,<sup>120,121</sup> ball milling,<sup>122,125,129</sup> and micelles.<sup>123</sup> Zinc ferrite films have been indirectly electrodeposited by codepositing Zn and Fe and then electrochemically oxidizing the metals in base and sintering between 500 and 800°C.<sup>130</sup> Zinc ferrite powders are produced from an alkaline Zn(II)-Fe(III)-TEA bath using reducing agents and thermal decomposition.<sup>131</sup> Paper III reports the direct electrodeposition of zinc ferrite from the alkaline Fe(III)-TEA deposition bath of magnetite and ferrihydrite with the addition of 0.03 M Zn(II).

Just as in the electrodeposition of magnetite, the electrochemical-chemical (EC) nature of this deposition bath is used. The composition of the electrodeposited zinc ferrite

is controlled by applying different potentials (Table 1). The atomic percentage of Zn detected in these films ranges from 32% at -0.97 V to 20% at -1.05 V vs. Ag/AgCl. The Zn detected from EDS measurements is comparable to that calculated from the linear sweeps. The lattice parameters of the zinc ferrite films also decrease as the applied overpotential increases. Zinc ferrite films electrodeposited on gold single crystals are epitaxial. For instance, the epitaxial relationships of these films on Au(111) are  $\text{ZnFe}_2\text{O}_4(111)[01\bar{1}]//\text{Au}(111)[0\bar{1}1]$  for the main (antiparallel) domain and  $\text{ZnFe}_2\text{O}_4(111)[0\bar{1}1]//\text{Au}(111)[0\bar{1}1]$  for the minor (parallel) domain.

Table 1. Comparison of compositions of zinc ferrite films as a function of applied potential measured from energy dispersive spectroscopy and calculated from the linear sweep voltammetry.

Applied potential (V vs. Ag/AgCl)	Lattice Parameter (nm)	Ratio of Zn/Fe from EDS	Measured Composition	Surface $[\text{Fe}^{2+}]$ from LSV (mM)	Calculated Composition
-0.97	0.8443	0.47	$\text{Zn}_{0.96}\text{Fe}_{2.04}\text{O}_4$	5	$\text{Zn}_{0.86}\text{Fe}_{2.14}\text{O}_4$
-0.99	0.8431	0.39	$\text{Zn}_{0.84}\text{Fe}_{2.16}\text{O}_4$	8	$\text{Zn}_{0.79}\text{Fe}_{2.21}\text{O}_4$
-1.01	0.8435	0.32	$\text{Zn}_{0.72}\text{Fe}_{2.28}\text{O}_4$	14	$\text{Zn}_{0.68}\text{Fe}_{2.32}\text{O}_4$
-1.03	0.8426	0.27	$\text{Zn}_{0.63}\text{Fe}_{2.37}\text{O}_4$	22	$\text{Zn}_{0.58}\text{Fe}_{2.42}\text{O}_4$
-1.05	0.8415	0.25	$\text{Zn}_{0.60}\text{Fe}_{2.40}\text{O}_4$	34	$\text{Zn}_{0.47}\text{Fe}_{2.53}\text{O}_4$

## 1.4 SUPERLATTICES

Because superlattices are crystallographically coherent, they are produced with alternating layers of materials with very low lattice mismatch. Superlattices of semiconductors, ceramics, and metals have shown enhanced optical, electronic, magnetic, and mechanical properties compared with the properties of each individual component of the superlattice.<sup>1,2,132,133</sup> Initially, most work on superlattices has used vacuum techniques such as chemical vapor deposition and molecular beam epitaxy to produce semiconductor superlattices with engineered band gaps for quantum well lasers, photodiodes, and heterojunction field-effect transistors<sup>1,2,133</sup> and to produce metallic superlattices with giant magnetoresistance for magnetic storage, sensors, and spintronics.<sup>1,132</sup> However, electrodeposition has several advantages over these vacuum-based methods for the production of superlattices.<sup>1,2,134</sup> In addition to its cost-effectiveness, electrodeposition uses low processing temperatures, which minimize interdiffusion of the layers. Superlattices are produced within minutes from a single deposition bath as the composition is controlled by the potential or current applied.

Electrodeposition has been used to produce compositionally modulated multilayers such as Co-Cu/Cu,<sup>135-139</sup> Co-Ni(-Cu)/Cu,<sup>139-145</sup> and Ni/Cu.<sup>139,142,146-153</sup> These metallic superlattices have improved wear resistance<sup>146,147,150</sup> and magnetic anisotropy.<sup>139,142,144,145,153</sup> Lashmore and Dariel demonstrated the coherent nature of the multilayers by X-ray diffraction, verifying the production of Ni/Cu superlattices on the three low-index orientations of copper single crystals.<sup>148</sup> Moffat then proved that epitaxial Ni/Cu superlattices on Cu(100) are strained, which inhibits the formation of defects.<sup>149</sup> The prevention of dislocations in the layers is attributed to the enhanced

mechanical and wear properties of the Ni/Cu superlattices.<sup>150</sup> After dissolving the copper substrate, Schwarzacher's group showed giant magnetoresistance (a large change in electrical resistance due to an applied external magnetic field) in Co-Ni(-Cu)/Cu metallic superlattices.<sup>139,141,142</sup> They showed that by altering the nonmagnetic Cu layer thickness, the giant magnetoresistance (GMR) changed. The increase in the Cu layer decreases the GMR because both the interaction between the magnetic layers and the interface density decrease.<sup>139,154</sup> Other studies report oscillatory GMR dependent on the Cu layer thickness.<sup>137,139,140</sup> The orientation of the substrate also affects the MR because the substrate can influence film texture and orientation. The Co-Ni(-Cu)/Cu superlattices have maximum MR values of 9% on Cu(111),<sup>143</sup> 15% on Cu(100),<sup>143</sup> 25% on polycrystalline Cu,<sup>143</sup> 12% on n-GaAs(001),<sup>145</sup> 5% on n-GaAs(111),<sup>145</sup> and 10% on n-Si(100).<sup>144</sup> Further research has produced electrodeposited metallic superlattice nanowires<sup>139,143,156,157</sup> with similar MR values by depositing the superlattice in a porous template such as anodized aluminum or polycarbonate membrane, a technique first proposed by Martin.<sup>1,155</sup> Besides producing nanowires with GMR for potential spintronic devices, other metallic superlattice nanowires have been reported such as Ni/Au for high frequency filters<sup>158</sup> and Co/Pt for magnetic barcodes.<sup>159</sup>

Although most electrochemical research on superlattices has been based on metals, semiconductor compounds<sup>1,160-166</sup> and metal oxide<sup>1,2,38-43</sup> superlattices have been electrodeposited. Semiconductor compound superlattices with observed bandgap shifts are produced by electrochemical atomic layer epitaxy (ECALE).<sup>1,160-164</sup> Electrodeposition has also been used to produce semiconductor superlattice nanowires for potential applications in thermoelectrics.<sup>165,166</sup> The Switzer group has previously used

electrodeposition to produce both compositional and defect-chemistry superlattices of conductive metal oxides.<sup>1,2,38-43</sup> Paper III demonstrates that epitaxial superlattices based on the metal oxides magnetite and zinc ferrite are electrodeposited on Au(111).

Superlattices may be electrodeposited by pulsing between two potentials or two currents. As described by Ross,<sup>134</sup> the pulsing between potentials will give sharper interfaces, but the layer thickness may vary. The film thickness depends on the charge passed at each potential, which may change if the transport of material to the electrode is fluctuating.<sup>134</sup> The pulsing between two currents will reduce the clear division between the layers, but the layer thicknesses will be more uniform.<sup>134</sup> Both methods have been used by this group to make superlattices.<sup>1,2,38-43</sup> Paper III reports the electrodeposition of superlattices by pulsing between two potentials to produce sharper interfaces for FIB imaging and to control the composition and defect chemistry of the layers.

Previously,  $\text{Fe}_3\text{O}_4/\text{NiO}$ <sup>167,168</sup> and  $\text{Fe}_3\text{O}_4/\text{CoO}$ <sup>169,170</sup> superlattices have been produced on (001)MgO by molecular beam epitaxy, whereas [111] oriented  $\text{ZnFe}_2\text{O}_4/\text{ZnGa}_2\text{O}_4$  superlattice has been produced by pulsed laser deposition onto (0001) sapphire.<sup>171</sup> By exploiting the EC nature of the reaction, we show in Paper III that magnetite and zinc ferrite superlattices are produced. By applying different potentials, the lattice parameters of the magnetite and zinc ferrite films are tunable, as is the composition of the zinc ferrite films. In this study, the magnetite superlattices were deposited by pulsing between -1.01 and -1.05 V vs. Ag/AgCl, whereas compositional superlattices of zinc ferrite were deposited by pulsing between -0.99 V and -1.05 V vs. Ag/AgCl. The lattice mismatches are 0.24% for the magnetite superlattices and 0.19% for the zinc ferrite superlattices. By systematically changing the deposition times,

superlattices with different modulation wavelengths were produced. The superlattice formations were verified by cross-sectional FIB images and X-ray diffraction patterns. Figure 19 shows the (444) reflections of the superlattices on Au(111). These layered structures in the magnetite and zinc ferrite system have modulation wavelengths ranging from 78 to 9.5 nm.

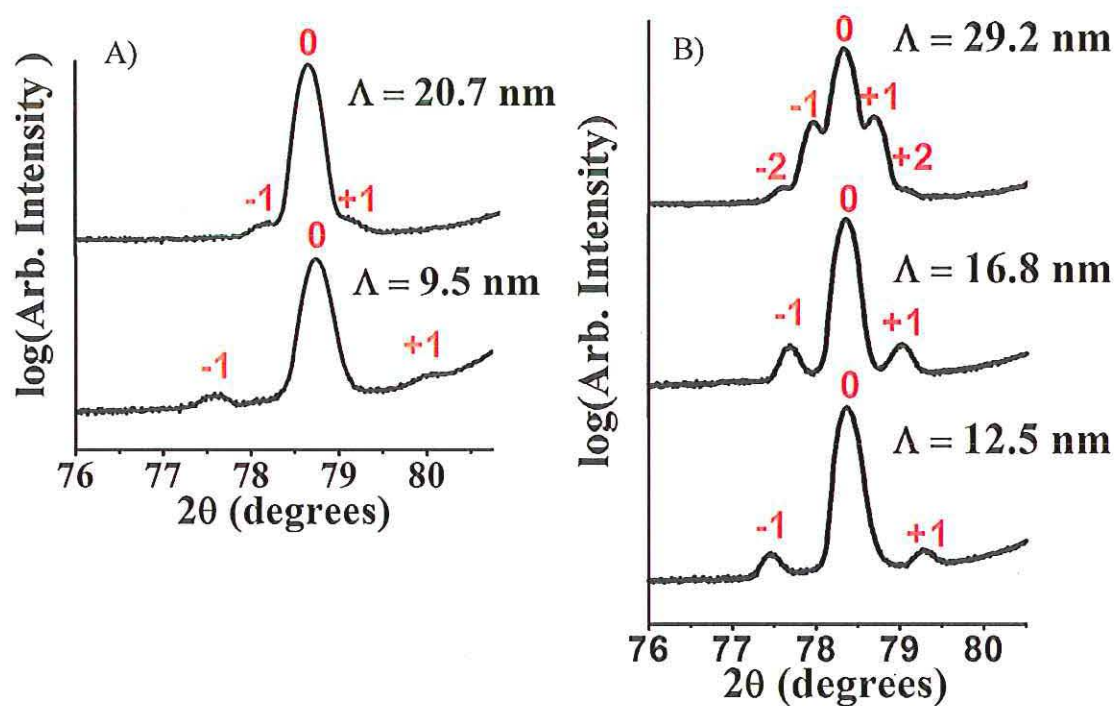


Figure 19. A) The (444) X-ray diffraction peaks of magnetite superlattices with a range of modulation wavelengths. Magnetite superlattices were produced by pulsing between -1.01 V and -1.05 V vs. Ag/AgCl in an alkaline Fe(III)-TEA bath with modulation wavelength of 20.7 (top) and 9.5 nm (bottom). B) The (444) X-ray diffraction peaks of zinc ferrite superlattices with a range of modulation wavelengths. Zinc ferrite superlattices were electrodeposited using -0.99 V and -1.05 V vs. Ag/AgCl from an alkaline Zn(II)-Fe(III)-TEA deposition bath with modulation wavelengths of 29.2 (top), 16.8 (middle), and 12.5 nm (bottom). The main Bragg peak is indicated with a "0".

The low temperature and the negative overpotentials should allow the deposition of these superlattices onto semiconductors for integration with electronics. Because the orientations of epitaxial films are controlled by the substrate, the deposition of these superlattices on different orientations of substrates permits study of the effect of orientation on their magnetoresistance. These superlattices can also be electrodeposited in porous membranes to produce superlattice nanowires for additional magnetoresistance and magnetoreceptor studies. Superlattices fabricated electrochemically based on magnetite/zinc ferrite systems and other metal ferrites that may be produced in the future along with their superlattices have the potential to become devices for microwave, entertainment, power, and magnetic applications.<sup>117</sup>

### 1.5 CHIRALITY OF COPPER(II) OXIDE

A chiral structure is nonsuperimposable on its mirror image. Because one chiral molecule, known as an enantiomer, may be beneficial and another toxic, research has focused on methods to produce enantiomerically pure forms of drugs and their precursors.<sup>172</sup> A research focus is to use chiral surfaces as catalysts and sensors. One method to produce chiral surfaces is to break the symmetry of a metal surface by irreversibly adsorbing chiral molecules on the surface. For example, an achiral Ni surface modified by adsorbing (R,R)-tartaric acid has been used to catalyze the hydrogenation of  $\beta$ -ketoesters, producing the R-product with over 90% enantiomeric excess, whereas the surface modified with (S,S)-tartaric acid selectively produces the S-product.<sup>173</sup> An alternative to the adsorption approach is to develop surfaces that are intrinsically chiral. McFadden et al. showed that high-index surfaces of face-centered cubic metals are

chiral.<sup>174</sup> The chirality of these high-index surfaces is attributed to the presence of right- and left-handed kink sites.<sup>174</sup> Scholi et al. simulated the enantiospecific adsorption of chiral molecules on Pt(643) using Monte Carlo simulations,<sup>175</sup> whereas Attard et al. showed experimental evidence of chiral recognition by enantiospecific electrooxidation of glucose in aqueous solutions on surfaces of Pt(643) and its enantiomer, Pt( $\overline{643}$ ).<sup>176,177</sup> Paper IV describes an approach to the development of chiral catalysts that requires electrodeposition of chiral films of an achiral material on an achiral substrate.

The chirality of a crystal depends on the symmetry operations present in the structure. Proper symmetry operations are those that do not change the handedness of an object. These operations include rotation axes, translations, and screw axes. In Figure 20, a left hand is used to show the symmetry operation of A) a two-fold rotation ( $2$ ), B) a translation, and C) a screw rotation ( $2_1$ ). These proper symmetry operations do not change the “handedness” because they are just movements of the same object.<sup>178</sup> If only these operations are present, then the structure is chiral. However, improper symmetry operations such as rotoinversion operations ( $\overline{1} = i, \overline{2} = m, \overline{3}, \overline{4}, \overline{6}$ ) or glide reflection (a, b, c, n, and d) invert an object’s geometry. These operations produce the opposite “hand” of the object; such objects cannot be produced by a direct movement of the original object. In Figure 21, A) an inversion (i), B) a mirror (m), C) a rotation inversion ( $\overline{4}$ ), and D) a glide plane (a, b, c, and d) are shown using the left hand as the object of interest. Any structure with one of these improper symmetry operators will produce the opposite “hand” of the object; therefore, the structure will be achiral.<sup>178</sup>

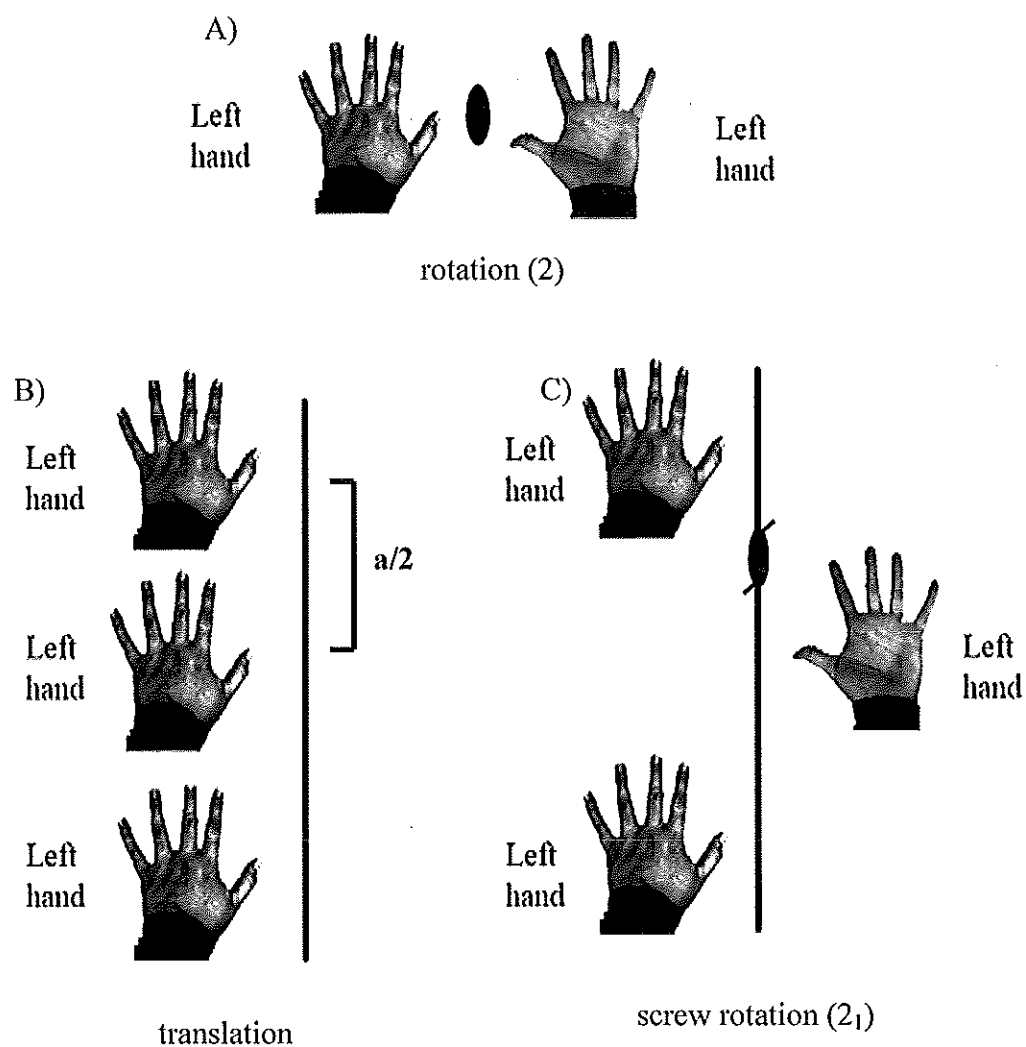


Figure 20. Chiral structures exist if they contain only proper symmetry operators such as A) a two-fold rotation ( $2$ ), B) a translation, and C) a screw rotation ( $2_1$ ). These symmetry operations do not produce the opposite “hand” of the object; therefore, structures with only these operations will be chiral.

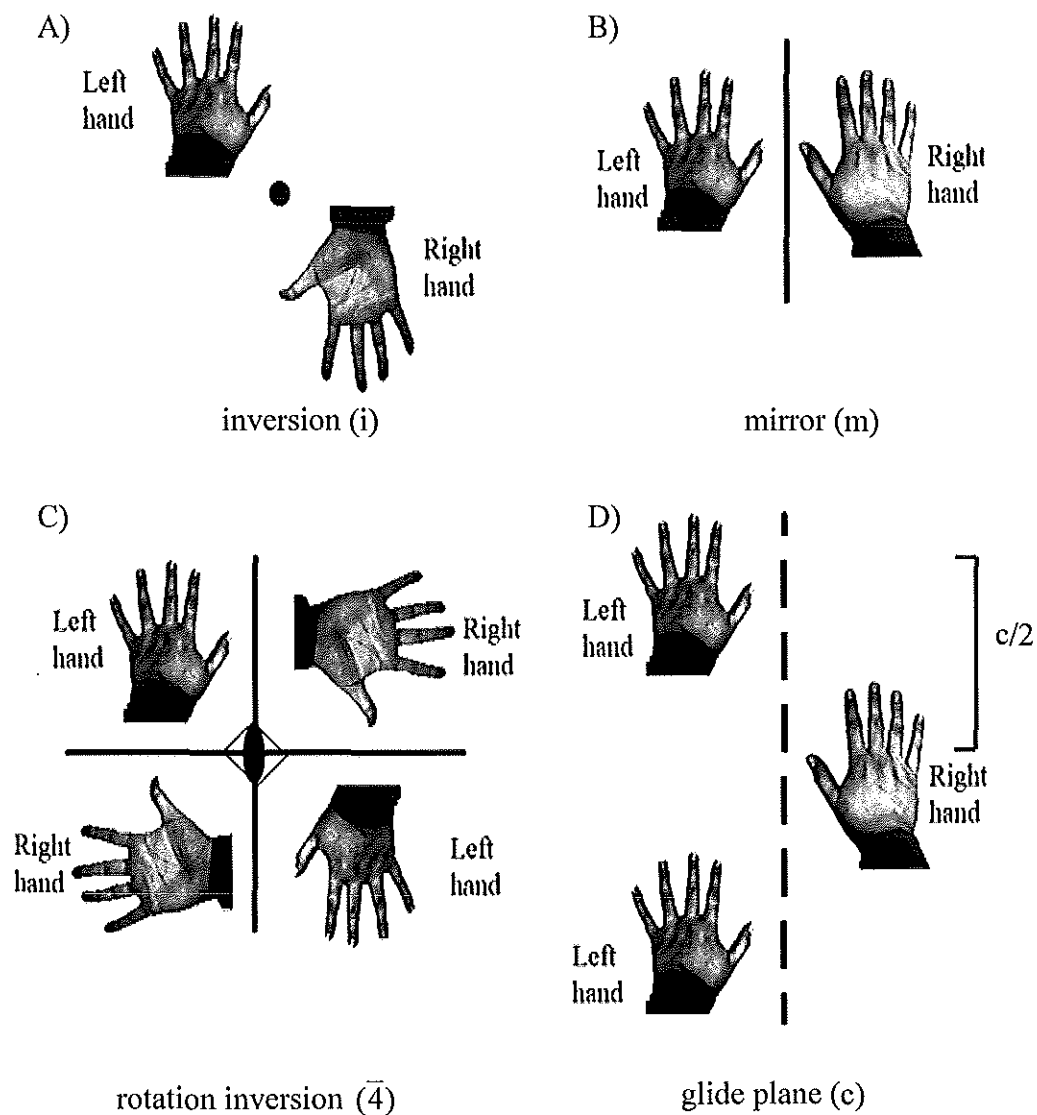


Figure 21. Achiral structures exist if they contain improper symmetry operators such as A) inversion (i), B) a mirror plane (m), C) a rotation inversion ( $\bar{4}$ ), or D) a glide plane (c). These symmetry operations produce the opposite “hand” of the object; therefore, structures with one of these operations will be achiral due to the presence of both “hands.”

The symmetry of the system determines what planes of a material are chiral. For example, Paper IV describes the electrochemical deposition of chiral orientations of copper(II) oxide (CuO). For CuO (space group  $C2/c$ ), the lattice parameters are  $a = 0.4685$  nm,  $b = 0.3430$  nm,  $c = 0.5139$  nm,  $\alpha = \gamma = 90^\circ$ , and  $\beta = 99.08^\circ$ . This monoclinic structure is shown in Figure 22 where the copper atoms are blue and the oxygen atoms are red. The structure is centrosymmetric (i.e. it has an inversion center,  $i$ ); therefore, the bulk crystal structure of CuO is achiral. However, crystallographic orientations/planes may be chiral. A monoclinic system has three axes of unequal length and an angle normally greater than  $90^\circ$  between two axes. In this arrangement, the  $b$ -axis is unique. The  $c$  and  $a$  axes do not intersect each other at right angles, but they are perpendicular to the  $b$  axis. Based on the space group, a glide plane is along the  $c$ -axis; therefore, a glide plane is perpendicular to the  $b$ -axis. An achiral plane has a mirror or glide plane perpendicular to it. Therefore, achiral planes of CuO are planes that are parallel to the  $b$ -axis, planes  $k = 0$ . Thus, planes such as (202), (002), and (203) are achiral. Chiral CuO planes lack glide plane symmetry; chiral planes are those with  $k \neq 0$  such as (111), (110), (022), and (020). For a chiral plane  $(hkl)$ , its enantiomer is  $(\overline{hkl})$ .

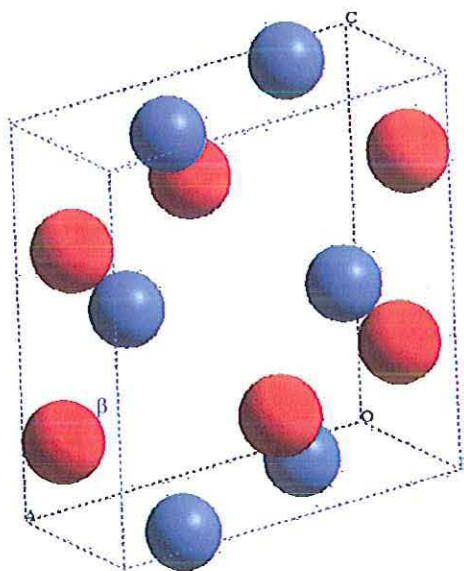


Figure 22. The crystal structure of CuO. For CuO (space group  $C2/c$ ), the lattice parameters are  $a = 0.4685$  nm,  $b = 0.3430$  nm,  $c = 0.5139$  nm,  $\alpha = \gamma = 90^\circ$ , and  $\beta = 99.08^\circ$ . The copper atoms are in blue, and the oxygen atoms are in red. A  $c$  glide plane is perpendicular to the  $b$ -axis.

Table 2 lists the symmetry of specific planes depending on the point group.<sup>179</sup> Screw axes are replaced by the highest possible rotation, and glides are replaced by mirrors. Planes that lack mirror symmetry ( $m$ ) are chiral. For example, whereas all planes of triclinic structures are chiral, all planes of orthorhombic structures are achiral except where  $h \neq k \neq l \neq 0$ . The space group of CuO is  $C2/c$  (15); its point group is  $2/m$ . According to Table 2, chiral planes are  $\{010\}$ ,  $\{0kl\}$ ,  $\{hk0\}$ , and  $\{hkl\}$ , whereas achiral planes are  $\{100\}$ ,  $\{001\}$ , and  $\{h0l\}$ . From these select planes, a trend is visible; achiral planes are those that  $k = 0$  (consistent with the results reported above). This trend is true for all monoclinic structures.

Table 2. Symmetry of the planes of a point group. Orientations that lack mirror symmetry (i.e. having rotational symmetry) are chiral. The chiral orientations are highlighted in yellow.<sup>179</sup>

System	Space Group	Point Group	{100}	{010}	{001}	{0kl}	{h0l}	{hk0}	{hkl}
Triclinic	1	1	1	1	1	1	1	1	1
	2	$\bar{1}$	2	2	2	2	2	2	2
Monoclinic (2 <sup>nd</sup> setting)	3-5	2	m	2	m	1	m	1	1
	6-9	m	m	1	m	1	m	1	1
	10-15	2/m	2mm	2	2mm	2	2mm	2	2
Orthorhombic	16-24	222	2mm	2mm	2mm	m	m	m	1
	25-46	mm2	m	m	2mm	m	m	m	1
		m2m	m	2mm	m	m	m	m	1
		2mm	2mm	m	m	m	m	m	1
	47-74	mmm	2mm	2mm	2mm	2mm	2mm	2mm	2
System	Space Group	Point Group	{001}	{100}	{110}	{hk0}	{h0l}	{hhl}	{hkl}
Tetragonal	75-80	4	4	m	m	m	1	1	1
	81-82	$\bar{4}$	4	m	m	m	1	1	1
	83-88	4/m	4	2mm	2mm	2mm	2	2	2
	89-98	422	4mm	2mm	2mm	m	m	m	1
	99-110	4mm	4mm	m	m	m	m	m	1
	111-122	$\bar{4}2m$	4mm	m	2mm	m	m	m	1
	123-142	$\bar{4}m2$	4mm	2mm	2mm	2mm	2mm	2mm	2

Continuation of Table 2. Symmetry of the planes of a point group.<sup>179</sup>

System	Space Group	Point Group	{001}	{100}	{110}	{hk0}	{h0l}	{hhl}	{hkl}	
Trigonal (hexagonal axes)	143-146	3	3	1	1	1	1	1	1	
	147-148	$\bar{3}$	6	2	2	2	2	2	2	
	149-155	321	31m	m	2	1	m	1	1	
		312	3m1	2	m	1	1	m	1	
	156-161	3m1	3m1	m	1	1	m	1	1	
	162-167	$\bar{3}m1$	6mm	2mm	2	2	2mm	2	2	
		$\bar{3}1m$	6mm	2	2mm	2	2	2mm	2	
Hexagonal	168-173	6	6	m	m	m	1	1	1	
	174	$\bar{6}$	3	m	m	m	1	1	1	
	175-176	6/m	6	2mm	2mm	2mm	2	2	2	
	177-182	622	6mm	2mm	2mm	m	m	m	1	
	183-186	6mm	6mm	m	m	m	m	m	1	
	187-190	$\bar{6}m2$	3m1	2mm	m	m	m	m	m	1
		$\bar{6}2m$	31m	m	2mm	m	m	m	m	1
	191-194	6/mmm	6mm	2mm	2mm	2mm	2mm	2mm	2	
System	Space Group	Point Group	{100}	{111}	{110}	{hk0}	$\frac{\{hhl\}}{h>l}$	$\frac{\{hhl\}}{h<l}$	{hkl}	
Cubic	195-199	23	2mm	3	m	m	1	1	1	
	200-206	m3	2mm	6	2mm	2mm	2	2	2	
	207-214	432	4mm	3m	m	m	m	m	1	
	215-220	$\bar{4}3m$	4mm	3m	m	m	m	m	1	
	221-230	m3m	4mm	6mm	2mm	2mm	2mm	2mm	2	

Other methods to determine whether a surface is chiral or achiral are stereographic projections and interface models. Like a point group, a stereographic projection is a two-dimensional plot that shows the angular relationships of the crystal's planes and directions based on its crystallographic symmetry. Simply, a stereographic projection is a way to represent a three-dimensional crystal on a two-dimensional page. If two orientations have stereographic projections that are superimposable mirror images, then the orientations are achiral. If the two orientations produce stereographic projections that are nonsuperimposable mirror images, then the orientations are chiral. In this dissertation, CaRIne Crystallography 3.1 is used to produce the stereographic projections.

An interface model is a 2-D or 3-D periodic representation of the interface between two crystallographic planes. Each plane of the crystal is specified by the Miller indices,  $hkl$ . A match direction and point for each plane are indicated in which the program will "match" the direction and point of one plane to the other. If the interface model produces identical surfaces that are superimposed on each other, then those planes are achiral. If the planes are nonsuperimposable in the model, then those planes are chiral. These interface models are generated using Cerius 2.0 from Molecular Simulations, Inc.

Calculated stereographic projections are shown in Figure 23 for the achiral planes (001) and  $(00\bar{1})$  of CuO and in Figure 24 for the chiral planes (111) and  $(\bar{1}\bar{1}\bar{1})$  of CuO. In Figures 23A and 23B, the stereographic projections of the (001) and  $(00\bar{1})$  planes are superimposable mirror images of each other. In addition, each projection has mirror symmetry. This mirror symmetry in the stereographic projection indicates that there is an improper symmetry operator perpendicular to this surface, resulting in planes that are

achiral. The interface model in Figure 23C shows that these two surfaces are also superimposable on each other; therefore, the  $(001)$  and  $(00\bar{1})$  planes of CuO are achiral.

In Figures 24A and 24B, although the stereographic projections of the  $(111)$  and  $(\bar{1}\bar{1}\bar{1})$  planes are mirror images of each other, they are not superimposable. Also, neither projection has mirror symmetry. The absence of mirror symmetry in the stereographic projection indicates that only proper symmetry operators are perpendicular to this surface. The presence of only proper symmetry operators indicates that these planes are chiral. The interface model in Figure 24C shows that these two surfaces are not superimposable on each other; therefore, the  $(111)$  and  $(\bar{1}\bar{1}\bar{1})$  planes of CuO are chiral.

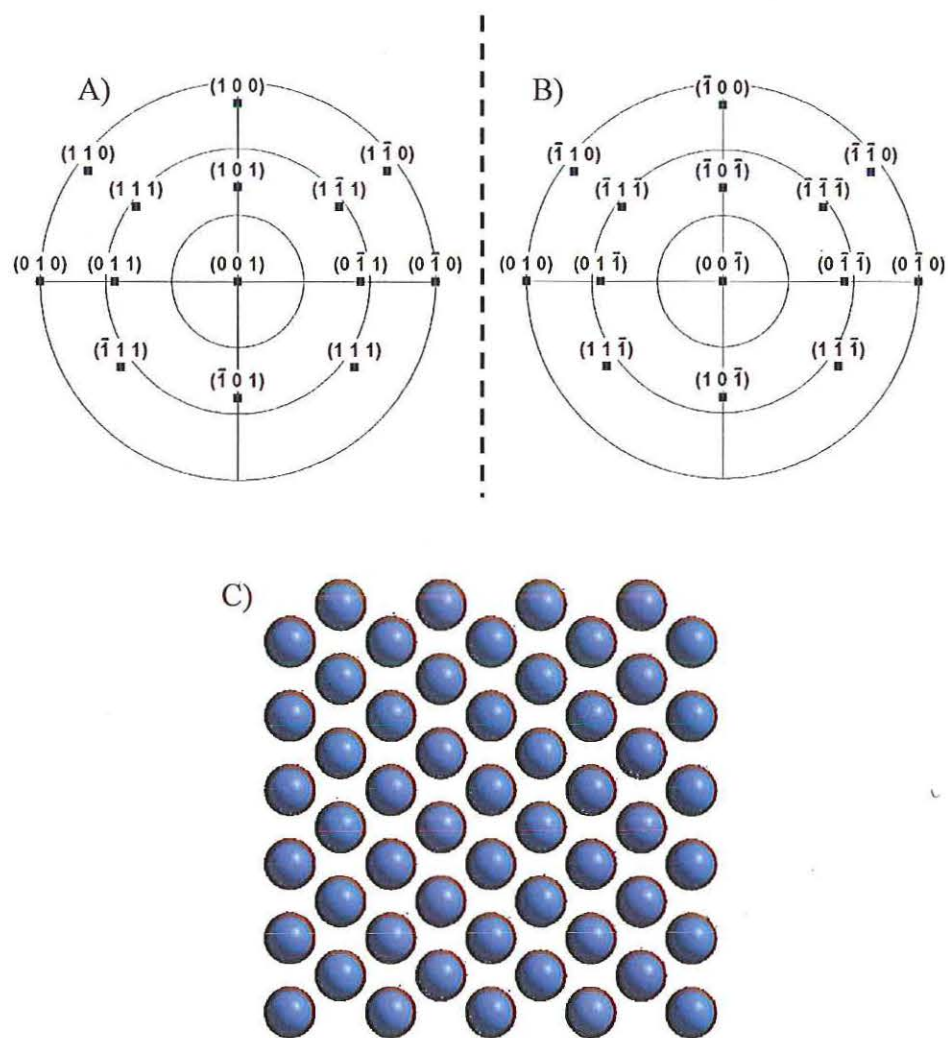


Figure 23. Stereographic projections of the A)  $(001)$  and B)  $(00\bar{1})$  orientations of CuO. These two orientations are superimposable mirror images of each other; they are achiral. The radial grid lines on the stereographic projections correspond to  $30^\circ$  increments of the tilt angle,  $\chi$ . C) The interface model of  $(00\bar{1})$  CuO (front, blue Cu atoms) on  $(001)$  CuO (back, brown Cu atoms) with a common  $[010]$  direction. These two orientations are superimposed onto each other, indicating that they are achiral.

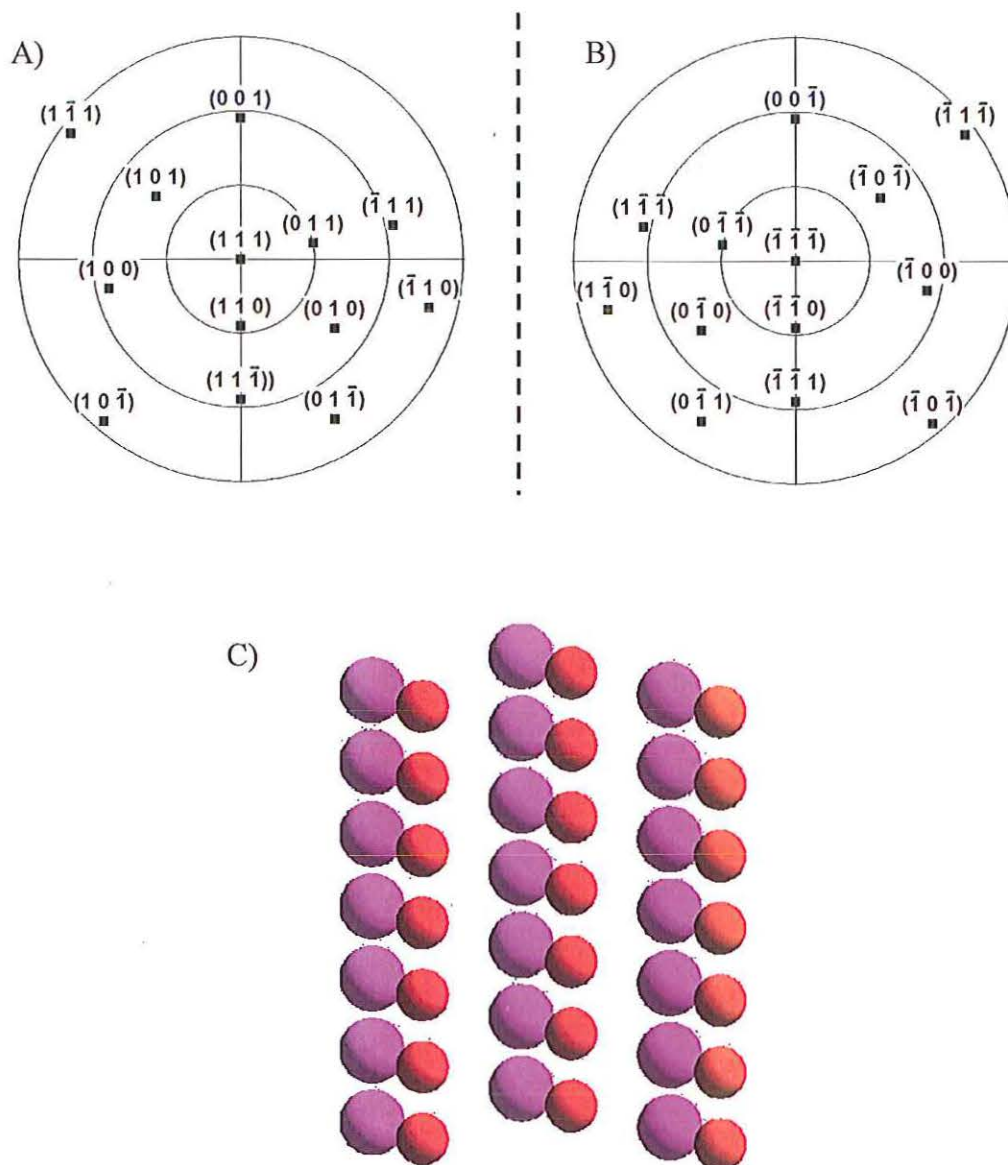


Figure 24. Stereographic projections of A) (111) and B)  $(\bar{1}\bar{1}\bar{1})$  orientations of CuO. These two orientations are nonsuperimposable mirror images of each other; they are chiral. The radial grid lines on the stereographic projections correspond to  $30^\circ$  increments of the tilt angle,  $\chi$ . C) The interface model of  $(\bar{1}\bar{1}\bar{1})$  CuO (red oxygen atoms) on (111)CuO (violet oxygen atoms) with a common  $[1\bar{1}0]$  direction. These two surfaces are nonsuperimposable; therefore, they are chiral.

Paper IV explains that the chirality of the electrodeposited CuO film is controlled by the enantiomer used to form Cu(II) complexes. Epitaxial films of cupric oxide (CuO) can be electrodeposited on Au(001)<sup>7,8</sup> and Cu(111)<sup>9</sup> single crystals. Paper IV presents details on the electrodeposition of chiral CuO films onto Au(001) from solutions using an enantiomer of tartaric acid to direct the chirality. In particular, it shows how X-ray diffraction pole figures and stereographic projections can be used to determine the absolute configuration of the film and how azimuthal scans can be used to determine the enantiomeric excess of the orientations of the films. In addition, these results are contrasted with chiral and achiral CuO films deposited onto Au(001) using Cu(II) complexes of the amino acids alanine, valine, and glycine as precursors for the deposition bath.

Films of CuO were deposited on Au(001) single crystals from an alkaline solution of copper(II) complexed with tartaric acid. The deposition bath was prepared by dissolving 7.5 grams of copper(II) sulfate pentahydrate in a solution containing 4.5 grams of tartaric acid dissolved in 100 ml of deionized water. A second solution of 12.0 grams of NaOH pellets in 50 ml of deionized water was added to this solution, resulting in a dark blue solution. The base solution must be cooled to room temperature or a white precipitate forms in the deposition solution. The final concentration of the deposition bath was 0.2 M CuSO<sub>4</sub>\*5H<sub>2</sub>O, 0.2 M L-, D-, or DL tartaric acid, and 3 M NaOH. Films were deposited at a constant anodic current density of 1 mA/cm<sup>2</sup> at 30°C for 30 minutes.

The solutions for deposition from amino acids were prepared by forming complexes of Cu(II) with an excess amount of amino acid in base. The solution for depositing CuO from amino acids in this paper was first reported by Nakaoka and Ogura

and consisted of 50 mM amino acid, 5 mM Cu(II), and 0.2 M NaOH.<sup>180</sup> Like the copper(II)-tartrate bath, the Cu(II) forms a complex with amino acid before the base solution is added to the solution. The amino acids studied were achiral glycine and the L-, D-, and racemic forms of alanine and valine. The racemic amino acid solutions were made using equal amounts of the L- and D-amino acids. Films were deposited on Au(001) single crystal at a constant anodic current density of 100  $\mu\text{A}/\text{cm}^2$  at 30°C for 5 minutes.

The X-ray diffraction patterns of films grown from an L-tartrate bath were identical to those of films grown from a D-tartrate bath. In these diffraction patterns, only the  $\text{CuO}\{\bar{1}11\}$  family of planes was present. However, based on the chiral selection rules determined in the previous section, the  $(\bar{1}11)$  and  $(1\bar{1}\bar{1})$  planes are chiral. Both of these orientations have the same d-spacing of 0.2525 nm. To determine absolute orientations of the films,  $\text{CuO}(111)$  pole figures and stereographic projections were used. Because the  $\text{CuO}(200)$  d-spacing is similar to the  $\text{CuO}(111)$  d-spacing, reflections due to  $\text{CuO}(200)$  reflections are observed in the pole figure. Likewise, the  $\text{CuO}(111)$  d-spacing is similar to the  $(111)\text{Au}$  d-spacing. Although this pole figure is maximized for  $\text{CuO}(111)$  reflections,  $\text{Au}(111)$  reflections are seen in the pole figures. These Au reflections provided an internal standard for comparing the pole figures of the two films.

Figure 25 shows the stereographic projection of the A)  $(1\bar{1}\bar{1})$  and B)  $(\bar{1}11)$  orientations indicating the positions where the  $\{111\}$  and  $\{100\}$  reflections would occur. Figure 24A shows that for the  $(1\bar{1}\bar{1})$  orientation, the reflections from the  $(1\bar{1}\bar{1})$  plane at a tilt angle,  $\chi$ , of 57° and from the  $(\bar{1}\bar{1}\bar{1})$  plane at  $\chi = 63^\circ$  are separated azimuthally by 115° rotated counter-clockwise ( $\Delta\phi = -115^\circ$ ). Figure 24B shows that for the  $(\bar{1}11)$

orientation, reflections from the  $(\bar{1}\bar{1}\bar{1})$  plane at  $\chi = 57^\circ$  and from the  $(111)$  plane at  $\chi = 63^\circ$  are separated azimuthally by  $\Delta\phi = +115^\circ$ . In both stereographic projections, the  $\{100\}$  reflections are at  $\chi = 62^\circ$  and  $\Delta\phi = 180^\circ$  from the  $(111)$  and  $(\bar{1}\bar{1}\bar{1})$  reflections. These stereographic projections of the  $(1\bar{1}\bar{1})$  and  $(\bar{1}11)$  orientations are nonsuperimposable mirror images of each other; the two orientations are enantiomorphs. By using the positions of the peaks in the pole figures, the absolute chiral orientations of the two films can be determined.

Figure 25 also shows the CuO(111) pole figures for CuO films on Au(001) grown from C) L-tartaric acid and D) D-tartaric acid. The Au(111) reflections at  $\chi = 55^\circ$  coincide with the  $(1\bar{1}1)$  reflection of the  $(1\bar{1}\bar{1})$  orientation and the  $(\bar{1}1\bar{1})$  reflection of the  $(\bar{1}11)$  orientation at  $\chi = 57^\circ$ . The overlapping peaks provide an internal reference for comparing the pole figures. The chirality of these pole figures is evident. The stereographic projection of the corresponding orientation is overlaid on these pole figures. The films from L-tartaric acid solution grew with a  $\{1\bar{1}\bar{1}\}$  orientation, whereas films grown from D-tartaric acid solution had a  $\{\bar{1}11\}$  orientation. The comparison of the pole figure to the stereographic projection also indicates that four CuO domains exist on the symmetric four-fold symmetry of Au(001). Although not shown in Figure 25, the CuO(111) pole figure for a CuO film on Au(001) grown from DL-tartaric acid has both chiral orientations with equal intensity, making the film achiral.

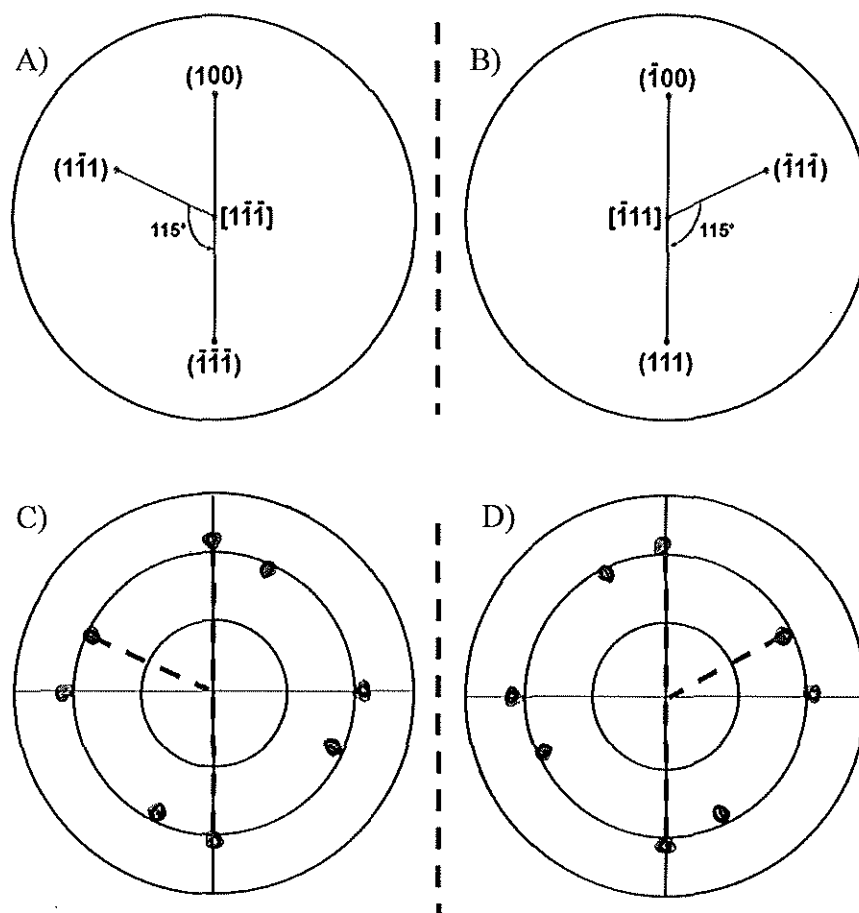


Figure 25. The stereographic projection of A)  $\text{CuO}(1\bar{1}\bar{1})$  and B)  $\text{CuO}(\bar{1}11)$ , indicating the positions where the  $\{111\}$  and  $\{100\}$  reflections occur. The  $\text{CuO}(111)$  pole figures for  $\text{CuO}$  films on  $\text{Au}(001)$  grown from C) L-tartaric acid and D) D-tartaric acid. Based on the stereographic projections and pole figures, the films from L-tartaric acid solution grow with a  $\{1\bar{1}\bar{1}\}$  orientation whereas films grown from D-tartaric acid solution have a  $\{\bar{1}11\}$  orientation.

A comparison of the area under the  $\{111\}$  reflections in an azimuthal scan for each orientation indicates that the  $\{1\bar{1}\bar{1}\}$  films from L-tartaric acid solution have an enantiomeric excess of 95%;  $\{\bar{1}11\}$  films grown from D-tartaric acid solution have an enantiomeric excess of 93%. A racemic mixture of tartaric acid has equal amounts of the

two enantiomeric orientations. The chiral films also showed chiral recognition of tartrate. Cyclic voltammograms showed that the film grown from L-tartaric acid selectively oxidized L-tartaric acid over D-tartaric acid, whereas the film grown from D-tartaric acid selectively oxidized D-tartaric acid over L-tartaric acid. Cyclic voltammograms on a racemic film from DL-tartaric acid solution showed no enantioselectivity for the electrooxidation of tartaric acid.

In contrast to the films grown from Cu(II) complexes of tartaric acid, which have only one chiral orientation with high enantiomeric excess, the films grown from Cu(II) complexes of amino acids have two chiral orientations on Au(001), with smaller enantiomeric excesses. The films grown from L-alanine and L-valine solution have small excesses of  $\{\bar{1}11\}$  and  $\{\bar{1}\bar{1}\bar{1}\}$  orientations, whereas the films grown from D-alanine and D-valine have small excesses of the  $\{1\bar{1}\bar{1}\}$  and  $\{111\}$  orientations. Films grown from a glycine bath have equivalent amounts of the  $\{\bar{1}11\}$  and  $\{1\bar{1}\bar{1}\}$  orientations and no indication of the  $\{\bar{1}\bar{1}\bar{1}\}$  and  $\{111\}$  orientations.

## 1.6 ELECTROCHEMICAL BIOMINERALIZATION

Biom mineralization is “the study of the formation, structure, and properties of inorganic solids deposited in biological systems”.<sup>181</sup> Research in biom mineralization generally involves the chemical precipitation, etching, and spray coating of calcium salts such as calcium carbonates, oxalates, and phosphates.<sup>181-185</sup> As research in biomaterials has developed, electrodeposition has been introduced to produce biocompatible coatings of brushite and hydroxyapatite on metal implants.<sup>186,187</sup> Electrodeposition has also been used to study the effects of metal ions and the deposition conditions on development of

calcium carbonates.<sup>188-190</sup> Unlike chemical precipitation, in which homogenous nucleation occurs throughout the solution, electrodeposition occurs by heterogeneous nucleation on the electrode surface. The electrodeposition of biomaterials occurs by electrochemically generating hydroxide ions, increasing the local pH at the electrode surface.

Previously, the production of calcite, a calcium carbonate polymorph, has been studied by altering the surface the material. Specifically, it has been chemically etching with, or precipitated in, the presence of various modifiers.<sup>191-201</sup> The use of chiral organic modifiers has produced the precipitated and etched calcite crystals with chiral formations.<sup>191-195</sup> Research by the Switzer group in chirality had shown that chiral CuO films are produced by electrodeposition from enantiomeric copper(II) tartrate and amino acid deposition baths.<sup>7-9</sup> Inspired by the chiral structures of nature and these chiral studies, the group began to explore electrochemical biomineralization of chiral calcite.

Paper V describes the production of chiral facets of calcite by electrodepositing the films in the presence of chiral additives. The calcium carbonate films were deposited at 30°C using a constant potential of -1.1 V vs. Ag/AgCl for 1800-3600 s. The argon purged deposition solution consisted of 4.1 mM CaCl<sub>2</sub>\*2H<sub>2</sub>O, 7.1 mM NaHCO<sub>3</sub>, and 3.2 mM MgCl<sub>2</sub>. One organic additive was introduced to this solution for film morphology comparison. The concentration of the additive was 2.5 mM of succinic acid, 2.2 mM of racemic malic acid, 2.0 mM of the enantiomer of tartaric acid, 2.2 mM of the enantiomer of malic acid, or 4.5 mM of the enantiomer of aspartic acid. All of the films were deposited onto stainless steel substrates via the electrochemical production of hydroxide ions, increasing the local pH and forcing CaCO<sub>3</sub> to precipitate on the substrate (Equations

8 and 9). Because the various polymorphs of calcium carbonate have different crystal structures, the deposited calcium carbonate films are easily differentiated by X-ray diffraction.

Figure 26 shows the crystal structure of calcite (space group,  $R\bar{3}c$ ) with reference to the hexagonal axes. This space group is centrosymmetric. Although calcite crystallizes in an achiral space group, chiral planes do exist. A rhombohedral system transformed onto hexagonal axes has two axes of equal length and a  $120^\circ$  angle ( $\gamma$ ) between the two axes. In this arrangement, the c-axis is the unique axis. The a and b axes do not intersect each other at right angles, but they are perpendicular to the c axis. Based on the space group, the improper rotation ( $\bar{3}$ ) is along the c-axis. A c glide plane is perpendicular to the  $[100]$ ,  $[010]$  and  $[\bar{1}\bar{1}0]$  directions. Therefore, a glide plane is perpendicular to the a- and b-axes. In hexagonal and transformed rhombohedral structures, the Miller indices have four numbers, h, k, i, and l. The third number, i, is equal to  $\overline{(h+k)}$ , which is considered a redundant index along the  $[\bar{1}\bar{1}0]$ . Therefore, a glide plane is also perpendicular to this axis. Since an achiral plane has an improper symmetry operator, such as a mirror or glide plane, perpendicular to it, the achiral planes of calcite are parallel to the a-, b-, or i-axes, when  $h=0$ ,  $k=0$ , or  $i=0$ , respectively. Consistent with the point group  $\bar{3}m1$  in Table 2, chiral planes are those on which  $h \neq 0$ ,  $k \neq 0$ , or  $i \neq 0$ . The common cleavage  $\{10\bar{1}4\}$  planes of calcite, (i.e. planes such as  $(10\bar{1}4)$ ,  $(01\bar{1}4)$ , and  $(1\bar{1}04)$ ), are achiral. An example of a set of chiral planes is the  $\{21\bar{3}1\}$  planes of dog-tooth calcite.

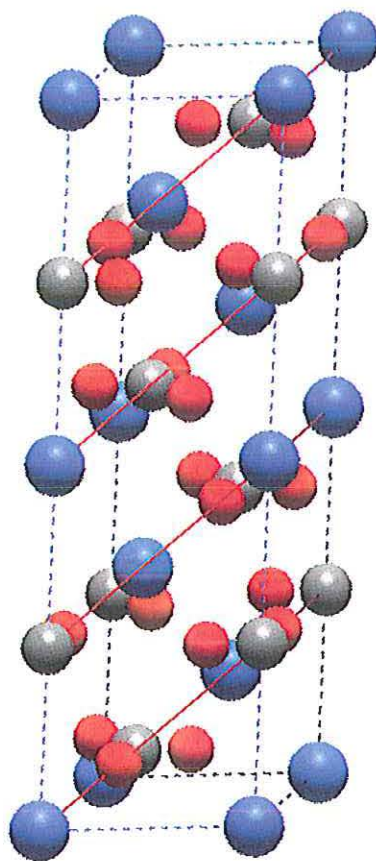


Figure 26. The crystal structure of calcite. For calcite (space group,  $R\bar{3}c$ ), the lattice parameters are  $a = b = 0.4989$  nm,  $c = 1.7062$  nm,  $\alpha = \beta = 90^\circ$ , and  $\gamma = 120^\circ$ . The calcium atoms are blue, the carbon atoms are gray, and the oxygen atoms are red. The  $\{10\bar{1}4\}$  family of planes is indicated with red lines.

In the present research, calcite deposits were electrochemically produced that exhibit achiral and chiral facets when grown in the presence of magnesium and the dicarboxylic acids, as indicated in the SEM images in Figure 27. Symmetric calcite facets were produced in the presence of an asymmetric dicarboxylic acid, succinic acid, (Figure 27A) and in the presence of a racemic mixture of malic acid (Figure 27B). Chiral facets were produced in the presence of L- and D-tartaric acid (Figures 27C and 27D) as well as

L- and D-malic acid. The addition of L- and D- aspartic acid, a dicarboxylate amino acid, also generated chiral faceted calcite (Figures 27E and 27F, respectively). Due to the precipitation of calcium DL-tartrate in the deposition bath, a calcite deposit illustrating the influence of DL-tartaric acid has not been produced. Films that were grown from L-tartaric acid had morphologies that rotated in the same direction as that of calcite deposited in the presence of D-malic and D-aspartic acids. Using the Cahn-Ingold-Prelog nomenclature for the additives, a relationship among these deposits materialized. Deposits from chiral molecules with an R designation, such as L-tartaric, D-malic, and D-aspartic acids, have morphologies that rotate clockwise whereas deposits from S-molecules have morphologies that rotate counterclockwise.

The SEM images of the deposit morphologies grown in the presence of the L- and D-forms of the acids were nonimsuperposable mirror images of each other. The rhombohedral facets were consistent with the  $\{10\bar{1}4\}$  facets. However, this plane of calcite is achiral. These chiral morphologies have been attributed to the reduction of symmetry of the  $\{10\bar{1}4\}$  plane due to the step edge selectivity of the enantiomer. According to Orme *et al.*, a dicarboxylate enantiomer binds to two sites: on the  $\{10\bar{1}4\}$  terrace and on a  $\{11\bar{2}0\}$  step.<sup>194</sup> Whereas the  $\{10\bar{1}4\}$  planes are achiral, the  $\{11\bar{2}0\}$  planes are chiral. The selective bidentate bonding of chiral dicarboxylate additives on these two calcite surfaces renders an overall chiral morphology.

Other chiral additives such as glucose have been studied, but these have not exhibited this visible chirality seen in SEM images of calcite from L- and D-tartaric, L- and D-malic, and L- and D-aspartic acid. Appendix C provides examples of the effect of other chiral additives on the morphology of calcium carbonate films.

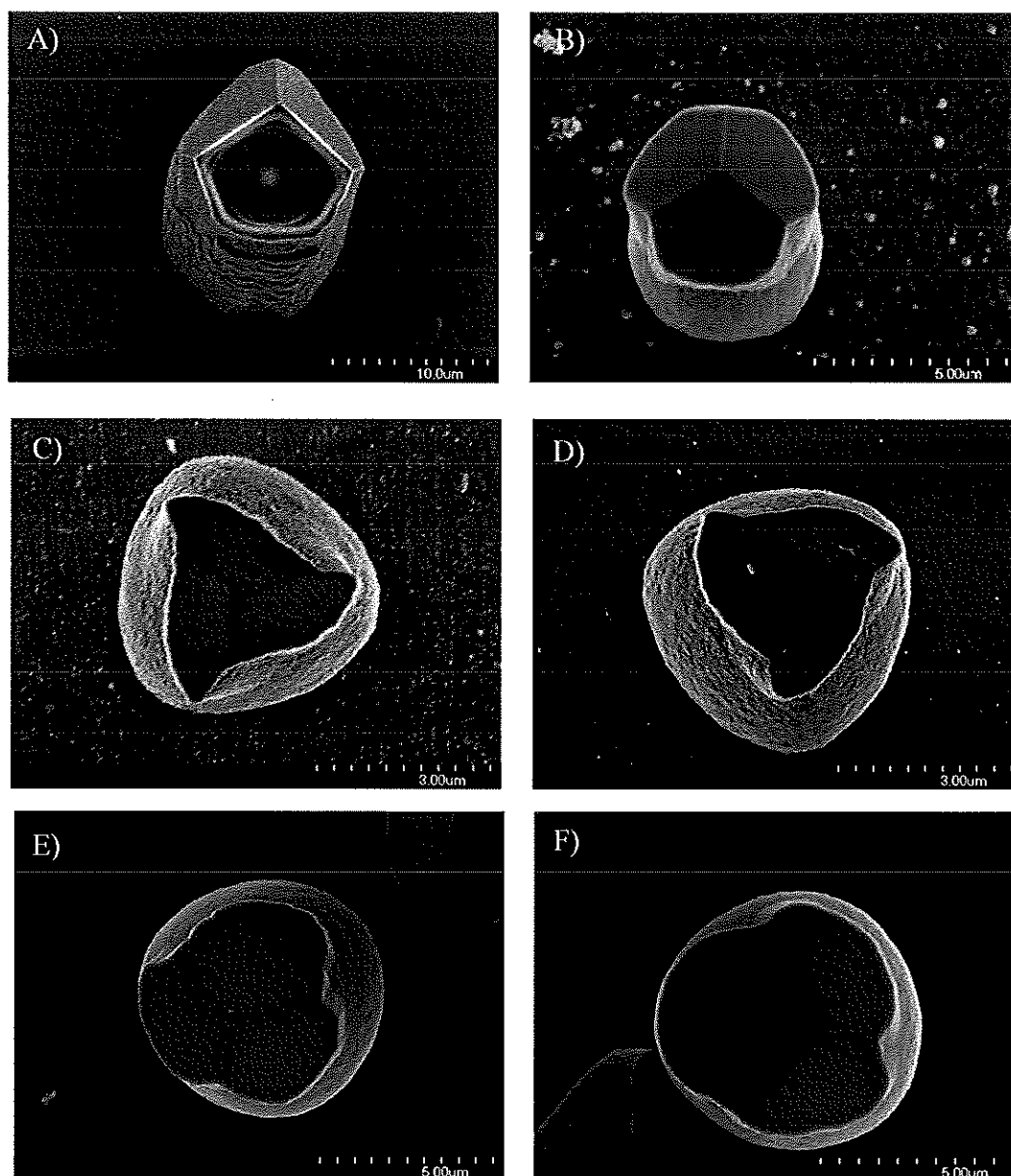


Figure 27: Achiral and chiral facets of calcite. Achiral morphologies of calcite are deposited from A) succinic acid and B) racemic malic acid solutions. Calcite with chiral facets are electrodeposited from C) L-tartaric acid, D) D-tartaric acid, E) L-aspartic acid, and F) D-aspartic acid solutions. Films deposited from solution with R molecules have morphologies that rotate counterclockwise, whereas those from solutions with S molecules rotate clockwise.

## REFERENCES

1. J. A. Switzer, in *Electrochemistry of Nanomaterials*, G. Hodes, Ed. (Wiley-VCH, Weinheim, 2001) chap. 3.
2. J. A. Switzer, in *Handbook of Nanophase Materials*, A. Goldstein, Ed. (Marcel Dekker, New York, 1996) chap. 4.
3. R. Liu, E. W. Bohannon, J. A. Switzer, F. Oba, F. Ernst, *Appl. Phys. Lett.* **83**, 1944-1946 (2003).
4. R. Liu, F. Oba, E. W. Bohannon, F. Ernst, J. A. Switzer, *Chem. Mater.* **15**, 4882-4885 (2003).
5. R. Liu, E. A. Kulp, F. Oba, E. W. Bohannon, F. Ernst, J. A. Switzer, *Chem. Mater.* **17**, 725-729 (2005).
6. J. A. Switzer, H. M. Kothari, E. W. Bohannon, *J. Phys. Chem. B* **106**, 4027-4031 (2002).
7. J. A. Switzer, H. M. Kothari, P. Poizot, S. Nakanishi, E. W. Bohannon, *Nature* **425**, 490-493 (2003).
8. H. M. Kothari, E. A. Kulp, S. Boonsalee, M. P. Nikiforov, E. W. Bohannon, P. Poizot, S. Nakanishi, J. A. Switzer, *Chem. Mater.* **16**, 4232-4244 (2004).
9. E. W. Bohannon, H. M. Kothari, I. M. Nicic, J. A. Switzer, *J. Amer. Chem. Soc.* **126**, 488-489 (2004).
10. J. A. Switzer, C.-J. Hung, E. W. Bohannon, M. G. Shumsky, T. D. Golden, D. C. van Aken, *Adv. Mater.* **9**, 334-338 (1997).
11. J. A. Switzer, C.-J. Hung, L.-Y. Huang, E. R. Switzer, D. R. Kammler, T. D. Golden, E. W. Bohannon, *J. Amer. Chem. Soc.* **120**, 3530-3531 (1998).
12. E. W. Bohannon, L.-Y. Huang, F. S. Miller, M. G. Shumsky, J. A. Switzer, *Langmuir* **15**, 813-818 (1999).
13. M. J. Siegfried, K.-Y. Choi, *J. Amer. Chem. Soc.* **154**, D674-D677 (2007).
14. M. J. Siegfried, K.-Y. Choi, *Angew. Chem. Int. Ed.* **47**, 368-372 (2008).
15. E. A. Kulp, S. J. Limmer, E. W. Bohannon, J. A. Switzer, *Solid State Ionics* **178**, 749-757 (2007).
16. A.Q. Wang, T.D. Golden, *J. Electrochem. Soc.* **150**, C616-C620 (2003).

17. T.D. Golden, A.Q. Wang, *J. Electrochem. Soc.* **150**, C621-C624 (2003).
18. M. Abe, Y. Tamaura, *Jpn. J. Appl. Phys.* **22**, L511-L513 (1983).
19. T. A. Sorenson, S. A. Morton, D. G. Waddill, J. A. Switzer, *J. Amer. Chem. Soc.* **124**, 7604-7609 (2002).
20. D. Carlier, C. Terrier, C. Arm, J-Ph. Ansermet, *Electrochem. Solid State Lett.* **8**, C43-C46 (2005).
21. K. Nishimura, Y. Kitamoto, M. Abe, *IEEE Trans. Magn.* **35**, 3043-3045 (1999).
22. S. Peulon, H. Antony, L. Legrand, A. Chausse, *Electrochim. Acta* **49**, 2891-2899 (2004).
23. S.-Y Wang, K.-C. Ho, S.-L. Kuo, N.-L. Wu, *J. Electrochem. Soc.* **153**, A75-A80 (2006).
24. L. Martinez, D. Leinen, F. Martin, M. Gabas, J. R. Ramos-Barrado, E. Quagliata, E. A. Dalchiele, E. A., *J. Electrochem. Soc.*, **154**, D126-D133 (2007).
25. S. Chatman, A. J. G. Noel, K. M. Poduska, *J. Appl. Phys.* **98**, 113902/1-113902/6 (2005).
26. C.-L. Teng, M. P. Ryan, *Electrochem. Solid State Lett.* **10**, D108-D112 (2007).
27. H. M. Kothari, E. A. Kulp, S. J. Limmer, P. Poizot, E. W. Bohannon, J. A. Switzer, *J. Mater. Res.* **21**, 293-301 (2006).
28. S. Mitra, P. Poizot, A. Finke, J.-M. Tarascon, *Adv. Funct. Mater.* **16**, 2281-2287 (2006).
29. E. A. Kulp, H. M. Kothari, S. J. Limmer, J. Yang, R. V. Gudavarthy, E. W. Bohannon, J A. Switzer, *unpublished results*.
30. J. K. Barton, A. A. Vertegel, E. W. Bohannon, J. A. Switzer, *Chem. Mater.* **13**, 952-959 (2001).
31. E. W. Bohannon, M. G. Shumsky, J. A. Swizer, *Chem. Mater.* **11**, 2289-2291 (1999).
32. J. A. Switzer, *J. Electrochem. Soc.* **133**, 722-728 (1986).

33. R. A. van Leeuwen, C.-J. Hung, D. R. Kammler, J. A. Switzer, *J. Phys. Chem.* **99**, 15247-15252 (1995).
34. B. E. Breyfogle, C. J. Hung, M. G. Shumsky, J. A. Switzer, *J. Electrochem. Soc.* **143**, 2741-2746 (1996).
35. J. A. Switzer, M. G. Shumsky, E. W. Bohannan, *Science* **284**, 293-296 (1999).
36. E. W. Bohannan, C. C. Jaynes, M. G. Shumsky, J. K. Barton, J. A. Switzer, *Solid State Ionics* **131**, 97-107 (2000).
37. A. A. Vertegel, E. W. Bohannan, M. G. Shumsky, J. A. Switzer, *J. Electrochem. Soc.* **148**, C253-C256 (2001).
38. J. A. Switzer, *et al.*, *Science* **264**, 1573-1576 (1994).
39. J. A. Switzer, M. J. Shane, R. J. Phillips, *Science* **247**, 444-446 (1990).
40. J. A. Switzer, R. P. Raffaele, R. J. Phillips, C.-J. Hung, T. D. Golden, *Science* **258**, 1918-1921 (1992).
41. H. M. Kothari, A. A. Vertegel, E. W. Bohannan, J. A. Switzer, *Chem. Mater.* **14**, 2750-2756 (2002).
42. R. J. Phillips, T. D. Golden, M. G. Shumsky, E. W. Bohannan, and J. A. Switzer *Chem. Mater.* **9**, 1670-1677 (1997).
43. J. A. Switzer, T. D. Golden, *Adv. Mater.* **5**, 474-476 (1993).
44. S. J. Limmer, E. A. Kulp, E. W. Bohannan, J. A. Switzer, *Langmuir* **22**, 10535-10539 (2006).
45. E. A. Kulp, J. A. Switzer, *J. Amer. Chem. Soc.* **129**, 15120-15121 (2007).
46. Y. Zhou, R. J. Phillips, J. A. Switzer, *J. Am. Ceram. Soc.* **78**, 981-985 (1995).
47. J. A. Switzer, *Ceram. Bull.* **66**, 1521-1524 (1987).
48. J. A. Switzer, R. J. Phillips, *J. Mater. Res. Soc. Symp. Proc.*, **121**, 111-114 (1988).
49. D. R. Lide, *CRC Handbook of Chemistry and Physics* (CRC Press, New York, ed. 77, 1996).
50. J. A. Dean, *Lange's Handbook of Chemistry* (McGraw-Hill, New York, ed. 15, 1999).

51. A. J. Bard, L. R. Faulkner, *Electrochemical Methods: Fundamentals and Applications* (Wiley, New York, ed. 2, 2001).
52. E. Gileadi, E. Kirowa-Eisner, J. Penciner, *Interfacial Electrochemistry: An Experimental Approach* (Addison-Wesley, Reading, MA, 1975).
53. J. O'M. Bockris, A. K. N. Reddy, *Modern Electrochemistry: An Introduction to an Interdisciplinary Area*. (Plenum, New York, 1973).
54. D. T. Sawyer, A. Sobkowiak, J. L. Roberts, *Electrochemistry for Chemists* (Wiley, New York, ed. 2, 1995).
55. D. A. Buttry, M. D. Ward, *Chem. Rev.* **92**, 1355-1379 (1992).
56. B. D. Cullity, *Elements of X-ray Diffraction* (Addison-Wesley, Reading, MA, ed. 2, 1978).
57. R. Jenkins, R. L. Snyder, *Introduction to X-ray Powder Diffractometry* (Wiley, New York, 1996).
58. J. J. Rousseau, *Basic Crystallography* (Wiley, New York, 1999).
59. A. R. West, *Solid State Chemistry and Its Applications* (Wiley, New York, 1984).
60. J. I Goldstein, A.D. Roming, Jr., D. E. Newbury, C. E. Lyman, P. Echlin, C. Fiori, D. C. Joy, E. Lifshin, *Scanning Electron Microscopy and X-ray Microanalysis: A Text for Biologists, Materials Scientists, and Geologists* (Plenum, New York, ed. 2, 1992).
61. E. Meyer, H. J. Hug, R. Bennewitz, *Scanning Probe Microscopy: The Lab on a Tip* (Springer, Berlin, 2004).
62. D. Briggs, M. P. Seah, *Practical Surface Analysis by Auger and X-ray Photoelectron Spectroscopy* (Wiley, New York, 1983).
63. A. G. Maddock, *Mössbauer Spectroscopy Principles and Applications* (Horwood, Chichester, 1997).
64. D. Eyidi, M.D. Croitoru, O. Eibl, R. Nemetschek, W. Prusseit, *J. Mater. Res.* **18**, 14-26 (2003).
65. X.D. Wu, R.C. Dye, R.E. Muenchausen, S.R. Foltyn, M. Maley, A. D. Rollett, A.R. Garcia, N.S. Nogar, *Appl. Phys. Lett.* **58**, 2165-2167 (1991).

66. J.-M. Lee, K.-T. Kim, C.-I. Kim, *Thin Solid Films* **447-448**, 322-326 (2004).
67. C. Kwon, Y. Gim, Y. Fan, M.F. Hundley, J.M. Roper, P.N. Arendt and Q.X. Jia, *Appl. Phys. Lett.* **73**, 695-697 (1998).
68. H. Matsuda, H. Sakakima, H. Adachi, A. Odagawa, K. Setsune, *J. Mater. Res.* **17**, 1985-1991 (2002).
69. R. Doshi, V.L. Richards, J.D. Carter, X. Wang, M. Krumpelt, *J. Electrochem. Soc.* **146**, 1273-1278 (1999).
70. T. Hibino, A. Hashimoto, T. Inoue, J.-I. Tokuno, S.-I. Yoshida, M. Sano, *Science* **288**, 2031-2033 (2000).
71. C. Xia, F. Chen, M. Liu, *Electrochem. Solid-State Lett.* **4**, A52-A54 (2001).
72. R. Peng, C. Xia, X. Liu, D. Peng, G. Meng, *Solid State Ionics* **152-153**, 561-565 (2002).
73. C. Lu, W.L. Worrell, R.J. Gorte, J.M. Vohs, *J. Electrochem. Soc.* **150**, A354-A358 (2003).
74. T. Matsui, M. Inaba, A. Mineshige, Z. Ogumi, *Solid State Ionics* **176**, 647-654 (2005).
75. E.P. Murray, T. Tsai, S.A. Barnett, *Nature* **400**, 649-651 (1999).
76. O.A. Marina, C. Bagger, S. Primdahl, M. Mogensen, *Solid State Ionics* **123**, 199-208 (1999).
77. P. Seungdoo, J.M. Vohs, *Nature* **404**, 265-267 (2006).
78. H. Uchida, S. Suzuki, M. Watanabe, *Electrochem. Solid-State Lett.* **6**, A174-A177 (2003).
79. H. He, R.J. Gorte, J.M. Vohs, *Electrochem. Solid-State Lett.* **8**, A279-A280 (2005).
80. H. Uchida, S.-i. Arisaka, M. Watanabe, *Electrochem. Solid-State Lett.* **2**, 428-430 (1999).
81. T.L. Nguyen, K. Kobayashi, T. Honda, Y. Iimura, K. Kato, A. Neghisi, K. Nozaki, F. Tappero, K. Sasaki, H. Shirahama, *Solid State Ionics* **174**, 163-174 (2004).

82. M. Shiono, K. Kobayashi, T. Lan Nguyen, K. Hosoda, T. Kato, K. Ota, M. Dokiya, *Solid State Ionics* **170**, 1-7 (2004).
83. B.P. Gorman, H.U. Anderson, *J. Am. Ceram. Soc.* **88**, 1747-1753 (2005).
84. J.-H. Wang, M. Liu, M.C. Lin, *Solid State Ionics* **177**, 939-947 (2006).
85. A. Trovarelli, *Catalysis by Ceria and Related Materials* (Imperial College Press: London, 20002).
86. E. Aneggi, M Boaro, C. de Leitenburg, G. Dolcetti, A. Trovarelli, *J. Alloy Compd.* **408-412**, 1096-1102 (2006).
87. A.J. Davenport, H.S. Isaacs, M.W. Kendig, *Corros. Sci.* **32**, 653-663 (1991).
88. Y. Zhou, J.A. Switzer, *J. Alloys Compd.* **237**, 1-5 (1996).
89. I. Zhitomirsky, A. Petric, *Mater. Lett.* **40**, 263-268 (1990).
90. R. M. Cornell, U. Schwertmann, *The Iron Oxides: Structure, Properties, Reactions, Occurrences, and Uses* (Wiley: Weinheim, 1996).
91. U. Schwertmann, R. M. Cornell, *Iron Oxides in the Laboratory: Preparation and Characterization* (Wiley, New York, 2 ed., 2000).
92. A. Yanase, K. Siratori, *J. Phys. Soc. Japan* **53**, 312-317 (1984).
93. Z. Zhang, S. Satpathy, *Phys. Rev. B* **44**, 13319-13331 (1991).
94. F. Walz, *J. Phys.: Condens. Mater.* **14**, R285-R340 (2002).
95. J. Garcia, G. Subias, *J. Phys.: Condens. Mater.* **16**, R145-R178 (2004).
96. E. J. W. Verwey, *Nature* **144**, 327-328 (1939).
97. G. T. Rado, J. M. Ferrari, *Phys. Rev. B* **15**, 290-297 (1977).
98. Y. Miyamoto, S. Ishihara, T. Hirano, M. Takada, N. Suzuki, *Solid State Commun.* **89**, 51-54 (1994).
99. S. Lee, *et al.*, *Nature Materials* **7**, 130-133 (2008).
100. J. van den Brink, D. I. Khomskii, *J. Phys.: Condens. Matter* **20**, 434217/1-434217/12 (2008).
101. G. A. Prinz, *Science* **282**, 1660-1663 (1998).

102. S. A. Wolf, *et al.*, *Science* **294**, 1488-1495 (2001).
103. J. L. Kirshvink, D. S. Jones, B. J. MacFadden, Eds. *Magnetite Biomineralization and Magnetoreception in Organisms: A New Biomagnetism* (Plenum, New York, 1985).
104. R. Wiltschko, W. Wiltschko, *Magnetic Orientation in Animals* (Springer, New York, 1995).
105. C. V. Mora, M. Davison, J. M. Wild, M. M. Walker, *Nature* **432**, 508-511 (2004).
106. M. M. Walker, J. L. Kirschvink, S.-B. R. Chang, A. E. Dizon, *Science* **224**, 751-753 (1984).
107. A. Scheffel, *et al.*, *Nature* **440**, 110-114 (2006).
108. S. Johnsen, K. J. Lohmann, *Phys. Today* 29-35 (2008).
109. G. Fleissner, B. Stahl, P. Thalau, G. Falkenberg, G. Fleissner, *Naturwissenschaften* **94**, 631-642 (2007).
110. J. van den Brink, D. I. Khomskii, *J. Phys.: Condens. Matter* **20**, 434217/1-434217/12 (2008).
111. S.-W. Cheong, M. Mostovoy, *Nature Mater.* **6**, 13-20 (2007).
112. H. Béa, M. Gajek, M. Bibes, A. Barthélémy, *J. Phys.: Condens. Matter* **20**, 434221/1-434217/11 (2008).
113. R. S. Sapieszko, E. Matijevic, *J. Colloid Interface Sci.* **74**, 405-422 (1980).
114. J. L. Jambor, J. E. Dutrizac, *Chem. Rev.* **98**, 2549-2586 (1998).
115. F. M. Michel, L. Ehm, S. M. Antao, P. L. Lee, P. J. Chupas, G. Liu, D. R. Strongin, M. A. A. Schoonen, B. L. Phillips, J. B. Parise, *Science*. **316**, 1726-1729 (2007).
116. J.-M. R. Genin, C. Ruby, A. Gehin, P. Refait, *C. R. Geoscience*. **338**, 433-446 (2006).
117. A. Goldman, *Modern Ferrite Technology* (Plenum, New York, 2 ed., 1985).
118. E. W. Gorter, *Nature* **165**, 798-800 (1950).

119. T. Kamiyama, K. Heneda, T. Sato, S. Ikeda, H. Asano, *Solid State Commun.* **81**, 563-566 (1992).
120. H. H. Hamdeh, J. C. Ho, S. A. Oliver, R. J. Willey, J. Kramer, Y. Y. Chen, S. H. Lin, Y. D. Yao, M. Daturi, G. Busca, *IEEE Trans. Magn.* **31**, 3808-3810 (1995).
121. H. H. Hamdeh, J. C. Ho, S. A. Oliver, R. J. Willey, G. Oliveri, G. Busca, *J. Appl. Phys.* **81**, 1851-1857 (1997).
122. P. A. Dickof, P. J. Schurer, A. H. Moriish, *Phys. Rev. B.* **22**, 115-127 (1980).
123. J. F. Hochepped, P. Bonville, M. P. Pileni, *J. Phys. Chem. B* **104**, 905-912 (2000).
124. S. Ammar, N. Jouini, F. Fievet, Z. Beji, L. Smiri, P. Moline, M. Danot, J.-M. Greneche, *J. Phys.: Condens. Matter* **18**, 9055-9069 (2006).
125. V. Sepelak, S. Wissmann, K. D. Becker, *J. Mater. Sci.* **33**, 2845-2850 (1998).
126. S. L. Darshane, R. G. Deshmukh, S. S. Suryanshi, I. S. Mulla, *J. Amer. Ceram. Soc.* **90**, 2724-2726 (2008)
127. F. Tomas-Alonso, J. M. Palacios Latasa, *Fuel Process. Technol.* **86**, 191-203 (2004).
128. M. Pineda, J. L. G Fierro, J. M. Palacios, C. Cilleruelo, J. V. Ibarra, *J. Mater. Sci.* **30**, 6171-6178 (1995).
129. M. Ahmed, L. Alonso, J. M. Palacios, C. Cilleruelo, J. C. Abanades, *Solid State Ionics* **138**, 51-61 (2000).
130. M. K. Roy, H.C. Verma, *J. Magn. Magn. Mater.* **306**, 98-102 (2006).
131. M. Andres Verges, M. Martinez, E. Matijevic, *J. Mater. Res.* **8**, 2916-2920 (1993).
132. M. Hong, S. Wolf, D.C. Gubser, Eds. *Metallic Multilayers and Epitaxy* (Metallurgical Society, USA, 1988).
133. L. L. Chang, B. C. Giessen., Eds. *Synthetic Modulated Structures* (Academic, Orlando, 1985).
134. C.A. Ross, *Annu. Rev. Mater. Sci.* **24**, 159-188 (1994).
135. S. S. P. Parkin, R. Bhadra, K. P. Roche, *Phys. Rev. Lett.* **66**, 2152-2155 (1991).

136. S. S. P. Parkin, Z. G. Li, D. J. Smith, *Appl. Phys. Lett.* **58**, 2710-2712 (1991)
137. K. D. Bird, M. Schlesinger, *J. Electrochem. Soc.*, **142**, L65-L66 (1995).
138. A. Cziráki, L. Péter, B. Arnold, J. Thomas, H.D. Bauer, K. Wetzig, I. Bakonyi, *Thin Solid Films* **424**, 229-238 (2003).
139. W. Scharzacher, D. S. Lashmore, *IEEE Trans. Magn.* **32**, 3133-3153 (1996).
140. S. Z. Hua, D. S. Lashmore, L. Salamanca-Riba, W. Schwarzacher, L. J. Swartzendruber, R. D. McMichael, L. H. Bennett, and R. Hart, *J. Appl. Phys.* **76**, 6519 (1994)
141. M. Alper, K. Attenborough, R. Hart, S.J. Lane, D.S. Lashmore, C. Younes, W. Schwarzacher, *Appl. Phys. Lett.* **63**, 2144 (1993).
142. M. Alper, W. Schwarzacher, S.J. Lane, *J. Electrochem. Soc.* **144**, 2346-2352 (1997).
143. G. Nabyouni, W. Schwarzacher, *J. Cryst. Growth* **275**, e1259-e1262 (2005).
144. A. P. O'Keeffe, O. I. Kasyutich, W. Schwarzacher, L. S. de Oliveira, A. A. Pasa, *Appl. Phys. Lett.* **73**, 1002-1004 (1998).
145. O. I. Kasyutich, W. Schwarzacher, V. M. Fedosyuk, P. A. Laskarzhevskiy, A. I. Masliy, *J. Electrochem. Soc.* **147**, 2964-2968 (2000).
146. D. Simunovich, M. Schlesinger, D. D. Synder, *J. Electrochem. Soc.* **141**, L10-L11 (1994).
147. S.K. Ghosh, P.K. Limaye, B.P. Swain, N.L. Soni, R.G. Agrawal, R.O. Dusane, A.K. Grover, *Surf. Coatings Technol.* **201**, 4609-4618 (2007).
148. D. S. Lashmore, M. P. Dariel, *J. Electrochem. Soc.* **135**, 1218-1221 (1988).
149. T. Moffat, *J. Electrochem. Soc.* **142**, 3767-3770 (1995).
150. D. Tench, J. White, *J. Electrochem. Soc.* **137**, 3061-3066 (1990).
151. C. Ogden, *Plating Surface Finishing* **5**, 130-134 (1986).
152. J. Yahalom, O. Zadok, *J. Mater. Sci.* **22**, 499-503 (1987).
153. A. Tokarz, A. Wolkenberg, T. Przeslawski, *J. Electrochem. Soc.* **149**, C607-C609 (2002).

154. A. Fert, P. Grünberg, A. Barthélémy, F. Petroff, W. Zinn, *J. Magn. Magn. Mater.* **140-144**, 1-8 (1995).
155. C. R. Martin, *Science* **266**, 1961-1966 (1994).
156. L. Piraux, J. M. George, J. F. Despres, C. Leroy, E. Ferain, R. Legras, K. Ounadjela, A. Fert, *Appl. Phys. Lett.* **65**, 2484-2486 (1994).
157. A. Blondel, J. P. Meier, B. Doudin, J.-Ph. Ansermet, *Appl. Phys. Lett.* **65**, 3019-3021 (1994).
158. B. Ye, F. Li, D. Cimpoesu, J. B. Wiley, J.-S. Jung, A. Stancu, L. Spinu, *J. Magn. Magn. Mater.* **316**, e56-e58 (2007).
159. J. Choi, S. J. Oh, H. Ju, J. Cheon, *Nano Lett.* **5**, 2179-2183 (2005).
160. T. Torimoto, A. Obayashi, S. Kuwabata, H. Yoneyama, *Electrochem. Comm.* **2**, 359-362 (2000).
161. R. Vaidyanathan, S. M. Cox, U. Happek, D. Banga, M. K. Mathe, J. L. Stickney, *Langmuir*, **22**, 10590-10595 (2006).
162. V. Venkatasamy, N. Jayaraju, S. M. Cox, C. Thambidurai, J. L. Stickney, *J. Electrochem. Soc.* **154**, H720-H725 (2007).
163. S. Zou, M. J. Weaver, *Chem. Phys. Lett.* **312**, 101-107 (1999).
164. T. L. Wade, R. Vaidyanathan, U. Happek, J. L. Stickney, *J. Electroanal. Chem.* **500**, 322-332 (2001).
165. B. Yoo, F. Xiao, K.N. Bozhilov, J. Herman, M. A. Ryan, N. V. Myung, *Adv. Mater.* **19**, 296-299 (2007).
166. X. Dou, G. Li, H. Lei, *Nano Lett.* **8**, 1286-1290 (2008).
167. S. D. Berry, D. M. Lind, G. Chern, H. Mathias, *J. Magn. Magn. Mater.* **123**, 126-132 (1993).
168. T. Terashima, Y. Bando, *Thin Solid Films* **152**, 455-463 (1987).
169. P. J. van der Zaag, A. R. Ball, L. F. Feiner, R. M. Wolf, P. A. A. van der Heijden, *J. Appl. Phys.* **79**, 5103-5105 (1996).
170. Y. Ijiri, J. A. Borchers, R. W. Erwin, S.-H. Lee, P.J. van der Zaag, R. M. Wolf, *J. Appl. Phys.* **83**, 6882-6887 (1996).

171. H. Yahiro, H. Tanaka, Y. Yamamoto, T. Kawai, *Jpn. J. Appl. Phys.* **41**, 5153-5154 (2002).
172. S. C. Stinson, *Chem. Eng. News* **79**, 79-97 (2001).
173. Y. Izumi, *Adv. Catal.* **32**, 215-271 (1983).
174. C. F. McFadden, P.S. Cremer, A.J. Gellman, *Langmuir* **12**, 2483-2487 (1996).
175. D. S. Scholl, *Langmuir* **14**, 862-867 (1998).
176. G. A. Attard, *J. Phys. Chem. B* **105**, 3158-3167 (2001).
177. A. Ahmadi, G. Attard, J. Feliu, A. Rodes, *Langmuir* **15**, 2420-2424 (1999).
178. J. P. Glusker, M. Lewis, and M. Rossi, *Crystal Structure Analysis for Chemists and Biologists* (Wiley, New York, 1994).
179. N. F. Henry, K. Lonsdale *International Tables for X-ray Crystallography Vol. One* (Kynoch, Birmingham, 1952) pp 37-38.
180. K. Nakaoka, K. Ogura, *J. Electrochem. Soc.* **149**, C579-C585 (2002).
181. S. Mann, *Biom mineralization: Principles and Concepts in Bioinorganic Materials Chemistry* (Oxford University, New York, 2001).
182. P. M. Dove, J. J. De Yoreo, S. Weiner, *Biom mineralization* (Mineralogical Society, Washington, D.C., 2003).
183. H. A Lowenstam, S. Weiner, *On Biom mineralization* (Oxford University, New York, 1989).
184. S. R. Khan, *Calcium Oxalate in Biological Systems* (CRC, Boca Raton, 1995).
185. P. W. Brown, B. Constantz, *Hydroxyapatite and Related Materials* (CRC, Boca Raton, 1994).
186. J. Redepenning, T. Schlessinger, S. Burnham, L. Lippiello, J. Miyano, *J. Biomed. Mater. Res.* **30**, 287-294 (1996).
187. H. Monma, *J. Ceram. Soc. Jpn.* **101**, 737-739 (1993).
188. S. Xu, C. A. Melendres, J. H. Park, M. A. Kamrath, *J. Electrochem. Soc.* **146**, 3315-3323 (1999).

189. L. Beaunier, L.; Gabrielli, C., Poindessous, G, Maurin, G.; Rosset, R. *J. Electroanal. Chem.* **501**, 41-53 (2001).
190. C. Gabrielli, G. Maurin, G. Poindessous, R. Rosset, *J. Cryst. Growth* **200**, 236-250 (1999).
191. J. M. Thomas, G. D. Renshaw, C. Roscoe, *Nature* **203**, 72-73 (1964).
192. A. P. Honess, J. R. Jones, *Bull. Geol. Soc. Amer.* **48**, 667-722 (1937).
193. A. J. Barwise, R. G. Compton, P. R. Unwin, *J. Chem. Soc. Faraday Trans.* **86**, 137-144 (1990).
194. C. A. Orme, A. Noy, A. Wierzbicki, M. T. McBride, M. Grantham, H. H. Teng, P. M. Dove, J. J. DeYoreo, *Nature* **411**, 775-779 (2001).
195. J. J. De Yoreo, P. M. Dove, *Science* **306**, 1301-1302 (2004).
196. K. J. Davis, P. M. Dove, J. J. De Yoreo, *Science* **290**, 1134-1137 (2000).
197. H. H. Teng, P. M. Dove, C. A. Orme, J. J. De Yoreo, *Science* **282**, 724-727 (1998).
198. H. H. Teng, Y. Chen, E. Pauli, *J. Am. Chem. Soc.* **128**, 14482-14484 (2006).
199. S. Mann, J. M. Didymus, N. P. Sanderson, B. R. Heywood, E. J. A. Samper, *J. Chem. Soc. Faraday Trans.* **86**, 1873-1880 (1990).
200. S. Mann, D. D. Archibald, J. M. Didymus, T. Douglas, B. R. Heywood, F. C. Meldrum, N. J. Reeves, *Science* **261**, 1286-1292 (1993).
201. Y.-J. Han, J. Aizenberg, *J. Am. Chem. Soc.* **125**, 4032-4033 (2003).

## PAPER

**I. Electrodeposition of Nanometer-Thick Ceria Films by Oxidation of  
Cerium(III)-Acetate**

Elizabeth A. Kulp<sup>‡</sup>, Steven J. Limmer<sup>‡</sup>, Eric W. Bohannon and Jay A. Switzer\*

Department of Chemistry and Graduate Center for Materials Research, University of

Missouri-Rolla, Rolla, Missouri 65409-1170 USA

<sup>‡</sup> Authors are equal contributors

\* E-mail: jswitzer@umr.edu

## ABSTRACT

Thin films of ceria were electrodeposited onto Hastelloy substrates by the electrochemical oxidation of Ce(III) acetate complexes. The mode of deposition was dependent on the applied potential. At a potential of +0.5 V vs. Ag/AgCl, the deposition proceeded by a direct oxidation of Ce(III) to ceria. Films deposited at this potential were smooth and crack-free as observed by SEM. Film thicknesses were determined by X-ray reflectivity and ellipsometry. For a deposition time of 1000 s, the ceria deposited to a thickness of approximately 40 nm and a density of 65%. The deposition exhibited self-limiting growth, with growth rates rapidly decreasing with deposition time. At a higher potential of +1.1 V vs. Ag/AgCl, the films appear to grow by an indirect mechanism, in which the oxidation of water forms O<sub>2</sub> which then reacts with Ce(III) to form ceria nanoparticles in the growth solution. It was also shown that nanometer-scale ceria powder could be produced by bubbling the solution with molecular oxygen.

## INTRODUCTION

Cerium(IV) oxide (ceria) attracts research interest for a number of applications. Many researchers are examining ceria as a buffer layer for the growth of textured superconducting films. [1, 2] The high electrical resistivity of ceria makes it an ideal buffer layer for ferroelectric films[3], as well as a tunnel barrier in magnetotransport devices.[4, 5] Due to its insulating behavior, high dielectric constant, and good lattice match with Si, ultrathin ceria layers are a promising replacement for SiO<sub>2</sub> as a gate dielectric in complementary metal–oxide–semiconductor (CMOS) transistors.[6, 7] Ceria is also important for use in solid oxide fuel cells (SOFCs), where both doped and undoped CeO<sub>2</sub> have been investigated for nearly every aspect of such devices. Ceria-based electrolytes are widely used, especially for intermediate-temperature SOFCs.[8-13] Anodes are often made with ceria,[14-18] as are interlayers.[19-22] Recent work has even examined ceria cathodes.[23] SOFCs containing ceria are widely used with both hydrocarbon and hydrogen fuels.[8-10, 12, 14, 16]

Numerous methods exist for the deposition of ceria films, including sputtering[24], e-beam evaporation[25], chemical vapor deposition[26], and sol-gel processing.[27] However, the low cost and low processing temperatures (near room temperature) of electrodeposition make it an especially appealing means to deposit thin ceria films. This is particularly true for the many applications in which the films are desired on a conducting substrate. Ceria powders[28, 29] and films[30-32] have been electrochemically prepared previously by cathodic deposition, in which the pH is increased at the electrode surface by electrochemical reactions such as the reduction of water to hydrogen gas. There have also been recent reports on the anodic deposition of

ceria films [33, 34] and powders.[35] One problem encountered with the direct oxidation of Ce(III) to produce ceria films is that the anodically deposited films were highly cracked, exhibiting a dried mud morphology.[33] In this paper we report the anodic deposition of ceria films, in which the mechanism of ceria deposition depends on the applied potential. Smooth films are deposited when Ce(III) is directly oxidized at an applied potential of 0.5 V vs. Ag/AgCl. Rougher, cracked films are deposited at a more positive potential of 1.1 V vs. Ag/AgCl, in which the Ce(III) is indirectly oxidized by electrochemically-generated oxygen gas.

## EXPERIMENTAL SECTION

The ceria deposition solution used acetate ions as stabilizing ligands, similar to the method reported by Golden et al.[33] The deposition bath was formed by first dissolving 0.1 M ammonium acetate in de-ionized water. This solution was bubbled with Ar for at least 1 hr to remove O<sub>2</sub>, and then 0.1 M Ce(NO<sub>3</sub>)<sub>3</sub> was added. This yielded a solution with a final pH of 6.1. It is also possible to deposit films from a solution containing 0.4 M ammonium acetate and 0.1 M Ce(NO<sub>3</sub>)<sub>3</sub>. This yields similar results, despite having different species present in the solution. If either solution is not bubbled with Ar to remove dissolved oxygen gas, a colloidal suspension of ceria powder is formed.

Films were deposited with a PARStat 2273 potentiostat at 65 °C under an Ar atmosphere. Deposition was at a constant potential of either +0.5 V or +1.1 V vs. Ag/AgCl, with the films deposited on electropolished tapes of Hastelloy C-276 which were provided by Los Alamos National Laboratory. These working electrodes were 1 cm

wide, 2-3 cm long, and 50  $\mu\text{m}$  thick. The substrates had an average surface roughness of about 1 nm. A Pt wire was used as the counter electrode.

Films were imaged with scanning electron microscopy (SEM, Hitachi S-4700 FESEM) and atomic force microscopy (AFM, Digital Instruments Nanoscope IIIa). Film thickness and density was determined by ellipsometry (Gaertner L116A), using a He-Ne laser (632.8 nm wavelength) at an incident angle of  $70^\circ$ . Grazing incidence x-ray diffraction (XRD) patterns were obtained with a Philips X'Pert diffractometer using  $\text{Cu K}\alpha$  source radiation with an x-ray mirror (PW3088/60) as the incident beam module and a  $0.18^\circ$  parallel plate collimator as the diffracted beam module. A fixed incident angle of  $1^\circ$  was maintained and the instrument was operated in the continuous mode with a step size of  $0.03^\circ$  and a counting time of 70 seconds. Reflectivity measurements were obtained using the same instrument and configuration, although for these measurements a symmetric scan was obtained with a step size of  $0.001^\circ$  and a counting time of 3 seconds. The powder XRD pattern was obtained using a Scintag XDS 2000 diffractometer using  $\text{Cu K}\alpha$  source radiation and a liquid nitrogen cooled Ge detector. Data was collected in the step mode with a step size of  $0.05^\circ$  and a counting time of 50 seconds per point. X-ray photoelectron spectra were collected using a Kratos Axis 165 X-ray photoelectron spectrometer utilizing monochromatic  $\text{Al K}\alpha$  radiation.

## RESULTS AND DISCUSSION

Acetate ions can act as a stabilizing ligand for  $\text{Ce}^{3+}$  species[34], where the ion may be complexed with up to four acetate ligands. To determine the predominant species in the deposition solution, we have calculated a solution species distribution for a solution

containing 0.1 M  $\text{Ce}^{3+}$  and 0.1 M acetate. The dissociation and formation constants tabulated in Table 1[36] and the following distribution fraction,  $\alpha$ , equations 1-8 of the cerium(III) species were used to calculate the distribution diagram of this system:

$$\alpha_{\text{Ce}^{3+}} = \frac{[\text{Ce}^{3+}]}{[\text{Ce}^{\text{III}}]} \quad (1)$$

$$\alpha_{\text{CeOH}^{2+}} = \frac{[\text{CeOH}^{2+}]}{[\text{Ce}^{\text{III}}]} = \frac{[\text{Ce}^{3+}]\beta_1^*[\text{OH}^-]}{[\text{Ce}^{\text{III}}]} \quad (2)$$

$$\alpha_{\text{CeOAc}^{2+}} = \frac{[\text{CeOAc}^{2+}]}{[\text{Ce}^{\text{III}}]} = \frac{[\text{Ce}^{3+}]\beta_1[\text{OAc}^-]}{[\text{Ce}^{\text{III}}]} \quad (3)$$

$$\alpha_{\text{Ce(OAc)}_2^+} = \frac{[\text{Ce(OAc)}_2^+]}{[\text{Ce}^{\text{III}}]} = \frac{[\text{Ce}^{3+}]\beta_2[\text{OAc}^-]^2}{[\text{Ce}^{\text{III}}]} \quad (4)$$

$$\alpha_{\text{Ce(OAc)}_3} = \frac{[\text{Ce(OAc)}_3]}{[\text{Ce}^{\text{III}}]} = \frac{[\text{Ce}^{3+}]\beta_3[\text{OAc}^-]^3}{[\text{Ce}^{\text{III}}]} \quad (5)$$

$$\alpha_{\text{Ce(OAc)}_4^-} = \frac{[\text{Ce(OAc)}_4^-]}{[\text{Ce}^{\text{III}}]} = \frac{[\text{Ce}^{3+}]\beta_4[\text{OAc}^-]^4}{[\text{Ce}^{\text{III}}]} \quad (6)$$

$$\begin{aligned} [\text{Ce}^{\text{III}}] &= [\text{Ce}^{3+}] + [\text{CeOH}^{2+}] + [\text{Ce(OAc)}_2^+] + [\text{Ce(OAc)}_3] + [\text{Ce(OAc)}_4^-] \\ &= [\text{Ce}^{3+}] (1 + \beta_1^*[\text{OH}^-] + \beta_1[\text{OAc}^-] + \beta_2[\text{OAc}^-]^2 + \beta_3[\text{OAc}^-]^3 + \beta_4[\text{OAc}^-]^4) \quad (7) \end{aligned}$$

Initially, the concentration of acetate,  $[\text{OAc}^-]$ , as a function of pH was determined via Maple 7.0 software where the total acetate concentration,  $[\text{OAc}^-]_{\text{T}}$ , is equal to the sum of all the acetate species in solution:

$$[\text{OAc}^-]_{\text{T}} = 0.1 \text{ M} = [\text{HOAc}] + [\text{OAc}^-] + [\text{CeOAc}^{2+}] + 2[\text{Ce(OAc)}_2^+] + 3[\text{Ce(OAc)}_3] + 4[\text{Ce(OAc)}_4^-] \quad (8)$$

The resulting distribution diagram of 0.1 M  $\text{Ce}^{3+}$  and 0.1 M acetate system is shown in Figure 1. From the distribution diagram, one can see the manner in which acetate acts as a stabilizing ligand for Ce(III). At the deposition bath pH of 6.1, the solution consists of 39.75%  $\text{Ce}^{3+}$ , 0.02%  $\text{CeOH}^{2+}$ , 47.33%  $\text{CeOAc}^{2+}$ , 12.05 %  $\text{Ce(OAc)}_2^+$ , 0.83%  $\text{Ce(OAc)}_3$ , and 0.02%  $\text{Ce(OAc)}_4^-$ .

Additionally, we have calculated two approximate E-pH diagrams for the Ce(III) species oxidized to  $\text{CeO}_2$  (s) in Figure 2A and  $\text{Ce(OH)}_4$  (aq) in Figure 2B at 25 °C between the pH values of 5 and 8. These equilibria are calculated using values from Table 1[36], along with standard reduction potential of  $\text{Ce}^{4+}/\text{Ce}^{3+}$  [37] and Gibbs free energy values in Table 2[38]. For instance, to determine the  $E^\circ$  in base for the  $\text{CeO}_2(\text{s})/\text{CeOAc}^{2+}$ , the following equations are used:



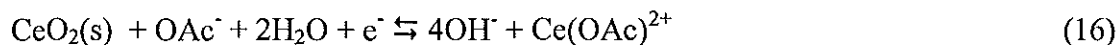
The Gibbs free energy of Equation 9 is calculated using  $\Delta G^\circ = -nFE^\circ$  where n is the number of electrons, F is 96484.5, and  $E^\circ$  is the  $\text{Ce}^{4+}/\text{Ce}^{3+}$  potential of 1.743 V vs. NHE. In Equation 10, the Gibbs free energy of the reaction is determined by  $\Delta G^\circ = -RT\ln K$  where R is the constant 8.31451, T is the temperature in Kelvin, and K is  $1.8 \times 10^{16}$ . Likewise, the formation constant of  $10^{1.68}$  was used to determine the Gibbs free energy of Equation 11. By means of the standard Gibbs free energy equation of  $\Delta G^\circ_{\text{reaction}} =$

$\Delta G^{\circ}_{\text{products}} - \Delta G^{\circ}_{\text{reactants}}$ , the Gibbs free energy of Equation 12 is determined using the values listed in Table 3. Summing the above  $\Delta G^{\circ}$ s of Equations 9, 10, 11, and 12, the new  $\Delta G^{\circ}$  for Equation 13 is found. Solving  $\Delta G^{\circ} = -nFE^{\circ}$  for the potential of the reaction in Equation 13, a value of -1.954 V vs. NHE for the  $\text{CeO}_2/\text{CeOAc}^{2+}$  potential is found.

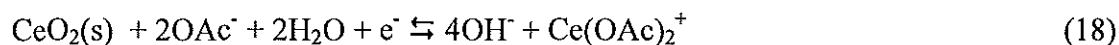
Employing the same principles, the equilibria of the cerium-water-acetate system at 25°C were calculated. The reactions and the equations used to calculate the formal potentials from the Nernst equation for the production of  $\text{CeO}_2(\text{s})$  are as follows:



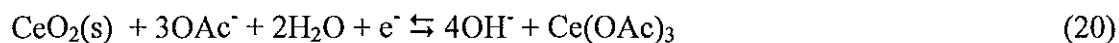
$$E = -2.053 - 0.236(\text{pH} - 14) - 0.059 \log[\text{Ce}^{3+}] \quad (15)$$



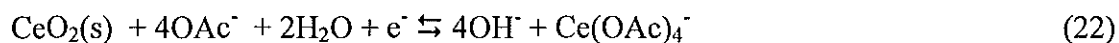
$$E = -1.954 - 0.236(\text{pH} - 14) + 0.059 \log[\text{OAc}^-] - 0.059 \log[\text{Ce}(\text{OAc})_2^{2+}] \quad (17)$$



$$E = -1.894 - 0.236(\text{pH} - 14) + 0.059 \log[\text{OAc}^-]^2 - 0.059 \log[\text{Ce}(\text{OAc})_2^+] \quad (19)$$



$$E = -1.868 - 0.236(\text{pH} - 14) + 0.059 \log[\text{OAc}^-]^3 - 0.059 \log[\text{Ce}(\text{OAc})_3] \quad (21)$$



$$E = -1.865 - 0.236(\text{pH} - 14) + 0.059 \log[\text{OAc}^-]^4 - 0.059 \log[\text{Ce}(\text{OAc})_4^-] \quad (23)$$

For the production of aqueous  $\text{Ce(OH)}_4$ , the reactions and equations are:



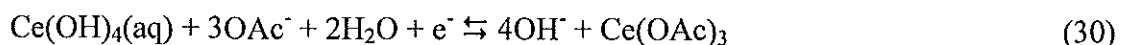
$$E = -1.325 - 0.236(\text{pH} - 14) - 0.059 \log[\text{Ce}^{3+}] + 0.059 \log[\text{Ce(OH)}_4] \quad (25)$$



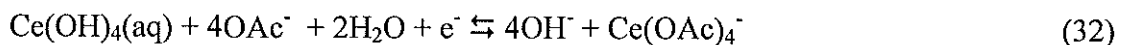
$$E = -1.226 - 0.236(\text{pH} - 14) + 0.059 \log[\text{OAc}^-] - 0.059 \log[\text{Ce(OAc)}^{2+}] + 0.059 \log[\text{Ce(OH)}_4] \quad (27)$$



$$E = -1.166 - 0.236(\text{pH} - 14) + 0.059 \log[\text{OAc}^-]^2 - 0.059 \log[\text{Ce(OAc)}_2^+] + 0.059 \log[\text{Ce(OH)}_4] \quad (29)$$



$$E = -1.140 - 0.236(\text{pH} - 14) + 0.059 \log[\text{OAc}^-]^3 - 0.059 \log[\text{Ce(OAc)}_3] + 0.059 \log[\text{Ce(OH)}_4] \quad (31)$$



$$E = -1.137 - 0.236(\text{pH} - 14) + 0.059 \log[\text{OAc}^-]^4 - 0.059 \log[\text{Ce(OAc)}_4^-] + 0.059 \log[\text{Ce(OH)}_4] \quad (33)$$

The potentials vs. NHE of  $\text{CeO}_2(\text{s})/\text{Ce}^{3+}$ ,  $\text{CeO}_2(\text{s})/\text{Ce(OAc)}_i^{3-i}$  species,  $\text{Ce(OH)}_4(\text{aq})/\text{Ce}^{3+}$ , and  $\text{Ce(OH)}_4(\text{aq})/\text{Ce(OAc)}_i^{3-i}$  species at pH values of 0, 6.1, and 14

are listed in Table 3 assuming unit activity. In the pH region studied, Ce(III) species can be directly oxidized to ceria. For example, at a pH of 6.1, the oxidation of  $\text{Ce}^{3+}$  to  $\text{CeO}_2(\text{s})$  would take place at a potential of  $-0.1886 \text{ V}$  vs. NHE ( $-0.3856 \text{ V}$  vs. Ag/AgCl) whereas the oxidation of  $\text{Ce}^{3+}$  to  $\text{Ce}(\text{OH})_4(\text{aq})$  occurs at  $0.5394 \text{ V}$  vs. NHE ( $0.3424 \text{ V}$  vs. Ag/AgCl).

Figure 3 shows a cyclic voltammogram (CV) of a Pt working electrode in the deposition solution, recorded at a scan rate of  $100 \text{ mV/s}$ . On the first cycle, a peak is clearly evident at  $+0.5 \text{ V}$  vs. Ag/AgCl with a broader one maximizing around  $+0.8 \text{ V}$  vs. Ag/AgCl. These potentials are much lower than the deposition potentials in previous reports.[33] The peaks become smaller upon successive cycles, and by the fifth cycle they are no longer observed. This suggests that only a thin film of ceria can be deposited under such conditions.

Calculated potentials for oxidizing the three major Ce(III) ions to  $\text{CeO}_2(\text{s})$  in solution are  $-0.3856 \text{ V}$  vs. Ag/AgCl for  $\text{CeO}_2/\text{Ce}^{3+}$ ,  $-0.2866 \text{ V}$  vs. Ag/AgCl for  $\text{CeO}_2/\text{CeOAc}^{2+}$ , and  $-0.2266 \text{ V}$  vs. Ag/AgCl for  $\text{CeO}_2/\text{Ce}(\text{OAc})_2^+$ . For the oxidation of Ce(III) species to  $\text{Ce}(\text{OH})_4(\text{aq})$ , potentials of  $0.3424 \text{ V}$  vs. Ag/AgCl for  $\text{Ce}(\text{OH})_4/\text{Ce}^{3+}$ ,  $0.4413 \text{ V}$  vs. Ag/AgCl for  $\text{Ce}(\text{OH})_4/\text{CeOAc}^{2+}$ , and  $0.5014 \text{ V}$  vs. Ag/AgCl for  $\text{Ce}(\text{OH})_4/\text{Ce}(\text{OAc})_2^+$  are determined. The resulting CV suggests that we are oxidizing  $\text{Ce}^{3+}$  to  $\text{Ce}(\text{OH})_4(\text{aq})$  at  $0.5 \text{ V}$  vs. Ag/AgCl followed by a combined oxidation of the  $\text{Ce}(\text{OAc})_i^{3-i}$  species to  $\text{Ce}(\text{OH})_4(\text{aq})$  at  $0.8 \text{ V}$  vs. Ag/AgCl. The electrochemically produced aqueous cerium(IV) hydroxide will dehydrate to produce solid ceria as follows.



Additionally, Figure 3 shows a CV of a ceria film in a solution of 0.1 M ammonium acetate with the pH adjusted to about 6.1 by addition of  $\text{HNO}_3$ . The increase in current at potentials above about 1.1 V vs. Ag/AgCl is due to oxygen evolution at the ceria surface. These CVs also show unexpected cathodic currents upon the return scan. These cathodic currents are observed even when the potential is not scanned above +0.5 V vs. Ag/AgCl, suggesting that the processes at higher potentials, such as oxygen evolution, are not involved. Rather, it seems likely that the cathodic currents are due to a partial reduction of the ceria films. While one would not expect the Ce(III)- $\text{CeO}_2$  reaction to be fully reversible, it is interesting to note that the open circuit potential of a ceria film in the growth solution is about 0.2 V vs. Ag/AgCl while the half-wave potential determined from the first scan in Figure 3 is approximately 0.3 V vs. Ag/AgCl for the first peak. Indicative of the reacting species in solution of a reversible couple, the  $E_{1/2}$  is close to that of the  $\text{Ce}(\text{OH})_4/\text{Ce}^{3+}$  electrode potential of 0.3424 V vs. Ag/AgCl at a pH of 6.1.

The CV data suggests that thin films of ceria could be deposited at a potential between +0.5 V and +1.1 V vs. Ag/AgCl. This is further supported by monitoring the current during deposition at constant potential. Figure 4 shows the chronoamperometry (CA) for ceria films grown on Hastelloy for 1000 s. For growth at +0.5 V vs. Ag/AgCl, the anodic current density drops off rapidly, reaching a limiting value of about 0.01  $\text{mA}/\text{cm}^2$  after approximately 200 sec. This suggests that the bulk of the film growth is occurring near the beginning of the deposition, and that the insulating film thus formed inhibits further growth. A potential of +1.1 V vs. Ag/AgCl is suitable for water oxidation

at a pH of 6.1. Hence, the higher measured current density at this potential is due to oxygen evolution.

Figure 5 shows SEM micrographs of a ceria film grown at +0.5 V vs. Ag/AgCl for 1000 s, corresponding to a final charge density of about 12 mC/cm<sup>2</sup>. This film is crack-free, as seen in both the lower (5A) and higher (5B) magnification micrographs. The films exhibit a very uniform morphology across the entire area. The grain size of the film is too small to determine from the SEM micrograph. AFM analysis of this sample shows that the films have a mean roughness of about 9 nm (compared with about 1 nm roughness for the Hastelloy substrates).

To verify that the films formed were both crystalline and of the desired phase, x-ray diffraction (XRD) was used. Figure 6 shows the glancing angle XRD analysis of a ceria film grown at +0.5 V vs. Ag/AgCl for 1000 s. Glancing angle XRD was used to emphasize diffraction from the thin film rather than the substrate. Small broad peaks corresponding to ceria are observed, with no other phase obvious. From the breadth of the (111) peak, the Scherrer formula can be used to calculate an average grain size of about 6 nm in the film.

The films can also be studied by x-ray reflectivity, because the Hastelloy substrates are smooth enough that interface roughness effects do not completely overwhelm the reflectivity signal. The reflectance data for a ceria film grown at +0.5 V vs. Ag/AgCl for 1000 s are shown in Figure 7A. X-ray reflectivity can be used to determine both the thickness and density of thin films. [39] From the fringes in the reflectance it is possible to calculate the film thickness of the sample, using a modified Bragg equation[40]:

$$\sin^2\theta_i = \theta_c^2 + \frac{(n_i + \Delta n)^2 \lambda^2}{4t^2} \quad (35)$$

Here both the maxima and minima are used, with  $\theta_i$  the observed angle,  $\theta_c$  the critical angle for total external reflection,  $\lambda$  the x-ray wavelength,  $t$  the film thickness,  $n_i$  an integer for the  $i^{\text{th}}$  fringe, and  $\Delta n = 0$  or  $1/2$  for minima and maxima respectively. Plotting  $(n_i + \Delta n)^2$  versus  $\sin^2\theta_i$  yields the film thickness and critical angle. The data for a ceria film grown at +0.5 V vs. Ag/AgCl for 1000 s are shown in Figure 7B. This plot yields a thickness of about 39 nm for the film, which agrees well with both the ellipsometrically determined thickness (40 nm), and the thickness calculated from Faraday's law (46 nm, assuming 100% current efficiency and 65% density).

The density of the film can be determined from the critical angle, assuming negligible anomalous dispersion, by the following[41]:

$$\theta_c^2 = \frac{N_A r_e \lambda^2 f}{\pi A} \rho \quad (36)$$

where  $N_A$  is Avogadro's number,  $r_e$  is the classical electron radius ( $2.8179 \times 10^{-13}$  cm),  $\lambda$  is the x-ray wavelength,  $f$  is the real part of the atomic scattering factor ( $\approx Z$ ),  $A$  is the average atomic mass, and  $\rho$  is the density. For the critical angle ( $\theta_c = 5 \times 10^{-3}$  rad, or  $2\theta_c = 0.573^\circ$ ) determined in Figure 7B, this gives a density of  $4.48 \text{ g/cm}^3$ , or about 61% of the bulk density for ceria.

Similarly, the density can be estimated ellipsometrically. Using the Lorentz-Lorentz formula one can relate the measured refractive index to the density:

$$\text{Relative density} = \left( \frac{n^2 - 1}{n^2 + 2} \right) \left( \frac{n_0^2 + 2}{n_0^2 - 1} \right) \quad (37)$$

Here  $n$  is the measured refractive index of the porous film of 1.78, and  $n_0$  is the bulk refractive index ( $= 2.47$ ), giving a value of about 67% bulk density for this film.

Ellipsometry can also be used to track the film thickness as a function of the deposition time. Figure 8 shows the change in thickness for samples grown between 50-2000 s at +0.5 V vs. Ag/AgCl. For this figure, the thickness was measured numerous ( $>12$ ) times at various spots across a single film, with error bars corresponding to  $\pm$  one standard deviation. From this figure, one can see that the film does not reach a set thickness after which the growth “turns off.” Rather, because the deposition current does not decay to zero, there is continued film growth until at least 2000 s. However, the bulk of the growth takes place in the initial few hundred seconds, with the film deposition rate dropping off rapidly with increasing deposition time. Some of the thickness for longer deposition times may also be due to deposition of ceria caused by dissolved oxygen in the solution, as discussed below. However, when no potential is applied, the Hastelloy substrates only develop a non-uniform film of about 8 nm thickness after 2000 s. Thus the bulk of the film growth for extended times is due to the electrochemical oxidation of Ce(III).

Ceria films were also formed at +1.1 V vs. Ag/AgCl, which corresponds to the potentials seen by Golden et al. in their galvanostatic anodic deposition from unpurged solutions.[33] Unlike films grown at +0.5 V vs. Ag/AgCl, those grown at this higher potential are cracked. Figure 9 shows the SEM image of a ceria film grown for 6000 s at +1.1 V vs. Ag/AgCl, in which the cracked morphology is clearly evident. During deposition at this potential, the current remains much higher than at the lower potential, as seen in Figure 4. These higher currents are likely due to the oxidation of water to form

O<sub>2</sub> gas at the working electrode. Figure 3 shows a scan of a ceria film on Pt scanned in 0.1 M acetate at a pH about 6.1, demonstrating a current increase presumably due to oxygen evolution at potentials above about 1.1 V vs. Ag/AgCl.

The oxidation state of the cerium in the electrodeposited films was determined by x-ray photoelectron spectroscopy. A typical Ce 3d spectrum of the electrodeposited films at 1.1 V vs. Ag/AgCl is shown in Figure 10. This Ce 3d spectrum is in agreement with cerium in the tetravalent state when compared to those spectra reported on deposited CeO<sub>2</sub> films deposited by rf magnetron sputtering[42] and chemical vapor deposition[43] and XPS studies of standard CeO<sub>2</sub> and other Ce(IV) compounds[44]. The group labeled with v's are due to 3d<sub>5/2</sub> ionization while the u's are associated with 3d<sub>3/2</sub> ionization[42]. Consistent with the literature, the peaks associated with the ground state are indicated with u and v and their excited states with primes [42,44].

All solutions for the CeO<sub>2</sub> electrodeposition are purged with Ar to remove dissolved O<sub>2</sub> from the water prior to adding Ce(III). However, CeO<sub>2</sub> can be produced by chemical means as well as anodic electrodeposition. If the deposition solution at a pH of 6.1 is bubbled with O<sub>2</sub> gas, ceria powder is precipitated. Figure 11A shows the x-ray diffraction pattern of such powders. This diffraction pattern has fairly broad peaks, which may be attributed to both the nanocrystalline nature of the powders and any residual strain there may be in the sample. Williamson-Hall analysis was applied to this pattern to determine the amount of line broadening due to both particle size and strain. A plot of the peak breadth (corrected for instrumental broadening) times cos( $\theta$ ) vs. 4sin( $\theta$ ) is shown in Figure 11B, where the slope is the residual strain, and the intercept yields the particle size. This analysis yields a particle size of about 7 nm, and shows that the

powders are largely strain-free, having a  $\Delta d/d$  of about 0.5%. Additionally, the lattice parameter was determined to be 5.428 Å, which is slightly larger (about 0.3%) than the value of 5.411 Å in JCPDS card 34-0349. The XPS spectra of tetravalent ceria powders are comparable to the spectrum seen in Figure 10 of a film electrodeposited at 1.1 V vs. Ag/AgCl.

The formation of ceria nanopowders by O<sub>2</sub> bubbling suggests that films grown at a high potential are likely to be cracked or porous, since they comprise loosely-adhered nanoparticles generated by oxygen evolution, along with the thin film deposited electrochemically. These two deposition methods are shown in Schemes 1 and 2. In Scheme 1, we see that Ce(III) is directly electrochemically oxidized to ceria. In Scheme 2, on the other hand, water is electrochemically oxidized to form O<sub>2</sub> gas, which then oxidizes the Ce(III) to ceria away from the electrode. To test this mechanism, a glass slide was deposited in the growth solution during a deposition at +1.1 V vs. Ag/AgCl. Afterwards, the sample was rinsed with DI water and dried, then studied by x-ray diffraction. Figure 12 shows the presence of CeO<sub>2</sub> on this glass slide. This supports the proposed deposition scheme, which also corresponds to the cracked films seen in other anodic depositions of ceria [33].

## CONCLUSION

Deposition of ceria films by oxidation Ce(III) stabilized with acetate ligands can proceed by one of two mechanisms, depending on the applied potential. At a potential of +0.5 V vs. Ag/AgCl, thin films are formed by the direct oxidation of Ce(III) to ceria. This is possible because the Ce(III)-CeO<sub>2</sub> redox potential is strongly pH dependant, so

that only a low positive potential is required to form a film from solutions at a pH of about 6.1. At a higher potential of +1.1 V vs. Ag/AgCl, cracked films are formed due to the formation of ceria nanoparticles in the bulk solution. This results from the electrolysis of water to yield O<sub>2</sub>, which reacts with Ce(III) away from the electrode.

#### ACKNOWLEDGEMENTS

This work was supported by National Science Foundation grants CHE-0243424, CHE-0437346, DMR 0071365 and DMR-0071365, and Department of Energy grant DE-FC07-03ID14509. The authors thank Dr. Dean Peterson of Los Alamos National Laboratory for supplying the electropolished hastelloy C-276 tapes. EAK thanks Alexey A. Vertegel for initial studies of a cerium(III) solution and Phillipe Poizot for his assistance with an early version of the Pourbaix and solution species diagrams.

## REFERENCES

1. D. Eyidi, M.D. Croitoru, O. Eibl, R. Nemetschek and W. Prusseit, *J. Mater. Res.* 18 (2003), 14.
2. X.D. Wu, R.C. Dye, R.E. Muenchausen, S.R. Foltyn, M. Maley, A. D. Rollett, A.R. Garcia and N.S. Nogar, *Appl. Phys. Lett.* 58 (1991), 2165.
3. J.-M. Lee, K.-T. Kim and C.-I. Kim, *Thin Solid Films* 447-448 (2004), 322.
4. C. Kwon, Y. Gim, Y. Fan, M.F. Hundley, J.M. Roper, P.N. Arendt and Q.X. Jia, *Appl. Phys. Lett.* 73 (1998), 695.
5. H. Matsuda, H. Sakakima, H. Adachi, A. Odagawa and K. Setsune, *J. Mater. Res.* 17 (2002), 1985.
6. Y. Nishikawa, T. Yamaguchi, M. Yoshiki, H. Satake and N. Fukushima, *Appl. Phys. Lett.* 81 (2002), 4386.
7. J.C. Wang, K.C. Chiang, T.F. Lei and C.L. Lee, *Electrochem. Solid-State Lett.* 7 (2004), E55.
8. R. Doshi, V.L. Richards, J.D. Carter, X. Wang and M. Krumpelt, *J. Electrochem. Soc.* 146 (1999), 1273.
9. T. Hibino, A. Hashimoto, T. Inoue, J.-i. Tokuno, S.-i. Yoshida and M. Sano, *Science* 288 (2000), 2031.
10. C. Xia, F. Chen and M. Liu, *Electrochem. Solid-State Lett.* 4 (2001), A52.
11. R. Peng, C. Xia, X. Liu, D. Peng and G. Meng, *Solid State Ionics* 152-153 (2002), 561.
12. C. Lu, W.L. Worrell, R.J. Gorte and J.M. Vohs, *J. Electrochem. Soc.* 150 (2003), A354.
13. T. Matsui, M. Inaba, A. Mineshige and Z. Ogumi, *Solid State Ionics* 176 (2005), 647.
14. E.P. Murray, T. Tsai and S.A. Barnett, *Nature* 400 (1999), 649.
15. O.A. Marina, C. Bagger, S. Primdahl and M. Mogensen, *Solid State Ionics* 123 (1999), 199.
16. P. Seungdoo and J.M. Vohs, *Nature* 404 (2000), 265.

17. H. Uchida, S. Suzuki and M. Watanabe, *Electrochem. Solid-State Lett.* 6 (2003), A174.
18. H. He, R.J. Gorte and J.M. Vohs, *Electrochem. Solid-State Lett.* 8 (2005), A279.
19. H. Uchida, S.-i. Arisaka and M. Watanabe, *Electrochem. Solid-State Lett.* 2 (1999), 428.
20. T.L. Nguyen, K. Kobayashi, T. Honda, Y. Iimura, K. Kato, A. Neghisi, K. Nozaki, F. Tappero, K. Sasaki and H. Shirahama, *Solid State Ionics* 174 (2004), 163.
21. M. Shiono, K. Kobayashi, T. Lan Nguyen, K. Hosoda, T. Kato, K. Ota and M. Dokiya, *Solid State Ionics* 170 (2004), 1.
22. B.P. Gorman and H.U. Anderson, *J. Am. Ceram. Soc.* 88 (2005), 1747.
23. J.-H. Wang, M. Liu and M.C. Lin, *Solid State Ionics* 177 (2006), 939.
24. R.M. Bueno, J.M. Martinez-Duart, M. Hernandez-Velez and L. Vazquez, *J. Mater. Sci.* 32 (1997), 1861.
25. P. Patsalas, S. Logothetidis and C. Metaxa, *Appl. Phys. Lett.* 81 (2002), 466.
26. R.G. Toro, G. Malandrino, I.L. Fragała, R.L. Nigro, M. Losurdo and G. Bruno, *J. Phys. Chem. B* 108 (2004), 16357.
27. I.K. Skofic, S. Sturm, M. Ceh and N. Bukovec, *Thin Solid Films* 422 (2002), 170.
28. R.T. Coyle and J.A. Switzer, *Electrochemical synthesis of ceramic films and powders*, Union Oil Co., USA, Application: US (1989), p. 5.
29. J.A. Switzer, *Am. Ceram. Soc. Bull.* 66 (1987), 1521.
30. A.J. Davenport, H.S. Isaacs and M.W. Kendig, *Corros. Sci.* 32 (1991), 653.
31. Y. Zhou and J.A. Switzer, *J. Alloys Compd.* 237 (1996), 1.
32. I. Zhitomirsky and A. Petric, *Mater. Lett.* 40 (1999), 263.
33. A.Q. Wang and T.D. Golden, *J. Electrochem. Soc.* 150 (2003), C616.
34. T.D. Golden and A.Q. Wang, *J. Electrochem. Soc.* 150 (2003), C621.
35. A.Q. Wang, N. D'Souza and T.D. Golden, *J. Mater. Chem.* 16 (2006), 481.

36. J.A. Dean, Editor, *Lange's Handbook of Chemistry*, McGraw-Hill, New York, NY (1985).
37. R.C. Weast, Editor, *CRC Handbook of Chemistry and Physics*, CRC Press, Inc., Boca Raton, FL (1988).
38. S.A. Hayes, P. Yu, T. J. O'Keefe, M. J. O'Keefe, and J. O. Stoffer. *J. Electrochem. Soc.* 149 (2002), C623.
39. T.C. Huang, R. Gilles and G. Will, *Thin Solid Films* 230 (1993), 99.
40. T.C. Huang and W. Parrish, Characterization of single- and multiple-layer films by x-ray reflectometry, In: C.S. Barrett, J.V. Gilfrich, T.C. Huang, R. Jenkins, G.J. McCarthy, P.K. Predecki, R. Ryon and D.K. Smith, Editors, *Adv. X-Ray Anal.*, Plenum Press, New York, NY (1992).
41. K. Nakajima, S. Aoki, S. Sudo, M. Mondo, H. Kudo, S. Fujiwara and T. Arai, *Jpn. J. Appl. Phys., Part 1* 32 (1993), 164.
42. S. Guo, H. Arwin, S.N. Jacobsen, K. Jarrendahl, and U. Helmersson. *J. Appl. Phys.* 77 (1995), 5369.
43. D. Barreca, G.A. Battiston, R. Gerbasi, and E. Tondello. *Surf. Sci. Spectra* 7 (2000), 297.
44. P. Burroughs, A. Hamnett, A.F. Orchard, and G. Thornton. *J. Chem. Soc., Dalton Trans.* 16 (1976), 1686.

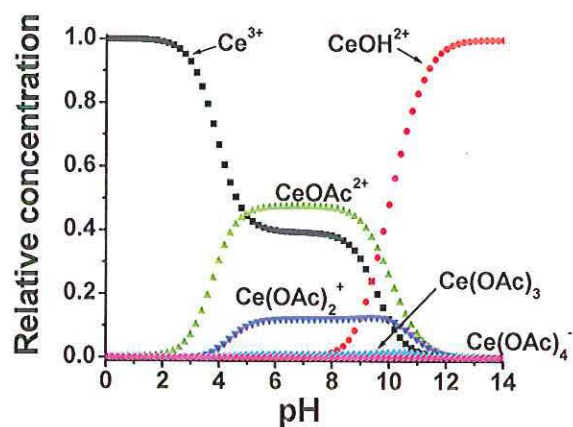


Figure 1. Calculated solution species distribution for 0.1 M  $\text{Ce}^{3+}$  and 0.1 M acetate at 25 °C.

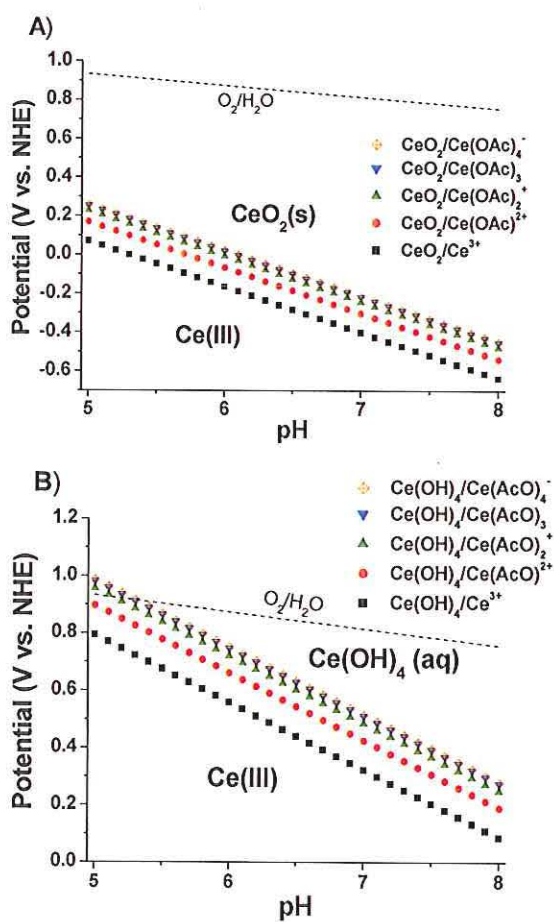


Figure 2. (A) E-pH diagrams for  $\text{CeO}_2(\text{s})/\text{Ce}^{3+}$  and  $\text{CeO}_2(\text{s})/\text{Ce(OAc)}_i^{3-i}$  species and (B) E-pH diagrams for  $\text{Ce(OH)}_4(\text{aq})/\text{Ce}^{3+}$  and  $\text{Ce(OH)}_4(\text{aq})/\text{Ce(OAc)}_i^{3-i}$  species assuming unit activity at 25 °C.

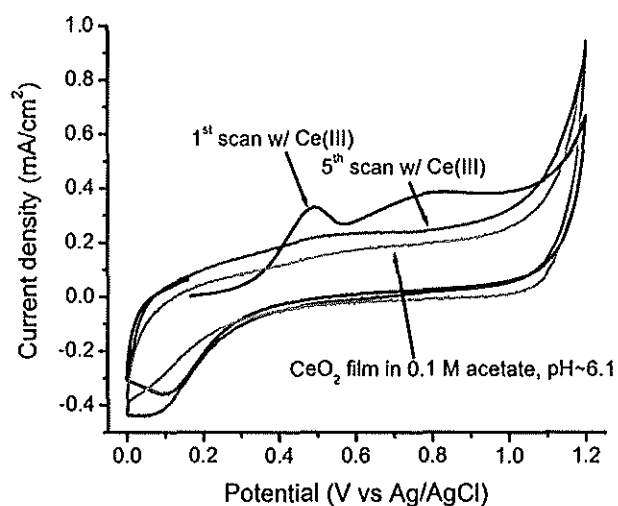


Figure 3. Cyclic voltammetry at 100 mV/s scan rate in the deposition solution on a Pt electrode, showing an oxidation peak at about 0.5 V vs. Ag/AgCl in the initial scan, which disappears upon successive scans. Also shown is a scan of a ceria film on Pt in 0.1 M acetate at a pH of about 6.1, demonstrating a current increase presumably due to oxygen evolution at potentials above about 1.0 V vs. Ag/AgCl.

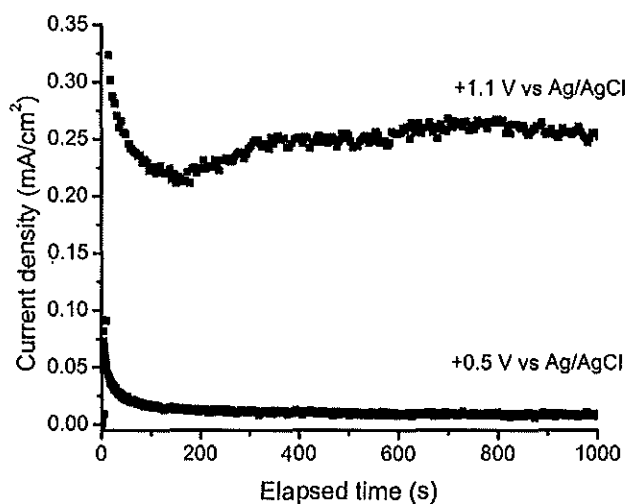


Figure 4. Chronoamperometry of deposition on Hastelloy substrates at +0.5 and +1.1 V vs. Ag/AgCl and 65 °C, showing the rapid decay in current at low potential, compared to the consistently larger currents at higher potential.

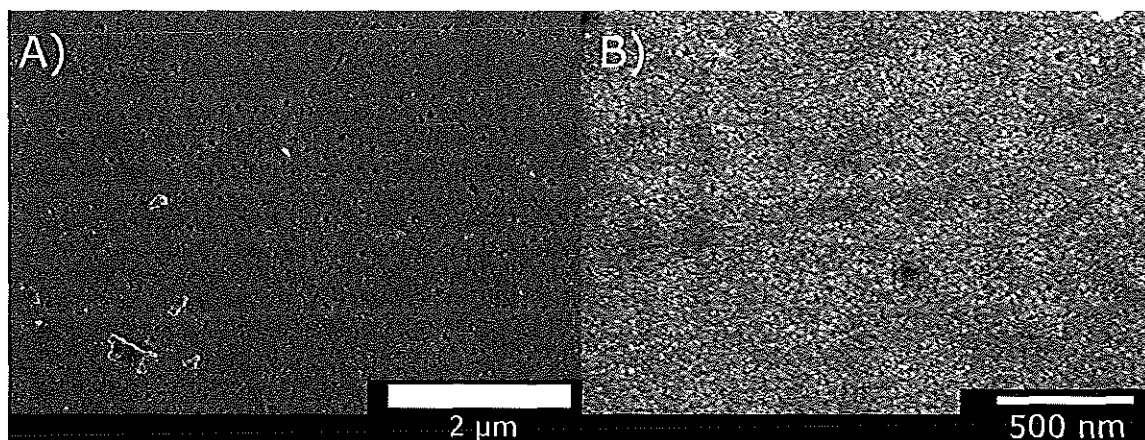


Figure 5. SEM micrographs of ceria films grown for 1000 s at +0.5 V vs. Ag/AgCl and 65 °C, at both lower (A) and higher (B) magnifications.

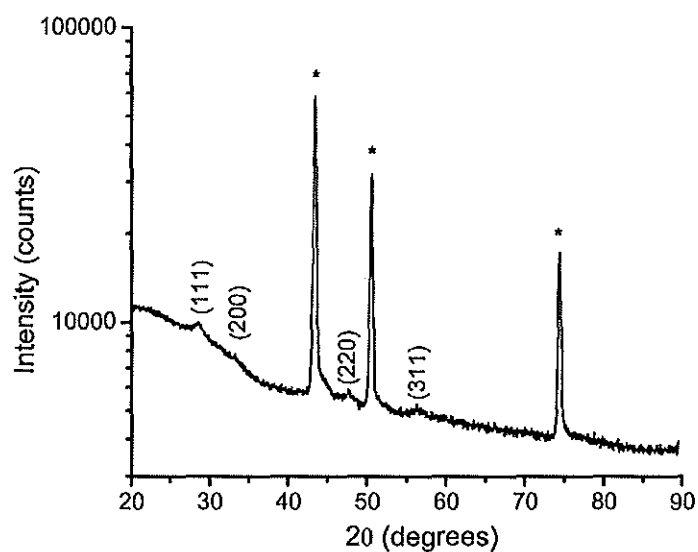


Figure 6. X-ray diffraction pattern of a ceria film grown for 1000 s at +0.5 V vs. Ag/AgCl and 65 °C, showing the presence of ceria with no other phases observed. Peaks marked with a \* belong to the Hastelloy substrate.

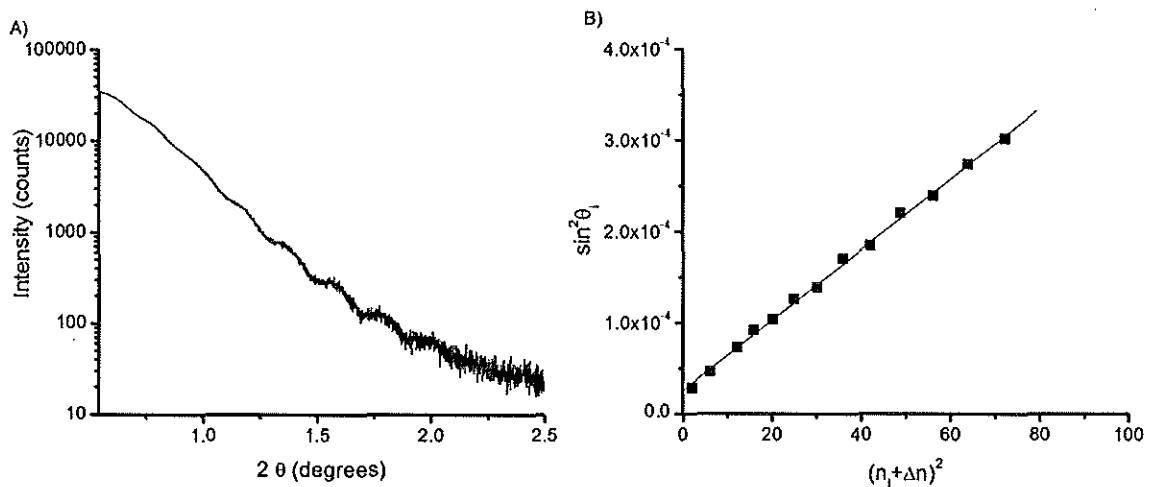


Figure 7. (A) X-ray reflectivity of a ceria film grown for 1000 s at +0.5 V vs. Ag/AgCl and 65 °C, showing a number of interference fringes. (B) Least-squares fit of the fringe numbers to determine film thickness (39 nm) and critical angle ( $\theta_c = 5 \times 10^{-3}$  rad, or  $2\theta_c = 0.573^\circ$ ) for this sample.

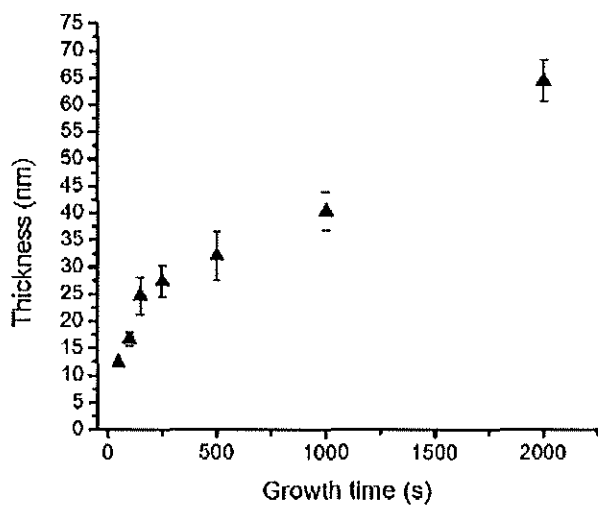


Figure 8. Film thickness as a function of time, as determined by ellipsometry.

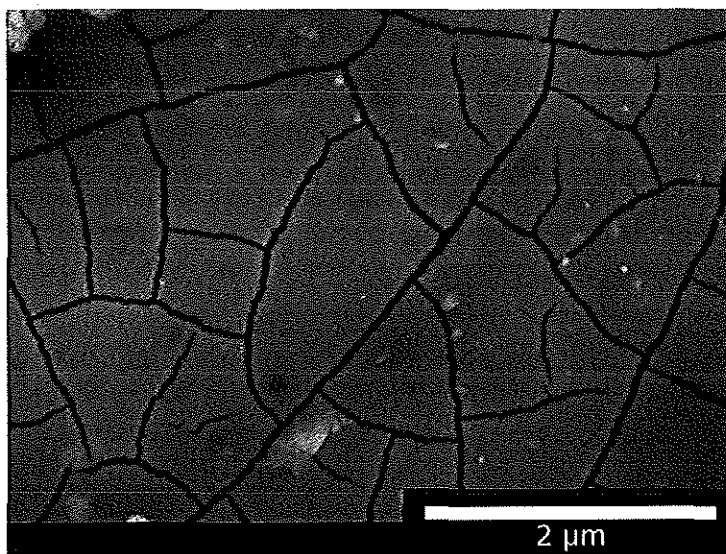


Figure 9. SEM micrograph of ceria film grown for 6000 s at +1.1 V and 65 °C, showing the cracked morphology of such films.

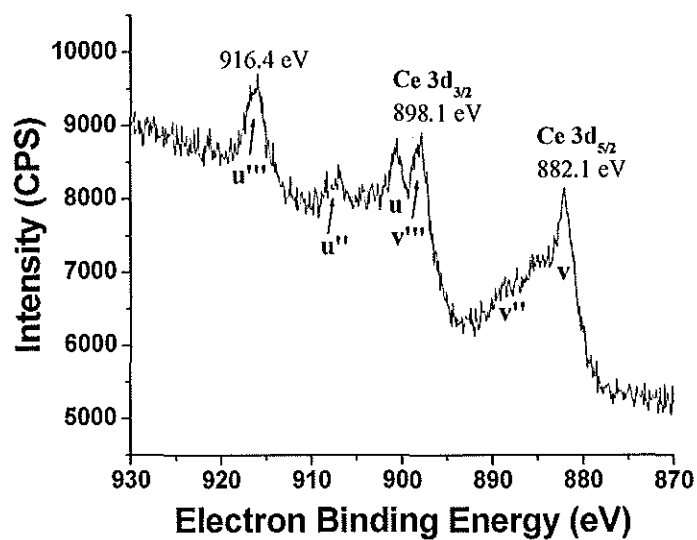


Figure 10. Ce 3d XPS spectrum of a CeO<sub>2</sub> film electrodeposited at +1.1 V vs. Ag/AgCl for 1000 s.

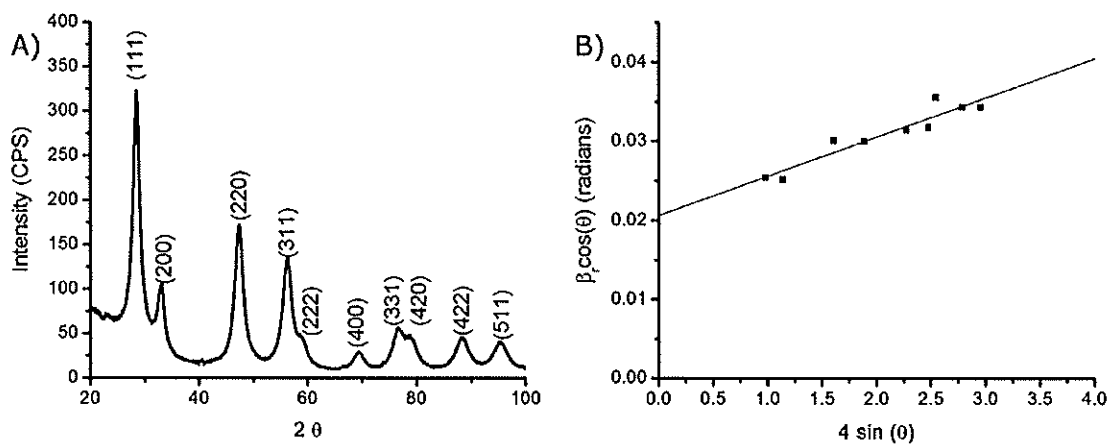


Figure 11. (A) Powder X-ray diffraction pattern of ceria nanopowders precipitated from the growth solution by bubbling with  $O_2$  at  $65^\circ C$ . (B) Williamson-Hall analysis of the powders, showing that the particle size is  $\sim 7$  nm, with a residual strain of about 0.5%.

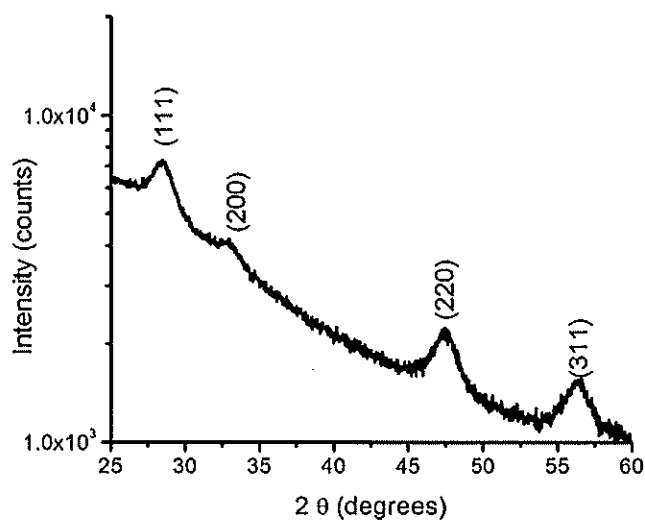


Figure 12. X-ray diffraction pattern of a ceria film deposited on a glass slide during growth at  $+1.1$  V and  $65^\circ C$ , showing that ceria is formed away from the electrodes at this potential.

Table 1. The water ionization constant, acid dissociation constant for acetic acid, and formation constants of cerium(III) complexes with hydroxide and acetate ions at 25 °C [36].

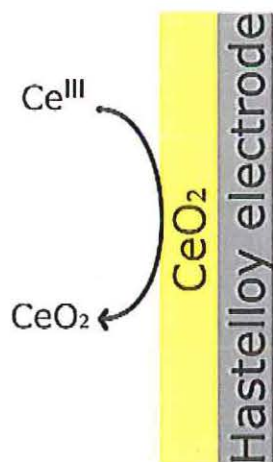
Reaction	Constant
$\text{H}_2\text{O} \rightleftharpoons \text{H}^+ + \text{OH}^-$	$K = 1.8 \times 10^{-16}$
$\text{HOAc} \rightleftharpoons \text{H}^+ + \text{OAc}^-$	$K_a = 10^{-4.75}$
$\text{Ce}^{3+} + \text{OH}^- \rightleftharpoons \text{CeOH}^{2+}$	$\beta_1^* = 10^{4.8}$
$\text{Ce}^{3+} + \text{OAc}^- \rightleftharpoons \text{CeOAc}^{2+}$	$\beta_1 = 10^{1.68}$
$\text{Ce}^{3+} + 2\text{OAc}^- \rightleftharpoons \text{Ce}(\text{OAc})_2^+$	$\beta_2 = 10^{2.69}$
$\text{Ce}^{3+} + 3\text{OAc}^- \rightleftharpoons \text{Ce}(\text{OAc})_3$	$\beta_3 = 10^{3.13}$
$\text{Ce}^{3+} + 4\text{OAc}^- \rightleftharpoons \text{Ce}(\text{OAc})_4^-$	$\beta_4 = 10^{3.18}$

Table 2. The standard Gibbs free energy of formation of selected substances [38].

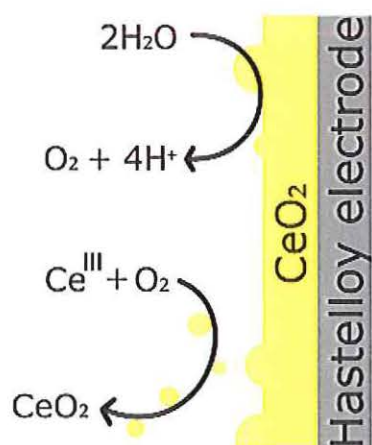
Species	$\Delta G_f^\circ$ (kJ/mol)
H <sub>2</sub> O (l)	-237.10
H <sup>+</sup> (aq)	0
OH <sup>-</sup> (aq)	-157.20
Ce <sup>3+</sup> (aq)	-672.00
Ce <sup>4+</sup> (aq)	-503.80
Ce(OH) <sub>4</sub> (aq)	-1428.66
CeO <sub>2</sub> (s)	-1024.60

Table 3. Calculated formal potentials for the equilibria at pH values of 0, 6.1, and 14 at 25°C assuming unit activity.

Reaction	Potential (V vs. NHE)		
	<i>pH</i> =0	<i>pH</i> =6.1	<i>pH</i> =14
<b>Solid</b>			
CeO <sub>2</sub> /Ce <sup>3+</sup>	1.251	-0.189	-2.053
CeO <sub>2</sub> /CeOAc <sup>2+</sup>	1.350	-0.090	-1.954
CeO <sub>2</sub> /Ce(OAc) <sub>2</sub> <sup>+</sup>	1.410	-0.030	-1.894
CeO <sub>2</sub> /Ce(OAc) <sub>3</sub>	1.436	-0.004	-1.868
CeO <sub>2</sub> /Ce(OAc) <sub>4</sub> <sup>-</sup>	1.439	-0.001	-1.865
<b>Aqueous</b>			
Ce(OH) <sub>4</sub> /Ce <sup>3+</sup>	1.979	0.539	-1.325
Ce(OH) <sub>4</sub> /CeOAc <sup>2+</sup>	2.078	0.638	-1.226
Ce(OH) <sub>4</sub> /Ce(OAc) <sub>2</sub> <sup>+</sup>	2.138	0.698	-1.166
Ce(OH) <sub>4</sub> /Ce(OAc) <sub>3</sub>	2.164	0.724	-1.140
Ce(OH) <sub>4</sub> /Ce(OAc) <sub>4</sub> <sup>-</sup>	2.167	0.727	-1.137



Scheme 1. Anodic deposition of ceria films at a low potential. For clarity, ligands on the cerium ions have been omitted.



Scheme 2. Possible route for ceria formation at a higher potential. For clarity, ligands on the cerium ions have been omitted.

## II. Electrodeposition of Magnetite Films and Ferrihydrite Nanoribbons on Single-Crystal Gold

Elizabeth A. Kulp, Hiten M. Kothari, Steven J. Limmer, Jinbo Yang,  
Rakesh V. Gudavarthy, Eric W. Bohannon and Jay A. Switzer\*

Department of Chemistry, Missouri University of Science and Technology,  
103 Materials Research Center, Rolla, MO 65409-1170

\*AUTHOR EMAIL ADDRESS [jswitzer@mst.edu](mailto:jswitzer@mst.edu)

### ABSTRACT

Magnetite ( $\text{Fe}_3\text{O}_4$ ) and ferrihydrite ( $\text{Fe}_{10}\text{O}_{14}(\text{OH})_2$ ) films were deposited by applying different cathodic potentials during the deposition from an alkaline Fe(III)—triethanolamine solution. The ratio of Fe(III) to Fe(II) at the electrode surface is controlled by the applied potential. The films were characterized using X-ray diffraction, scanning electron microscopy, and Mössbauer spectroscopy. Epitaxial magnetite films on low-index gold crystals were produced at three different potentials. X-ray diffraction analysis of the magnetite films deposited at -1.01 V, -1.05 V, and -1.10 V vs. Ag/AgCl showed [111] oriented films on Au(111) and Au(001). Due to twinning of the {111} planes, the [511] orientation is present in thicker films. Magnetite grew with a [110] orientation on Au(110). At the more negative potentials of -1.10 V and -1.20 V vs. Ag/AgCl, ferrihydrite deposits with an  $(11\bar{2}0)$  orientation.

KEYWORDS Iron oxides, magnetite, ferrihydrite, epitaxy, electrodeposition

## INTRODUCTION

Abundant in Nature, iron oxides, including iron hydroxides and iron (oxy)hydroxides, have been used as catalysts, pigments, and magnetic coatings due to their chemical and physical properties.<sup>1</sup> The iron oxide magnetite ( $\text{Fe}_3\text{O}_4$ ) is a ferrimagnetic material with an inverse spinel structure with space group  $\text{Fd}\bar{3}\text{m}$ . This mixed-valence transition metal oxide has  $\text{Fe}^{3+}$  and  $\text{Fe}^{2+}$  ions in the octahedral sites and  $\text{Fe}^{3+}$  ions in the tetrahedral sites. The net ferrimagnetism is due to the moments on the  $\text{Fe}^{2+}$  ions since the moments of the  $\text{Fe}^{3+}$  ions are antiferromagnetically coupled. The ferrimagnetism of  $\text{Fe}_3\text{O}_4$  is observed below the Curie temperature of 860 K making the material viable for room temperature devices. Around 120 K,  $\text{Fe}_3\text{O}_4$  undergoes a metal to insulator transition (Verwey transition). The electrical conductivity of this material at room temperature is reported to be the result of hopping of the charge carriers between the  $\text{Fe}^{2+}$  and  $\text{Fe}^{3+}$  ions in the octahedral sites. Calculations have indicated that the Fermi level electrons are 100% spin-polarized in this material.<sup>2,3</sup> These properties make magnetite a potential candidate for applications in magnetic memory and spin-dependent transport devices.

One of the various methods to produce magnetite is by electrodeposition.<sup>4-14</sup> Most of the electrochemical studies have involve the anodic deposition of magnetite from an Fe(II)-acetate bath.<sup>4-12</sup> Previously, we have electrodeposited epitaxial films of  $\text{Fe}_3\text{O}_4$  films onto gold single crystals by this method.<sup>4,5</sup> However, this deposition bath is unstable at high temperatures, reacting with the oxygen in air to produced magnetite powder. Another method to produce magnetite electrochemically is by the reduction of Fe(III).<sup>13,14</sup> In an earlier study, we modified an alkaline Fe(III)-triethanolamine bath,

developed by Sapiieszko and Matijevic,<sup>15</sup> for cathodic electrodeposition of  $\text{Fe}_3\text{O}_4$  on polycrystalline substrates.<sup>13</sup>

Another iron compound, ferrihydrite, is a poorly crystalline material with various reported chemical structures.<sup>1,16</sup> Recently, a new ferrihydrite model (space group,  $\text{P6}_3\text{mc}$ ) using synchrotron data was determined.<sup>17</sup> The proposed ideal chemical structure is  $\text{Fe}_{10}\text{O}_{14}(\text{OH})_2$  with 1/5 of the  $\text{Fe}^{3+}$  in tetrahedral sites and 4/5 in octahedral sites.<sup>17</sup> Due to its poor crystalline quality, ferrihydrite is further labeled as 2-line or 6-line ferrihydrite based on the number of observed peaks in the x-ray diffraction pattern. Ferrihydrite is superparamagnetic at room temperature and shows magnetic ordering at 4.2 K.<sup>1,16</sup> Ferrihydrite is observed in the corrosion of iron and steel and as a byproduct in mining.<sup>16</sup> Also found in soil and sediments, this nanomaterial naturally adsorbs cations, anions, and organic species such as insecticides and herbicides.<sup>16</sup> Due to this adsorption, ferrihydrite has been studied for the removal of heavy metals in water treatment.<sup>16</sup> Generally this material is made synthetically by rapid oxidation of  $\text{Fe}(\text{II})$  or by hydrolysis of  $\text{Fe}(\text{III})$  salts.<sup>1,16,18</sup> Typically, this metastable material is then used as a precursor for the production of goethite and hematite.<sup>1,16,18</sup>

Although various methods are used to produce iron compounds,<sup>1,18</sup> here, a novel approach to electrochemically produce magnetite ( $\text{Fe}_3\text{O}_4$ ) and ferrihydrite ( $\text{Fe}_{10}\text{O}_{14}(\text{OH})_2$ ) from the same alkaline  $\text{Fe}(\text{III})$ -triethanolamine deposition bath is discussed. In this deposition bath,  $\text{Fe}(\text{III})$  is electrochemically reduced to  $\text{Fe}(\text{II})$ . Therefore, the concentration of the  $\text{Fe}(\text{II})$  at the electrode surface is controlled by the applied potential. This ability to change the  $\text{Fe}(\text{II})$  concentration by changing the applied potential allows for magnetite films to be electrodeposited between -1.01 V and -1.10 V vs.  $\text{Ag}/\text{AgCl}$  and

for ferrihydrite films to be deposited at potentials from -1.10 V to -1.20 V vs. Ag/AgCl. These films are characterized as a function of applied potential by x-ray diffraction (XRD), scanning electron microscopy (SEM), and Mössbauer spectroscopy. Electrodeposited films of these materials on low-index gold crystals are epitaxial as characterized by XRD and SEM.

#### EXPERIMENTAL SECTION

The deposition bath was prepared by dissolving 2.6 gram of iron(III) sulfate hydrate in 15 ml of 1 M triethanolamine (TEA) resulting in a deep red colored solution. This solution was diluted with 50 ml of distilled, deionized water. This Fe(III)-TEA solution was then added to a solution produced by dissolving 12.0 g of NaOH pellets in 85 ml of distilled, deionized water. The resulting deposition bath was a gray-green solution that was then heated to 80 °C. All chemicals were ACS reagent grade and purchased from Sigma-Aldrich. The water was produced in house by a Millipore system (18 M $\Omega$ -cm).

The stoichiometry of the magnetite films was controlled by using constant potentials between -1.01 V and -1.10 V vs. Ag/AgCl. Ferrihydrite films were deposited between -1.10 V and -1.20 V vs. Ag/AgCl. Films were deposited on 430 stainless steel substrates for film characterization and lattice parameter calculations. The films were rinsed with 80 °C distilled, deionized water. Prior to use, the stainless steel substrates were mechanically polished and sonicated in acetone and deionized water. Epitaxial films were deposited at -1.01 V, -1.05 V, -1.10 V, and -1.20 V vs. Ag/AgCl on gold single crystals. The films were rinsed with 80 °C distilled, deionized water. The gold crystals

were electropolished before they were used. The gold electropolishing solution consisted of 100 ml of ethanol, 50 ml of ethylene glycol, and 50 ml of concentrated hydrochloric acid and was heated to 55 °C. Each gold single crystal was positioned in this stirred solution to form a meniscus in the electropolishing solution. An anodic constant current density of 1.6 A/cm<sup>2</sup> was applied for 45 s. The single crystals were thoroughly rinsed with ethanol and water.

X-ray analyses of the polycrystalline and epitaxial films were determined using a high-resolution Philips X-Pert MRD X-ray diffractometer with a Cu K<sub>α1</sub> radiation source ( $\lambda = 0.154056$  nm). The symmetric x-ray diffraction patterns were obtained using the line focus mode with the primary optics of a combination Göbel mirror and a two crystal Ge(220) two-bounce hybrid monochromator (PW3147/00) producing pure CuK<sub>α1</sub> radiation on the incident beam side, and a 0.18° parallel plate collimator (PW3098/18) as the secondary (diffracted beam) optics. Scans were run from 2 $\theta$  values of 10° to 100°. The lattice parameter of each film was determined using RIQAS software from Materials Data Inc. for Reitveld analysis.

The in-plane orientation of the films relative to the Au single crystal was determined by x-ray pole figure analysis. For the pole figure measurement of the epitaxial films, the diffractometer was operated in the point focus mode with a crossed slit collimator module (PW3084/62) as the primary optics and a 0.27° parallel plate collimator (PW3098/27) equipped with a flat graphite monochromator (PW3121/00) as the secondary optics for pole figures and azimuthal scans. To perform the pole figure analysis, the 2 $\theta$  was set to the angle of the Fe<sub>3</sub>O<sub>4</sub>(311) plane (2 $\theta = 35.426^\circ$ ) for the films analyses and Au(311) plane (2 $\theta = 77.547^\circ$ ) for the substrate analyses. The sample was

moved through a sequence of tilt angles,  $\chi$ , from  $0^\circ$  to  $90^\circ$ , and at each  $\chi$ , the sample was rotated azimuthally,  $\phi$ , from  $0^\circ$  to  $360^\circ$ . Data was collected in the continuous mode over  $3^\circ$  intervals for both  $\chi$  and  $\phi$  with a count time of 5 seconds per point. Azimuthal scans were performed under the same conditions as the pole figures but using  $\chi = 58.5^\circ$  for the films on Au(111) and Au(100) and  $\chi = 31.5^\circ$  for the films on Au(110). Following the X-ray diffraction analyses, the film morphologies were studied using a field emission Hitachi S-4700 scanning electron microscope.

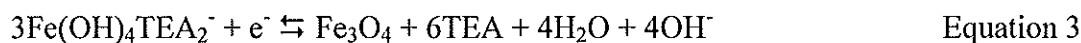
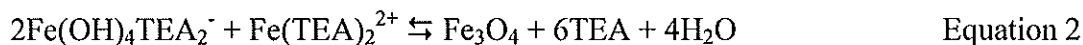
The Mössbauer spectra were obtained using an Austin S-600 Mössbauer spectrometer with a conventional constant accelerated driver at room temperature with 70 mCi  $\text{Co}^{57}$  in a Rh matrix. The spectrometer was calibrated using  $\alpha$ -Fe foil. The isomer shift is calibrated using an  $\alpha$ -Fe foil at room temperature. Spectra were collected on 10 films deposited on highly oriented pyrolytic graphite (HOPG) at three different potentials. The film and an underlying HOPG layer were removed with tape. The HOPG was cleaned for every deposit with hydrochloric acid to remove the previous deposition along the edges and rinse with water. A fresh surface of HOPG was prepared by removing the surface layers with tape. Analysis of the measured spectra was performed using a least-squares program.

## RESULTS AND DISCUSSION

Figure 1 shows linear sweep voltammograms on a gold rotating disk electrode at 100 rpm in an alkaline TEA bath (blue squares) and the alkaline Fe(III)—TEA deposition bath (black solid line) at  $80^\circ\text{C}$  at 50 mV/sec from their open circuit potentials of -0.41 V for the TEA bath and -0.47 V for the Fe(III)—TEA bath to -1.400 V vs. Ag/AgCl. The

linear sweep voltammogram of 0.1 M TEA in 2 M NaOH (Figure 1, blue squares) shows that the alkaline TEA is electrochemically inactive and that the electrochemical generation of hydrogen gas begins around -1.25 V vs. Ag/AgCl. The electrochemical reduction of the alkaline Fe(III)—TEA (Figure 1, black solid line) is observed at potentials negative of -0.950 V vs. Ag/AgCl. The initial part of this linear sweep is a one electron reaction involving the reduction of an Fe(III) species to an Fe(II) species. Black films are produced from -1.01 V to -1.08 V vs. Ag/AgCl. As the more negative potentials are applied, the electrodeposited films are green and convert to black and reddish brown films as they dry in air. As the potential becomes more negative than -1.23 V vs. Ag/AgCl, a two electron process occurs as the Fe(II) is reduced to Fe as indicated by the gray films produced at -1.3 V vs. Ag/AgCl and confirmed by XRD (not shown). The competing reaction of hydrogen evolution continues as the potential becomes more negative.

Electrochemical studies utilizing cyclic voltammetry have shown that the reduction of Fe(III)—triethanolamine complexes is a one-electron process where a Fe(III)—TEA complex is reduced to a Fe(II)-TEA complex.<sup>13,19-23</sup> Utilizing literature stability constants of iron-triethanolamine complexes,<sup>24,25</sup> this reduction may occur as seen in Equation 1. Other studies have suggested complexes with a Fe(III) to TEA ratio of 1:1 and hydroxide coordination dependent on pH, but their stability constants have not been determined.<sup>19,22,26</sup> The Fe(III)-TEA complex then chemically reacts with the generated Fe(II)-TEA to produce magnetite (Equation 2). A proposed overall electrochemical-chemical reaction for magnetite deposition of this solution is shown in Equation 3.



The calculated  $E^0$  of the overall reaction in Equation 3 is -0.745 V vs. NHE (-0.944 V vs. Ag/AgCl) at room temperature. This value was calculated from the equations and constants found in Table 1.<sup>24,25,27-29</sup>

The surface concentration of Fe(III) is dependent on the departure from equilibrium. At low overpotentials, the Fe(III) surface concentration is nearly the same as the bulk concentration whereas at high overpotentials, at which the current becomes mass-transport controlled, the surface concentration of Fe(III) approaches zero. For the linear sweep voltammogram of the reduction of the Fe(III)-TEA complex to the Fe(II)-TEA complex in Figure 1 (solid black line), Equation 4 is used

$$\frac{i}{i_{l,c}} = \frac{[C_{\text{Fe(III)}}^* - C_{\text{Fe(III)}}(y)]}{C_{\text{Fe(III)}}^*} \quad \text{Equation 4}$$

where  $i$  is the measured current,  $i_{l,c}$  is the limiting current,  $C_{\text{Fe(III)}}^*$  is the bulk concentration of Fe(III) in solution, and  $C_{\text{Fe(III)}}(y)$  is the Fe(III) concentration at the electrode surface.<sup>30</sup> Initially, the surface concentration of Fe(III) is equal to the bulk concentration of Fe(III), resulting in the numerator of the Equation 4 to be equal to 0. So, the ratio of the measure current to the limiting current would be equal to 0 as seen in Equation 5.

$$\frac{i}{i_{l,c}} = \frac{[C_{\text{Fe(III)}}^* - C_{\text{Fe(III)}}^*]}{C_{\text{Fe(III)}}^*} = \frac{0}{C_{\text{Fe(III)}}^*} = 0 \quad \text{Equation 5}$$

At the plateau in the linear sweep voltammogram where the current is mass-transport limited, the surface concentration of Fe(III) is 0 since all the Fe(III) has been reduced to Fe(II). As seen in Equation 6, this ratio would be equal to 1.

$$\frac{i}{i_{lc}} = \frac{[C_{\text{Fe(III)}} - 0]}{C_{\text{Fe(III)}}^*} = \frac{C_{\text{Fe(III)}}^*}{C_{\text{Fe(III)}}^*} = 1 \quad \text{Equation 6}$$

For stoichiometric magnetite, 2/3 of the iron is Fe<sup>3+</sup> and 1/3 of the iron is Fe<sup>2+</sup>. So to produce stoichiometric magnetite, the Fe(III) surface concentration need to be equal to 2/3 of the bulk concentration of Fe(III) or where the current ratio is equal to 1/3 (Equation 7).

$$\frac{i}{i_{lc}} = \frac{[C_{\text{Fe(III)}}^* - \frac{2}{3}C_{\text{Fe(III)}}^*]}{C_{\text{Fe(III)}}^*} = \frac{\frac{1}{3}C_{\text{Fe(III)}}^*}{C_{\text{Fe(III)}}^*} = \frac{1}{3} \quad \text{Equation 7}$$

Figure 2 shows the calculated plot of the surface concentrations of Fe(III) and Fe(II) using an initial concentration 86 mM Fe(III) verses potential. Stoichiometric magnetite would be deposited at approximately -1.045 V vs. Ag/AgCl where 1/3 of the total concentration of Fe(III) has been reduced to Fe(II). Theoretically, any potential more positive than this value should produce magnetite with excess Fe(III) while potentials more negative of -1.045 V vs. Ag/AgCl should produce magnetite with excess Fe(II).

X-ray diffraction patterns of the black films deposited by applying potentials between -1.01 V and -1.08 V vs. Ag/AgCl were consistent with magnetite. All these films were crystalline as seen in the XRD patterns of films deposited on stainless steel at -1.01 V vs. Ag/AgCl and -1.05 V vs. Ag/AgCl in Figure 3A and 3B, respectively. The magnetite films deposited at -1.01 V vs. Ag/AgCl in Figure 3A had no preferred orientation whereas the magnetite films deposited at -1.05 V vs. Ag/AgCl in Figure 3B shows a

strong [100] preferred orientation. The X-ray diffraction patterns of a black and reddish brown films deposited at -1.10 V vs. Ag/AgCl, as seen in Figure 3C, showed two main peaks that can be attributed to (311) and (440) peaks of magnetite. X-ray diffraction patterns of the reddish brown films deposited at -1.20 V vs. Ag/AgCl (not shown) are similar to the patterns from films deposited at -1.10 V vs. Ag/AgCl. Other than the substrate peaks, no other peaks related to maghemite, green rust, or any other iron oxide/hydroxides were present in any of the XRD patterns. Similar results are also seen on gold sputtered on glass substrates (results not shown).

As the deposition potential becomes more negative, the lattice parameter of the magnetite decreases. A plot of the lattice parameter with respect to applied potential is shown in Figure 4. At low overpotentials, the films have larger lattice parameters than stoichiometric magnetite. At a potential of -1.04 V vs. Ag/AgCl, the lattice parameter of 0.8396 nm is comparable to the reported lattice parameter of magnetite of 0.8397 nm (JCPDS # 19-0629), represented as a dash line in Figure 4. This potential for stoichiometric magnetite is comparable to the calculated potential of -1.045 V vs. Ag/AgCl from the linear sweep voltammogram. As the applied potential becomes more negative, the lattice parameter becomes smaller than the reported literature value for the lattice parameter of magnetite.

When the overpotential is increased, the morphology of the film changes. SEM images in Figure 5 show the effect of potential on the surface morphology of the iron oxides on stainless steel. The magnetite films grown at lower overpotentials have highly faceted, dense morphologies as shown in the SEM image of a film deposited on stainless steel by applying -1.01 V vs. Ag/AgCl (Figure 5A). In Figure 5B, films deposited at -1.05

V vs. Ag/AgCl are featureless, yet dense. The films grown in the mass-transport limited region between -1.10 V and -1.20 V vs. Ag/AgCl have ribbon-like microstructures as seen in Figure 5C.

To determine the phases and stoichiometry of the films, Mössbauer spectroscopy was performed on films deposited at four different potentials on HOPG. Figure 6 and Table 2 shows the room temperature Mössbauer spectra and corresponding parameters of films deposited at A) -1.01 V, B) -1.05 V, C) -1.10 V and D) -1.20 V vs. Ag/AgCl. A single phase exists in films where -1.01 V and -1.05 V vs. Ag/AgCl were applied (Figure 6A and 6B). These spectra were fit with two Lorentzian sextets which provide the intensity values from the tetrahedral sites ( $\text{Fe}^{3+}$ ) and from the octahedral sites ( $\text{Fe}^{2.5+}$ ). The spectra indicate that the final products are nonstoichiometric magnetite. Of the two, the films deposited at -1.05 V vs. Ag/AgCl are closer to stoichiometric magnetite than the film deposited at -1.01 V vs. Ag/AgCl. In Figure 6C, an applied potential of -1.10 V produced films with two phases. This spectrum, as shown in Figure 6C, was fit with two Lorentzian sextets (tetrahedral sites ( $\text{Fe}^{3+}$ ), red and octahedral sites ( $\text{Fe}^{2.5+}$ ), blue) and a doublet (green). About 70% of the film is nonstoichiometric magnetite represented by the two sextets. The quadrupole splitting of the doublet for this film is 0.72 mm/s. Since most Fe(III) oxides produce a doublet with a quadrupole splitting of 0.5-0.6 mm/s in the Mossbauer spectra, the remaining 30% of this film is determined to be ferrihydrite, consistent with the reported quadrupole split doublet of paramagnetic ferrihydrite (0.7-0.85 mm/s).<sup>1,16</sup> In Figure 6D, the Mössbauer spectrum of films deposited at -1.20 V vs. Ag/AgCl shows just a doublet (QS = 0.75 mm/s) indicating that only ferrihydrite present.

The production of ferrihydrite, a Fe(III) compound, is unexpected since it is produced at more negative potentials in which the surface concentration of Fe(II) is high. Films deposited at -1.10 V and -1.20 V vs. Ag/AgCl are initially green which then air oxidize to a black and then reddish brown films. The green film is consistent with the production of green rust (GR). Green rust is a mixed iron(II)—iron(III) hydroxide containing an anion such as chloride, sulfate, or carbonate. In this study, a feasible type of a green rust would be sulfate green rust ( $\text{Fe}_4^{\text{II}}\text{Fe}_2^{\text{III}}(\text{OH})_{12}\text{SO}_4 \cdot n\text{H}_2\text{O}$ ). SEM images of sulfate GR resembling those found in Figure 5C have been electrodeposited from a slightly basic Fe(II)-sulfate solution at 25 °C.<sup>31,32</sup> However, the Mössbauer spectrum of the film deposited at -1.10 V and -1.20 V vs. Ag/AgCl in Figure 6C and 6D shows no indication of GR in comparison to the GR spectra reported.<sup>33-37</sup> However, the conversion of sulfate GR to magnetite has been reported.<sup>31,36-38</sup> Cellular structures of magnetite, similar to those seen in Figure 5C, have been produced by the chemical oxidation of electrodeposited sulfate GR films by using 0.1 M NaOH at 70 °C.<sup>38</sup> A study has also shown that the aerial oxidation of  $\text{Fe}(\text{OH})_2$  in basic medium produces GR which is converted to magnetite and ferrihydrite.<sup>37</sup> The adsorption of anions stabilizes ferrihydrite and hinders further oxidation to more stable iron hydroxides or oxides.<sup>1,16,37,39</sup> Therefore, the broadening of the film peaks in the XRD pattern in Figure 3C may be attributed to two-line ferrihydrite. The two film peaks can be indexed as (110) at 35.04° and (300) at 62.69° for a two-line ferrihydrite film utilizing JCPDS # 29-712. Therefore, the production of ferrihydrite at these potentials is consistent with the aerial oxidation of an electrodeposited GR film in basic conditions.

Films were then deposited at -1.01 V, -1.05, -1.10 V, and -1.20 V vs. Ag/AgCl on Au(111), Au(001), and Au(110) for epitaxial studies. An epitaxial film has out-of-plane and in-plane orientation. X-ray diffraction patterns were used to determine the out-of-plane orientations of the films. Figure 7 shows x-ray diffraction patterns of magnetite films deposited at a potential of -1.01 V vs. Ag/AgCl on gold single crystals. On Au(111) and Au(001), (111)-type peaks of  $\text{Fe}_3\text{O}_4$  were detected as seen in Figure 7A and 7B, respectively. On Au(110), only the (220) and (440) peaks for  $\text{Fe}_3\text{O}_4$  were observed in Figure 7C. No other peaks are present in any of the diffraction patterns. Therefore, thin films of magnetite on Au(111) and Au(001) grow with a [111] out-of-plane orientation while the film on Au(110) grow with a [110] out-of-plane orientation.

The in-plane orientations of the films were determined by X-ray pole figures. Since a polycrystalline film has no out-of-plane or in-plane orientation, a pole figure of a polycrystalline film would have uniform intensity. A film with fiber texture results in a ring pattern in the pole figure whereas an epitaxial film has distinct peaks in the pole figure. Figure 8 shows the (311) pole figures of  $\text{Fe}_3\text{O}_4$  films on gold single crystals using -1.01 V vs. Ag/AgCl. Figure 8A shows the (311) pole figure from a  $\text{Fe}_3\text{O}_4$  film deposited on Au(111) with six reflections at azimuthal angles,  $\chi$ , at  $29.5^\circ$ ,  $58.5^\circ$ , and  $80^\circ$ . The presence of six peaks in the pole figure at  $29.5^\circ$  and  $80^\circ$  indicates two {111} domains of  $\text{Fe}_3\text{O}_4$  rotated  $180^\circ$  on Au(111). One set of the three reflections are more intense than the other three reflections. A pole figure of a magnetite film on Au(001) in Figure 8B reveals in-plane [111] and [511] orientations. The presence of [511] orientations is common due to the twinning of the {111} planes.<sup>5</sup> Since the (333) and (511) planes have the same d-spacing, the presence of the (511) is difficult to verify by examining an x-ray

diffraction pattern. The clearest indication of the presence of the (511) orientation is in pole figures. When running a (311) pole figure, the {311} reflections related to the [511] orientation has  $\chi$ 's equal to  $9.5^\circ$ ,  $29.5^\circ$ ,  $41^\circ$ ,  $58.5^\circ$ ,  $66^\circ$ ,  $80^\circ$ , and  $86.7^\circ$ . Some of these  $\chi$ 's coincide with  $\chi$ 's of the reflections due to [111] orientation. The number of (511) domains was determined using  $\chi = 9.5^\circ$  since a single domain of (511) has one peak at this  $\chi$ . Therefore, the epitaxial magnetite film on Au(001) in Figure 8B has four domains of the three-fold symmetric [111] orientation as well 12 domains of the [511] orientation. The pole figure analysis of Figure 8C for a film on Au(110) is simpler. The interplanar angles between {311} and {110} planes are  $31.5^\circ$ ,  $64.8^\circ$ , and  $90^\circ$ . This pole figure is consistent with one domain, with [110] in-plane orientation of  $\text{Fe}_3\text{O}_4$  on Au(110).

The SEM images of magnetite on the gold single crystals deposited at -1.01 V vs. Ag/AgCl are shown in Figure 9. Consistent with the pole figure analysis of a film on Au(111), the micrograph in Figure 9A reveals two sets of [111] triangular facets rotated  $180^\circ$  with respect to each other. The majority of the facets point upwards and to the left compared to those pointing downwards and to the right. Figure 9B shows similar underlying [111] triangular facets pointing in 4 directions on Au(001). On these triangular facets are elongated pyramids which are attributed to the [511] orientation from the twinning of the {111} facets. Figure 9C shows pyramidal crystallites that indicate an underlying [110] orientation.

Azimuthal scans, in conjunction with the pole figures and stereographic projections of the films and substrate, were used to determine the epitaxial relationships. An epitaxial relationship describes how the film is oriented relative to the substrate by finding a direction of the film that is parallel to a direction in the substrate. Evident in the

azimuthal scans in Figure 10A and 10B, respectively, the main  $\{111\}$   $\text{Fe}_3\text{O}_4$  domain on the Au(111) aligns antiparallel to the substrate whereas the four  $\{111\}$   $\text{Fe}_3\text{O}_4$  domains are equivalent on Au(001). For the magnetite films on Au(111), the epitaxial relationships can be expressed as  $\text{Fe}_3\text{O}_4(111)[01\bar{1}]//\text{Au}(111)[0\bar{1}1]$  for the antiparallel domain and  $\text{Fe}_3\text{O}_4(111)[0\bar{1}\bar{1}]//\text{Au}(111)[0\bar{1}\bar{1}]$  for the parallel domain. That is for the dominate domain (antiparallel), the  $\text{Fe}_3\text{O}_4(111)$  and Au(111) planes are parallel and the  $\text{Fe}_3\text{O}_4[01\bar{1}]$  and Au $[0\bar{1}\bar{1}]$  in-plane directions are coincident. Similarly for the parallel domain, the  $\text{Fe}_3\text{O}_4(111)$  and Au(111) planes are parallel but the  $\text{Fe}_3\text{O}_4[0\bar{1}\bar{1}]$  and Au $[0\bar{1}\bar{1}]$  in-plane directions are coincident. The epitaxial relationships for the four  $\text{Fe}_3\text{O}_4$  domains on Au(001) are,  $\text{Fe}_3\text{O}_4(111)[0\bar{1}\bar{1}]//\text{Au}(001)[110]$ ,  $\text{Fe}_3\text{O}_4(111)[0\bar{1}\bar{1}]//\text{Au}(001)[\bar{1}\bar{1}0]$ ,  $\text{Fe}_3\text{O}_4(111)[0\bar{1}\bar{1}]//\text{Au}(001)[\bar{1}\bar{1}0]$ , and  $\text{Fe}_3\text{O}_4(111)[0\bar{1}\bar{1}]//\text{Au}(001)[\bar{1}\bar{1}0]$ . For each of these four relationships, three arrangements due to the (511) exist:  $(511)[\bar{2}55]$ ,  $(511)[\bar{1}14]$ , and  $(511)[\bar{1}41]$ . Figure 10C shows that the  $[110]$  oriented magnetite film has one domain and is aligned on the Au(110). Therefore, the epitaxial relationship for the (110) magnetite films on Au(110) is  $\text{Fe}_3\text{O}_4(110)[001]//\text{Au}(110)[001]$ . Thin magnetite films deposited at the more negative potentials of -1.05 V produced the same out-of-plane and in-plane orientations although the films were deposited at a different potential (not shown).

The x-ray diffraction patterns of the film grown at -1.10 V and -1.20 V vs. Ag/AgCl on Au(110) are shown in Figure 11A and 11B, respectively. The film deposited at -1.10 V vs. Ag/AgCl (Figure 11A) has two out-of-plane orientations:  $[110]$  oriented magnetite and  $(11\bar{2}0)$  oriented ferrihydrite. The SEM images in Figure 12 shows the

morphologies of the film deposited at -1.10 V vs. Ag/AgCl on Au(110). Figure 12A shows an area where two morphologies are present. In this image, the nanoribbon morphology seems to grow along the grain boundaries of the underlying material. Figure 12B shows the ribbon-like morphology that covers the surface. These ribbons are 20 to 30 nm wide. Figure 12C shows the morphology of the underlying film. Two phase morphologies of films deposited at -1.10 V vs. Ag/AgCl are produced on Au(001) and Au(111) (not shown). The films deposited at a more negative potential of -1.20 V vs. Ag/AgCl have similar ribbon morphologies yet the x-ray diffraction pattern (Figure 12B) and Mossbauer spectrum (Figure 6D) have no indication of magnetite being present. In the x-ray diffraction pattern of the film deposited at -1.20 V vs. Ag/AgCl on Au(110), only the  $(11\bar{2}0)$  and  $(22\bar{4}0)$  peaks of ferrihydrite are present (Figure 11B). Since only ferrihydrite is detected for the films deposited at -1.20 V vs. Ag/AgCl, the ribbon morphology is attributed to the ferrihydrite. Therefore, the SEM image in Figure 12C shows the morphology of the magnetite film under the ribboned ferrihydrite seen in Figure 12B.

The  $(311)$ magnetite pole figures are shown in Figure 13A and 13B for films deposited at -1.10 V and -1.20 V vs. Ag/AgCl on Au(110), respectively. However, the d-spacing of magnetite $(311)$  is very close to the d-spacing of ferrihydrite $(11\bar{2}0)$ , which results in the reflection of ferrihydrite $(11\bar{2}0)$ peaks in the same pole figure. Similarly, the d-spacing of magnetite $(311)$  is nearby the d-spacing of Au $(111)$ . So for the thin films,  $\{111\}$  reflections from the Au $(110)$  planes can also be evident in the same pole figure. Although the  $2\theta$  is maximized to observe the reflection from the magnetite $(311)$  planes,

the final pole figure is actually a superposition of the magnetite(311), ferrihydrite( $11\bar{2}0$ ), and Au(111) pole figures.

For a film deposited at -1.10 V vs. Ag/AgCl, the pole figure in Figure 13A is consistent with one domain of magnetite with a [110] in-plane orientation on Au(110). The pole figure analysis of the film deposited at -1.10 V vs. Ag/AgCl is equivalent to the pole figure analysis of Figure 8C for a film deposited at -1.01 V vs. Ag/AgCl on Au(110). In addition to these {311} reflections of [110] oriented magnetite in Figure 13A, three low intensity, broad peaks at  $\chi = 0^\circ$  and  $\chi = 60^\circ$  ( $180^\circ$  apart) are present in the pole figure. These peaks cannot be explained by (311) pole figure of any orientation of magnetite.

As seen in the XRD pattern in Figure 11A, magnetite and ferrihydrite are present in this film deposited at -1.10 V vs. Ag/AgCl. The x-ray diffraction pattern in Figure 11B indicated that the film deposited at -1.20 V vs. Ag/AgCl was ( $11\bar{2}0$ ) oriented ferrihydrite on Au(110). A pole figure of this film was run to determine if the broad peaks were due to an epitaxial ( $11\bar{2}0$ ) ferrihydrite film. The pole figure of this film (Figure 13B) had higher intensity peaks with azimuthal FWHM of  $46^\circ$  at  $\chi = 0^\circ$  and  $60^\circ$ , the same azimuthal angles of the broad peaks seen in Figure 13A. The nanoribbon morphology of the ferrihydrite causes the anisotropy observed in the pole figure shown in Figure 13A and 13B. This idea can be explained by reexamining SEM images of ferrihydrite such as Figure 12B. As the ferrihydrite nanoribbons begin their growth at the magnetite grain boundaries, the resulting electrodeposit is not compact. This loose packing allows for the loss of coherency, preferentially along the nanoribbons. This reduction of order

manifests itself in the wavy appearance of the nanoribbons seen in Figure 12B as well as the anisotropic character of the pole figure in Figure 13B.

The broad peaks in Figure 13B are assigned to the  $\{11\bar{2}0\}$  reflections of  $(11\bar{2}0)$  oriented ferrihydrite. Although the x-ray diffraction pattern of the film deposited at -1.20 V vs. Ag/AgCl in Figure 11B shows no magnetite, the pole figure does indicate that an  $[110]$  oriented magnetite film is present by the weak four  $\{311\}$  reflections of magnetite(111) at  $\chi = 30^\circ$ . The additional two sharp peaks at  $\chi = 35^\circ$ ,  $180^\circ$  apart, are  $\{111\}$  reflections of Au due to the Au(110) in Figure 13A and 13B. The Au(111) pole figure for the Au(110) substrate is shown in Figure 13C to confirm the location of the Au reflections in these pole figures. Based on the pole figure analyses, the epitaxial relationship for the two films on Au(110) are  $\text{Fe}_{10}\text{O}_{14}(\text{OH})_2(11\bar{2}0)[0001] // \text{Fe}_3\text{O}_4(110)[001] // \text{Au}(110)[001]$ . The epitaxial relationships for the films deposited on Au(001) and Au(111) are  $\text{Fe}_{10}\text{O}_{14}(\text{OH})_2(11\bar{2}0)[0001] // \text{Fe}_3\text{O}_4(001)[110] // \text{Au}(001)[110]$ ,  $\text{Fe}_{10}\text{O}_{14}(\text{OH})_2(11\bar{2}0)[\bar{1}100] // \text{Fe}_3\text{O}_4(001)[110] // \text{Au}(001)[110]$ , and  $\text{Fe}_{10}\text{O}_{14}(\text{OH})_2(11\bar{2}0)[\bar{1}100] // \text{Fe}_3\text{O}_4(111)[01\bar{1}] // \text{Au}(001)[01\bar{1}]$ .

## CONCLUSIONS

Varying the reduction potential allows for the deposition of magnetite, ferrihydrite, and iron from the Fe(III)-TEA deposition bath. The stoichiometry of the magnetite films can be controlled by varying the potential as shown theoretically and experimentally. At the potentials of -1.10 V and -1.20 V vs. Ag/AgCl, ferrihydrite films are deposited through the aerial oxidation of green rust. The magnetite and ferrihydrite

films are epitaxial on gold single crystals. Magnetite deposited on Au(111) and Au(001) is [111] oriented while magnetite is [110] oriented on Au(110). Films deposited at -1.10 V and -1.20 V vs. Ag/AgCl produced epitaxial (11 $\bar{2}$ 0)ferrihydrite on epitaxial [110] magnetite on Au(110).

Work needs to be done to determine the magnetic properties of these electrodeposited magnetite and ferrihydrite films. With the ability to tune the stoichiometry of ferrimagnetic magnetite, to produce superparamagnetic ferrihydrite and ferromagnetic iron from the same solution, and to deposit epitaxial films on gold single crystals from one deposition bath, the fabrication of superlattices and layered films for giant magnetoresistance and spintronic devices are well within reach.

#### ACKNOWLEDGEMENT

The authors thank the Department of Energy DE-FG02-08ER46518.

#### FOOTNOTES

- (1) Cornell, R. M.; Schwertmann, U. *The Iron Oxides: Structure, Properties, Reactions, Occurrences, and Uses*; VCH: Weinheim, 1996.
- (2) Zhang, Z.; Spatpathy, S. *Phys. Rev. B* **1991**, *44*, 13319.
- (3) A. Yanase, K. Siratori, *J. Phys. Soc. Japan* **53**, 312 (1984).
- (4) Abe, M.; Tamaura, Y. *J. Appl. Phys.* **1983**, *22*, L511.
- (5) Sorenson, T. A.; Morton, S. A.; Waddill, D. G.; Switzer, J. A. *J. Amer. Chem. Soc.* **2002**, *124*, 7604.
- (6) Carlier, D.; Terrier, C.; Arm, C.; Ansermet, J-Ph. *Electrochem. Solid State Lett.* **2005**, *8*, C43.
- (7) Nishimura, K.; Kitamoto, Y.; Abe, M. *IEEE Trans. Magn.* **1999**, *35*, 3043.
- (8) Peulon, S.; Antony, H.; Legrand, L.; Chausse, A. *Electrochim. Acta* **2004**, *49*, 2891.

- (9) Wang, S.-Y.; Ho, K.-C.; Kuo, S.-L.; Wu, N.-L. *J. Electrochem. Soc.* **2006**, *153*, A75.
- (10) Martinez, L.; Leinen, D.; Martin, F.; Gabas, M.; Ramos-Barrado, J. R.; Quagliata, E.; Dalchiele, E. A.. *J. Electrochem. Soc.* **2007**, *154*, D126.
- (11) Chatman, S.; Noel, A. J. G.; Poduska, K. M. *J. Appl. Phys.* **2005**, *98*, 113902.
- (12) Teng, C.-L.; Ryan, M. P. *Electrochem. Solid State Lett.* **2007**, *10*, D108.
- (13) Kothari, H. M.; Kulp, E. A.; Limmer, S. J.; Poizot, P.; Bohannan, E. W.; Switzer, J. A. *J. Mater. Res.* **2006**, *21*, 293.
- (14) Mitra, S.; Poizot, P.; Finke, A.; Tarascon, J.-M. *Adv. Funct. Mater.* **2006**, *16*, 2281.
- (15) Sapieszko, R. S.; Matijevic, E. *J. Colloid Interface Sci.* **1980**, *74*, 405.
- (16) Jambor, J. L.; Dutrizac, J. E. *Chem. Rev.* **1998**, *98*, 2549.
- (17) Michel, F. M.; Ehm, L.; Antao, S. M.; Lee, P. L.; Chupas, P. J.; Liu, G.; Strongin, D. R.; Schoonen, M. A. A.; Phillips, B. L.; Parise, J. B. *Science*. **2007**, *316*, 1726.
- (18) Schwertmann, U.; R. M. Cornell. *Iron Oxides in the Laboratory: Preparation and Characterization*; VCH: Weinheim, 2000.
- (19) Mohr, S.; Bechtold, T. *J. Appl. Electrochem.* **2001**, *31*, 363.
- (20) Wen, Y. H.; Zhanag, H. M.; Qian, P.; Zhou, H. T.; Zhao, P.; Yi, B. L.; Yang, Y. S. *Electrochim. Acta* **2006**, *51*, 3769.
- (21) Bechtold, T.; Burtscher, E.; Amann, A.; Bobleter, O. *J. Chem. Soc. Faraday Trans.* **1993**, *89*, 169.
- (22) Ibanez, J. G.; Choi, C.; Becker, R. S. *J. Electrochem. Soc.* **1987**, *134*, 8.
- (23) Thomas, B.; Aurora, T. *J. Electroanal. Chem.* **2005**, *580*, 173.
- (24) *Stability Constants Supplement No. 1* Chemical Society: London, 1971.
- (25) Perrin, D. D. *IUPAC Stability Constants of Metal-Ion Complexes: Part B Organic Ligands*. Pergamon Press: New York, 1979.
- (26) Polcyn, D. S.; Shain, I. *Anal. Chem.* **1966**, *38*, 376.
- (27) Frings, J.; Wondrak, C.; Schink, B. *Ach. Microbiol.* **1994**, *162*, 103.
- (28) Bard, A. J.; Parsons, R.; Jordan, J. *Standard Potentials in Aqueous Solution*. Marcel Dekker: New York, 1985.
- (29) Lide, D. R. *CRC Handbook of Chemistry and Physics 77<sup>th</sup> edition*. CRC Press: New York, 1996.

- (30) Bard, A. J.; Faulkner, L. R. *Electrochemical Methods: Fundamentals and Applications*. 2<sup>nd</sup> Edition. John Wiley & Sons: New York, 2001.
- (31) Antony, H.; Legrand, L.; Chausse, A. *Electrochim. Acta* **2008**, *53*, 7146.
- (32) Antony, H.; Labrit, A.; Rouchaud, J. C.; Legrand, L.; Chausse, A. *Electrochim. Acta* **2008**, *53*, 7173.
- (33) Ruby, C.; Aissa, R.; Gehin, A.; Cortot, J.; Abdelmoula, M.; Genin, J.-M. *C. R. Geoscience*. **2006**, *338*, 420.
- (34) Genin, J.-M. R.; Refait, P.; Bourrie, G.; Abdelmoula, M.; Trolad, F. *Appl. Geochem.* **2001**, *16*, 559.
- (35) Genin, J.-M. R.; Abdelmoula, M.; Aissa, R.; Ruby, C. *Hyper. Inter.* **2005**, *166*, 391.
- (36) Ruby, C.; Gehin, A.; Aissa, R.; Genin, J.-M. R. *Corrosion Sci.* **2006**, *48*, 3824.
- (37) Genin, J.-M. R.; Ruby, C.; Gehin, A.; Refait, P. *C. R. Geoscience*. **2006**, *338*, 433.
- (38) Chung, K. W.; Kim, K. B.; Han, S.-H.; Lee, H. *Electrochem. Solid State Lett.* **2005**, *8*, A259.
- (39) Furukawa, Y.; Kim, J.-W.; Watkins, J.; Wilkens, R. T. *Environ. Sci. Technol.* **2002**, *36*, 5469.

**Table 1.** Potentials and constants used to calculate the reduction potential of  $\text{Fe}(\text{OH})_4\text{TEA}_2^-$  to  $\text{Fe}_3\text{O}_4$ .

Equations	Constant at 25 °C
$\text{Fe}(\text{OH})_4\text{TEA}_2^- \rightleftharpoons \text{Fe}^{3+} + 2\text{TEA} + 4\text{OH}^-$	$K = 10^{-44.6}$ (25)
$\text{Fe}^{3+} + e^- \rightleftharpoons \text{Fe}^{2+}$	$E^\circ = 0.771 \text{ V vs. NHE}$ (29)
$\text{Fe}^{2+} + 2\text{TEA} \rightleftharpoons \text{FeTEA}_2^{2+}$	$K = 10^{3.59}$ (24)
$\text{Fe}(\text{OH})_4\text{TEA}_2^- + e^- \rightleftharpoons \text{Fe}(\text{TEA})_2^{2+} + 4\text{OH}^-$	$E^\circ = -1.65 \text{ V vs. NHE}$
$2\text{Fe}(\text{OH})_4\text{TEA}_2^- + \text{Fe}(\text{TEA})_2^{2+} \rightleftharpoons \text{Fe}_3\text{O}_4 + 6\text{TEA} + 4\text{H}_2\text{O}$	$\Delta G_{\text{rxn}} = -87.82 \text{ kJ/mol}$
Species	$\Delta G_f^\circ$
TEA	-315.6 kJ/mol (27)
$\text{Fe}^{2+}$	-78.87 kJ/mol (28)
$\text{Fe}^{3+}$	-4.7 kJ/mol (28)
$\text{OH}^-$	-157.293 kJ/mol (29)
$\text{Fe}(\text{OH})_4\text{TEA}_2^-$	-1519.64 kJ/mol
$\text{Fe}_3\text{O}_4$	-1015.5 kJ/mol (28)
$\text{H}_2\text{O}$	-237.14 kJ/mol (29)
$\text{FeTEA}_2^{2+}$	-730.56 kJ/mol

**Table 2.** The Mössbauer spectral parameters at 25 °C obtained from the spectra in Figure 6 of films deposited from four different potentials vs. Ag/AgCl. The isomer shifts are given relative to the  $\alpha$ -Fe foil at 25 °C.

Potential (V)	Compound	Component	IS (mm/s)	QS (mm/s)	HF (kOe)	Ratio (%)
-1.01	Magnetite	Fe(3+)	0.3390	0.0878	488.87	26.51
		Fe(2.5+)	0.6820	0.0732	453.53	73.49
-1.05	Magnetite	Fe(3+)	0.3169	0.0768	488.22	28.78
		Fe(2.5+)	0.6645	0.0815	452.92	71.22
-1.10	Magnetite	Fe(3+)	0.3157	0.0622	489.80	17.13
		Fe(2.5+)	0.6716	0.1465	453.66	52.69
	Ferrihydrite		0.3091	0.7186		30.19
-1.20	Ferrihydrite		0.3291	0.7451		100

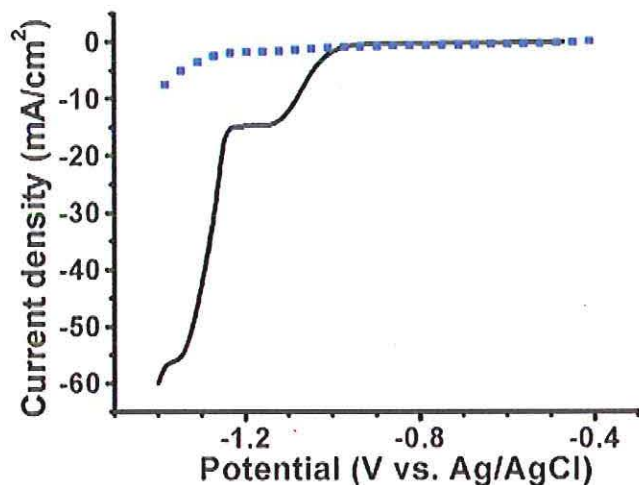


Figure 1. The linear sweep voltammograms of an alkaline TEA solution (blue squares) and Fe(III)-TEA solution (black solid line) at 80 °C scanned at 50 mV/s at a rotation of 100 rpm on a gold rotating disk electrode. The alkaline TEA solution consisted of 0.1 M TEA in 2 M NaOH. The alkaline Fe(III)-TEA solution consisted of 43 mM Fe<sub>2</sub>SO<sub>4</sub>, 0.1 M TEA, and 2 M NaOH.

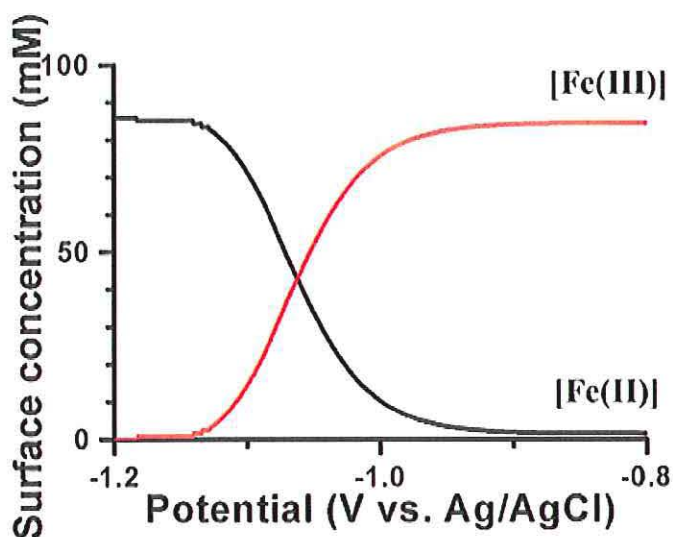


Figure 2. A plot of the surface concentrations of Fe(III) (red) and Fe(II) (black) as a function of potential based on the linear sweep voltammogram of the alkaline Fe(III)-TEA bath in Figure 1.

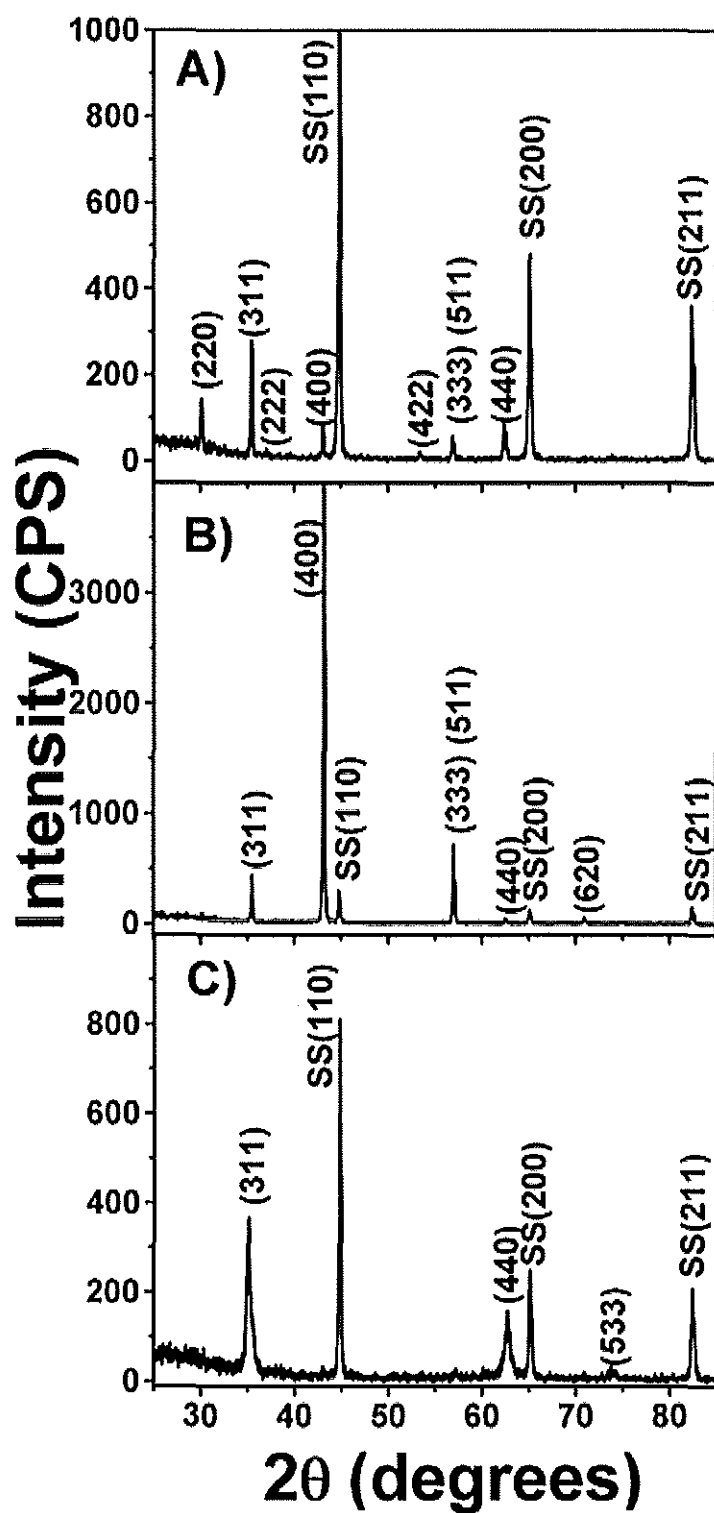


Figure 3. Symmetric X-ray diffraction patterns of magnetite films deposited on 430 stainless steel (SS) substrates at a potential of A) -1.01 V, B) -1.05 V, and C) -1.1 V vs. Ag/AgCl until  $1 \text{ C/cm}^2$  was passed at  $80^\circ\text{C}$ .

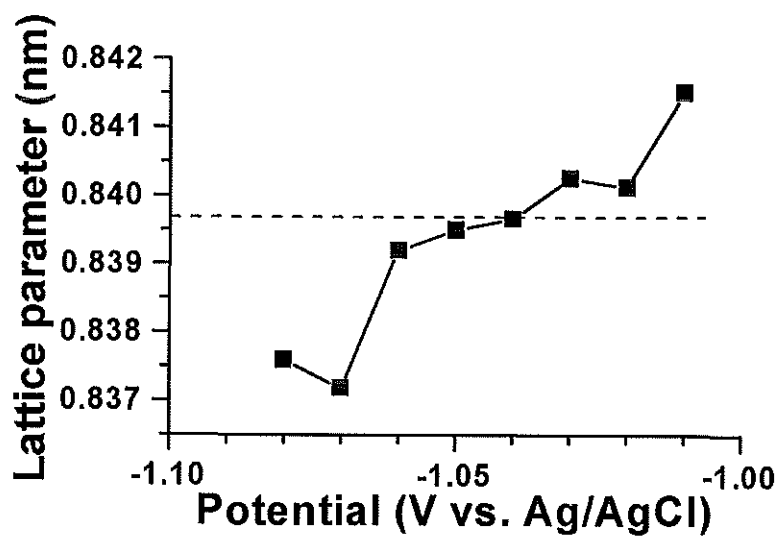


Figure 4. Lattice parameters from Rietveld analysis of XRD patterns of magnetite films deposited as a function of potential. All of the magnetite films were electrodeposited on 430 stainless steel electrodes until  $1 \text{ C/cm}^2$  was passed at  $80^\circ\text{C}$ .

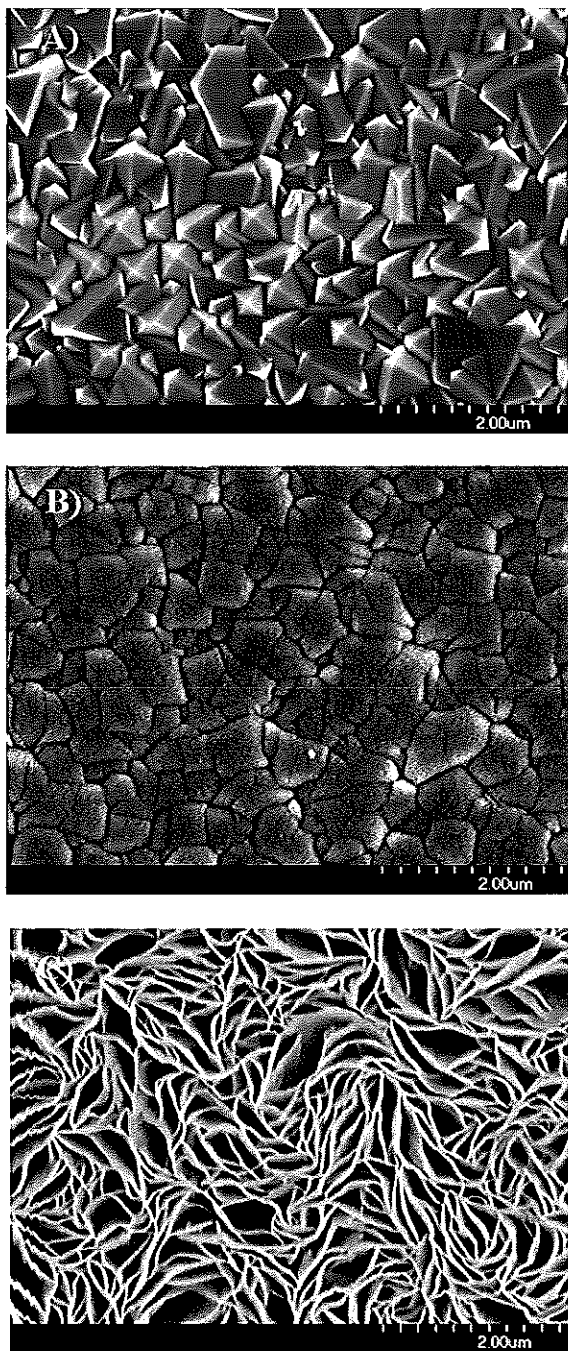


Figure 5. SEM images of magnetite films deposited on stainless steel at A) -1.01 V, B) -1.05 V, and C) -1.1 V vs. Ag/AgCl. The films were deposited at 80 °C until 1 C/cm<sup>2</sup> passed.

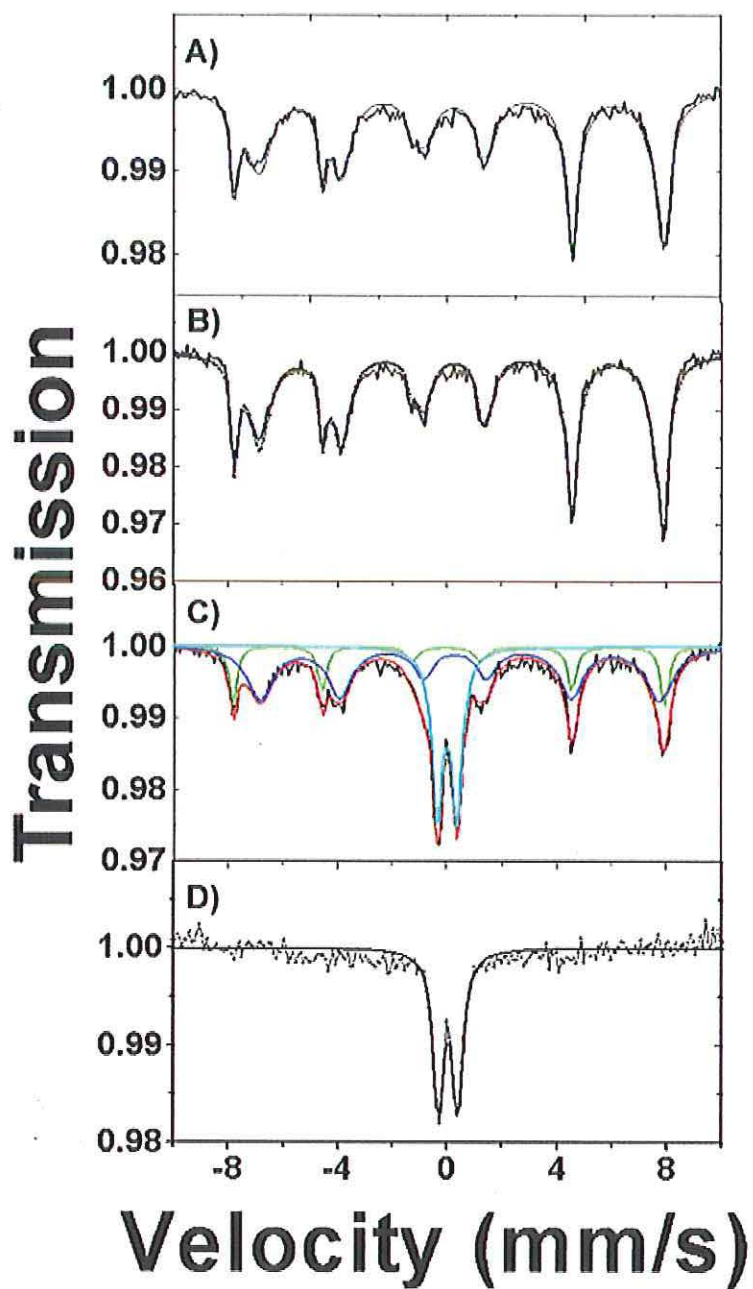


Figure 6. Room temperature Mössbauer spectra of magnetite deposited on HOPG at A) -1.01 V, B) -1.05 V, C) -1.10 V and D) -1.20 vs. Ag/AgCl. Spectra A and B are composed of two sets of sextets consistent with magnetite. Spectrum C shows two sets of sextets and a doublet associated with magnetite and ferrihydrite, respectively. Spectrum D shows a ferrihydrite doublet.

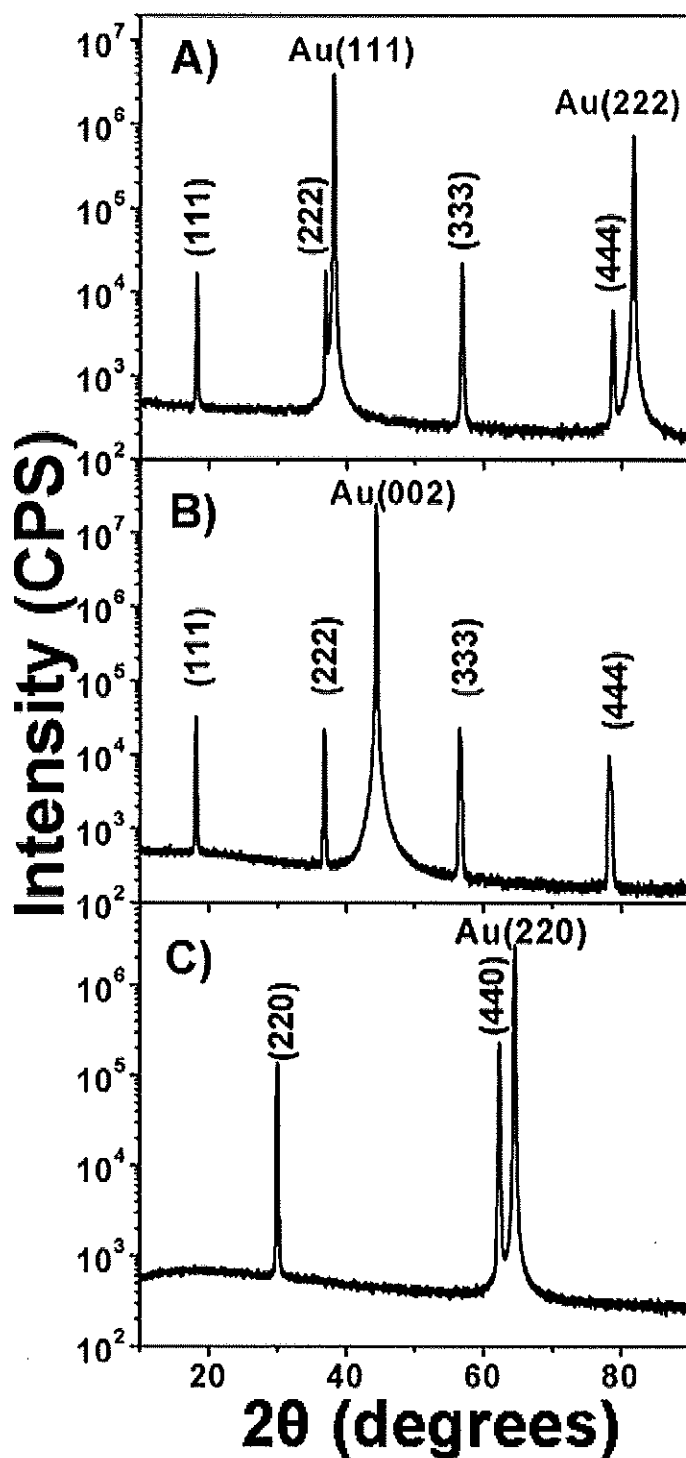


Figure 7. X-ray diffraction patterns of magnetite deposited on A) Au(111), B) Au(001), and C) Au(110) for 300 s at -1.01 V vs. Ag/AgCl at 80 °C. Magnetite films deposited on Au(111) and Au(001) are (111) oriented while films deposited on Au(110) are (110) oriented.

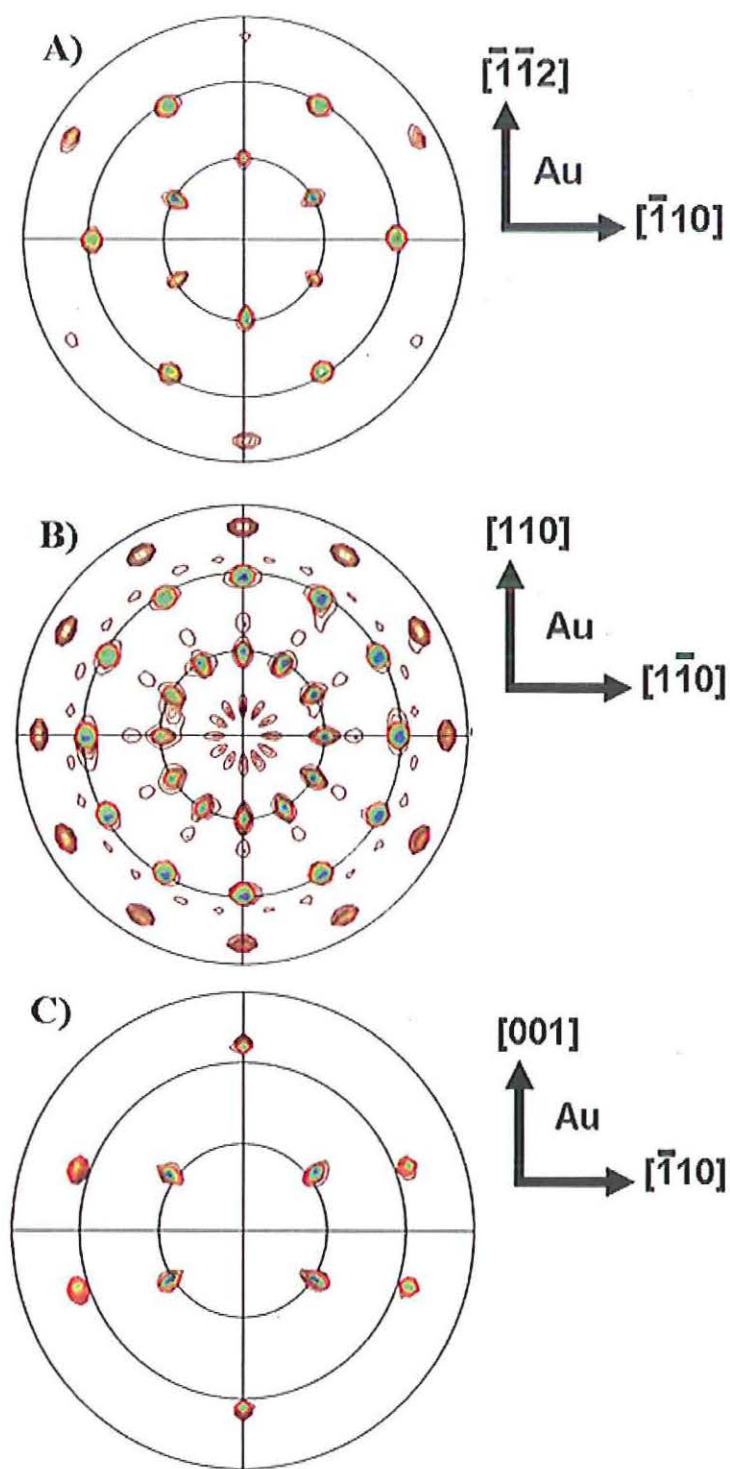


Figure 8. (311) pole figures of magnetite films deposited on A) Au(111), B) Au(001), and C) Au(110) for 300 s at -1.01 V vs. Ag/AgCl at 80 °C. The radial grid lines on the pole figure correspond to 30° increments of the tilt angle,  $\chi$ .

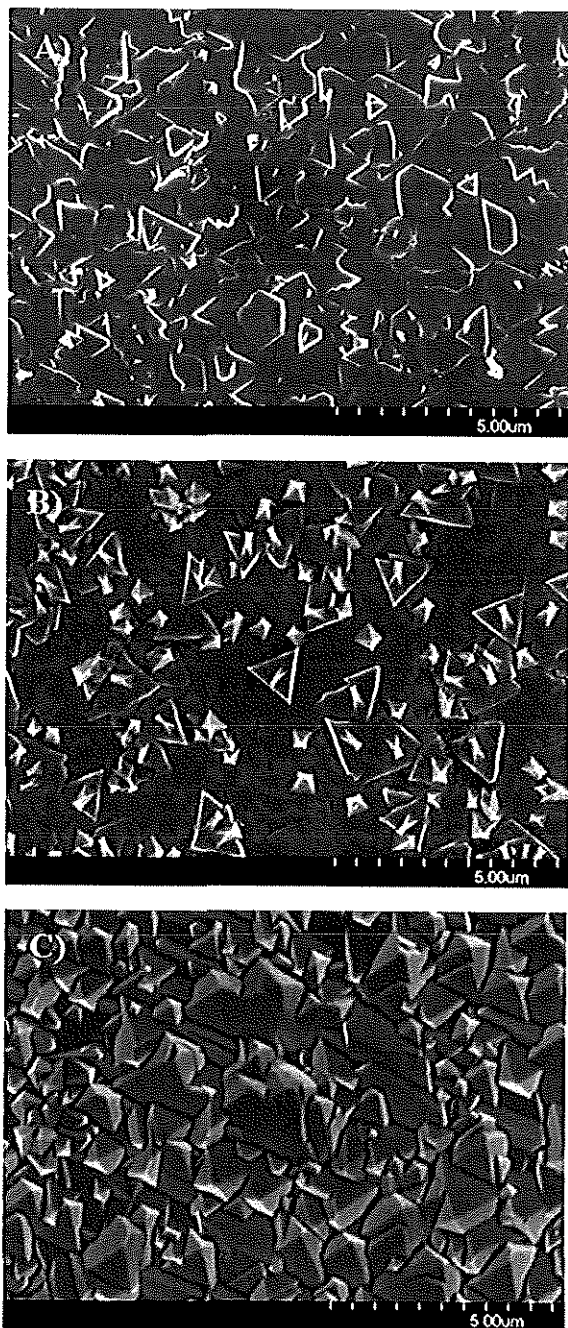


Figure 9. SEM images of magnetite deposited on A) Au(111), B) Au(001), and C) Au(110) for 300 s at -1.01 V vs. Ag/AgCl at 80 °C.

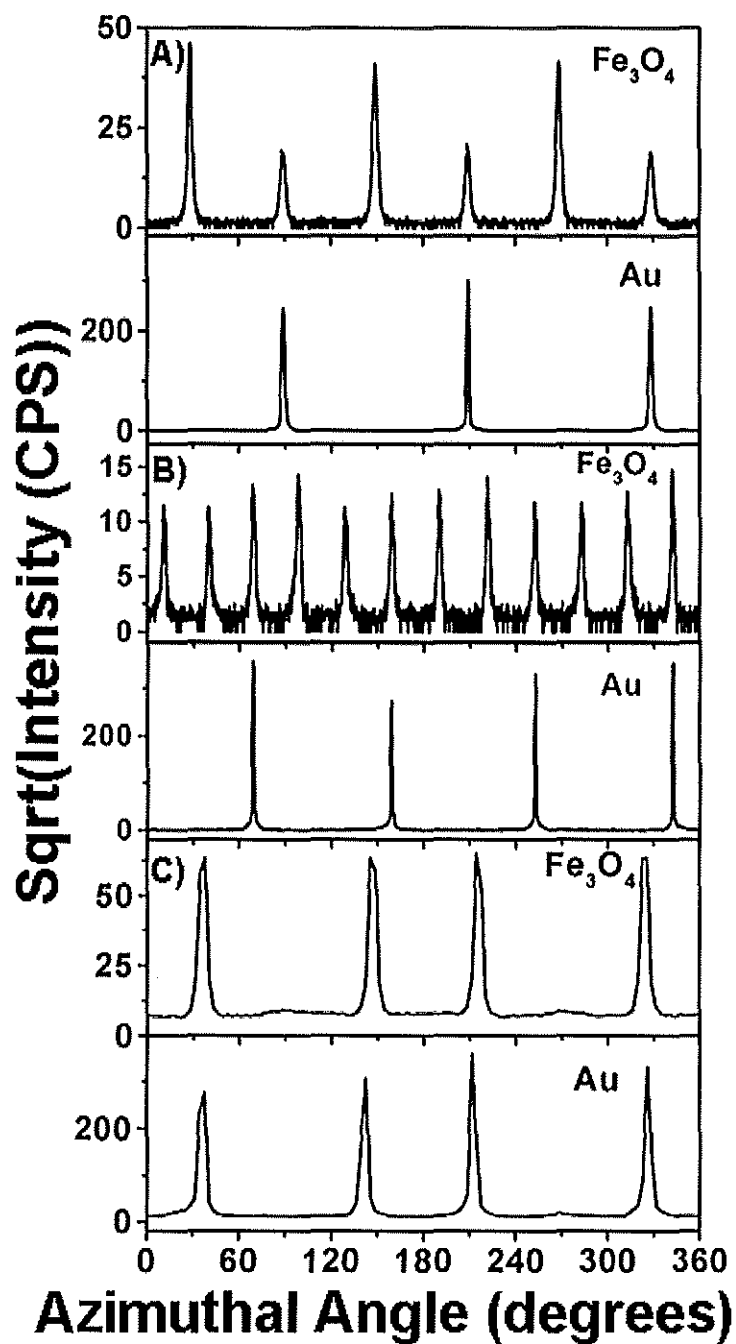


Figure 10. (311) azimuthal scans of magnetite and gold for magnetite films deposited on A) Au(111), B) Au(001), and C) Au(110). For a set of azimuthal scans, the top plot is the magnetite azimuthal scan and the bottom plot is the substrate azimuthal scan.

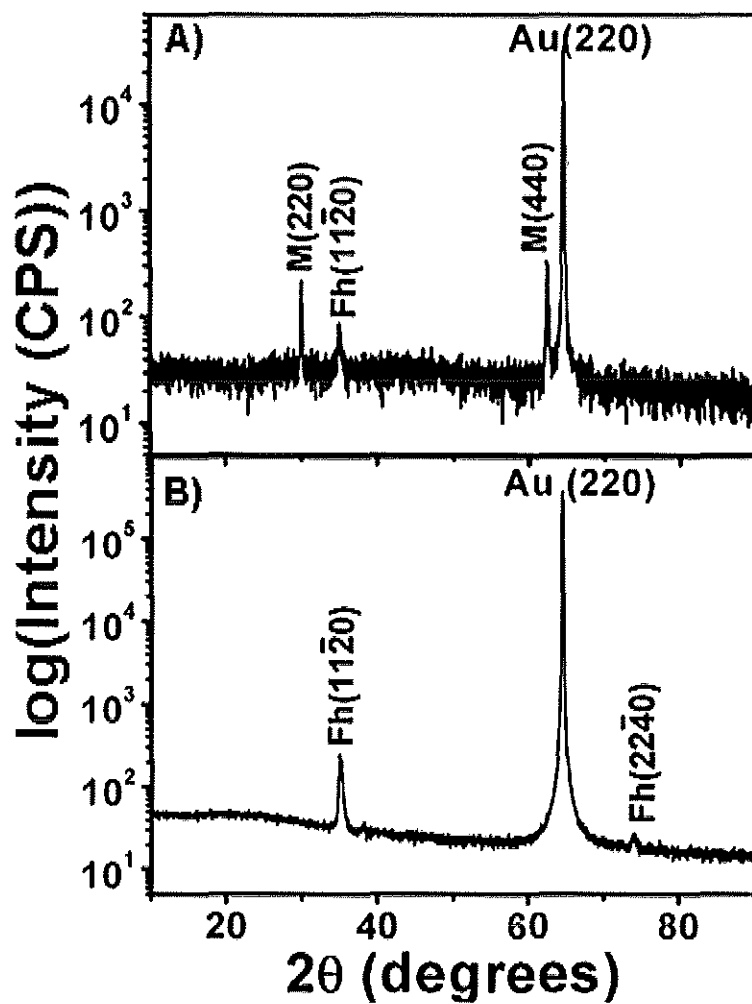


Figure 11. X-ray diffraction patterns of magnetite and ferrihydrite electrodeposited at A) -1.10 V and B) -1.20 V vs. Ag/AgCl on Au(110). M indicates a peak assigned to a magnetite plane whereas a Fh indicates a peak assigned to a ferrihydrite plane.

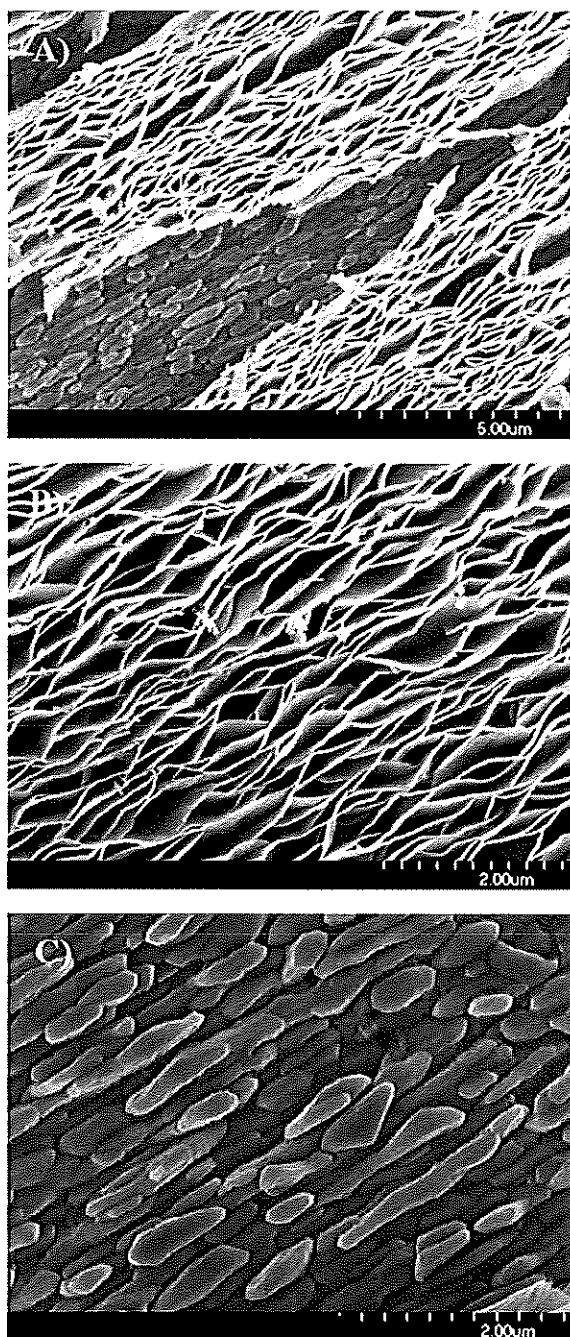


Figure 12. SEM images of a film deposited at -1.1 V vs. Ag/AgCl at 80 °C on Au(110). A) A SEM image of the overall view of the surface of the film showing two distinct morphologies. The ribbon-like morphology of ferrihydrite (B) on underlying nonstoichiometric magnetite (C) is shown.

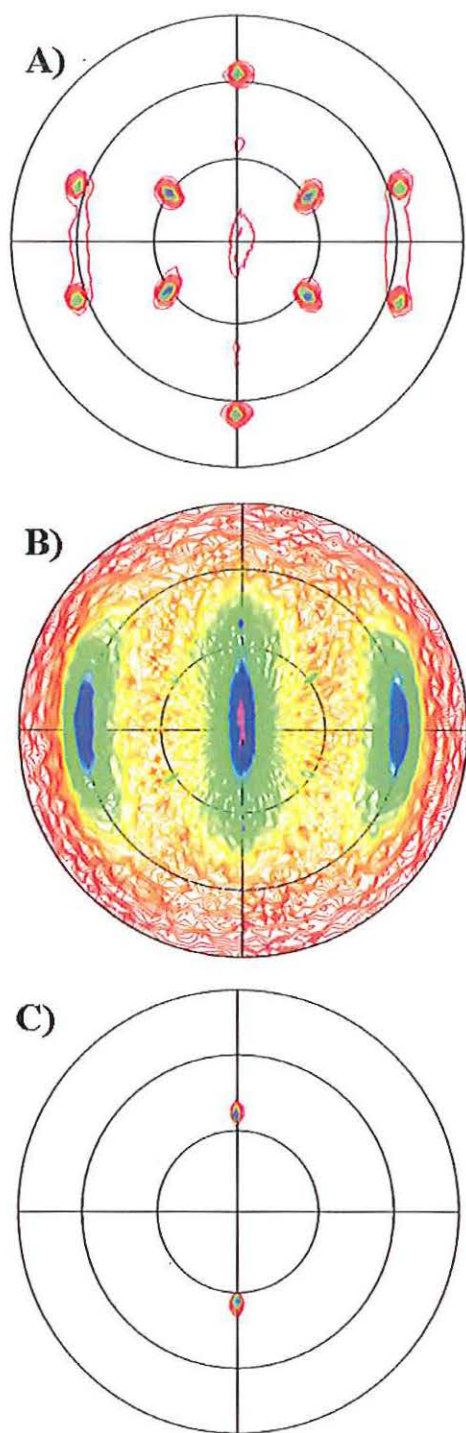


Figure 13. (311) magnetite pole figures of  $(11\bar{2}0)$  ferrihydrite on (110) magnetite on Au(110) electrodeposited at A) -1.10 V and B) -1.20 V vs. Ag/AgCl are shown. The (311) magnetite pole figure is actually probing three planes: (311) magnetite,  $(11\bar{2}0)$  ferrihydrite, and (111) Au due to their similar d-spacings. Figure C is a (111) Au pole figure of the Au(110) substrate. The radial grid lines on the pole figure correspond to  $30^\circ$  increments of the tilt angle,  $\chi$ .

### III. Epitaxial Electrodeposition of Ferrite Superlattices on Au(111)

Elizabeth A. Kulp<sup>1</sup>, Rakesh V. Gudavarthy<sup>1</sup>, Steven J. Limmer<sup>1</sup>,

Eric W. Bohannan<sup>1</sup>, F. Scott Miller<sup>2</sup>, Jay A. Switzer<sup>1,2</sup>

Department of Chemistry<sup>1</sup>, Department of Materials Science and Engineering<sup>2</sup>,  
Missouri University of Science and Technology, 103 Materials Research Center,  
Rolla, MO, 65401.

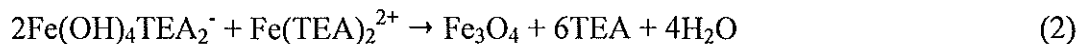
**Epitaxial magnetite superlattices are electrochemically produced on single-crystal Au(111) by pulsing the applied potential during deposition. Since magnetite is a half-metallic ferrimagnet with 100% spin polarization at the Fermi level, these superlattices are expected to show strong spintronic responses. We exploit the electrochemical-chemical (EC) nature of the reaction to deposit these superlattices. We show that the concentration of Fe(III) and Fe(II) at the electrode surface is controlled by the applied potential. The EC mechanism allows for the incorporation of electrochemically inactive cations into the system to produce other ferrite superlattices. We show by x-ray diffraction and cross-sectional FIB images that compositional superlattices based on zinc ferrite are deposited by varying the applied potential.**

Superlattices are periodic multilayers with the additional constraint of crystallographic coherency. Superlattices show enhanced optical, electronic, magnetic, or mechanical properties as a function of their nanoscale dimensions (1-3). We have previously shown that both defect (4) and compositional (5-7) superlattices based on conductive oxides can be electrodeposited. Other groups have produced superlattices of

metals (8-12) and of compound semiconductors (13) by electrodeposition. In this paper, we demonstrate that epitaxial superlattices based on magnetite ( $\text{Fe}_3\text{O}_4$ ) can be electrochemically produced by exploiting the electrochemical-chemical (EC) nature of the deposition reaction. This system has the potential to be used in magnetoelectronic devices such as magnetic recording, non-volatile memories, and spin valves (14, 15) and as an imitator of Nature's own magnetoreceptors (16-18).  $\text{Fe}_3\text{O}_4$  is an ideal candidate as a spin-polarized carrier layer in these materials because this magnetic, half-metallic material has a predicted 100% spin polarization at the Fermi level (19, 20). We have previously demonstrated that electrodeposited magnetite films have a magnetoresistance of -6.5% at 300 K in an applied field of 9 T, attributed to  $\alpha\text{-Fe}_2\text{O}_3$  at the grain boundaries (21). Besides being a ferrimagnetic material below 860 K,  $\text{Fe}_3\text{O}_4$  also undergoes a metal-insulator Verwey transition at 120 K in which this charge-ordered insulator has a magnetoelectronic effect, becoming ferroelectric below this Verwey temperature (22-27). Composites of multiferroics, such as  $\text{Fe}_3\text{O}_4$ , have potential applications for spintronic devices utilizing both ferrimagnetic and ferroelectric properties (27-29).

The superlattices were electrodeposited using 86 mM Fe(III), 100 mM triethanolamine (TEA), and 0.2 M sodium hydroxide, previously used for magnetite deposition (21). Fig. 1A shows a linear sweep voltammogram (LSV) on a gold rotating disk electrode at 100 rpm in an alkaline Fe(III)-TEA deposition bath at 80 °C scanned at 50 mV/sec from the open circuit potential of -0.47 V to -1.25 V vs. Ag/AgCl. The electrochemical reduction of the alkaline Fe(III)-TEA bath is observed at potentials negative of -0.95 V vs. Ag/AgCl. The region from -0.95 V to -1.20 V vs. Ag/AgCl on this linear sweep is a one electron reaction involving the reduction of an Fe(III) species to

an Fe(II) species. The proposed EC reactions for magnetite deposition of this solution is shown in Eq. 1 and 2.



The surface concentrations of these species are dependent on the departure from equilibrium. At low overpotentials, the Fe(III) surface concentration is nearly the same as the bulk concentration whereas at high overpotentials, at which the current becomes mass-transport controlled, the surface concentration of Fe(III) approaches zero.

Therefore, the surface concentrations of Fe(III) and Fe(II) can be controlled by varying the applied potential. The surface concentration of Fe(III) can be calculated from Eq. 3,

$$\frac{i}{i_{l,c}} = \frac{[C_{\text{Fe(III)}}(\text{bulk}) - C_{\text{Fe(III)}}(\text{surface})]}{C_{\text{Fe(III)}}(\text{bulk})} \quad (3)$$

where  $i$  is the measured current,  $i_{l,c}$  is the limiting current,  $C_{\text{Fe(III)}}(\text{bulk})$  is the bulk concentration of Fe(III) in solution, and  $C_{\text{Fe(III)}}(\text{surface})$  is the Fe(III) concentration at the electrode surface (30). The concentrations of Fe(III) (red line) and Fe(II) (black line) at the electrode surface are plotted in Fig. 1B. Stoichiometric magnetite would be deposited at approximately -1.045 V vs. Ag/AgCl, where 1/3 of the total concentration of Fe(III) has been reduced to Fe(II). Theoretically, any potential more positive than this value should produce magnetite with excess Fe(III), whereas potentials more negative of -1.045 V vs. Ag/AgCl should produce magnetite with excess Fe(II).

Fig. 1C shows the change in lattice parameter of the magnetite (black squares) films with respect to the deposition potential. As the overpotential increases, the lattice parameters of these films decrease. The film with a lattice parameter of 0.8396 nm is

produced at -1.04 V vs. Ag/AgCl, comparable to the literature value of 0.8397 nm (JCPDS # 19-0629) (black dashed line, Figure 1C). This result is in good agreement with the predicted potential of -1.045 V vs. Ag/AgCl from the LSV in Figure 1B for stoichiometric magnetite. Since the iron species concentrations at the electrode surface and lattice parameters of the magnetite films are defined by the applied potential, the magnetite superlattices can be deposited from a single bath by simply pulsing the applied potential during deposition.

In this study, the magnetite superlattices ( $\text{Fe}_a^{2+}\text{Fe}_b^{3+}\text{O}_c/\text{Fe}_d^{2+}\text{Fe}_e^{3+}\text{O}_f$ ) were deposited by pulsing the potential between -1.01 and -1.05 V vs. Ag/AgCl. The lattice mismatch between the layers deposited at the two potentials is 0.24%. The modulation wavelength of the superlattices is controlled by selecting appropriate dwell times for each of the deposition potentials. Fig. 2 shows the x-ray diffraction results of magnetite with 100 bilayers deposited on single-crystal Au(111). On the Au(111) single crystal, only {111}-type peaks of magnetite were detected as seen in Fig. 2A, indicating that the film grows epitaxially on the Au(111) crystal. The (311) pole figures of the magnetite superlattice (Fig. 2B, left) and Au substrate (Fig. 2B, right) show that the {111} magnetite domains on the Au(111) align mainly antiparallel to the substrate. The epitaxial relationships for this superlattice is  $[\text{Fe}_a^{2+}\text{Fe}_b^{3+}\text{O}_c(111)[0\bar{1}\bar{1}]]//[\text{Fe}_d^{2+}\text{Fe}_e^{3+}\text{O}_f(111)[0\bar{1}\bar{1}]]_{100} // \text{Au}(111)[0\bar{1}\bar{1}]$  and  $[\text{Fe}_a^{2+}\text{Fe}_b^{3+}\text{O}_c(111)[0\bar{1}\bar{1}]]//[\text{Fe}_d^{2+}\text{Fe}_e^{3+}\text{O}_f(111)[0\bar{1}\bar{1}]]_{100} // \text{Au}(111)[0\bar{1}\bar{1}]$  for the major antiparallel and minor parallel domains, respectively.

Although superlattices and multilayers are composed of alternating layers of materials, superlattices have the additional constraints of periodicity and crystallographic

coherency. Due to these constraints, satellite peaks are seen around the main Bragg peaks in x-ray diffraction patterns. In a superlattice, the bilayer thickness, known as the modulation wavelength,  $\Lambda$ , can be calculated from the satellite spacing utilizing Eq. 4:

$$\Lambda = \frac{\lambda(L_1 - L_2)}{2(\sin \theta_1 - \sin \theta_2)} \quad (4)$$

where  $\lambda$  is the wavelength of the x-ray source (Cu  $K_\alpha$  1.5401 Å),  $L$  is the order of the satellite and  $\theta$  is the diffraction angle of the satellite  $L$ . In Fig. 2A, first order satellite peaks flank the (333) and (444) reflections. Using Eq. 2, the modulation wavelength for each film was determined based on the (333) and (444) peaks of the magnetite superlattices. The (444) reflections and their satellite peaks of the x-ray diffraction patterns are shown in Fig. 2C for the magnetite superlattices. By systematically changing the deposition times, superlattices with different modulation wavelengths are produced. As the  $\Lambda$  increases from 9.5 to 20.7 nm, the satellites move closer to the main Bragg peak, labeled as 0. These epitaxial superlattices with tunable nanoscale layer thicknesses have the potential to show electronic transport measurements below the Verwey temperature (26).

In addition to producing defect chemistry superlattices based entirely on  $\text{Fe}_3\text{O}_4$ , it is also possible to deposit compositional superlattices containing Zn. The production of ferrites has applications in transformers, inductors, entertainment, and magnetic recording devices (31). Electrodepositing a basic ferrite such as zinc ferrite demonstrates that electrodeposition can be used to produce other ferrites and indicates a potential for the electrochemical development of zinc-substituted ferrites that show higher magnetic moments than the pure ferrites (31,32). Here, films and superlattices based on zinc ferrite

were produced from the same deposition solution to which 30 mM Zn(II) was added. An equivalent LSV as seen in Fig. 1A is produced from an alkaline Fe(III)-TEA bath with Zn(II) present, indicating that the Zn(II) in solution is electrochemically inactive in this range. Since the Zn(II) is electrochemically inactive in the range for the LSV, the concentration of Zn(II) at the electrode surface is fixed at the bulk concentration of 30 mM at any potential.

Like the magnetite films, the lattice parameters of the zinc ferrite films decrease as the overpotential increases (Fig. 3A). Zinc ferrite films deposited at -0.97 V vs. Ag/AgCl have a lattice parameter of 0.8443 nm, close to the literature value of 0.8446 nm (JCPDS # 79-1150) (red dashed line, Fig. 3A). The zinc content of these films based on metal-only energy dispersive spectroscopy (EDS) measurements varies from 32% at -0.97 V to 20% at -1.05 V vs. Ag/AgCl. As shown in Table I, the compositions calculated from the LSV agree well with the compositions measured from the EDS. The zinc ferrite superlattices ( $Zn_aFe_bO_c/Zn_dFe_eO_f$ ) are deposited by pulsing the potential between -0.99 V and -1.05 V vs. Ag/AgCl. The lattice mismatch between the layers deposited at the two potentials is 0.19%. These superlattices grew epitaxially with a {111} orientation on Au(111). The epitaxial relationships for the major (antiparallel) and minor (parallel) domains are  $[Zn_aFe_bO_c(111)[01\bar{1}]]//Zn_dFe_eO_f(111)[01\bar{1}]]_{100} // Au(111)[0\bar{1}1]$  and  $[Zn_aFe_bO_c(111)[0\bar{1}1]]//Zn_dFe_eO_f(111)[0\bar{1}1]]_{100} // Au(111)[0\bar{1}1]$ , respectively. The (444) reflections of the zinc ferrite superlattices are shown in Fig. 3B with a modulation wavelength ranging from 12.5 to 29.2 nm. A cross-sectional focused ion beam (FIB) image in Fig. 3C shows the compositional modulation of a zinc ferrite superlattice with a

measured bilayer thickness of 78 nm, consistent with the layers depositing with an 88% Faradaic efficiency.

Electrodeposition has several advantages over the traditional vacuum techniques used in most superlattice studies (3). In addition to its cost-effectiveness, electrodeposition uses low processing temperatures which should minimize interdiffusion of the layers in the superlattice. Superlattices are produced within minutes from a single deposition bath as the lattice parameter and composition are controlled by the potential or current applied and the deposition rate is monitored by the charge passed. The low temperature and reduction potentials should allow for the deposition of these superlattices onto semiconductors for transition into electronics (12). The electrochemical fabrication of superlattices based on magnetite/zinc ferrite systems and the future production of other metal ferrites and their superlattices have the potential to become devices for microwave, entertainment, power, and magnetic applications (31).

## REFERENCES

1. M. Hong, S. Wolf, D.C. Gubser, Eds. *Metallic Multilayers and Epitaxy* (Metallurgical Society, USA, 1988).
2. L. L. Chang, B. C. Giessen., Eds. *Synthetic Modulated Structures* (Academic, Orlando, 1985).
3. J. A. Switzer, in *Electrochemistry of Nanomaterials*, G. Hodes, Ed. (Wiley-VCH, Weinheim, 2001) chap. 3.
4. J. A. Switzer, C.-J. Hung, B. E. Breyfogle, M. G. Shumsky, R. Van Leeuwen, T. D. Golden, "Electrodeposited Defect Chemistry Superlattices" *Science* **264**, 1573-1576 (1994).
5. J. A. Switzer, M. J. Shane, R. J. Phillips, "Electrodeposited Ceramic Superlattices" *Science* **247**, 444-446 (1990).
6. J. A. Switzer, R. P. Raffaele, R. J. Phillips, C.-J. Hung, T. D. Golden, "Scanning Tunneling Microscopy of Electrodeposited Ceramic Superlattices" *Science* **258**, 1918-1921 (1992).
7. H. M. Kothari, A. A. Vertegel, E. W. Bohannon, J. A. Switzer, "Epitaxial Electrodeposition of Pb-Tl-O Superlattices on Single-Crystal Au(100)" *Chem. Mater.* **14**, 2750-2756 (2002).
8. D. S. Lashmore and M. P. Dariel, "Electrodeposited Cu-Ni Textured Superlattices," *J. Electrochem. Soc.* **135**, 1218-1221 (1988).
9. C. A. Ross, L. M. Goldman, and F. Spaepen, "An Electrodeposition Technique for Producing Multilayers of Nickel-Phosphorous and Other Alloys," *J. Electrochem. Soc.* **140**, 91-98 (1993).
10. T. P. Moffat, "Electrochemical Production of Single-Crystal Cu-Ni Strained-Layer Superlattices on Cu(100)," *J. Electrochem. Soc.* **142**, 3767-3770 (1995).
11. M. Alper, W. Schwarzacher, and S. J. Lane, "The Effect of pH Changes on the Giant Magnetoresistance of Electrodeposited Superlattices," *J. Electrochem. Soc.* **144**, 2346-2352 (1997).
12. W. Schwarzacher, D. S. Lashmore, "Giant Magnetoresistance in Electrodeposited Films," *IEEE Trans. Magn.* **32**, 3133-3153 (1996).
13. R. Vaidyanathan, S. M. Cox, U. Happek, D. Banga, M. K. Mathe, and J. L. Stickney, "Preliminary Studies in the Electrodeposition of PbSe/Pb/Te Superlattice Thin Films via Electrochemical Atomic Layer Deposition (ALD)," *Langmuir* **22**, 10590-10595 (2006).

14. G. A. Prinz, "Magnetoelectronics" *Science* **282**, 1660-1663 (1998).
15. S. A. Wolf, D. D. Awschalom, R. A. Buhrman, J. M. Daughton, S. von Molnár, M. L. Roukes, A. Y. Chtchelkanova, D. M. Treger, "Spintronics: A Spin-Based Electronics Vision for the Future" *Science* **294**, 1488-1495 (2001).
16. J. L. Kirshvink, D. S. Jones, B. J. MacFadden, Eds. *Magnetite Biomineralization and Magnetoreception in Organisms: A New Biomagnetism* (Plenum, New York, 1985).
17. R. Wiltschko, W. Wiltschko, *Magnetic Orientation in Animals* (Springer, New York, 1995).
18. S. Johnsen, K. J. Lohmann, "Magnetoreception in Animals" *Phys. Today* **61**, 29-35 (2008).
19. A. Yanase, K. Siratori, "Band Structure in High Temperature Phase of  $\text{Fe}_3\text{O}_4$ " *J. Phys. Soc. Japan* **53**, 312-317 (1984).
20. Z. Zhang, S. Satpathy, "Electron States, Magnetism, and the Verwey Transition in Magnetite" *Phys. Rev. B* **44**, 13319-13331 (1991).
21. H. M. Kothari, E. A. Kulp, S. J. Limmer, P. Poizot, E. W. Bohannon, J. A. Switzer, "Electrochemical Deposition and Characterization of  $\text{Fe}_3\text{O}_4$  Films Produced by the Reduction of Fe(III)-Triethanolamine" *J. Mater. Res.* **21**, 293-301 (2006).
22. G. T. Rado, J. M. Ferrari, "Electric Field Dependence of the Magnetic Anisotropy Energy in Magnetite ( $\text{Fe}_3\text{O}_4$ )" *Phys. Rev. B* **12**, 5166-5174 (1975).
23. G. T. Rado, J. M. Ferrari, "Linear and Bilinear Magnetoelectronic Effects in Magnetically Biased Magnetite ( $\text{Fe}_3\text{O}_4$ )" *Phys. Rev. B* **15**, 290-297 (1979).
24. Y. Miyamoto, S. Chikazumi, "Crystal Symmetry of Magnetite in Low Temperature Phase Deduced from Magnetoelectronic Measurements" *J. Phys. Soc. Japan* **57**, 2040-2050 (1988).
25. Y. Miyamoto, S. Ishihara, T. Hirano, M. Takada, N. Suzuki, "Ferroelectricity of Magnetite ( $\text{Fe}_3\text{O}_4$ ) Observed by Means of Magnetoelectric Effect" *Solid State Commun.* **89**, 51-54 (1994).
26. S. Lee, A. Fursina, J. T. Mayo, C. T. Yavuz, V. L. Colvin, R. G. S. Sofin, I. V. Shvets, D. Natelson, "Electrically Driven Phase Transition in Magnetite Nanostructures" *Nature Materials* **7**, 130-133 (2008).

27. J. van den Brink, D. I. Khomskii, "Multiferroicity Due to Charge Ordering" *J. Phys.: Condens. Matter* **20**, 434217/1-434217/12 (2008).
28. S.-W. Cheong, M. Mostovoy, "Multiferroics: A Magnetic Twist for Ferroelectricity" *Nature Mater.* **6**, 13-20 (2007).
29. H. Béa, M. Gajek, M. Bibes, A. Barthélémy, "Spintronics with Multiferroics" *J. Phys.: Condens. Matter* **20**, 434221/1-434217/11 (2008).
30. A. J. Bard, L. R. Faulkner, *Electrochemical Methods: Fundamentals and Applications* (Wiley, New York, ed. 2, 2001), pp. 340.
31. A. Goldman, *Modern Ferrite Technology* (Springer, New York, ed. 2, 2006).
32. E. W. Gorter, "Magnetization in Ferrites: Saturation Magnetization of Ferrites with Spinel Structure" *Nature* **165**, 798-800 (1950).
33. This work was supported by the Department of Energy (DE-FG02-08ER46518).

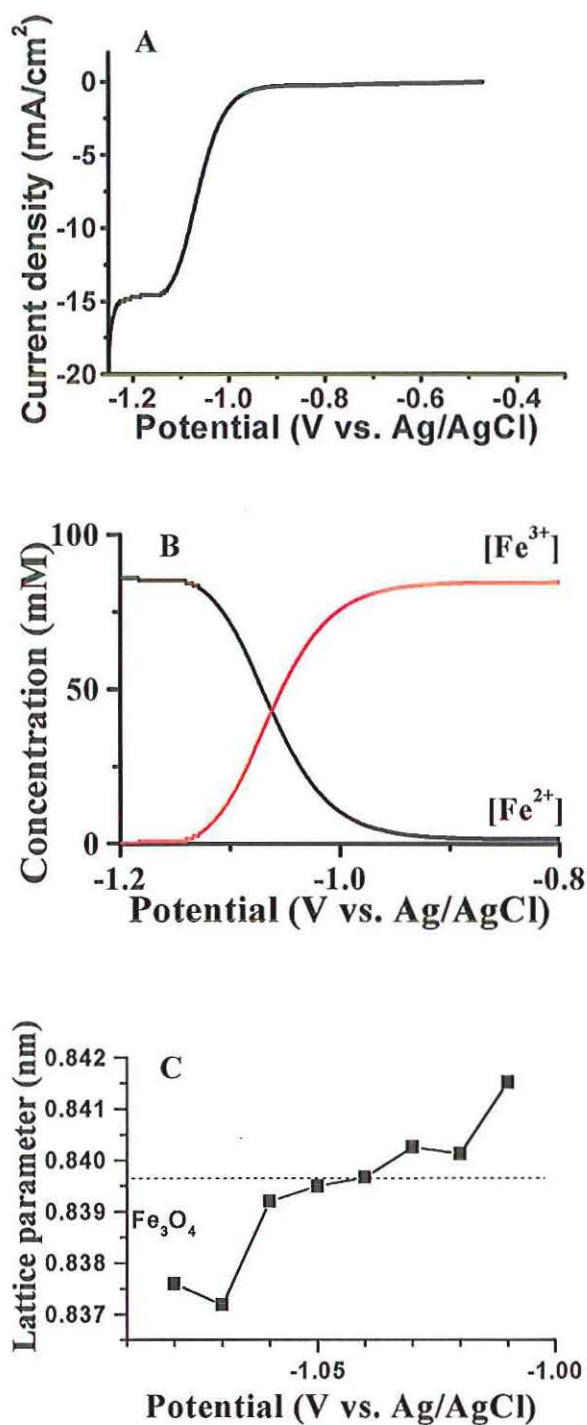


Fig. 1. (A) Linear sweep voltammogram of the alkaline Fe(III)-TEA deposition solution at 80°C scanned at 50 mV/s on a gold rotating disk electrode at 100 rpm. (B) Plot of the concentrations of Fe(III) and Fe(II) at the electrode surface as a function of potential. (C) Plot of the lattice parameters of the magnetite as a function of applied potential.

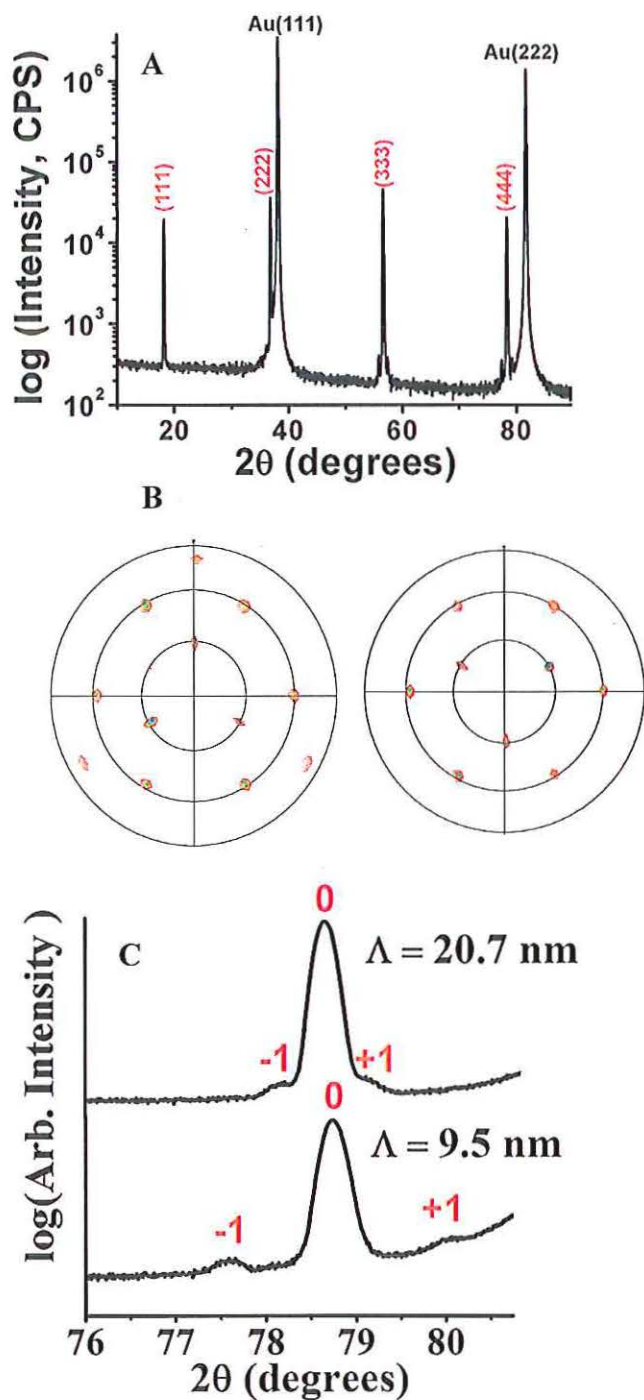


Fig. 2. (A) X-ray diffraction pattern for the  $\{111\}$  oriented magnetite superlattice on Au(111). (B) (311) pole figures of magnetite superlattice (left) and Au (right). (444) peaks of magnetite (C) superlattices from the x-ray diffraction patterns with a range of modulation wavelengths. Magnetite superlattices (C) were produced by pulsing between -1.01 V and -1.05 V vs. Ag/AgCl in an alkaline Fe(III)-TEA bath with modulation wavelength of 20.7 (top) and 9.5 nm (bottom).

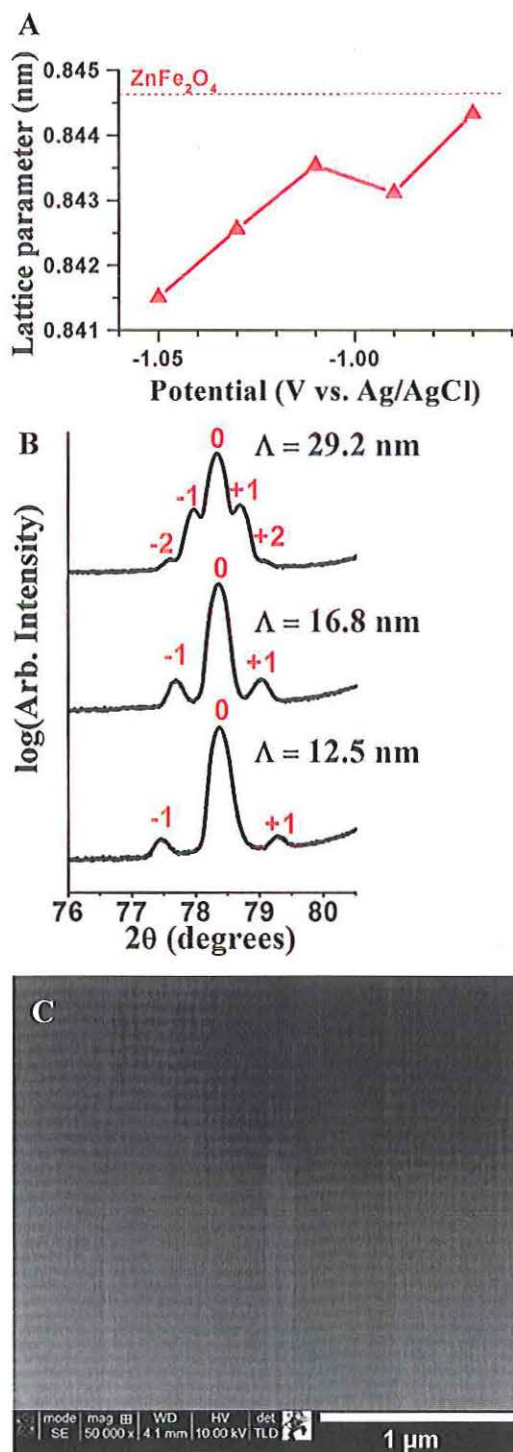


Fig. 3. (A) Plot of the lattice parameters of the zinc ferrite as a function of potential. (B) Zinc ferrite superlattices were electrodeposited by pulsing between -0.99 V and -1.05 V vs. Ag/AgCl from an alkaline Zn(II)—Fe(III)—TEA deposition bath with modulation wavelengths of 29.2 (top), 16.8 (middle), and 12.5 nm (bottom). (C) FIB image of a zinc ferrite superlattice showing a modulation wavelength of 78 nm.

Table I. Comparison of compositions of zinc ferrite films as a function of applied potential measured from energy dispersive spectroscopy and calculated from the linear sweep voltammetry.

Applied potential (V vs. Ag/AgCl)	Ratio of Zn/Fe from EDS	Measured Composition	Surface [Fe <sup>2+</sup> ] from LSV (mM)	Calculated Composition
-0.97	0.47	Zn <sub>0.96</sub> Fe <sub>2.04</sub> O <sub>4</sub>	5	Zn <sub>0.86</sub> Fe <sub>2.14</sub> O <sub>4</sub>
-0.99	0.39	Zn <sub>0.84</sub> Fe <sub>2.16</sub> O <sub>4</sub>	8	Zn <sub>0.79</sub> Fe <sub>2.21</sub> O <sub>4</sub>
-1.01	0.32	Zn <sub>0.72</sub> Fe <sub>2.28</sub> O <sub>4</sub>	14	Zn <sub>0.68</sub> Fe <sub>2.32</sub> O <sub>4</sub>
-1.03	0.27	Zn <sub>0.63</sub> Fe <sub>2.37</sub> O <sub>4</sub>	22	Zn <sub>0.58</sub> Fe <sub>2.42</sub> O <sub>4</sub>
-1.05	0.25	Zn <sub>0.60</sub> Fe <sub>2.40</sub> O <sub>4</sub>	34	Zn <sub>0.47</sub> Fe <sub>2.53</sub> O <sub>4</sub>

#### IV. Enantiospecific Electrodeposition of Chiral CuO Films from Copper(II) Complexes of Tartaric and Amino Acids on Single-Crystal Au(001)

*Hiten M. Kothari, Elizabeth A. Kulp, Sansanee Boonsalee, Maxim P. Nikiforov, Eric W. Bohannon, Philippe Poizot, Shuji Nakanishi, Jay A. Switzer\**

Department of Chemistry and Graduate Center for Materials Research, University of Missouri-Rolla, Rolla, Missouri 65409-1170, USA

AUTHOR EMAIL ADDRESS (jswitzer@umr.edu)

#### ABSTRACT

Chiral films of CuO have been electrochemically deposited onto achiral Au(001) using chiral precursors such as tartaric acid and the amino acids alanine, valine, and glycine to complex the Cu(II). The chirality of the electrodeposited films was dictated by the chiral solution precursor. X-ray diffraction pole figures and azimuthal scans, in conjunction with stereographic projections, were used to determine the absolute configuration and enantiomeric excess of the chiral CuO films. CuO films grown from L-tartaric acid have a  $(1\bar{1}\bar{1})$  orientation with an enantiomeric excess of 95%, while the films grown from D-tartaric acid have a  $(\bar{1}11)$  orientation with an enantiomeric excess of 93%. Films of CuO grown from chiral amino acids have two chiral orientations, each showing lower enantiomeric excess compared with the films deposited from tartaric acid. The films grown from L-alanine and L-valine solution have a small excess of the  $(\bar{1}11)$  and  $(\bar{1}\bar{1}\bar{1})$  orientations, while the films grown from D-alanine and D-valine have a small excess of  $(1\bar{1}\bar{1})$  and  $(111)$ .

## INTRODUCTION

Chiral molecules are ubiquitous in the living world. Enantiomeric forms of chiral molecules differ from each other only in that they are nonsuperimposable mirror images of one another. Because one enantiomer may be useful while the other toxic, the pharmaceutical industry is interested in devising processes to obtain enantiomerically pure forms of drugs and their precursors.<sup>1</sup> Traditionally, the industry has relied on using homogeneous solution-based catalysis or enzymatic reactions to carry out enantiospecific syntheses. Replacing homogeneous processes with heterogeneous processes could lead to improved process and cost efficiency.<sup>2</sup> Chiral surfaces may also be used to produce chiral sensors.

Efforts to develop enantiospecific heterogeneous catalytic systems have relied on breaking the symmetry of a metal surface by irreversibly adsorbing chiral molecules. A Raney Ni surface modified by adsorbing (*R,R*)-tartaric acid has been used to catalyze the hydrogenation of  $\beta$ -ketoesters, producing the R-product with over 90% enantiomeric excess (ee), while the surface modified with (*S,S*)-tartaric acid selectively produces the S-product.<sup>3</sup> Another example is the Orito<sup>4</sup> reaction, in which hydrogenation of  $\alpha$ -ketoesters over alumina supported platinum catalysts modified with chiral cinchonidine yields enantioselective products. Experimental and theoretical efforts to elucidate the mechanism for chiral recognition remain a topic of active research. Baiker<sup>5</sup> and McBreen<sup>6</sup> attribute the selectivity to a hydrogen bond between the cinchonidine and ketoester, while Sun and Houk<sup>7</sup> suggest that the formation of a covalent bond between the amine group of the cinchonidine with the carbonyl group of the ketone gives the observed selectivity. Separation of chiral molecules using chromatographic techniques

also relies on the extent of interaction between the enantiomeric forms with a chirally modified stationary phase.<sup>8,9</sup>

The durability of these adsorbed modifiers is a serious concern for practical applications. An alternative to the adsorption approach would be to develop surfaces that are intrinsically chiral. McFadden *et al.*<sup>10</sup> proposed one such approach, where high-index surfaces of FCC metals were shown to be chiral. They showed that even for a material with a highly symmetric space group, high-index surfaces could be chiral. The chirality is attributed to the presence of kink sites on these surfaces, and rules to identify and label these surfaces have been proposed.<sup>11,12</sup> Enantiospecific adsorption of chiral molecules on the Pt(643) surface was reported by Scholl *et al.*<sup>13</sup> using Monte Carlo simulations while experimental evidence of chiral recognition was reported by Attard *et al.*<sup>11,14</sup>, who showed enantiospecific electrooxidation of glucose in aqueous solutions on Pt(643) and Pt( $\overline{643}$ ) surfaces.

Our approach to the development of new chiral heterogeneous catalysts and sensors is to deposit chiral metal oxides films on achiral substrates. Recently, our group demonstrated that thin chiral films of CuO can be electrodeposited on Au(001)<sup>15</sup> and Cu(111)<sup>16</sup> single crystals using a simple and relatively inexpensive method. As is the case with fcc metals, it was observed that although the bulk crystal structure for CuO is centrosymmetric, the crystallographic orientation of the deposited film is chiral. The chirality of the electrodeposited film in the alkaline bath was determined by the enantiomer of tartrate used to complex Cu(II). Here we present details on the electrodeposition of chiral CuO films onto Au(001) from solutions using tartaric acid to direct the chirality. In particular, we show how x-ray diffraction pole figures and

azimuthal scans can be used to determine the absolute configuration and enantiomeric excess of the chiral films. We also contrast these results to CuO films deposited onto Au(001) using Cu(II) complexes of the amino acids alanine, valine and glycine as precursors for the deposition bath.

## EXPERIMENTAL SECTION

Electrochemical experiments were carried out using an EG&G Princeton Applied Research (PAR) model 273A potentiostat/galvanostat. The cell consisted of a platinum counter electrode and a standard calomel reference electrode (SCE). An Au(001) single crystal purchased from Monocrystal Company having a diameter of 10 mm and a thickness of 2 mm was used as a working electrode. A gold wire fitted around the single crystal served as an electrical contact to the working electrode. The working electrode was placed in solution using the meniscus method. The Au(001) single crystal was electropolished and annealed in a hydrogen flame prior to deposition. Electropolishing was carried out anodically, at a constant current density of  $1.5 \text{ A/cm}^2$  in a moderately stirred solution of 50 vol. % ethanol, 25 vol. % ethylene glycol, and 25 vol. % concentrated HCl at  $55^\circ\text{C}$ .

### Case 1: Deposition using tartaric acid

Thin films of CuO were deposited on Au(001) single crystals from an alkaline solution of copper(II) complexed with tartaric acid.<sup>15,16,18</sup> The concentrations in the deposition bath were 0.2 M Cu(II), 0.2 M tartaric acid and 3 M NaOH. Films were deposited on the Au(001) single crystal at a constant anodic current density of  $1 \text{ mA/cm}^2$

at 30°C for 30 minutes giving an approximate thickness of 300 nm. L-tartaric acid [(*R,R*)-(+)-tartaric acid], D-tartaric acid [(*S,S*)-(-)-tartaric acid] and DL-tartaric acid were purchased from Aldrich. The single enantiomers had an optical purity of  $\geq 99\%$  ee. The enantiomers were used without further purification.

#### Case 2: Deposition using amino acids

The solutions for deposition from amino acids were prepared by complexing  $\text{CuSO}_4$  with an excess amount of amino acid in base. The solution for depositing CuO from amino acids in this article was first reported by Ogura *et al.*<sup>17</sup>, and consisted of 50 mM amino acid, 5 mM Cu(II), and 0.2 M NaOH. The amino acids studied were achiral glycine and the L-, D-, and racemic forms of alanine and valine. Glycine with 98.5+% chemical purity was purchased from Aldrich. The L- and D-amino acids were purchased from Fluka with  $\geq 99.5\%$  and  $\geq 99\%$  chemical purity, respectively. The racemic amino acid solutions were made using equal amounts of the L- and D-amino acids. Films were deposited on Au(001) single crystal at a constant anodic current density of  $100 \mu\text{A}/\text{cm}^2$  at 30°C for 5 minutes.<sup>17</sup>

#### X-ray Diffraction Measurements

X-ray diffraction measurements were performed with a high-resolution Philips X'Pert MRD diffractometer. For the Bragg-Brentano scan the primary optics module was a combination Göbel mirror and a 2-crystal Ge(220) 2-bounce hybrid monochromator, and the secondary optics module was a  $0.18^\circ$  parallel plate collimator. The hybrid monochromator produces pure  $\text{Cu } k_{\alpha_1}$  radiation ( $\lambda = 0.1540562 \text{ nm}$ ) with a divergence of

25 arc seconds. Pole figures were obtained in point-focus mode using a crossed-slit collimator as the primary optics and a flat graphite monochromator as the secondary optics. Stereographic projections were generated using Desktop Microscopy software (version 2.1) on an Apple Macintosh computer.

### Electrochemical Selectivity

Electrochemical selectivity experiments to confirm the chirality of the electrodeposited CuO film were carried out in an aqueous solution of 0.1 M NaOH containing 5 mM L-tartaric acid or D-tartaric acid. The cyclic voltammograms (CV) were obtained in unstirred solutions at a scan rate of 10 mV/sec. The electrode was cleaned by scanning from the open circuit potential (OCP) to 0.75V vs. SCE in 0.1 M NaOH before changing solutions to remove remnants from the previous solution adsorbed on the electrode. The geometric area of the CuO film was controlled by mounting the electrode in a home-made Teflon cell holder.

## RESULTS AND DISCUSSION

CuO has a monoclinic structure with a centrosymmetric space group,  $C2/c$ .<sup>19-21</sup> Figure 1 shows two unit cells of monoclinic CuO with red atoms representing Cu and gray atoms representing O. The figure shows that each Cu atom is coordinated to four O atoms to form a distorted square-planar geometry. A unit cell contains two Cu atoms, each coordinated to four oxygen atoms to form a parallelogram parallel to the  $[110]$  and  $[\bar{1}\bar{1}0]$  directions. Figure 1 shows the parallelogram along the  $[110]$  direction in light gray while the parallelogram parallel to  $[\bar{1}\bar{1}0]$  direction is shown in dark gray. The Cu-O

bond distances are 0.1959 nm and 0.1957 nm and the O-Cu-O bond angles are  $84.3^\circ$  and  $95.7^\circ$ . Similarly, each O atom is coordinated to four Cu atoms resulting in a distorted tetrahedron (not shown in the figure). High-resolution powder diffraction studies on various CuO samples shows broadening and asymmetry in peak shapes. The asymmetry has been attributed to non-stoichiometry due to cation vacancies, possibly resulting in the change of bond length or angle.<sup>20</sup> In a recent high resolution X-ray diffraction study on single crystal CuO by Åsbrink<sup>22</sup>, the pattern is better fit by the noncentrosymmetric space group *Cc*.<sup>22</sup> The contrast is attributed to a more stoichiometric CuO having less cation deficiencies. Consistent with previous reports from our group and other studies on CuO, the centrosymmetric space group, *C2/c* is used for generating the stereographic projections to explain the pole figures.

#### Deposition from Tartaric Acid

Epitaxial films of CuO have been reported on MgO substrates under high vacuum and high temperature conditions using MBE<sup>23</sup> and MOCVD<sup>24</sup>. Polycrystalline films of CuO have been electrodeposited at room temperature on Au and Pt in alkaline solution using amino acids<sup>17</sup> to complex the Cu(II). Our group has previously reported electrodeposition of CuO on polycrystalline substrates using L-tartaric acid<sup>18</sup> as a complexing agent. We measured lattice parameters for CuO powder obtained from several films using Rietveld analysis with space group *C2/c*. The values reported were  $a = 0.4685$  nm,  $b = 0.3430$  nm,  $c = 0.5139$  nm,  $\beta = 99.08^\circ$  and  $\alpha = \gamma = 90^\circ$ . The thickness of the film deposited for 1200 sec at  $1\text{mA}/\text{cm}^2$  calculated by monitoring the frequency change on the Au electrochemical quartz crystal microbalance (EQCM) electrode (area =

$0.2 \text{ cm}^2$ ) as a function of time is 180 nm. The thickness measured by the EQCM matches closely with the thickness of 200 nm obtained from a cross-sectional SEM image on the same electrode. In the EQCM measurement, the plot of frequency change vs. time is linear indicating that the deposited film does not inhibit further film formation. Since the number of electrons involved in the reaction is not known, no estimate of the current efficiency was determined.

Figure 2 shows a  $\theta$ - $2\theta$  X-ray diffraction scan for a 300 nm CuO film deposited on Au(001) at an anodic current density of  $1 \text{ mA/cm}^2$  for 1800 seconds at  $30^\circ\text{C}$  from a solution of Cu(II) complexed with L-tartaric acid.  $\theta$ - $2\theta$  X-ray diffraction scans probe the orientation of the film perpendicular to the substrate. Only the  $\{1\bar{1}\bar{1}\}$  set of peaks are seen in the figure indicating the presence of a  $(1\bar{1}\bar{1})$  texture for the electrodeposited film. The results obtained here represent diffraction from the entire volume of the film and not just the surface. The CuO film in Figure 2 has a strong peak at  $2\theta = 35.57^\circ$  ( $d = 0.2525 \text{ nm}$ ). Table 1 lists of set of planes that have the same  $d$ -spacings. Based on the listings in Table 1, the peak in the X-ray scan could be assigned as any one of the four orientations. The  $(1\bar{1}\bar{1})$ ,  $(\bar{1}11)$ ,  $(11\bar{1})$  and  $(\bar{1}\bar{1}1)$  planes have identical  $d$ -spacing of 0.2525 nm and it is impossible to distinguish between the orientations based on the  $\theta$ - $2\theta$  scans. The orientations can be assigned with the help of X-ray diffraction pole figures and stereographic projections. As discussed later, the films grown from a solution of L-tartaric acid have a  $\{1\bar{1}\bar{1}\}$  out of plane orientation, i.e.,  $\text{CuO}(1\bar{1}\bar{1})//\text{Au}(001)$ . Similar scans obtained for a film deposited from a solution of Cu(II) complexed with D-tartaric acid have a  $\{\bar{1}11\}$  out of plane orientation, i.e.,  $\text{CuO}(\bar{1}11)//\text{Au}(001)$ .

Figure 3a and 3b show the  $(1\bar{1}\bar{1})$  and  $(\bar{1}11)$  stereographic projections of monoclinic CuO. A stereographic projection is a two-dimensional graphical representation of the crystal symmetry and the interplanar angles. The radial direction is the tilt angle,  $\chi$ , of the sample while the azimuthal angle,  $\phi$ , is the rotation of the sample about its axis. The positions of CuO{111} planes are specified. In addition, the positions of CuO{100} are also specified because the CuO(200)  $d$ -spacing is similar to the CuO(111)  $d$ -spacing, and reflections from the CuO{100} planes will be simultaneously observed in a CuO(111) pole figure. Clearly evident is that the two images are non-superimposable mirror images. Figure 3a shows that for the  $(1\bar{1}\bar{1})$  orientation, reflections from the  $(1\bar{1}1)$  plane at tilt angle of  $57^\circ$ , i.e.,  $\chi = 57^\circ$ , and the  $(\bar{1}\bar{1}\bar{1})$  plane at tilt angle of  $63^\circ$ , i.e.,  $\chi = 63^\circ$ , are separated azimuthally by  $115^\circ$  rotated counter-clockwise, i.e.,  $\Delta\phi = -115^\circ$ . Figure 3b shows that for the  $(\bar{1}11)$  orientation, reflections from the  $(\bar{1}1\bar{1})$  plane at  $\chi = 57^\circ$  and the  $(111)$  plane at  $\chi = 63^\circ$  are separated azimuthally by  $115^\circ$  rotated clockwise, i.e.,  $\Delta\phi = +115^\circ$ . The calculated interplanar angles for these planes of interest are summarized in Table 2. Figure 3 shows that although the  $(1\bar{1}\bar{1})$  and the  $(\bar{1}11)$  planes have identical  $d$ -spacings they are not really equivalent in the sense that the mirror images of their stereographic projections are not superimposable. Analyzing the stereographic projections for the other two planes,  $(11\bar{1})$  and  $(\bar{1}\bar{1}1)$ , and comparing them with the stereographic projections of  $(1\bar{1}\bar{1})$  and  $(\bar{1}11)$  shows that CuO( $\bar{1}11$ ) and CuO( $11\bar{1}$ ) are equivalent and CuO( $1\bar{1}\bar{1}$ ) and CuO( $\bar{1}\bar{1}1$ ) are equivalent.

The in-plane orientation, or the orientation of the film parallel with the substrate, is confirmed by running x-ray diffraction pole figures. For chiral films, the x-ray pole

figures can be used to determine the absolute configuration of the film. Pole figures are obtained by selecting a reflection to probe while measuring the diffracted intensity as a function of sample tilt ( $\chi$ ) and rotation ( $\phi$ ). The sample is tilted from  $\chi = 0^\circ$  to  $\chi = 90^\circ$  and for each tilt angle the sample is rotated through azimuthal angles,  $\phi$ , of  $0^\circ$  to  $360^\circ$ . Generally, a reflection with highest intensity for a randomly-oriented powder is probed to get high diffracted intensity. The (111) plane with  $2\theta = 38.742^\circ$  ( $d = 0.23223$  nm) has the highest intensity for polycrystalline CuO and was probed in the pole figures. As discussed later in the text, the added advantage of using the (111)-pole figure is that it provides an internal reference in the form of Au(111) reflections for comparing different pole figures.

Figure 4 shows (111) pole figures for 300 nm thick CuO films deposited on Au(001) from a solution of (a) L-tartaric acid, (b) D-tartaric acid and (c) DL-tartaric acid. The radial direction is the tilt of the sample with the grid lines in the figure spaced  $30^\circ$  apart. The  $d$ -spacing of CuO(111) is very close to the  $d$ -spacing of Au(111), which results in the reflection of Au(111) peaks in the same pole figure. Similarly, the  $d$ -spacing of CuO(200) is very close to the  $d$ -spacing of CuO(111), so reflections from the CuO(100) planes should also be evident in the same pole figure. Although the  $2\theta$  is maximized to observe the reflection from CuO(111) planes, the final pole figure is actually a superposition of the CuO(111), Au(111) and CuO(100) pole figures.

The interplanar angle between the (100) and (111) planes in a cubic system is  $54.7^\circ$ . Thus, the four intense peaks at approximately  $\chi = 55^\circ$  result from  $\{111\}$  reflections of Au. The Au $\{111\}$  reflections at  $\chi = 55^\circ$ , spaced  $90^\circ$  apart azimuthally, are much more intense than the corresponding CuO $\{111\}$  reflections at  $\chi = 57^\circ$ . The peaks

at  $\chi = 63^\circ$  are due to the  $\text{CuO}\{111\}$  and  $\text{CuO}\{100\}$  planes. Since the (111)-type planes of CuO and Au overlap we conclude that CuO deposits without rotation on the Au surface. The epitaxial relationship consistent with this observation is  $\text{CuO}[110]//\text{Au}[110]$ . While the X-ray results do not provide information on the structure of the CuO-Au interface they do provide information regarding the orientation of the bulk film with respect to the substrate. If only one domain of CuO was deposited, then only three peaks would be observed in the pole figure. The  $\text{CuO}(1\bar{1}1)$  would be obscured by the  $\text{Au}(111)$  peak at  $\chi = 55^\circ$  while the intense  $\text{CuO}(\bar{1}\bar{1}\bar{1})$  and the less intense  $\text{CuO}(100)$  would be observed opposite one another at  $\chi = 63^\circ$ . The presence of four peaks of equal intensity at  $\chi = 63^\circ$  in Figure 4a and 4b at  $\Delta\phi = 90^\circ$  shows that there are four equivalent in-plane orientations, with the  $[110]$  direction of CuO coincident with the  $[110]$ ,  $[1\bar{1}0]$ ,  $[\bar{1}10]$  and  $[\bar{1}\bar{1}0]$  directions of Au. This is reasonable because the  $\text{Au}(001)$  surface is four-fold symmetric. The presence of four different domains was cross-checked by running  $\text{CuO}(20\bar{2})$  pole figures.

Based on the above analyses we can conclude that the film grown in L-tartaric acid has a  $\text{CuO}(1\bar{1}\bar{1})$  or  $\text{CuO}(\bar{1}\bar{1}1)$  orientation. We arbitrarily assign it as  $\text{CuO}(1\bar{1}\bar{1})$ . Similarly the film grown in D-tartaric acid has a  $\text{CuO}(\bar{1}11)$  or  $\text{CuO}(11\bar{1})$  orientation. The film is assigned a  $\text{CuO}(\bar{1}11)$  orientation. In our previous reports,<sup>15,16</sup> L-tartaric acid was incorrectly identified as (*S,S*)-(-)-tartaric acid while D-tartaric acid was incorrectly identified as (*R,R*)-(+)-tartaric acid. Thus, although the pole figures were correctly analyzed, the assignment of CuO orientations to the solution precursors should be reversed. The mistake with the nomenclature is rectified in this report. The films grown

from L-tartaric acid [(*R,R*)-(+)-tartaric acid] have a  $\text{CuO}(1\bar{1}\bar{1})$  orientation while the films grown from D-tartaric acid [(*S,S*)-(-)-tartaric acid] have a  $\text{CuO}(\bar{1}11)$  orientation. With the intense Au peaks at  $\chi = 55^\circ$  acting as an internal reference it is evident that Figure 4a and 4b are non-superimposable mirror images of each other. Therefore, the two orientations are enantiomorphs. Figure 4c shows that the film grown from a racemic mixture of tartaric acid has equal amounts of two enantiomeric orientations. This can be quantified in terms of the enantiometric excess of one orientation with respect to the other.

The enantiomeric excess of one orientation over the other can be determined from azimuthal scans probing the  $\text{CuO}$  (111)-type reflections at  $\chi = 63^\circ$ . Figure 5 show the azimuthal scan extracted from the (111) pole figures at  $\chi = 63^\circ$  and for the azimuthal angle,  $\phi$ , varying from  $60^\circ$  to  $120^\circ$ . Figure 5a shows the scan for a film deposited from L-tartaric acid solution having a preferred  $(1\bar{1}\bar{1})$  orientation. Figure 5b shows the scan for a film deposited from D-tartaric acid solution having a preferred  $(\bar{1}11)$  orientation. Figure 5c shows that the film from DL-tartaric acid has an equal amount of both orientations. The area under the peaks in blue and red represent  $(\bar{1}\bar{1}\bar{1})$  and (111) reflections, respectively. The film grown from L-tartaric acid has a higher diffracted intensity for  $(\bar{1}\bar{1}\bar{1})$  reflection while the film grown from D-tartaric acid has a higher diffracted intensity for (111) reflection. The film deposited from the racemic mixtures has approximately equal intensity for the  $(\bar{1}\bar{1}\bar{1})$  and (111) reflections. The percentage enantiomeric excess for the  $(1\bar{1}\bar{1})$  orientation can be calculated quantitatively from the area under all the peaks obtained at  $\chi = 63^\circ$  using the formula

$$ee = \left( \frac{A_{(1\bar{1}\bar{1})} - A_{(\bar{1}11)}}{A_{(1\bar{1}\bar{1})} + A_{(\bar{1}11)}} \right) * 100$$

The film deposited from L-tartaric acid has an enantiometric excess of 95 % while the film deposited from D-tartaric acid has an enantiometric excess of 93 %. The film from DL-tartaric acid has equal amounts of both the orientations and has essentially zero enantiomeric excess. Also evident in the scans is the low background intensity. The peak to background ratio of the measured intensities ( $I_{\text{peak}}/I_{\text{background}}$ ) in the azimuthal scans is a good indicator of the nature of the epitaxy. A material with a fiber texture has a  $I_{\text{peak}}/I_{\text{background}}$  of unity. The films grown from solutions of L-tartaric acid and D-tartaric acid have  $I_{\text{peak}}/I_{\text{background}}$  ratios of 92 and 99, respectively. The film grown from solution of DL-tartaric acid has a  $I_{\text{peak}}/I_{\text{background}}$  ratio of 56.

Figure 6 shows polyhedral models for CuO when the  $(1\bar{1}\bar{1})$  and  $(\bar{1}11)$  planes are oriented parallel to the plane of the paper. This figure illustrates that the two faces are nonsuperimposable mirror images of each other, i.e. they are chiral. The Cu atoms are represented in red while the oxygen atoms are represented in gray. Although CuO has an achiral space group, the  $(1\bar{1}\bar{1})$  and  $(\bar{1}11)$  faces are enantiomorphs because they lack a center of symmetry. The asymmetry is explained by the arrangements of Cu or oxygen atoms on ideally terminated surfaces.<sup>16</sup>

We have not been able to correlate the handedness of the electrodeposited films with their microstructure, as observed by scanning electron microscopy (SEM). Figure 7 shows the SEM images of films grown from L-tartaric acid, D-tartaric acid and DL-tartaric acid. All the images show a cross-hatch pattern on the surface. The individual crystallites have a rice grain structure but multiple domains of each orientation rotated

90° result in the cross-hatch morphology, with crystallites that are approximately 100 nm long and 25 nm wide. The SEM images of films from D-tartaric acid and L-tartaric acid seem similar, while the DL-tartaric acid film in addition to the cross-hatch features shows larger, more symmetric features which could result from the grains of two different orientations growing together.

Organic additives are known to influence the morphology of the electrodeposited films.<sup>25-27</sup> We have previously shown that varying the solution pH and deposition potential controls the texture of electrodeposited Cu<sub>2</sub>O films. Polycrystalline Cu<sub>2</sub>O films grown from a Cu(II)-lactate complex show a preferred [100] orientation at pH 9 while the preferred orientation changes to [111] at pH 12.<sup>28</sup> Epitaxial Cu<sub>2</sub>O films grown on Au(001)<sup>29</sup> and InP(001)<sup>30</sup> at pH 12 undergo a thermodynamic to kinetic transition as a function of deposition potential. Films grown at low overpotentials follow the orientation of the substrate, but they undergo a transition to a kinetically controlled orientation when deposited at high overpotentials. In the present work, we show that the orientation and hence the chirality of the deposited film can be controlled at the molecular level by choosing the complexing agent used to prepare the solution. The handedness of the film is directed by the chirality of the deposition solution. The Au(001) surface is highly symmetric and does not impart chirality to the film.

Organic additives are also known to cause face-selective crystallization of inorganic crystals in biosystems.<sup>31-35</sup> Biomineralization studies have shown the selective nucleation of inorganic biominerals to be caused by the geometric matching, electrostatic interactions and stereochemistry or a combination of these variables at the organic-inorganic interface.<sup>32</sup> Aizenberg *et al.* in recent studies of calcite nucleation on patterned

self assembled monolayers of alkanethiols on Au and Ag have shown controlled calcite nucleation dependent on the surface termination of the thiol group.<sup>34,35</sup> In the presence of chiral amino acids, Cody crystallized asymmetric crystals of gypsum even though the space group of gypsum is symmetric. Changing the solution precursor systematically changed the handedness of the crystallites.<sup>33</sup> In related studies, Tend<sup>36</sup> and Orme<sup>37</sup> recently crystallized chiral single crystals of calcite using chiral aspartic acid in the solution. They also observed the formation of chiral etch pits during calcite dissolution in the presence of aspartic acid. Changes in step-edge free energies of the crystallized nuclei are suggested as a possible cause for the observed asymmetry.

Chirality can be bestowed on the surface by templating or by imprinting.<sup>38</sup> Chiral imprinting results when the adsorbed chiral molecule irreversibly reconstructs the substrate. The chirality of the substrate will remain intact on removal of the adsorbed molecule.<sup>39,40</sup> Chiral templating is induced by adsorbing chiral molecules on achiral surfaces without surface reconstruction. Adsorption of chiral tartaric acid on low-index surfaces on Cu<sup>41</sup> and Ni<sup>42</sup> has been shown to break the symmetry of the underlying substrates. Raval *et al.* have shown that the adsorption of (*R-R*)-tartaric acid on Cu(110) surface creates long range order through chiral channels or holes across the Cu surface. The holes or channels lead the incoming molecules to bind with the underlying Cu atoms in a nonrandom stereo-geometry subsequently aiding the formation of enantioselective products. No reconstruction of the underlying Cu atoms was evident. In contrast to the results on Cu(110), the same group showed that the adsorption of (*R-R*)-tartaric acid bestows chirality to the Ni(110) surface by causing extended chiral reconstruction of the underlying Ni(110) substrate.

In our case of electrodeposited chiral CuO films, it would not be unreasonable to expect tartaric acid or copper-tartrate<sup>43</sup> complexes to adsorb on the Au(001) surface and break its symmetry. Complexes of Cu(II)-tartrate have a dimeric structure with a symmetry that is determined by the handedness of the tartrate ligand.<sup>43</sup> In our previous reports, the asymmetry has been attributed to the adsorption of chiral molecules on the Au surface. Surface reconstruction of the underlying Au substrate from the adsorbed molecules could be another cause for the asymmetry. The precise mechanism, however, is not known at this time. The presence of chiral modifiers is, however, necessary for the nucleation of chiral CuO domains. Once the film growth is initiated, the system is able to maintain the orientation regardless of the solution precursor. This is evident from the results in Figure 8. Here, a thin film of CuO was first deposited from a solution of L-tartaric acid for 30 minutes at 1 mA/cm<sup>2</sup>. The film was grown thick enough to obtain a uniform deposit across the surface and eliminate any substrate influence on subsequent deposit. Following the initial growth, the same electrode was used to grow a thicker film from the D-tartaric acid solution under similar deposition conditions for 30 minutes. Only the peaks from the CuO(1  $\bar{1}$   $\bar{1}$ ) orientation are evident in the pole figure shown in Figure 8a. The pole figure and the orientation are identical to the results shown in figure 4a. Similarly, the film grown from D-tartaric acid continues to grow with { $\bar{1}11$ } orientation after switching the deposition bath, as evident in Figure 8b.

X-ray pole figures confirm the chirality of the bulk films but provide no information on the chirality of the surface. One way to test the surface chirality is to study the enantiospecific electrooxidation of a chiral molecule in solution. Attard<sup>11</sup> has studied the electrochemical oxidation of sugars on chiral Pt surfaces, while Gellman *et*

*al.*<sup>44</sup> have used temperature-programmed desorption (TPD) to study enantioselective desorption of chiral molecules from chiral metal surfaces. CuO electrodes have been shown to be catalytic for the electrooxidation of carbohydrates, amino acids, and amines with picomole sensitivity.<sup>45-47</sup> Xie and Huber<sup>46</sup> proposed a complex mechanism in which the (CuO.analyte) complex bridges with the adjacent CuO•OH active site to form a cyclic intermediate. The oxidation of this cyclic intermediate is reported to be the rate-limiting step. Lower hydroxide concentration was expected to lower the catalytic efficiency. Labuda *et al.*<sup>48</sup> have reported increased sensitivity for the electrooxidation of amino acids with an increase in solution pH. Consistent with other studies, the electrochemical oxidation using chiral CuO films were carried out in a solution containing 5 mM tartaric acid in 0.1 M NaOH. The cyclic voltammograms (CV) were obtained in unstirred solutions by scanning from OCP to 0.75V vs. SCE at a scan rate of 10 mV/sec. Before switching solutions the electrode was cleaned by scanning in 0.1 M NaOH from the OCP to 0.75V vs. SCE to remove adsorbed remnants from the electrode. Figures 9a, 9b and 9c shows the cyclic voltammograms for the films grown in L-tartaric acid, D-tartaric acid and DL-tartaric acid solutions respectively in 0.1 M NaOH and 5 mM D-tartaric acid or 5 mM L-tartaric acid solution. The scan in 0.1 M NaOH is a baseline scan which shows the onset potential for oxidation of water on a CuO electrode. Oxidation of water on CuO electrode occurs at approximately 0.6V vs. SCE. Figure 9a shows that the film grown from L-tartaric acid selectively oxidizes L-tartaric acid over D-tartaric acid. Figure 9b shows that the film grown from D-tartaric acid selectively oxidizes D-tartaric acid over L-tartaric acid. Figure 9c is a control experiment demonstrating that an achiral film shows no selectivity for the electrooxidation of tartaric acid.

### Deposition from Amino Acids

Films of CuO can also be deposited from alkaline solutions using amino acids to complex Cu(II) instead of tartaric acid. Polycrystalline films of CuO have been deposited from a solution of 5 mM CuSO<sub>4</sub> with excess amino acids (50 mM) in 0.2 M NaOH.<sup>17</sup> The same solution with the amino acids alanine, valine, and glycine as complexing agents was used in the present study to deposit films on an Au(001) single crystal. Alanine and valine are chiral, while glycine is achiral. The films on Au(001) substrates were deposited at 100  $\mu\text{A}/\text{cm}^2$  for 5 minutes.

Figure 10 shows the  $\theta$ - $2\theta$  x-ray diffraction scan of a CuO film grown using L-alanine as a complexing agent. The peaks at  $2\theta = 35.57^\circ$  ( $d = 0.2524$  nm) and  $2\theta = 38.74^\circ$  ( $d = 0.2322$  nm) indicate the presence of  $\{\bar{1}11\}$  and  $\{\bar{1}\bar{1}\bar{1}\}$  out-of-plane orientations for the electrodeposited film. In contrast to the films grown from tartaric acid we see that two different orientations are evident in the x-ray diffraction scan. Table 2 lists of set of planes that have the same  $d$ -spacings. The  $(1\bar{1}\bar{1})$ ,  $(\bar{1}11)$ ,  $(11\bar{1})$  and  $(\bar{1}\bar{1}1)$  planes all have identical  $d$ -spacing of 0.2524 nm and it is impossible to distinguish between the orientations based on the  $\theta$ - $2\theta$  scans. Similarly, the  $(111)$ ,  $(\bar{1}\bar{1}\bar{1})$ ,  $(1\bar{1}1)$  and  $(\bar{1}1\bar{1})$  planes all have identical  $d$ -spacing of 0.2322 nm and it is impossible to distinguish between the orientations based on the  $\theta$ - $2\theta$  scans. Nearly identical  $\theta$ - $2\theta$  x-ray diffraction scans are obtained for CuO films on Au(001) grown using the other amino acids.

Figure 11a and 11b show the  $(\bar{1}11)$  and  $(1\bar{1}\bar{1})$  stereographic projections of monoclinic CuO while probing the (100) and (111)-type reflections. Figure 11a shows

that for the  $(\bar{1}11)$  orientation, reflections from the  $(\bar{1}\bar{1}\bar{1})$  plane at  $\chi = 57^\circ$  and the  $(111)$  plane at  $\chi = 63^\circ$  are separated azimuthally by  $115^\circ$  rotated clockwise, i.e.,  $\Delta\phi = +115^\circ$ . Figure 11b shows that for the  $(1\bar{1}\bar{1})$  orientation, reflections from  $(1\bar{1}\bar{1})$  plane at  $\chi = 57^\circ$  and  $(\bar{1}\bar{1}\bar{1})$  plane at  $\chi = 63^\circ$  are separated azimuthally by  $115^\circ$  rotated counter-clockwise, i.e.,  $\Delta\phi = -115^\circ$ . Figure 11a and 11b shows that the stereographic projections of the  $(1\bar{1}\bar{1})$  and  $(\bar{1}11)$  planes are nonsuperimposable mirror images of each other. Figure 11c and 11d show the  $(\bar{1}\bar{1}\bar{1})$  and  $(111)$  stereographic projections for monoclinic CuO while probing the  $(100)$  and  $(111)$ -type reflections. Figure 11c shows that for the  $(\bar{1}\bar{1}\bar{1})$  orientation, reflections from the  $(\bar{1}00)$  plane at  $\chi = 55^\circ$  and the  $(\bar{1}1\bar{1})$  plane at  $\chi = 85^\circ$  are separated azimuthally by  $49^\circ$  rotated counter-clockwise, i.e.,  $\Delta\phi = -49^\circ$ . Figure 11d shows that for the  $(111)$  orientation, reflections from the  $(100)$  plane at  $\chi = 55^\circ$  and the  $(1\bar{1}\bar{1})$  plane at  $\chi = 85^\circ$  are separated azimuthally by  $49^\circ$  rotated clockwise, i.e.,  $\Delta\phi = +49^\circ$ . Figures 11c and 11d are nonsuperimposable mirror images of each other, i.e. the  $(\bar{1}\bar{1}\bar{1})$  and the  $(111)$  planes are enantiomers. The interplanar angles for these planes of interest are summarized in Table 3. This information is used to analyze the CuO(111) pole figure.

Figure 12 shows the stereographic projections for the (a)  $(1\bar{1}\bar{1})$ , (b)  $(\bar{1}11)$ , (c)  $(\bar{1}\bar{1}\bar{1})$  and (d)  $(111)$  orientations while probing the  $(10\bar{1})$ -type reflections for monoclinic CuO. The interplanar angles for these planes of interest are summarized in Table 3. In Figure 12(a) and 12(b), the peaks at  $\chi = 47^\circ$  are assigned to the  $\{10\bar{1}\}$  and  $\{\bar{1}01\}$  reflections for CuO( $\bar{1}11$ ) and CuO( $1\bar{1}\bar{1}$ ) orientations, respectively. Similarly, in Figure 12(c) and 12(d), the peaks at  $\chi = 86^\circ$  are assigned to the  $\{\bar{1}01\}$  and  $\{10\bar{1}\}$

reflections for  $\text{CuO}(\bar{1}\bar{1}\bar{1})$  and  $\text{CuO}(111)$  orientations, respectively. Figures 12a and 12d show that the  $(10\bar{1})$  reflection for the  $(\bar{1}11)$  orientation appears at  $\phi = 240^\circ$ , while the same reflection for the  $(111)$  orientation appears at  $\phi = 310^\circ$ . Similarly, Figure 12b and 12c shows that the  $(\bar{1}01)$  reflection for the  $(1\bar{1}\bar{1})$  and  $(\bar{1}\bar{1}\bar{1})$  orientations appear at  $\phi = 120^\circ$  and  $\phi = 50^\circ$  respectively.

Figures 13a and 13b show the  $\text{CuO}(111)$  and  $\text{CuO}(20\bar{2})$  pole figures for the film deposited from a L-alanine solution. As discussed earlier, the  $\text{CuO}(111)$  pole figure shown in Figures 13a is actually a superposition of  $\text{CuO}(111)$ ,  $\text{Au}(111)$  and  $\text{CuO}(100)$  pole figures. The reflections at  $\chi = 63^\circ$  from the domains due to the  $(\bar{1}11)$  and the  $(1\bar{1}\bar{1})$  orientations obtained from the amino acid solution give similar results to that obtained for the tartrate complexed films discussed earlier in the paper, albeit with substantially reduced enantioselectivity. The low intensity peaks to the left ( $\Delta\phi = -12.5^\circ$  from the nearest Au peak) and right ( $\Delta\phi = 12.5^\circ$  from the nearest Au peak) of the intense Au peaks at  $\chi \approx 55^\circ$ , result from the  $(100)$ -type reflections, as indicated by the stereographic projections shown in Figure 11c and 11d. Additional peaks at  $\chi \approx 85^\circ$  can be attributed to the reflection of  $(111)$ -type planes. The peaks at  $\Delta\phi = +115^\circ$  from the  $\text{Au}(111)$  peaks in Figure 13a are slightly more intense than the peaks at  $\Delta\phi = -115^\circ$  suggesting that the film grown from L-alanine solution has a slight excess of  $(\bar{1}11)$  orientation. In contrast to the films grown from pure L-tartaric acid or pure D-tartaric acid which have four equal intensity peaks at  $\chi = 63^\circ$ , the films grown from pure alanine enantiomers have eight peaks at  $\chi = 63^\circ$ . Although the  $(\bar{1}11)$  orientation is slightly preferred over the  $(1\bar{1}\bar{1})$ , the figure resembles the results obtained for DL-tartaric acid

films. This will be elucidated further later in the text. Similarly, the film grown from L-alanine solution seems to have a small preference for the  $(\bar{1}\bar{1}\bar{1})$  orientation but it is rather difficult to justify decisively based on the weak signal to noise ratio at high tilt angles and the overlapping of  $\{100\}$  reflections with the Au peaks at  $\chi = 55^\circ$ .

The (111) pole figure although very complicated is useful because it provides an internal reference in the form of Au peaks at  $\chi = 55^\circ$ , which aid in comparing and determining the chiral orientations in conjunction with the stereographic projections. A simpler pole figure is obtained by probing the  $\text{CuO}(20\bar{2})$  reflection. A  $\text{CuO}(20\bar{2})$  pole figure is run by fixing the  $2\theta$  to the  $d$ -spacing of the  $\text{CuO}(20\bar{2})$  reflection. The resulting pole figure shown in Figure 13b is simple compared with the  $\text{CuO}(111)$  pole figure but it fails to provide an internal reference to determine the precise chiral orientation. The Au[110] direction at  $\phi = 0^\circ$  is used as the reference. The peaks at  $\chi = 48^\circ$  and  $\chi = 86^\circ$  are due to the  $(10\bar{1})$ -type reflections for the four different orientations.

The analysis of the (111) pole figure can be verified by overlaying the stereographic projections for the four orientations in Figure 11. The resulting figure is shown in Figure 14a, assuming that only one domain of each orientation is deposited. But Au(001) is a four-fold symmetric surface so it is reasonable to expect four domains of each orientation being deposited on the surface. The resultant image with four domains of each orientation obtained by rotating Figure 14a by  $90^\circ$ ,  $180^\circ$  and  $270^\circ$  and overlaying them is shown in Figure 14b. The gray, green and red spots signify different domains obtained by rotating Figure 14a by  $90^\circ$ ,  $180^\circ$  and  $270^\circ$ , respectively. Identical analysis for the  $(20\bar{2})$  pole figure is shown in Figure 14c and 14d. The resultant figures shown in Figure 14b and 14d match the experimentally observed pole figures shown in Figure 13a

and 13b, respectively. The results of  $\text{CuO}(111)$  and  $\text{CuO}(20\bar{2})$  pole figures show that the film has four different chiral orientations with four domains of each orientation.

Figure 15 shows the  $\text{CuO}(20\bar{2})$  pole figures for various CuO films grown from solutions of (a) L-alanine, (b) D-alanine, (c) DL-alanine, (d) L-valine, (e) D-valine and (f) DL-valine. The pole figures show that the films grown from L-alanine and L-valine solution have a small excess of chiral  $(\bar{1}\bar{1}1)$  and  $(\bar{1}\bar{1}\bar{1})$  orientations compared to their mirror image counter-parts, the  $(1\bar{1}\bar{1})$  and  $(111)$  orientations, respectively. Similarly the films grown from D-alanine and D-valine have a small excess of  $(1\bar{1}\bar{1})$  and  $(111)$  compared to their mirror image counter-parts  $(\bar{1}11)$  and  $(\bar{1}\bar{1}\bar{1})$ , respectively. The films grown from racemic mixtures of alanine and valine show no enantiospecificity for any chiral orientations. Approximately equal distributions of the  $(\bar{1}11)$  and  $(1\bar{1}\bar{1})$  orientations and the  $(111)$  and  $(\bar{1}\bar{1}\bar{1})$  orientations are observed in the pole figures. Although not shown, pole figures obtained for films grown from achiral glycine as a complexing agent have equal amounts of the chiral  $\text{CuO}(\bar{1}11)$  and  $\text{CuO}(1\bar{1}\bar{1})$  orientations.

The enantiomeric excesses were determined from the azimuthal scans by probing the  $(111)$ -type reflections for the chiral orientations. The results obtained for films grown from tartaric acid and various amino acids are summarized in Table 4. In contrast to the films grown from pure L-tartaric acid and pure D-tartaric acid which have high ee for  $(1\bar{1}\bar{1})$  and  $(\bar{1}11)$  orientations respectively, the films grown from pure enantiomers of amino acids show lower ee for the two chiral orientations.

It was argued earlier in the article that the adsorption of the solution precursor on the  $\text{Au}(001)$  surface is an important factor governing the observed orientation. Although,

formation of extended surface chirality<sup>41,44</sup> is desired, it is not always the case. Studies on adsorption of organic molecules on surfaces have revealed formation of local chiral domains or local chiral imprinting without yielding extended surface chirality.<sup>40,49,50</sup> Energies for the adsorption of D- and L-glucose on chiral Pt(643) have been shown to differ by only 1.2 kJ/mole,<sup>51</sup> while the difference in the adsorption energies of two enantiomers of methylcyclohexanone on chiral Cu(643) surfaces have been shown to differ by only 0.9 kJ/mole.<sup>44</sup> Adsorption of (*R-R*)-tartaric acid on Cu(110) reconstructs the Cu surface to form two chiral domains differing in energies by 6 kJ/mole.<sup>42</sup> While a great deal of attention has focused on the adsorption of chiral amino acids on Cu<sup>52-53</sup> single crystals, similar studies on Au single crystals are limited. Adsorption of amino acids on Au<sup>54</sup> and Ag<sup>55</sup> surfaces are reported to be physical in nature,<sup>56</sup> while amino acids chemisorb on Cu single crystals. Cysteine is known to adsorb on Au,<sup>57</sup> but the high affinity of Au for sulfur groups is widely used to form self-assembled monolayers on gold.<sup>58</sup> Based on the argument that weak adsorption of amino acids on Au as compared to tartaric acid results in the formation of disoriented films, CuO films deposited on Cu single crystals from amino acid solution should be more ordered. Indeed, in unpublished work<sup>59</sup> we have shown that CuO films with just one chiral orientation are deposited on Cu(111) single crystals from identical amino acid solutions used in this study.

**Conclusion:**

Chiral films of CuO have been deposited on Au(001) single crystal surfaces from solutions of Cu(II) complexes of tartaric acid and the amino acids alanine, valine, and glycine in alkaline solution. The films from L-tartaric acid solution grow with a  $\{1\bar{1}\bar{1}\}$  orientation having an enantiomeric excess of 95% while the films grown from D-tartaric

acid solution have a  $\{\bar{1}11\}$  orientation with an enantiomeric excess of 93%. It is speculated that the adsorption of chiral solution precursors on to the Au(001) surface breaks the symmetry of the underlying surface ultimately aiding in the formation of chiral CuO films. In contrast to the films grown from Cu(II) complexes of tartaric acid which have only one chiral orientation with high enantiomeric excess the films grown from Cu(II) complexes of amino acids have two chiral orientation with a smaller enantiomeric excess. The films grown from L-alanine and L-valine solution have a small excess of  $(\bar{1}11)$  and  $(\bar{1}\bar{1}\bar{1})$  orientations, while the films grown from D-alanine and D-valine have a small excess of the  $(1\bar{1}\bar{1})$  and  $(111)$  orientations.

#### ACKNOWLEDGEMENTS

This work was supported by National Science Foundation grants CHE-0243424, CHE-0437346 DMR-0071365 and DMR-0076338, and Department of Energy grant DE-FC07-03ID14509.

## REFERENCES

- 1 Stinson, S. C.; *Chem. Eng. News* **2001**, 79(40), 79-97
- 2 Jacoby, M.; *Chem. Eng. News* **2004**, 82(11), 37-4
- 3 Izumi, Y.; *Adv. Catal.* **1994**, 32, 215
- 4 Orito, Y.; Imai, S.; Nyugen, G. *Synth. Org. Chem. Jpn.* **1979**, 37, 173
- 5 Bonalumi, N.; Burgi, T.; Baiker, A.; *J. Am. Chem. Soc.* **2003**, 125, 13342
- 6 Lavoie, S.; Laliberte, A.- M.; McBreen, H. P. *J. Am. Chem. Soc.* **2003**, 125, 13342
- 7 Vayner, G.; Houk, N. K.; Sun, K.- Y. *J. Am. Chem. Soc.* **2004**, 126, 199
- 8 Armstrong, D. W.; Tang, Y.; Chen, S. *Anal. Chem.* **1994**, 66, 1473
- 9 Armstrong, D. W.; Tang, Y.; Ward, T. *Anal. Chem.* **1993**, 65, 1114
- 10 McFadden, C. F.; Cremer, P.S.; Gellman, A. J.; *Langmuir* **1996**, 12, 2483
- 11 Attard, G. A. *J. Phys. Chem. B* **2001**, 105, 3158
- 12 Scholl, D. S.; Asthagiri, A.; Power, T. D. *J. Phys. Chem. B* **2001**, 105, 4771
- 13 Scholl, D. S. *Langmuir* **1998**, 14, 862
- 14 Ahmadi, A.; Attard, G.; Feliu, J.; Rodes, A. *Langmuir* **1999**, 15, 2420
- 15 Switzer, J. A.; Kothari, H. M.; Poizot, P., Nakanishi, S.; Bohannan, E. W. *Nature* **2003**, 425, 490
- 16 Bohannan, E. W.; Kothari, H. M.; Nicic, I. M.; Switzer, J. A. *J. Am. Chem. Soc.* **2004**, 126, 488
- 17 Nakaoka, K.; Ogura, K. *J. Electrochem. Soc.* **2002**, 149, C579
- 18 Poizot, P.; Hung, C.- J.; Nikiforov, M. P.; Bohannan, E. W.; Switzer, J. A. *Electrochem. Solid-State Lett.* **2003**, 6, C21
- 19 Åsbrink, S.; Norrby L.-J. *Acta Cryst.* **1970**, B26, 8
- 20 Langford, J. I.; Louër, D. *J. Appl. Cryst.* **1991**, 24, 149
- 21 Brese, N. E.; O'Keefe, M.; Ramakrishna, B. L.; Von Dreele, R. B. *J. Solid State Chem.* **1990**, 89, 184
- 22 Åsbrink, S.; Waśkowska, A. *J. Phys.: Condens. Matter* **1991**, 3, 8173

- 23 Catana, A.; Locquet, J.-P.; Paik, S. M.; Schuller, I. K. *Phys. Rev. B* **1992**, *46*, 15477
- 24 Watson, I.M.; Atwood, M. P.; Cumberbatch, T. J. *Thin Solid Films* **1994**, *251*, 51
- 25 Budevski, E.; Staikov, W.; Lorentz, W. J. *Electrochemical Phase Formation and Growth* VCH, New York, **1996**
- 26 Spyrellis, N.; Amblard, J.; Froment, M.; Maurin, G. *J. Microsc. Spectrosc. Electron* **1987**, *12*, 220
- 27 Paunovic, M.; Schlesinger, M. *Fundamentals of Electrochemical Deposition* (Wiley-Interscience, New York, 1998) 167-186
- 28 Golden, T. D.; Shumsky, M. G.; Zhou, G.-Y.; VanderWerf, R. A.; Van Leeuwen, R. A.; Switzer, J. A. *Chemistry of Materials* **1996**, *8*, 2499
- 29 Switzer, J. A.; Kothari, H. M.; Bohannon, E. W. *J. Phys. Chem. B* **2002**, *106*, 4027
- 30 Liu, R.; Oba, F.; Bohannon, E. W.; Ernst, F.; Switzer, J. A.; *Chemistry of Materials* **2003**, *15*, 4882
- 31 Addadi, L.; Weiner, S. *Proc. Natl. Acad. Sci. USA*. **1985**, *82*, 4110
- 32 Mann, S.; Archibald A. D.; Didymus J. M.; Douglas, T.; Heywood, B. R.; Meldrum, F.C.; Reeves, N. J.; *Science* **1993**, *261*, 1286
- 33 Cody, A. M.; Cody, R. D. *J. Cryst. Growth* **1991**, *113*, 508
- 34 Aizenberg, J.; Black, A. J.; Whitesides, G. M. *J. Am. Chem. Soc.* **1999**, *121*, 4500
- 35 Aizenberg, J.; Black, A. J.; Whitesides, G. M. *Nature* **1999**, *398*, 495
- 36 Teng, H. H.; Dove, P. M.; Orme, C. A.; DeYoreo, J. J. *Science* **1998**, *282*, 724
- 37 Orme, C. A.; Noy, A.; Wierzbicki, A.; McBribge, M. T.; Grantham, M.; Teng, H. H.; Dove, P. M.; DeYoreo, J. J. *Nature* **2001**, *411*, 775
- 38 Hovrath J. D.; Gellman, A. J. *Top. Catal.* **2003**, *25*, 9
- 39 Zhao, X.; *J. Am. Chem. Soc.* **2000**, *122*, 12584
- 40 Schunack, M.; Laegsgaard, E.; Stensgaard, I.; Johannsen, I.; Besenbacher, F. *Angew. Chem. Int. Ed.* **2001**, *40*, 2623
- 41 Lorenzo M. O.; Badelley, C. J.; Muryn, C.; Raval, R. *Nature*, **2000**, *404*, 376
- 42 Humblot, V.; Haq, S.; Muryn, C.; Hofer, W. A.; Raval, R. *J. Am. Chem. Soc.* **2002**, *124*, 503
- 43 Missavage, R. J.; Belford, R. L.; Paul, I. C. *J. Coord. Chem.* **1972**, *2*, 145

- 44 Gellman, A. J.; Hovrath, J. D.; Buelow, M. T. *J. Mol. Catal. A* **2001**, *167*, 3
- 45 Wels, B.; Johnson, D. C. *J. Electrochem. Soc.* **1990**, *137*, 2785
- 46 Xie, Y.; Huber, C. O. *Anal. Chem.* **1991**, *63*, 1714
- 47 Kano, K.; Torimura, M.; Esaka, Y.; Goto, M. *J. Electroanal. Chem.* **1994**, *372*, 137
- 48 Labuda, J.; Meister, A.; Gläser, P.; Werner, G. *Fresenius J. Anal. Chem.* **1998**, *360*, 654
- 49 Lopinski, G.P.; Moffat, D. J.; Wayner, D. M.; Wolkov, R. *Nature*, **1998**, *39*, 909
- 50 Vishwanathan, R.; Zazadzinski, J. A.; Schwartz, D. K. *Nature*, **1994**, *368*, 440
- 51 Attard, G. A.; Ahmadi, A.; Feliu, J.; Rodes, A.; Herrero, E.; Blais, S.; Jerkiewicz, G. *J. Phys. Chem. B* **1999**, *103*, 1381
- 52 Williams, J.; Haq, S.; Raval, R. *Surf. Sci.* **1996**, *368*, 303
- 53 Chen, Q.; Lee, C. W.; Frankel, D. J.; Richardson, N. V. *PhysChemComm*, **1999**, 9
- 54 Zhao, X.; Yan, H.; Zhao, R. G.; Yang, W. S. *Langmuir* **2002**, *18*, 3901
- 55 Zhao, X.; Yan, H.; Tu, X.; Zhao, R. G.; Yang, W. S. *Langmuir*, **2003**, *19*, 5542
- 56 Lange, W.; Jirikowsky, M.; Benninghoven, A. *Surf. Sci.* **1984**, *136*, 419
- 57 Di Felice, R.; Selloni, A.; Molinari, E. *J. Phys. Chem. B* **2003**, *107*, 1151
- 58 Ulman, A. *Chem. Rev.* **1996**, *96*, 1533
- 59 Bohannon, E. W.; Kothari, H. M.; Nicic, I. M.; Switzer, J. A. *Unpublished Work.*

Table 1: List of planes having identical d-spacing for monoclinic CuO.

$2\theta$ (degrees)	$d$ -spacing (nm)	Planes
35.570	0.25246	$(1\bar{1}\bar{1})$ , $(\bar{1}11)$ , $(11\bar{1})$ , $(\bar{1}\bar{1}1)$
38.742	0.23223	$(111)$ , $(\bar{1}\bar{1}\bar{1})$ , $(1\bar{1}1)$ , $(\bar{1}1\bar{1})$

Table 2: Calculated interplanar angles,  $\chi$ , between the observed orientation in the  $\theta$ - $2\theta$  X-ray diffraction scans and the CuO reflections probed in the pole figure.

Plane 1	Plane 2	$\chi^\circ$
$(1\bar{1}\bar{1})$	$(\bar{1}\bar{1}\bar{1})$	62.93
$(1\bar{1}\bar{1})$	$(1\bar{1}1)$	56.92
$(1\bar{1}\bar{1})$	$(100)$	62.44
$(\bar{1}11)$	$(111)$	62.93
$(\bar{1}11)$	$(\bar{1}\bar{1}\bar{1})$	56.92
$(\bar{1}11)$	$(\bar{1}00)$	62.44

Table 3: Calculated interplanar angles between the observed orientation in the  $\theta$ - $2\theta$  X-ray diffraction scans and the CuO reflections being probed in the pole figure.

Plane 1	Plane 2	$\chi^\circ$
( $\bar{1}11$ )	(111)	62.93
( $\bar{1}11$ )	( $\bar{1}\bar{1}\bar{1}$ )	56.92
( $\bar{1}11$ )	( $\bar{1}00$ )	62.44
( $\bar{1}11$ )	( $\bar{2}02$ )	47.53
( $\bar{1}\bar{1}\bar{1}$ )	( $\bar{1}\bar{1}\bar{1}$ )	85.44
( $\bar{1}\bar{1}\bar{1}$ )	( $\bar{1}00$ )	54.60
( $\bar{1}\bar{1}\bar{1}$ )	( $\bar{2}02$ )	86.15

Plane 1	Plane 2	$\chi^\circ$
( $1\bar{1}\bar{1}$ )	( $\bar{1}\bar{1}\bar{1}$ )	62.93
( $1\bar{1}\bar{1}$ )	( $1\bar{1}\bar{1}$ )	56.92
( $1\bar{1}\bar{1}$ )	(100)	62.44
( $1\bar{1}\bar{1}$ )	( $20\bar{2}$ )	47.53
(111)	( $1\bar{1}\bar{1}$ )	85.44
(111)	(100)	54.60
(111)	( $20\bar{2}$ )	86.15

Table 4: Enantiomeric excesses for CuO films grown from various solution precursors determined from the (111)-type reflections.

Solution Precursor	Major Orientation Type I (fraction)		Enantiomeric Excess Type I (%)	Major Orientation Type II (fraction)		Enantiomeric Excess Type II (%)
	(1 $\bar{1}\bar{1}$ )	( $\bar{1}11$ )		( $\bar{1}\bar{1}\bar{1}$ )	(111)	
L-tartaric acid	0.975	0.025	95	None	None	-
D-tartaric acid	0.032	0.968	93	None	None	-
DL-tartaric acid	0.50	0.50	0	None	None	
L-alanine	0.40	0.60	20	0.58	0.42	16
D-alanine	0.66	0.34	32	0.34	0.66	32
DL-alanine	0.49	0.51	2	0.50	0.50	0
L-valine	0.30	0.70	40	0.57	0.43	14
D-valine	0.76	0.24	52	0.38	0.62	24
DL-valine	0.50	0.50	0	0.51	0.49	2
Glycine	0.50	0.50	0	None	None	-

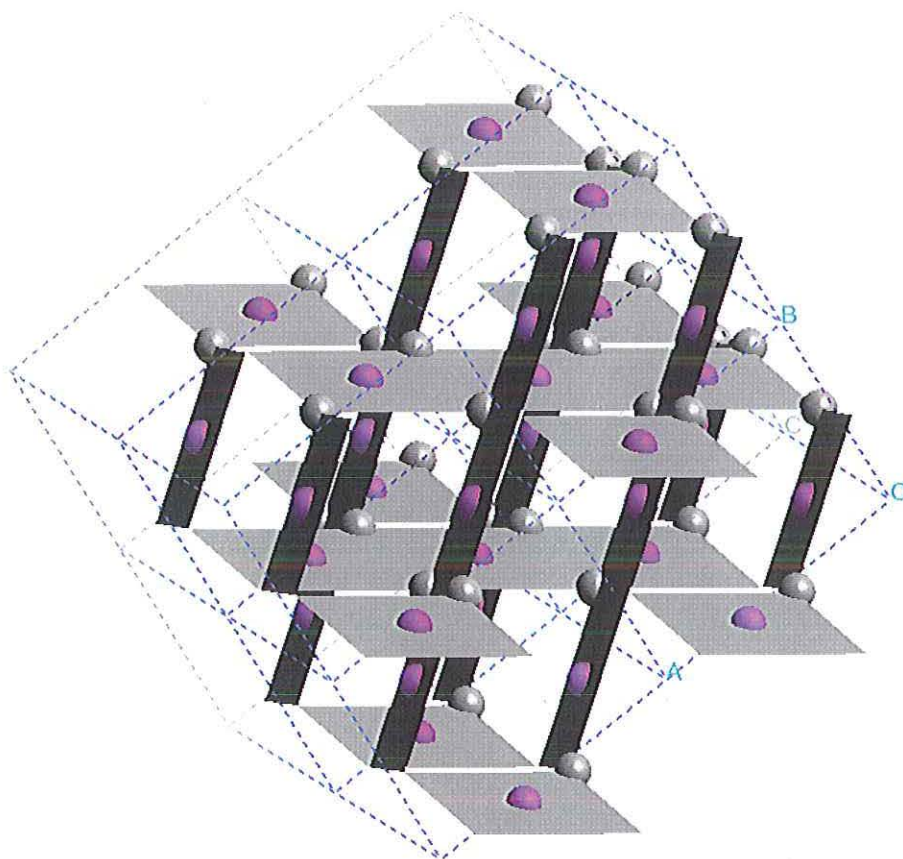


Figure 1: Structure of monoclinic CuO with space group  $C2/c$ . The Cu and O atoms are red and gray, respectively. The planes in light gray and dark gray show the Cu coordination with nearest O atoms along the  $[110]$  and  $[\bar{1}10]$  directions, respectively.

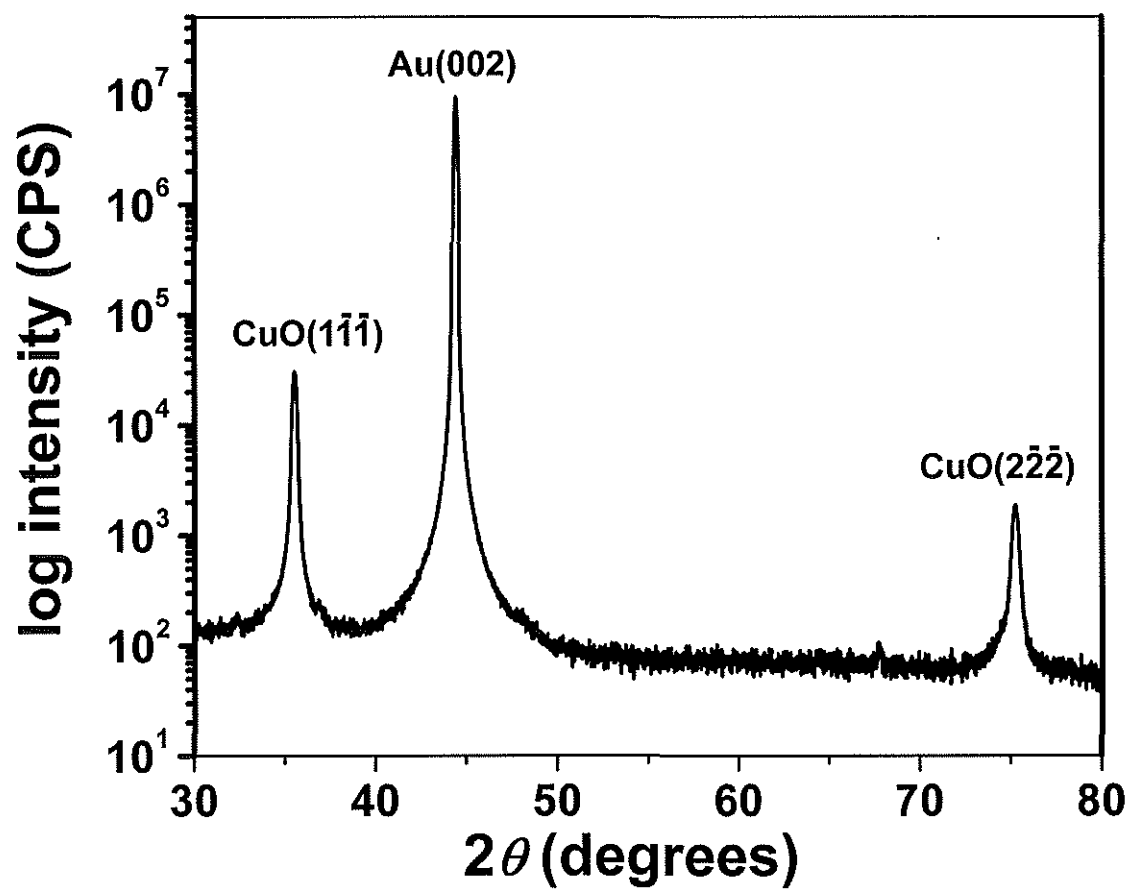


Figure 2: X-ray diffraction  $\theta$ - $2\theta$  scan for a 300 nm thick CuO film deposited on Au(001) from a solution of L-tartaric acid. Only the  $\{1\bar{1}\bar{1}\}$  planes are evident in the figure, indicating that the system has a CuO  $(1\bar{1}\bar{1})//\text{Au}(001)$  epitaxial relationship.

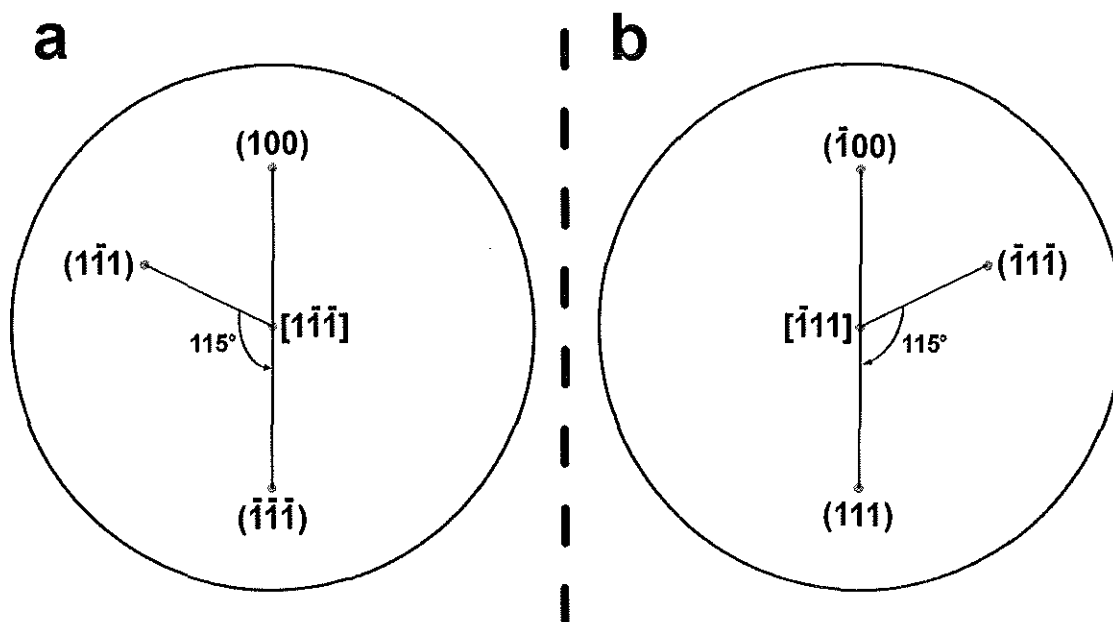


Figure 3: Stereographic projections for (a)  $(1\bar{1}\bar{1})$  and (b)  $(\bar{1}11)$  orientations indicating the positions where the (111)-type and the (100)-type reflections should be observed in the pole figures. The (100) and  $(\bar{1}00)$  reflections are shown, as the CuO(200)  $d$ -spacing is similar to the CuO(111)  $d$ -spacing, and reflections from the CuO(100) planes will be observed in a CuO(111) pole figure. For the  $(1\bar{1}\bar{1})$  orientation, reflections from the  $(1\bar{1}\bar{1})$  plane at  $\chi = 57^\circ$  and the  $(\bar{1}\bar{1}\bar{1})$  plane at  $\chi = 63^\circ$  are separated azimuthally by  $115^\circ$  rotated counter-clockwise, i.e.,  $\Delta\phi = -115^\circ$ . For the  $(\bar{1}11)$  orientation, reflections from  $(\bar{1}1\bar{1})$  plane at  $\chi = 57^\circ$  and (111) plane at  $\chi = 63^\circ$  are separated azimuthally by  $115^\circ$  rotated clockwise, i.e.,  $\Delta\phi = +115^\circ$ .

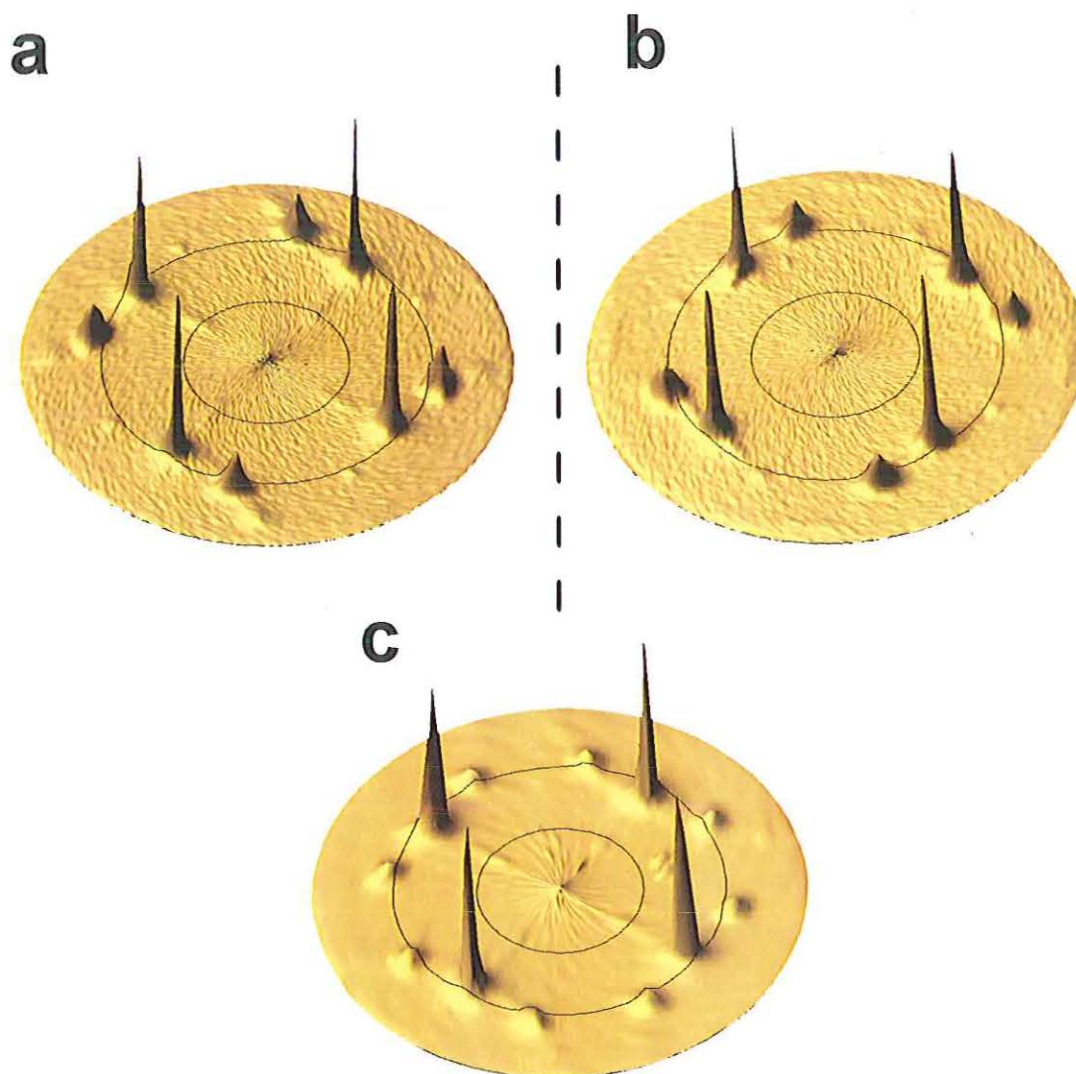


Figure 4: CuO(111) pole figures for films of CuO on Au(001) grown from a solution of (a) L-tartaric acid, (b) D-tartaric acid and (c) DL-tartaric acid. The film grown from L-tartaric acid has a  $(1\bar{1}\bar{1})$  orientation while the film grown from D-tartaric acid has a  $(\bar{1}11)$  orientation. The film deposited from the racemic mixtures has equal amounts of the  $(1\bar{1}\bar{1})$  and  $(\bar{1}11)$  orientations.

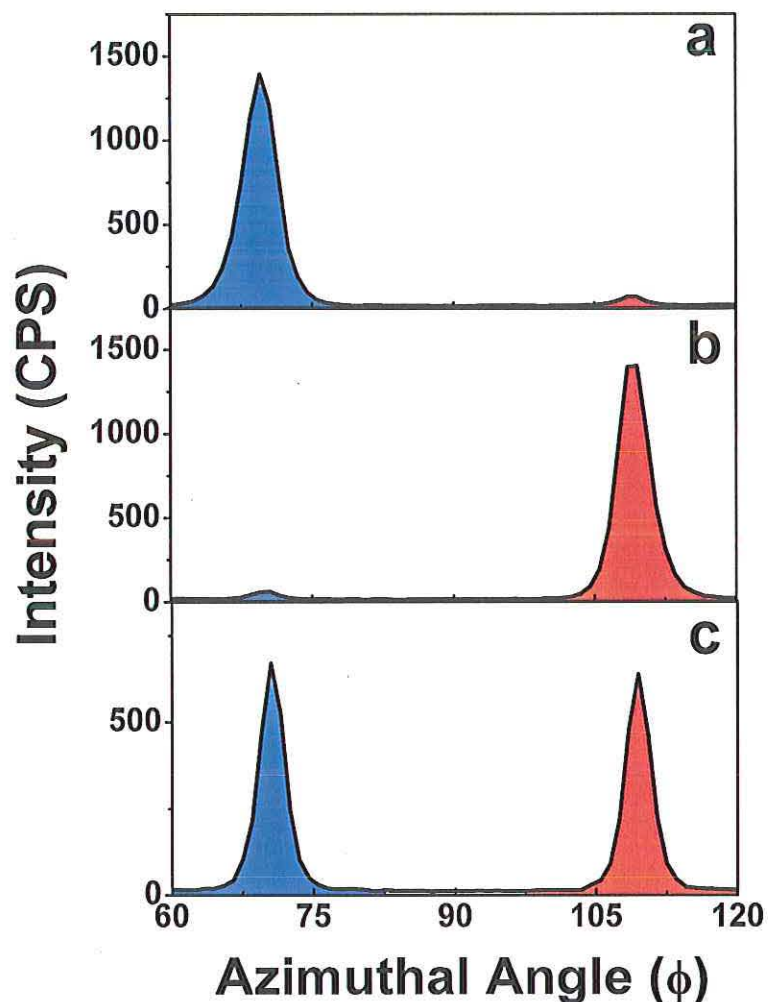


Figure 5: Azimuthal scans probing the  $\{111\}$  reflections at  $\chi = 63^\circ$  for films of CuO on Au(001) grown from a solution of (a) L-tartaric acid, (b) D-tartaric acid and (c) DL-tartaric acid. The peaks in blue and red represent the  $(\bar{1}\bar{1}\bar{1})$  and  $(111)$  reflections, respectively. The film grown from L-tartaric acid has a higher diffracted intensity for the  $(\bar{1}\bar{1}\bar{1})$  reflection (ee = 95%) while the film grown from D-tartaric acid has a higher diffracted intensity for the  $(111)$  reflection (ee = 93%). The film deposited from the racemic mixture has approximately equal intensity for the  $(\bar{1}\bar{1}\bar{1})$  and  $(111)$  reflections.

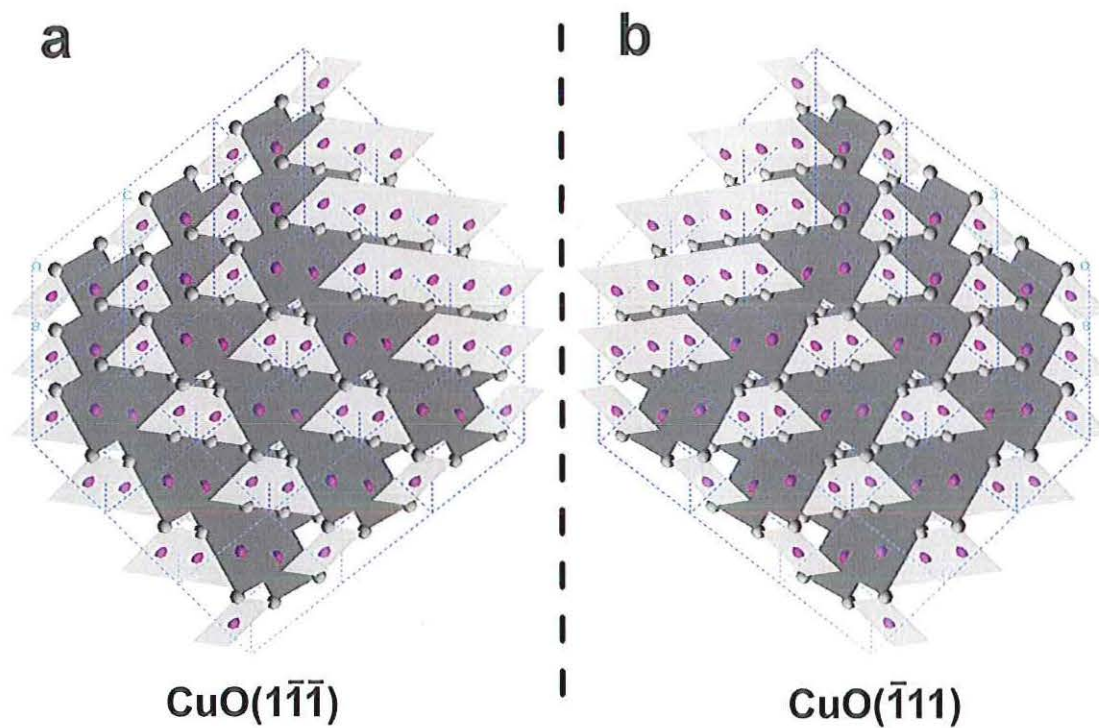


Figure 6: Polyhedra models for the  $(1\bar{1}\bar{1})$  and  $(\bar{1}\bar{1}1)$  orientations with the faces aligned parallel with the plane of the paper. The Cu and O atoms are shown in red and gray, respectively. The planes in light gray and dark gray show the Cu coordination with nearest O atoms along the  $[110]$  and  $[\bar{1}\bar{1}0]$  directions, respectively.

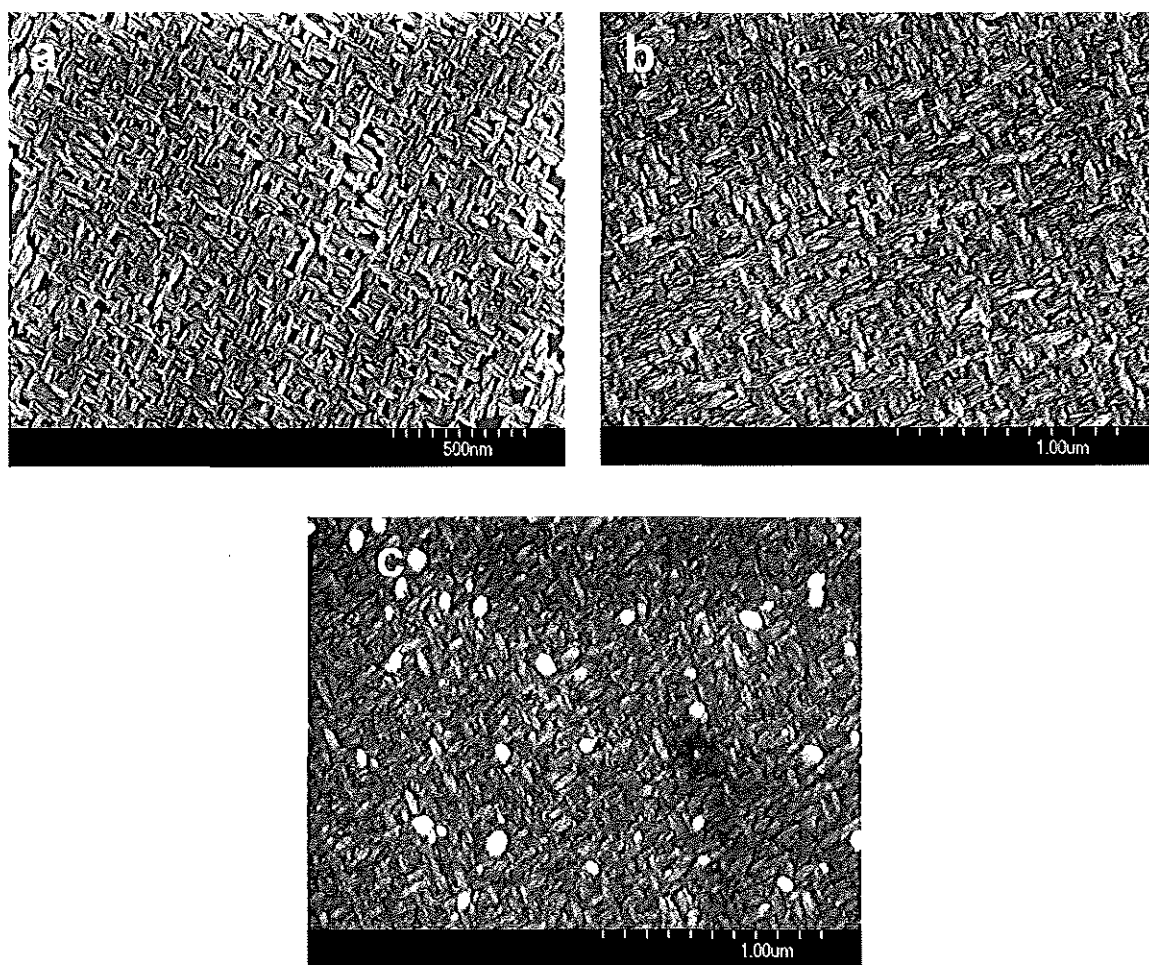


Figure 7: SEM images of CuO films on Au(100) grown from solutions of (a) L-tartaric acid (b) D-tartaric acid and (c) DL-tartaric acid.

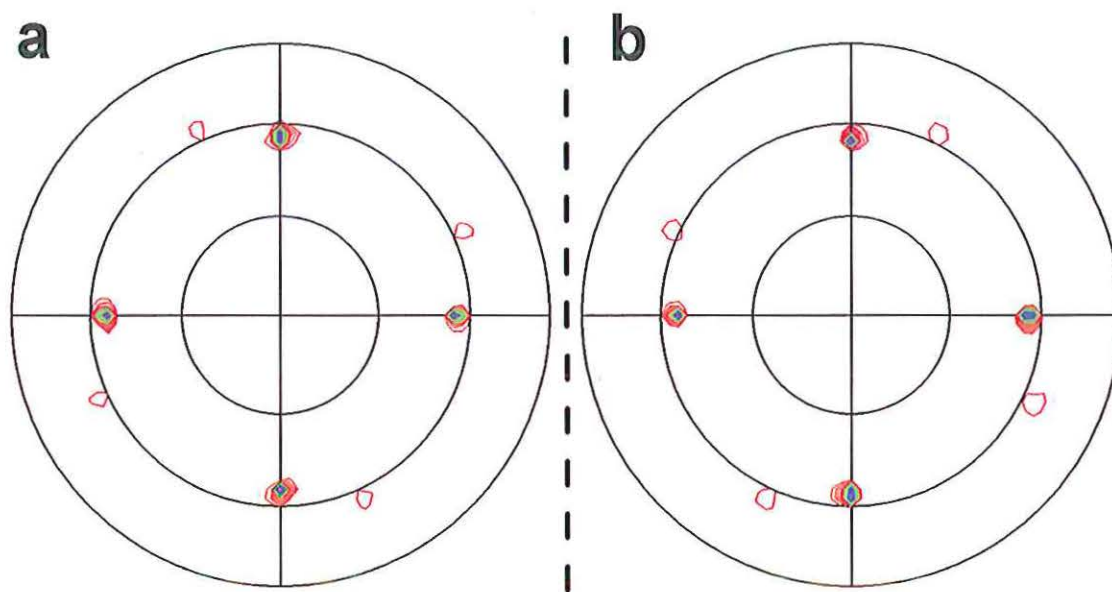


Figure 8: CuO(111) pole figures for films deposited from (a) L-tartaric acid before switching to D-tartaric acid, and (b) D-tartaric acid before switching to L-tartaric acid.

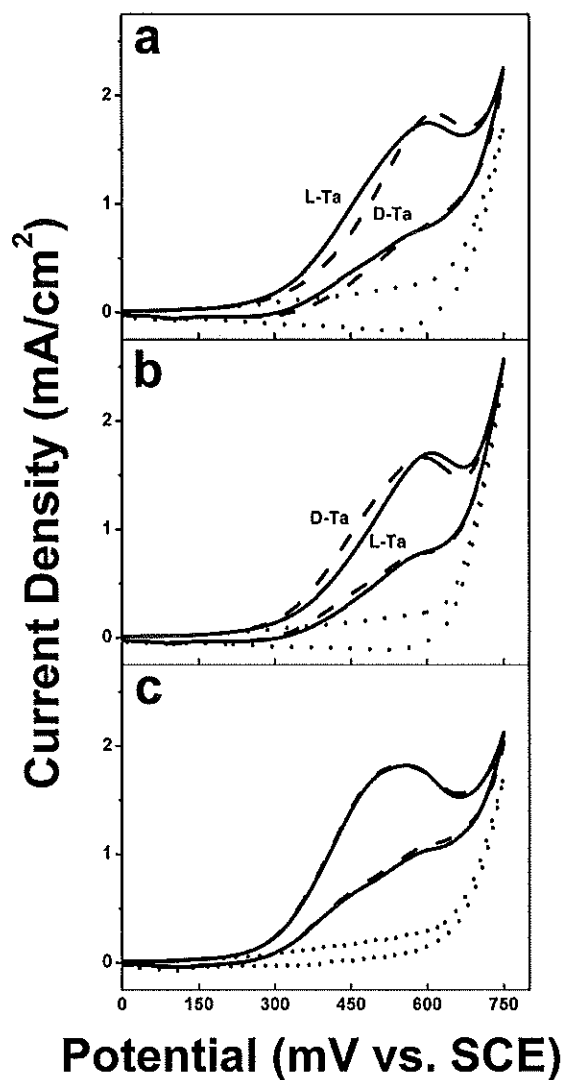


Figure 9: Chiral recognition of tartaric acid by chiral CuO. Cyclic voltammograms were run at room temperature in solutions of 5 mM L-tartaric acid (solid line) or 5 mM D-tartaric acid (dash) in 0.1 M NaOH (dot) for CuO films grown in (a) L-tartaric acid, (b) D-tartaric acid and (c) DL-tartaric acid solutions. The film grown from L-tartaric acid selectively oxidizes L-tartaric acid over D-tartaric acid while the film grown from D-tartaric acid selectively oxidizes D-tartaric acid over L-tartaric acid. A control experiment on an achiral film shows no selectivity for the electrooxidation of tartaric acid.

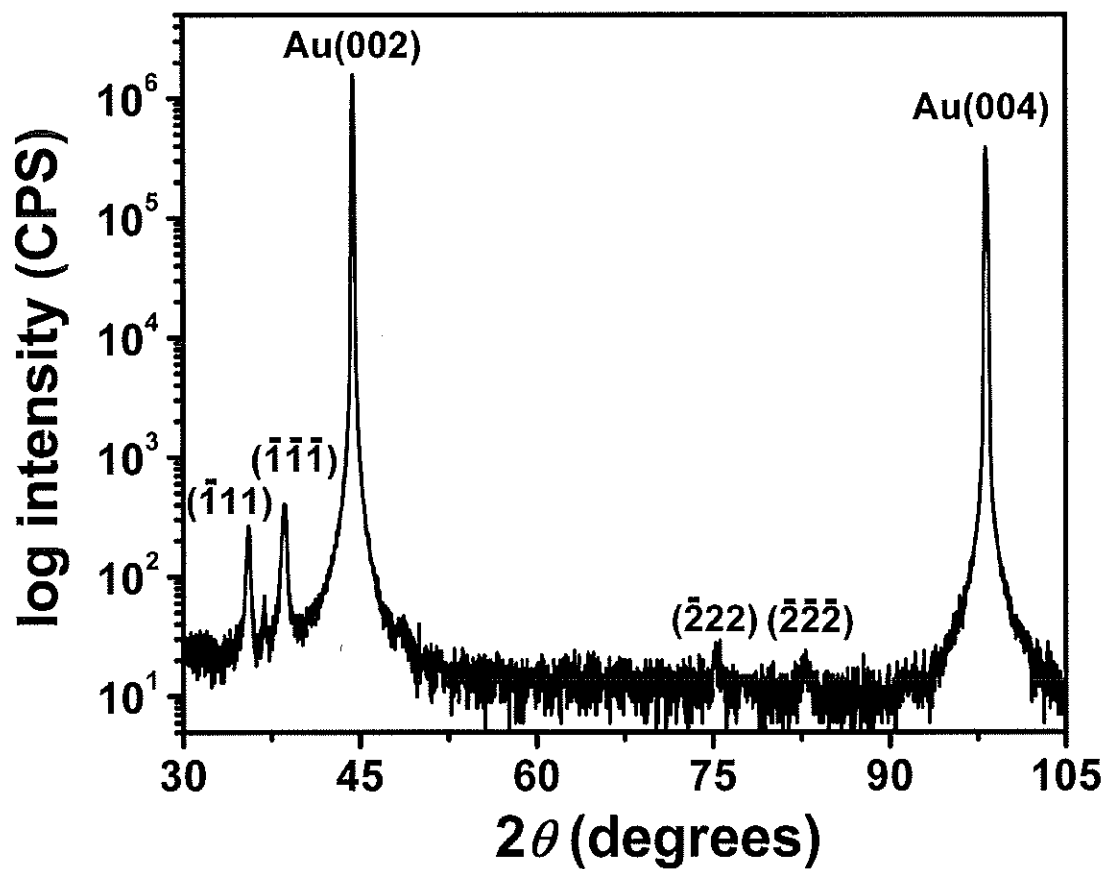


Figure 10: X-ray diffraction  $\theta$ - $2\theta$  scan of a CuO film on Au(001) from L-alanine solution. The unlabeled peak is due to a gold impurity.

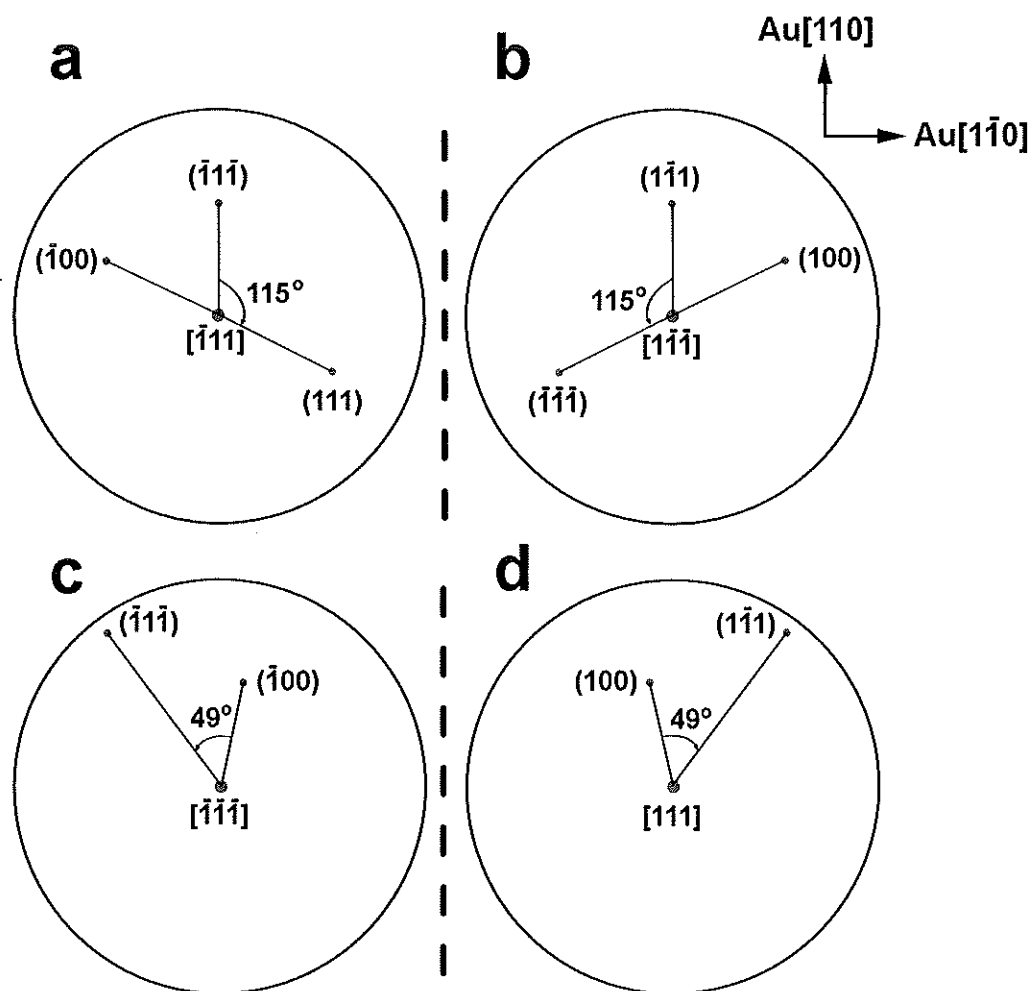


Figure 11: Stereographic projections for (a)  $(\bar{1}\bar{1}\bar{1})$ , (b)  $(1\bar{1}\bar{1})$ , (c)  $(\bar{1}\bar{1}\bar{1})$  and (d)  $(111)$  orientations indicating the positions where the  $(111)$ -type and  $(100)$ -type reflections should be observed in the pole figures. For the  $(1\bar{1}\bar{1})$  orientation, reflections from the  $(1\bar{1}\bar{1})$  plane at  $\chi = 57^\circ$  and the  $(\bar{1}\bar{1}\bar{1})$  plane at  $\chi = 63^\circ$  are separated azimuthally by  $115^\circ$  rotated counter-clockwise, i.e.,  $\Delta\phi = -115^\circ$ . For the  $(\bar{1}\bar{1}\bar{1})$  orientation, reflections from the  $(\bar{1}\bar{1}\bar{1})$  plane at  $\chi = 57^\circ$  and the  $(111)$  plane at  $\chi = 63^\circ$  are separated azimuthally by  $115^\circ$  rotated clockwise, i.e.,  $\Delta\phi = +115^\circ$ . For the  $(\bar{1}\bar{1}\bar{1})$  orientation, reflections from the  $(\bar{1}00)$  plane at  $\chi = 55^\circ$  and the  $(\bar{1}\bar{1}\bar{1})$  plane at  $\chi = 85^\circ$  are separated azimuthally by  $49^\circ$  rotated counter-clockwise, i.e.,  $\Delta\phi = -49^\circ$ . For the  $(111)$  orientation, reflections from the  $(100)$  plane at  $\chi = 55^\circ$  and the  $(1\bar{1}\bar{1})$  plane at  $\chi = 85^\circ$  are separated azimuthally by  $49^\circ$  rotated clockwise, i.e.,  $\Delta\phi = +49^\circ$ . The Au directions are given as a reference.

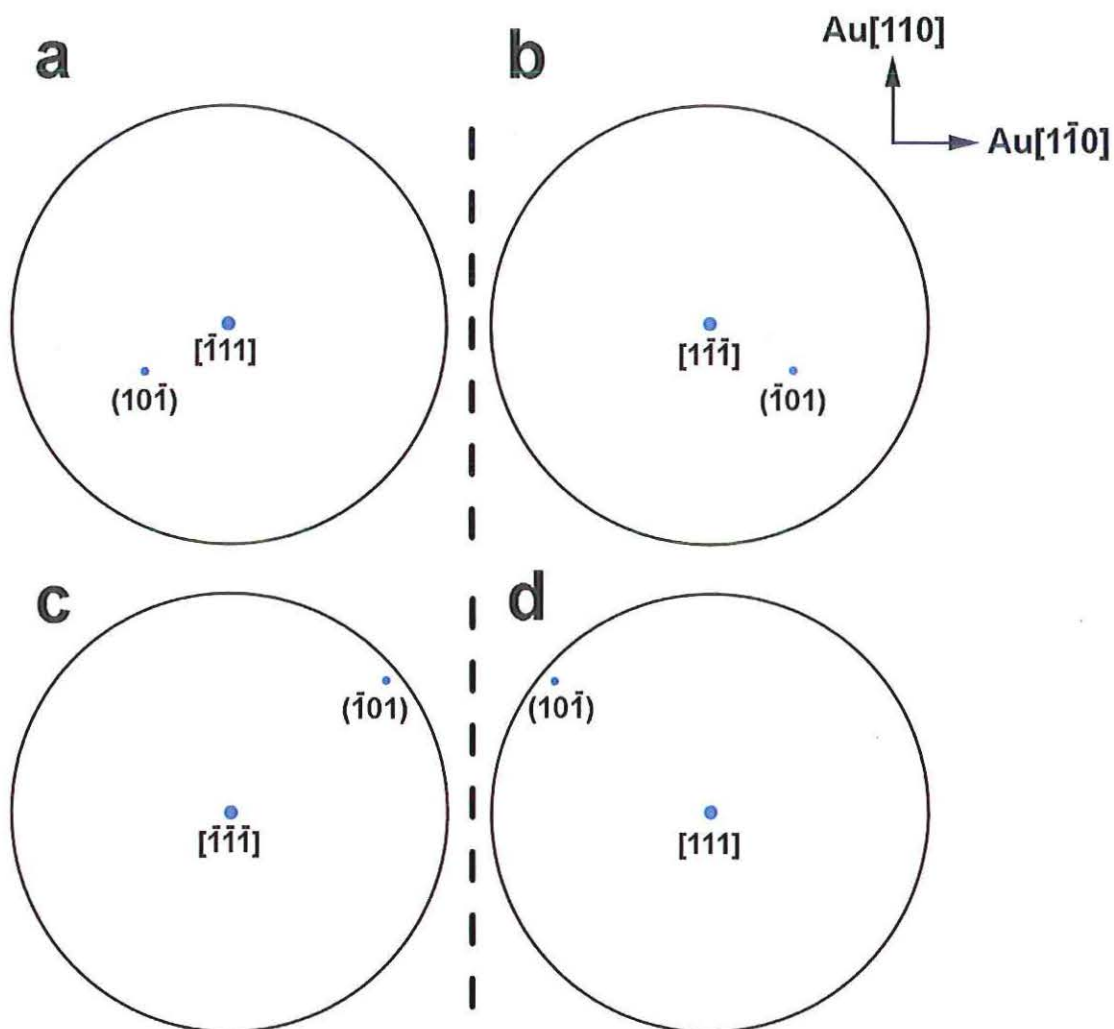


Figure 12: Stereographic projections for the (a)  $(\bar{1}\bar{1}\bar{1})$ , (b)  $(1\bar{1}\bar{1})$ , (c)  $(\bar{1}\bar{1}\bar{1})$  and (d)  $(111)$  orientations indicating the positions where the  $(10\bar{1})$ -type reflections should be observed in the pole figures. The Au directions provide the reference for comparing the positions of observed reflections in pole figures for films grown from different enantiomers.

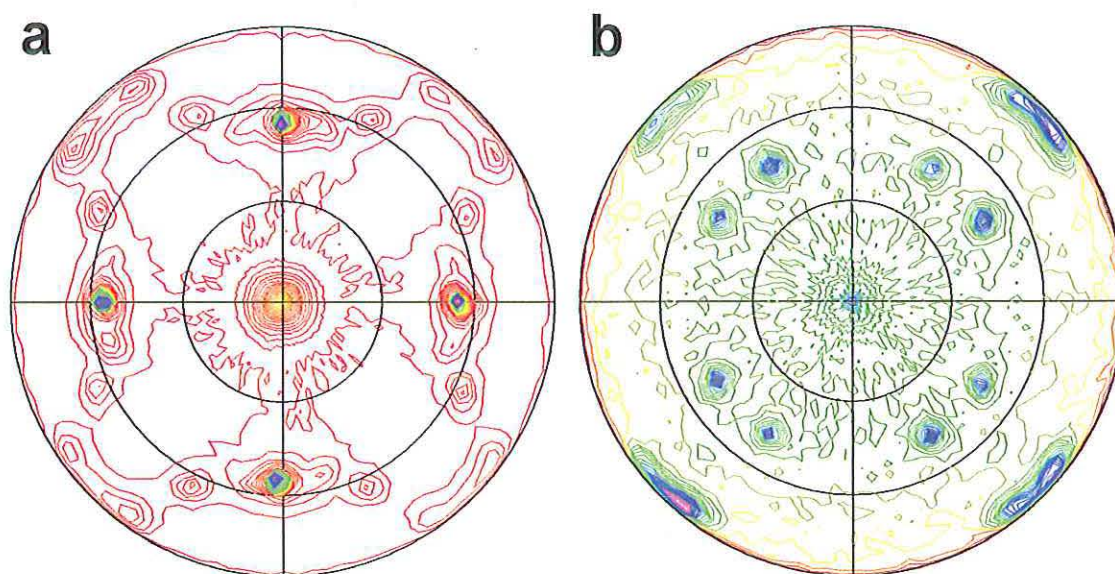


Figure 13: Pole figures probing the in-plane orientation for a CuO film on Au(001) grown from a solution of L-alanine using (a) (111) reflections and (b)  $(20\bar{2})$  reflections.

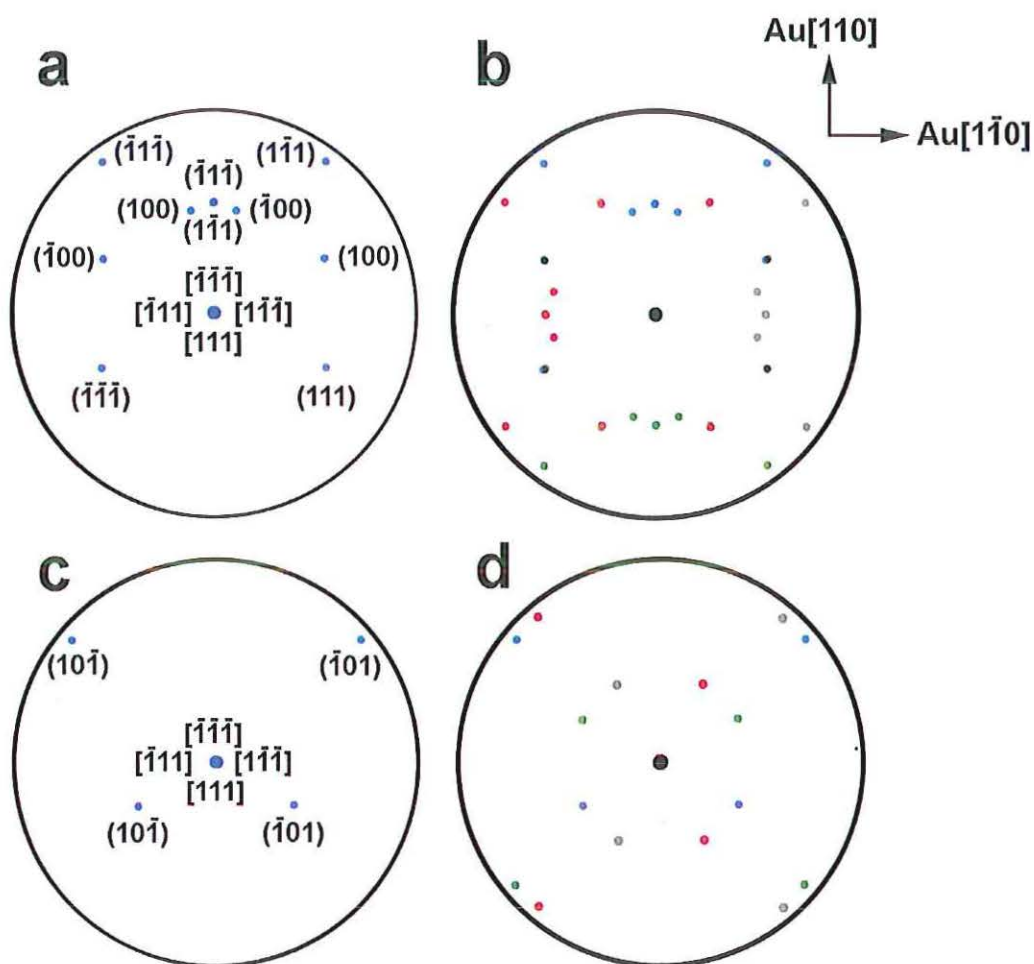


Figure 14: (a) Expected (111) pole figure obtained by overlaying the stereographic projections for the four orientations in Figure 12 under the assumption that only one domain of each orientation is deposited. (b) Expected (111) pole figure for four domains obtained by rotating part (a) by  $90^\circ$ ,  $180^\circ$  and  $270^\circ$  shown in gray, green and red respectively and overlaying them. (c) Expected  $(20\bar{2})$  pole figure obtained by overlaying the stereographic projections for the four orientations in Figure 14 under the assumption that only one domain of each orientation is deposited. (d) Expected (111) pole figure for four domains obtained by rotating part (a) by  $90^\circ$ ,  $180^\circ$  and  $270^\circ$  shown in gray, green and red respectively and overlaying them.

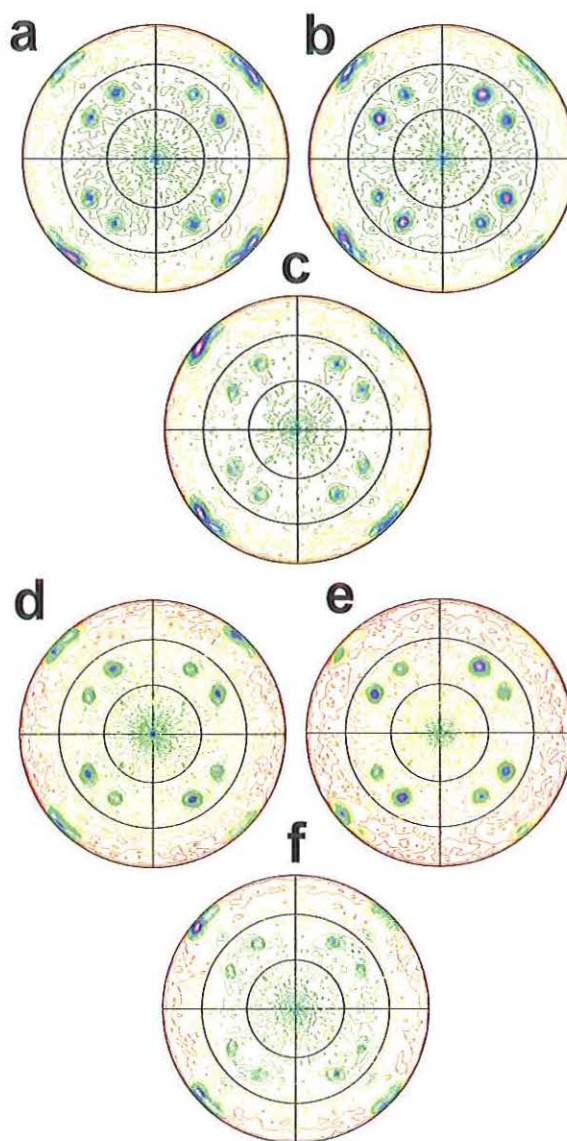


Figure 15: CuO ( $20\bar{2}$ ) pole figures for various CuO films grown from solutions of (a) L-alanine, (b) D-alanine, (c) DL-alanine, (d) L-valine, (e) D-valine and (f) DL-valine. The pole figures for films grown from L-alanine and L-valine solution have a small excess of the chiral  $(\bar{1}\bar{1}1)$  and  $(\bar{1}\bar{1}\bar{1})$  orientations. The films grown from D-alanine and D-valine have a small excess of  $(1\bar{1}\bar{1})$  and  $(111)$ . The films grown a racemic mixtures of alanine and valine show no enantiospecificity for any chiral orientations.

## V. Electrochemical Biomineralization: the Deposition of Calcite with Chiral Morphologies

*Elizabeth A. Kulp and Jay A. Switzer*

Department of Chemistry and the Graduate Center for Materials Research

University of Missouri – Rolla, Missouri, USA 65401

Email: [jswitzer@umr.edu](mailto:jswitzer@umr.edu)

Biomaterials such as foraminifers, coccoliths, and shells exist predominately as one of two nonsuperimposable mirror images of each other known as enantiomers.<sup>1</sup> Calcite can form these chiral microstructures even though the material crystallizes in an achiral space group.<sup>2</sup> Researchers have shown that enantiomorphs of calcite can be produced either by treating calcite with chiral etchants or by crystallizing calcite in the presence of amino acids like aspartic acid and proteins.<sup>3</sup> Electrodeposition, like biomineralization, is a near-equilibrium solution processing method in which solid inorganic materials are produced from solution precursors. The resulting morphologies depend strongly on the presence of solution precursors and additives. We have previously shown that chiral films of CuO can be electrodeposited in the presence of tartaric and amino acids.<sup>4</sup> Here, we electrodeposit the biominerals calcite and aragonite onto stainless steel substrates by electrochemically generating base at the electrode surface. We show that chiral morphologies of calcite can be electrodeposited in the presence of tartaric, malic and aspartic acid.

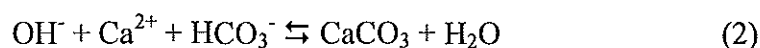
Studies in biomineralization have explored the influence of additives on the morphology of calcite crystals.<sup>3,5</sup> Magnesium additives are found to inhibit calcite

growth by limiting the step growth and substituting for calcium in the calcite structure, consequently increasing the solubility of the deposit and often producing a different polymorph such as aragonite.<sup>3e,5a</sup> The addition of carboxylic acids to calcite deposition solutions produces elongated calcite crystals, terminated with  $\{10\bar{1}4\}$  facets.<sup>3d,5d</sup> Similar structures have occurred in magnesium inhibition studies on calcite growth on carboxylate terminated self-assembled monolayers.<sup>5f</sup> Chiral organic acids with carboxylate groups have produced chiral etch-pit morphologies<sup>3a-d</sup> and chiral growth hillocks on calcite.<sup>3d,e</sup>

Chiral morphologies of calcite exist in nature even though the material crystallizes in the achiral space group  $R\bar{3}c$ .<sup>2</sup> In fact, enantioselective adsorption of molecules on the chiral surface of minerals such as calcite has been invoked to explain the genesis of biogenic homochirality.<sup>2c</sup> The chirality of certain faces of calcite can be understood from symmetry considerations. A chiral plane lacks mirror or glide plane symmetry.<sup>2a,b</sup> In order to determine which planes of calcite are chiral, one needs to determine from the space group the locations of mirror or glide planes in the structure. Achiral planes are those which are parallel with directions normal to these planes, and therefore satisfy the zonal equation ( $hu + kv + lw = 0$ ). This process can be simplified by considering the point group of the material,  $\bar{3}m$ , in which the c-glides are replaced by mirrors. Table 1 shows selection rules for chirality for the point group  $\bar{3}m$ . The highlighted plane groups  $\{11\bar{2}0\}$ ,  $\{hki0\}$ ,  $\{hh\bar{2}hl\}$ , and  $\{hkil\}$  are chiral because they lack mirror symmetry.<sup>6</sup> Hence, the common  $\{10\bar{1}4\}$  cleavage planes of calcite are achiral,

whereas the  $\{21\bar{3}1\}$  scalenohedral faces on dog-tooth calcite are chiral. For a chiral plane such as  $(hki\bar{l})$ , its enantiomer is  $(\bar{h}\bar{k}\bar{i}l)$ .

Electrodeposition has been used by other groups to deposit biominerals.<sup>7</sup> Although electrodeposition is usually a redox method in which metals are produced from metal ions by a cathodic process, it is also possible to deposit materials on an electrode surface by the electrochemical generation of acid or base.<sup>8</sup> The electrodeposition of biomaterials occurs by electrochemically generating hydroxide ions from water reduction, increasing the local pH at the electrode surface (Eq. 1). Base can also be electrochemically generated by reducing molecular oxygen, nitrate, or organic molecules such as quinones. The biominerals calcite and aragonite can then be electrodeposited by using the electrochemically generated base to react with  $\text{HCO}_3^-$  in solutions containing  $\text{Ca}^{2+}$  according to Eq. 2.



Scanning electron micrographs of electrodeposited calcite and aragonite are shown in Figure 1a – 1b. We observe that rhombohedral-shaped crystals of trigonal calcite are electrodeposited from a pure calcium bicarbonate solution (Figure 1a). The lattice parameters determined by Rietveld analysis are  $a = 0.4980$  nm and  $c = 1.7033$  nm for the electrodeposited calcite, compared with the literature values of  $a = 0.4991$  nm and  $c = 1.7062$  nm for trigonal calcite (JCPDS no. 81-2027). The addition of magnesium to the deposition bath inhibits the growth of the trigonal calcite and produces rosette formations of orthorhombic aragonite (Figure 1b). The lattice parameters are  $a = 0.4950$  nm,  $b = 0.7957$  nm and  $c = 0.5738$  nm for the orthorhombic aragonite, compared with the

literature values of  $a = 0.49598$  nm,  $b = 0.79641$  nm and  $c = 0.57379$  nm (JCPDS no. 76-0606). When the deposition bath contains both dicarboxylic acids and magnesium ions, the structure reverts back to trigonal calcite with lattice parameters of  $a = 0.4964$  nm and  $c = 1.6930$  nm. The electrodeposited calcite contains 0.6 – 0.8 atomic percent Mg. The morphology also changes when carboxylic acids are added to the bath. Instead of rhombohedral shaped morphologies, the electrodeposited calcite from solutions with achiral succinic acid (Figure 1c) or DL-malic acid (Figure 1d) are barrel-like structures with symmetrical facets. It is interesting to note that the racemic mixture of D- and L-malic acid does not produce a racemic mixture of chiral morphologies, but instead forms an achiral microstructure.

Calcite that is deposited in the presence of chiral molecules grows with a chiral morphology. Scanning electron micrographs of calcite deposited with tartaric, malic and aspartic acid additives are shown in Figure 2. For each of the acids, a seashell-like spiral morphology is produced, with the two enantiomers of the molecule producing chiral morphologies. Notice that L- tartaric acid produces calcite with a spiral that rotates to the left when viewed from above, while L-malic acid and L-aspartic acid produce calcite with spirals which rotate to the right. Hence, there is not a direct correlation between the L/D designation for the chiral molecule and the chiral orientation of the resulting calcite. We note that the L/D designation is an arbitrary label based on the glyceraldehyde molecule. Our results correlate better with the Cahn-Ingold-Prelog priority rules for assigning absolute configurations to chiral molecules. L-tartaric acid has two chiral sites and is labeled R,R, whereas L-malic acid and L-aspartic acid are both designated as S.

The electrodeposited calcite morphologies seen in Figure 1c, 1d, and 2a-2f are similar to the columnar calcite with three rhombohedral-like facets chemically deposited from supersaturated calcium bicarbonate solutions with organic additives such as malonic acid<sup>5d</sup> and aspartic acid.<sup>3d</sup> The overall chiral shape evolution of right- and left-handed morphologies is reported to be related to the reduction of symmetry of the  $\{10\bar{1}4\}$  plane and the step edge selectivity of the enantiomer.<sup>3d</sup> Orme et al. have shown by molecular modeling that D-aspartic acid will preferentially bind to a  $(01\bar{1}\bar{4})$  riser over a  $(1\bar{1}0\bar{4})$  riser.<sup>3d</sup> The enantiomeric selectivity to one riser over a flat terrace or another riser induces the handedness of the asymmetric plane.<sup>3d</sup>

Chiral electrodeposition should also be applicable to other biominerals such as hydroxyapatite, the inorganic component of bone. Because other workers have shown that epithelial cells will preferentially adhere to specific chiral faces of solids such as calcium tartrate,<sup>9</sup> it is interesting to speculate whether the surfaces of electrodeposited biominerals such as hydroxyapatite on metal bone implants can be made more biocompatible if they are deposited in the presence of the correct hand of a chiral imprinting agent.

**ACKNOWLEDGEMENT.** This work was funded by National Science Foundation Grant DMR-0504715.

**SUPPORTING INFORMATION AVAILABLE:** Experimental procedures and symmetry aspects of chirality. This material is available free of charge via the Internet at <http://pubs.acs.org>.

## REFERENCES

1. Addadi, L.; Weiner, S. *Nature* **2001**, *411*, 753.
2. (a) Hazen, R. M.; Sholl, D. S. *Nature Mater.* **2003**, *2*, 367. (b) Downs, R. T.; Hazen, R. M. *J. Mol. Catal. A: Chem.* **2004**, *216*, 273. (c) Hazen, R. M.; Filley, T. R.; Goodfriend, G.A. *Proc. Natl. Acad. Sci. USA* **2001**, *98*, 5487.
3. (a) Thomas, J. M.; Renshaw, G. D.; Roscoe, C. *Nature* **1964**, *203*, 72. (b) Honess, A. P.; Jones, J. R. *Bull. Geol. Soc. Amer.* **1937**, *48*, 667. (c) Barwise, A. J.; Compton, R. G.; Unwin, P. R. *J. Chem. Soc. Faraday Trans.* **1990**, *86*, 137. (d) Orme, C. A.; Noy, A.; Wierzbicki, A.; McBride, M. T.; Grantham, M.; Teng, H. H.; Dove, P. M.; DeYoreo, J. J. *Nature* **2001**, *411*, 775. (e) De Yoreo, J. J.; Dove, P. M. *Science* **2004**, *306*, 1301.
4. (a) Switzer, J. A.; Kothari, H. M.; Poizot, P.; Nakanishi, S.; Bohannan, E. W. *Nature* **2003**, *425*, 490. (b) Bohannan, E. W., Kothari, H. M., Nicic, I. M.; Switzer, J. A. *J. Am. Chem. Soc.* **2004**, *126*, 488. (c) Kothari, H. M.; Kulp, E. A.; Boonsalee, S.; Nikiforov, M. P.; Bohannan, E. W.; Poizot, P.; Nakanishi, S.; Switzer, J. A. *Chem. Mater.* **2004**, *16*, 4232.
5. (a) Davis, K. J.; Dove, P. M.; De Yoreo, J. J. *Science* **2000**, *290*, 1134. (b) Teng, H. H.; Dove, P. M.; Orme, C. A.; De Yoreo, J. J. *Science* **1998**, *282*, 724. (c) Teng, H. H.; Chen, Y.; Pauli, E. *J. Am. Chem. Soc.* **2006**, *128*, 14482. (d) Mann, S.; Didymus, J. M.; Sanderson, N. P.; Heywood, B. R.; Samper, E. J. A. *J. Chem. Soc. Faraday Trans.* **1990**, *86*, 1873. (e) Mann, S.; Archibald, D. D.; Didymus, J. M.; Douglas, T.; Heywood, B. R.; Meldrum, F. C.; Reeves, N. J. *Science* **1993**, *261*, 1286. (f) Han, Y.-J.; Aizenberg, J. *J. Am. Chem. Soc.* **2003**, *125*, 4032.
6. *International Tables for X-ray Crystallography* Vol. 1; Henry, N. F. M.; Lonsdale, K. Eds.; Kynoch: Birmingham, 1952; pp 37-38.
7. (a) Redepenning, J.; Schlessinger, T.; Burnham, S.; Lippiello, L.; Miyano, J. *J. Biomed. Mater. Res.* **1996**, *30*, 287. (b) Monma, H. *J. Ceram. Soc. Jpn.* **1993**, *101*, 737. (c) Xu, S.; Melendres, C. A.; Park, J. H.; Kamrath, M. A. *J. Electrochem. Soc.* **1999**, *146*, 3315. (d) Beaunier, L.; Gabrielli, C., Poindessous, G, Maurin, G.; Rosset, R. *J. Electroanal. Chem.* **2001**, *501*, 41. (e) Gabrielli, C.; Maurin, G.; Poindessous, G.; Rosset, R. *J. Cryst. Growth* **1999**, *200*, 236.
8. (a) Switzer, J. A. *Am. Ceram. Soc. Bull.* **1987**, *66*, 1521. (b) Limmer, S. J.; Kulp, E. A.; Switzer, J. A. *Langmuir* **2006**, *22*, 10535. (c) Liu, R.; Vertegel, A. A.; Bohannan, E. W.; Sorenson, T. A.; Switzer, J. A. *Chem. Mater.* **2001**, *13*, 508.
9. Hanein, D.; Geiger, B.; Addadi, L. *Science* **1994**, *263*, 1413.

**Table 1.** Selection rules for chirality of the calcite crystal system. The highlighted planes lack mirror symmetry.<sup>6</sup>

System	Point group	$\{0001\}$	$\{10\bar{1}0\}$	$\{11\bar{2}0\}$	$\{hki0\}$	$\{h0\bar{h}l\}$	$\{h\bar{h}2\bar{h}l\}$	$\{hkil\}$
Trigonal (hexagonal axes)	$\bar{3}m$	$6mm$	$2mm$	2	2	$2mm$	2	2

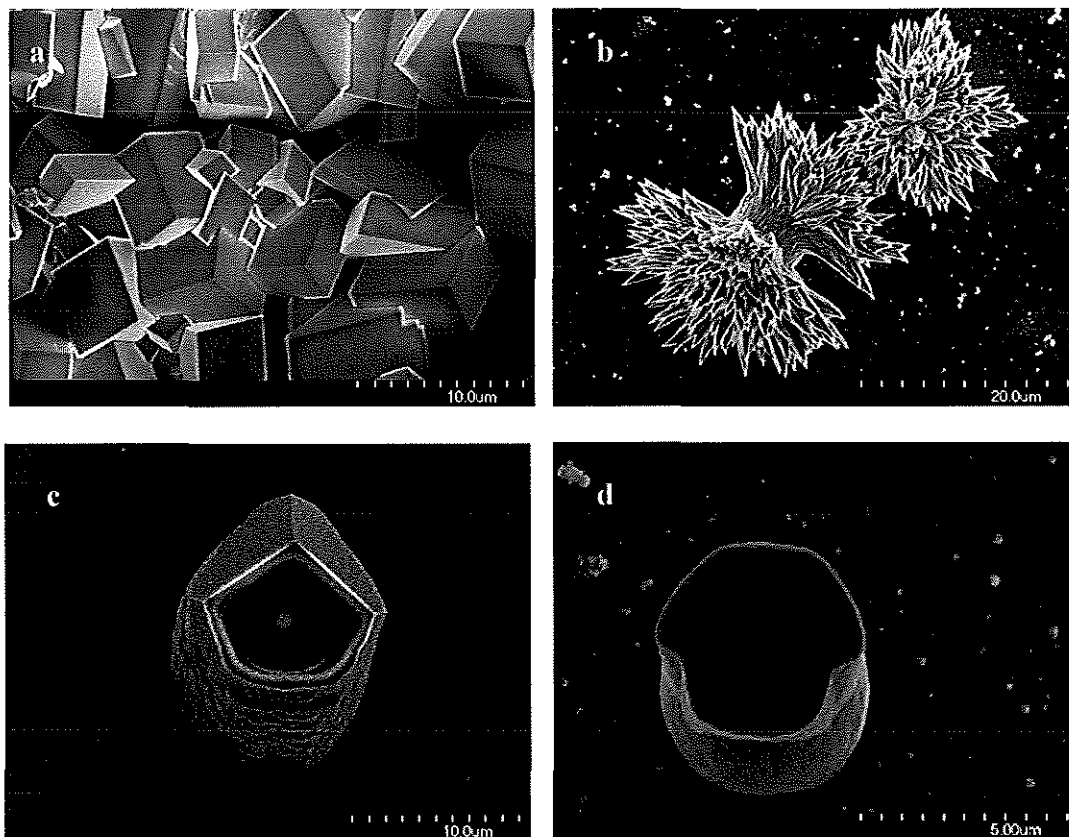


Figure 1. Deposition of calcite and aragonite by the electrochemical generation of base. Scanning electron micrographs of (a) trigonal calcite grown from a calcium bicarbonate solution, (b) rosettes of orthorhombic aragonite grown from the same solution with magnesium present, (c) calcite grown with added succinic acid, and (d) calcite grown with added DL-malic acid.

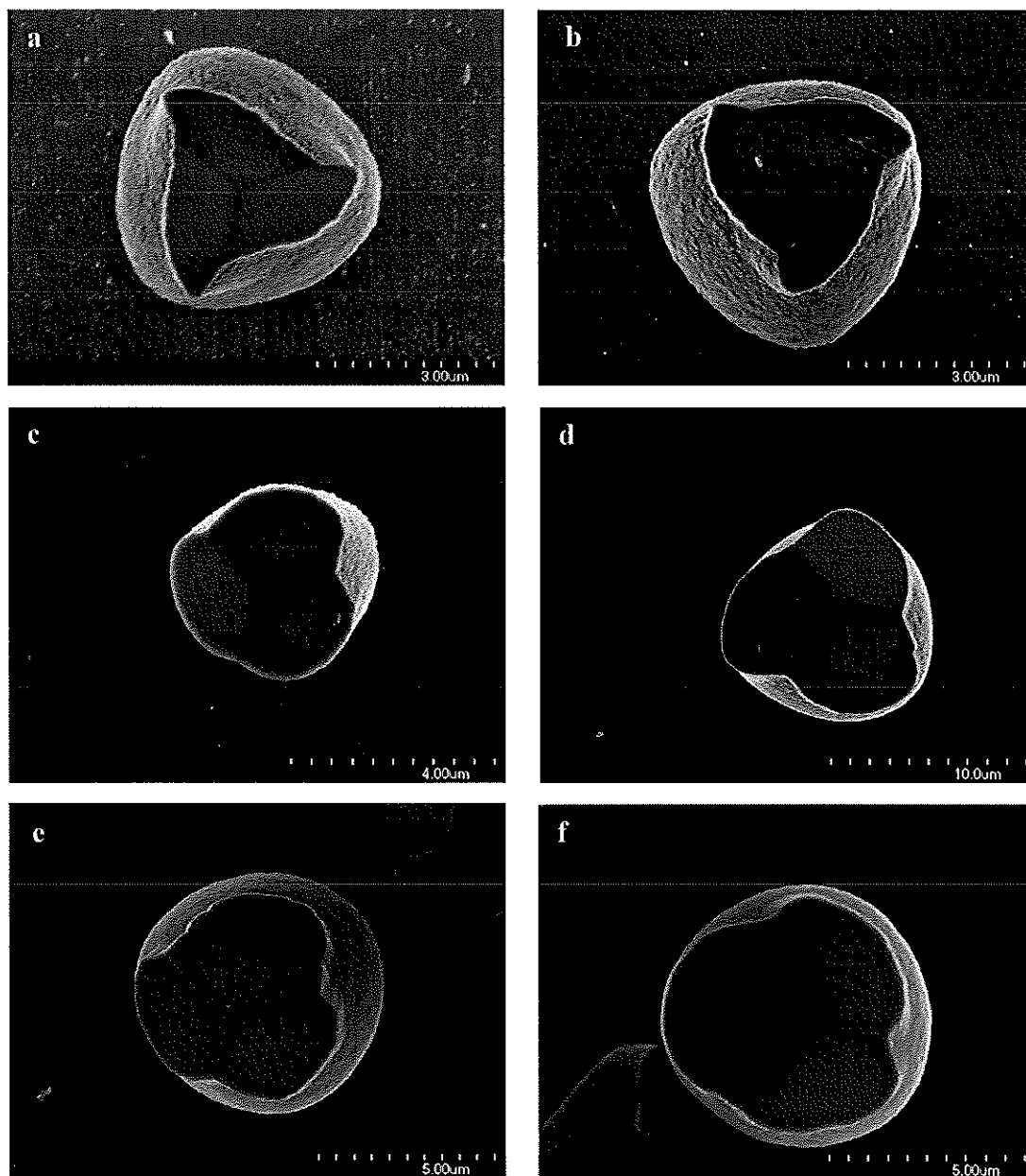


Figure 2. Electrodeposition of calcite with chiral facets. Scanning electron micrographs of calcite grown on polycrystalline stainless steel from calcium bicarbonate in the presence of magnesium and a) L-tartaric acid, b) D-tartaric acid, c) L-malic acid, d) D-malic acid, e) L-aspartic acid, and f) D-aspartic acid. Each chiral agent produces a chiral morphology with either a right- or left-handed spiral.

**APPENDIX A.**

**MORPHOLOGY CHARACTERIZATION**

The orientation of a surface and a plane is defined using Miller indices by how it intersects the crystallographic axes of a material.<sup>1-3</sup> The reciprocal of the  $(hkl)$  in the Miller index indicates where the plane intercepts the axes. So for a  $(100)$  Miller index, the plane intercepts at  $(1, \infty, \infty)$ . Therefore, the plane crosses at 1 on the x-axis and is parallel to the y- and z-axis. Likewise, a Miller index of  $(200)$  means that the plane intercepts at  $\frac{1}{2}$  on the x-axis and is parallel to the y- and z-axis. For a cubic crystal such as Au or  $\text{Cu}_2\text{O}$ , the  $(100)$ ,  $(110)$ , and  $(111)$  planes, also known as the low index surfaces, are illustrated in Figure 1. Likewise, Figure 1 also shows the symmetry and the morphology of the facets.

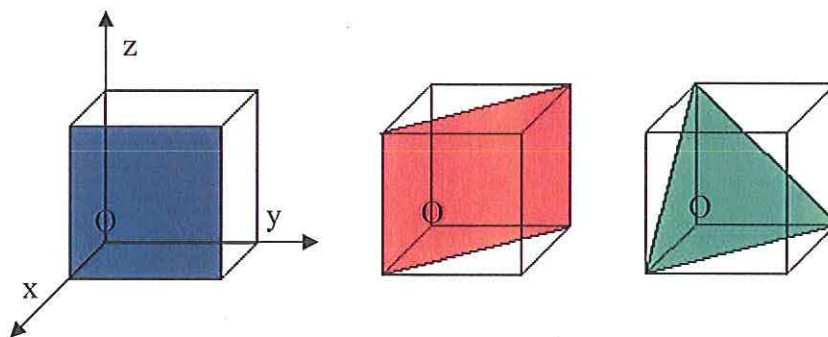


Figure 1. The low index Miller indices for a cubic system. The  $(100)$  facets (in blue, on left) will be square with four-fold symmetry. The  $(110)$  facets (in red, in the middle) will be rectangles with two-fold symmetry. The  $(111)$  facets (in green, on right) will be triangles with three-fold symmetry).

Film orientation and morphology are determined by the electrochemical/chemical reaction, potential, current, pH, temperature, and additives.<sup>4-9</sup> For example, the Switzer group has previously shown that varying the applied potential and pH changes the orientation and size of the electrodeposited  $\text{Cu}_2\text{O}$  films.<sup>4-7</sup> Films follow the orientation of the substrate at low overpotentials and change to a kinetically controlled orientation at a critical thickness.<sup>5</sup> As the overpotential increases, the critical thickness for the transition decreases.<sup>5</sup> Similarly,  $\text{Cu}_2\text{O}$  films from a pH 9 solution have a [001] preferred orientation while films from a pH 12 solution have a [111] preferred orientation.<sup>4,6</sup> Siegfried and Choi have examined the stability of facets of  $\text{Cu}_2\text{O}$  in the presence of additives where ammonium salts stabilize {111} planes, whereas sodium chloride stabilizes {100} planes.<sup>8</sup> They have also examined the effect of current density, potential, temperature, and time on the faceting and branching of the  $\text{Cu}_2\text{O}$  deposits.<sup>9</sup>

Growth rates are also affected by the experimental conditions. Generally, the morphology of a material is bounded by facets of low Miller indices,<sup>10-11</sup> but the preferential adsorption of an additive to a facet can inhibit the growth rate of one facet and increase the growth rate of another.<sup>12-16</sup> The fastest growing facets disappear while the slowest growing facets dominate the morphology,<sup>10-12</sup> as shown in Figure 2 for a cubic system. Both illustrations have a [100] orientation. In Figure 2A, the blue {100} facets are the fastest growing while the red {111} facets are the slowest. As the film continues to grow, the {100} facets grow out of existence as the slow growing {111} dominate the morphology. If the film were [100] oriented and the slowest facets were the {100}, the film would continue to grow larger with only {100} present as seen in Figure 2B.

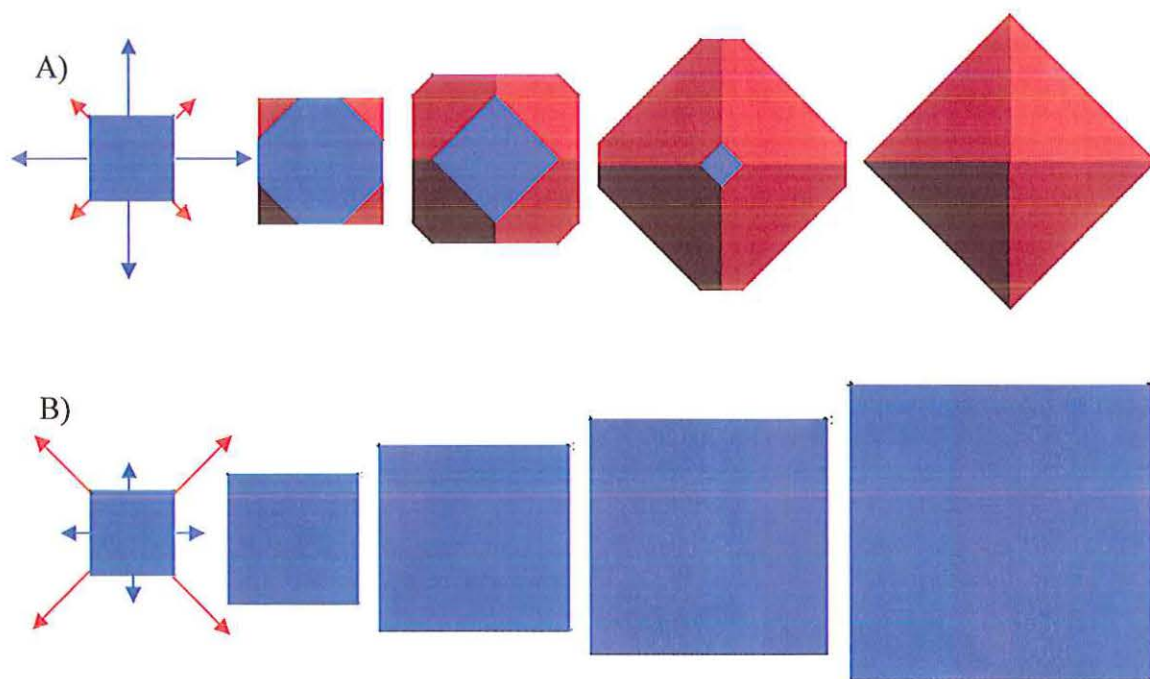


Figure 2. Growth mechanism. A) An (100) oriented film (blue) in which the growth of the {111} facets (red) is inhibited. The film morphology would be {111} faceted. B) An (100) oriented film (blue) with the growth of the {100} facets inhibited resulting in a {100} faceted morphology.

For morphology studies, the scanning electron microscope (SEM) is used. In Figure 3, the SEM images of  $\text{Cu}_2\text{O}(100)$  films electrodeposited on  $\text{Au}(100)$  in the presence of chloride and acetate, respectively, are shown. In Figure 3A, the deposits are square meaning {100} facets of  $\text{Cu}_2\text{O}$  are showing while in Figure 3B the facets are triangular indicating {111} facets are exposed. So, based on these morphologies, {100} facets are the slowest growing facets in the presence of chloride and the fastest in the presence of acetate.

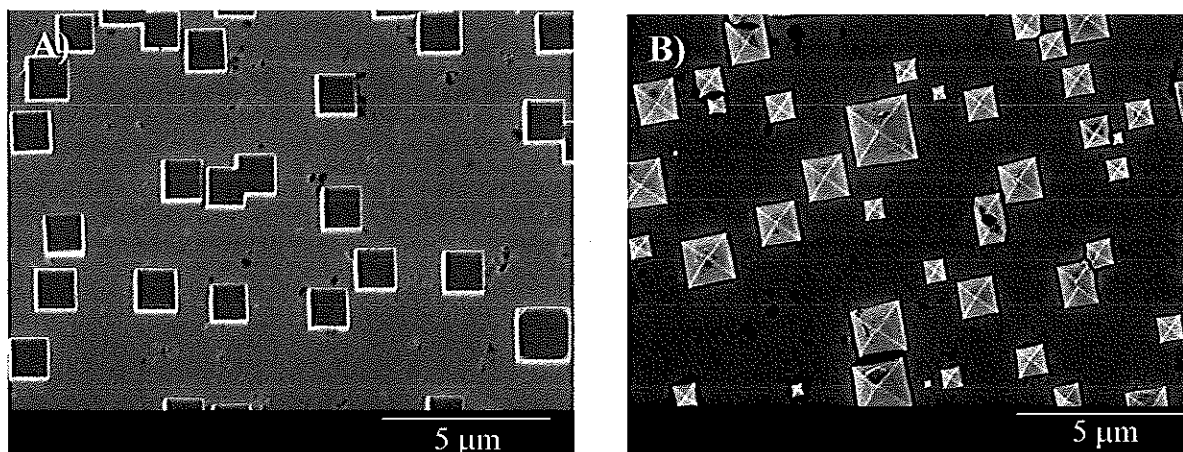


Figure 3. SEM images of  $\text{Cu}_2\text{O}(100)$  films deposited on  $(100)\text{Au}$ . A)  $\text{Cu}_2\text{O}$  deposited from a copper(II) nitrate and sodium nitrate solution contaminated with chloride from a reference electrode where the exposed facets of  $\text{Cu}_2\text{O}$  are  $\{100\}$ . B) The  $\{111\}$  facets of  $\text{Cu}_2\text{O}$  are evident in micrograph B from a copper(II) acetate and sodium acetate solution. The deposition solution consisted of 100 mM sodium salt and 10 mM copper(II) salt with a pH of 5.2. A cathodic current density of  $50 \mu\text{A}/\text{cm}^2$  was applied for 2000 s at  $25^\circ\text{C}$ . (unpublished results)

## REFERENCES

1. B. D. Cullity, *Elements of X-ray Diffraction* (Addison-Wesley, Reading, 2<sup>nd</sup> ed., 1978) pp. 41-47.
2. C. Hammond, *The Basics of Crystallography and Diffraction* (Oxford University, New York, 2<sup>nd</sup> ed., 2001) pp. 106-119.
3. A. R. West, *Solid State Chemistry and its Applications* (Wiley, New York, 1984) pp. 134-137.
4. T. D. Golden, M. G. Shumsky, Y. Zhou, R. A. VanderWerf, R. A. Van Leeuwen, J. A. Switzer, *Chem. Mater.* **8**, 2499-2504 (1996).
5. J. A. Switzer, H. M. Kothari, E. W. Bohannon, *J. Phys. Chem. B* **106**, 4027-4031 (2000).
6. R. Liu, F. Oba, E. W. Bohannon, F. Ernst, J. A. Switzer, *Chem. Mater.* **15**, 4882-4885 (2003).
7. R. Liu, E. A. Kulp, E. W. Bohannon, F. Ernst, J. A. Switzer, *Chem. Mater.* **17**, 725-729 (2005).
8. M. Siegfried, K.-S. Choi, *Angew. Chem. Int. Ed.* **44**, 3218-3223 (2005).
9. M. J. Siegfried, K.-S. Choi, *J. Amer. Chem. Soc.* **128**, 10356-10357 (2006).
10. J. O'M. Bockris, A. K. N. Reddy, *Modern Electrochemistry 2* (Plenum, New York, 1970) pp. 1214-1217.
11. W. Borchardt-Ott, *Crystallography* (Springer, New York, 2<sup>nd</sup> ed., 1995) pp. 31-33.
12. S. Mann, *Angew. Chem. Int. Ed.* **39**, 3392-3406 (2000).
13. H. H. Teng, P. M. Dove, C. A. Orme, J. J. De Yoreo, *Science* **282**, 725-727 (1998).
14. C. A. Orme, A. Noy, A. Wierzbicki, M. T. McBride, M. Grantham, H. H. Teng, P. M. Dove, J. J. De Yoreo, *Nature* **117**, 775-779 (2001).

15. J. J. De Yoreo, P. Dove, *Science* **306**, 1301-1302 (2004).
16. J. J. De Yoreo, A. Wierzbicki, P. M. Dove, *Cryst. Eng. Comm.* **9**, 1144-1152 (2007).

## APPENDIX B

## X-RAY DIFFRACTION CHARACTERIZATION

One of the most useful methods to characterize electrodeposited films is the nondestructive technique known as X-ray diffraction (XRD). Because every crystalline material has a unique diffraction pattern, the pattern can be used to characterize the material.<sup>1-9</sup> The location of each peak represents a position where the X-rays have been coherently diffracted by the atoms in the crystal lattice. The d-spacings (the distance between adjacent planes of atoms) can easily be calculated from these peaks using their  $2\theta$  values. The angle and the d-spacings are related by Bragg's Law in Equation 1:

$$n\lambda = 2d_{hkl}\sin\theta \quad (1)$$

where  $n$  is an integer 1, 2, 3, etc. normally designated as 1,  $\lambda$  is the wavelength in angstroms which is dependent on the source,  $d_{hkl}$  (d-spacing) is the interplaner spacing between the atoms in the crystal measured in angstroms, and  $\theta$  is the diffraction angle in degrees.<sup>1-9</sup> The lattice parameters of a material can then be calculated provided that the peaks have been properly assigned their Miller indices (hkl) and their d-spacings have been accurately measured. Table 1 lists the equations for calculating the d-spacing for the seven crystal systems based on the plane and the lattice parameters of the material.<sup>1</sup>

A set of equivalent lattice planes in any crystal system is indicated by braces {hkl}.<sup>1</sup> The planes have the same d-spacing, but different Miller indices.<sup>1</sup> The equations in Table 1 are also beneficial in determining planes that have an equivalent d-spacing. Whereas the {111} planes, e.g. (111), ( $\bar{1}\bar{1}\bar{1}$ ), ( $1\bar{1}\bar{1}$ ), ( $\bar{1}11$ ), ( $\bar{1}\bar{1}1$ ), ( $1\bar{1}1$ ), ( $\bar{1}\bar{1}1$ ), and ( $11\bar{1}$ ), have an identical d-spacing in a cubic system, this is not true in a monoclinic system. The ( $1\bar{1}\bar{1}$ ), ( $\bar{1}11$ ), ( $11\bar{1}$ ), ( $\bar{1}\bar{1}1$ ) planes have one d-spacing, whereas the (111), ( $\bar{1}\bar{1}\bar{1}$ ), ( $1\bar{1}1$ ), ( $\bar{1}\bar{1}1$ ) have another. This difference is related by symmetry in each crystal system.<sup>1</sup>

Table 1. The d-spacing (d) equations for the 7 systems are listed where h, k, and l are the assigned Miller indices of the peak, a, b, c,  $\alpha$ ,  $\beta$ , and  $\gamma$  are the lattice parameters of the material, and V is the volume of the cell.<sup>1</sup>

System	Interplanar Spacing
Cubic	$\frac{1}{d^2} = \frac{h^2 + k^2 + l^2}{a^2}$
Tetragonal	$\frac{1}{d^2} = \frac{h^2 + k^2}{a^2} + \frac{l^2}{c^2}$
Orthorhombic	$\frac{1}{d^2} = \frac{h^2}{a^2} + \frac{k^2}{b^2} + \frac{l^2}{c^2}$
Hexagonal	$\frac{1}{d^2} = \frac{4}{3} \left( \frac{h^2 + hk + k^2}{a^2} \right) + \frac{l^2}{c^2}$
Rhombohedral	$\frac{1}{d^2} = \frac{(h^2 + k^2 + l^2) \sin^2 \alpha + 2(hk + kl + hl)(\cos^2 \alpha - \cos \alpha)}{\alpha^2 (1 - 3 \cos^2 \alpha + 2 \cos^3 \alpha)}$
Monoclinic	$\frac{1}{d^2} = \frac{1}{\sin^2 \beta} \left( \frac{h^2}{a^2} + \frac{k^2 \sin^2 \beta}{b^2} + \frac{l^2}{c^2} - \frac{2hl \cos \beta}{ac} \right)$
Triclinic	$\frac{1}{d^2} = \frac{1}{V^2} (S_{11}h^2 + S_{22}k^2 + S_{33}l^2 + 2S_{12}hk + 2S_{23}kl + 2S_{13}hl)$ $V = abc \sqrt{1 - \cos^2 \alpha - \cos^2 \beta - \cos^2 \gamma + 2 \cos \alpha \cos \beta \cos \gamma}$ $S_{11} = b^2 c^2 \sin^2 \alpha$ $S_{22} = a^2 c^2 \sin^2 \beta$ $S_{33} = a^2 b^2 \sin^2 \gamma$ $S_{12} = abc^2 (\cos \alpha \cos \beta - \cos \gamma)$ $S_{23} = a^2 bc (\cos \beta \cos \gamma - \cos \alpha)$ $S_{13} = ab^2 c (\cos \gamma \cos \alpha - \cos \beta)$

**Symmetric and Asymmetric Scans.** The two methods to obtain x-ray diffraction patterns are symmetric and asymmetric (also known as grazing incidence or glancing angle) scans.<sup>1-10</sup> A standard  $2\theta$  diffraction is a symmetric x-ray diffraction technique in which the incident angle (from the source) is equal to the angle of the diffracted beam (to the detector). This method is used for thick films and powder samples. For the asymmetric diffraction method, the incident angle is fixed at a small angle such as  $1^\circ$  and the detector angle is scanned. Using this fixed incident angle, the depth of penetration is decreased; thus, asymmetric diffraction is beneficial for thin film detection. Regardless of the configuration, Bragg's condition is met because the incident and diffracted beam is always  $2\theta$  and the Bragg angle,  $\theta$ , used in calculations is half the total angle ( $2\theta$ ). Good examples comparing the x-ray diffraction patterns of symmetric and asymmetric scans are found in Ref. 10.

**Williamson-Hall Analysis.** Peak shifts and broadening are seen in x-ray diffraction patterns. Uniform strain in the sample shifts the position of the diffraction peak compared to an unstrained sample.<sup>3</sup> The d-spacing will become smaller when the strain is uniformly compressive whereas it will be larger when the strain is uniformly tensile.<sup>3</sup> Broad peaks in a diffraction pattern may be attributed to both the nanocrystalline particle size of the powders and non-uniform strain in the sample.<sup>1-4,7,8,10,11</sup> The diffraction peaks broaden as the particle size decreases.<sup>1-4,7,8,10,11</sup> Non-uniform tensile and compressive forces produce a range of d-spacings that will broaden the peak instead of shifting the peak.<sup>1-4,7,8,10,11</sup> After taking into account instrumental broadening,

Williamson-Hall analysis can be applied to determine the contribution of peak broadening due to both particle size and strain.

The Williamson-Hall analysis assumes that peak broadening is due to a linear combination of broadening due to particle size,  $\beta_{\text{particle\_size}}$ , and non-uniform strain,  $\beta_{2\theta,\text{strain}}$ :

$$\beta_{\text{total}} = \beta_{\text{particle\_size}} + \beta_{2\theta,\text{strain}} \quad (2)$$

The Scherrer equation is used to determine the contribution of the particle size,  $\beta_{\text{particle\_size}}$ , in radians to the peak broadening.<sup>1,3</sup> The Scherrer equation is

$$\beta_{\text{particle\_size}} = \frac{0.94\lambda}{t \cos \theta} \quad (3)$$

where  $\lambda$  is the x-ray wavelength ( $\text{Cu}_{K\alpha} = 1.54 \text{ \AA}$ ),  $t$  is the particle size ( $\text{\AA}$ ), and  $\theta$  is half of the total angle ( $2\theta$ ).<sup>1,3</sup> The breadth due to particle size is eliminated once the particle size is above  $1 \text{ }\mu\text{m}$ .<sup>3</sup> Likewise, as the particle size decreases, the peaks become broader. Eventually, as these particles decrease in size, normally below  $1 \text{ nm}$ , the peaks will be indisquitable from the background.<sup>1,3,7</sup>

To determine the strain of the film, a derivative of Bragg's Law is used

$$\beta_{2\theta,\text{strain}} = 4 \tan \theta \frac{\Delta d}{d} \quad (4)$$

where  $\beta_{2\theta,\text{strain}}$  is the peak broadening due to strain in radians,  $\frac{\Delta d}{d}$  is the strain due to compressive and tensile strain, and  $\theta$  is half of the total angle ( $2\theta$ ).<sup>3,10</sup> Equation 5 shows the substituted equation of the Williamson-Hall analysis.

$$\beta_{\text{total}} = \beta_{\text{particle\_size}} + \beta_{2\theta,\text{strain}} = \frac{0.94\lambda}{t \cos \theta} + 4 \tan \theta \frac{\Delta d}{d} \quad (5)$$

A plot of the of the peak breadth total (corrected for instrumental broadening) in radians times  $\cos(\theta)$  versus  $4\sin(\theta)$  results in a straight line. As seen in Equation 6, the slope is the residual strain  $\left(\frac{\Delta d}{d}\right)$  and a quick calculation using the intercept yields the particle size ( $t$ ).

$$\beta_{\text{total}} \cos\theta = \frac{0.94\lambda}{t} + 4\sin\theta \frac{\Delta d}{d} \quad (6)$$

An example of this calculation is shown in Figure 1 for a ceria powder. In these results, the ceria powder has no preferred orientation with an average particle size of 7 nm and a residual strain of 0.5 %.

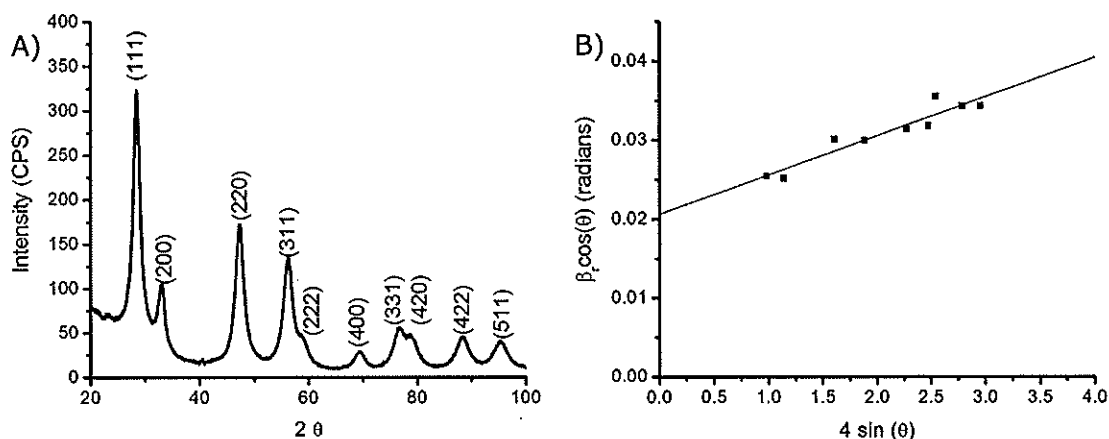


Figure 1. XRD scan and Williamson-Hall analysis of a ceria powder. Figure 1A shows a powder x-ray diffraction pattern of ceria nanopowders precipitated from a 0.1 M  $\text{Ce}(\text{NO}_3)_2$  and 0.1 M  $\text{NH}_4\text{C}_2\text{H}_3\text{O}_2$  solution bubbled with  $\text{O}_2$  at 65 °C. In Figure 1B, the Williamson-Hall analysis of the powder suggests a particle size of  $\sim 7$  nm and the residual strain of  $\sim 0.5\%$ .<sup>13</sup>

**Rietveld Refinement.** Originally created for crystal structure refinement using neutron diffraction, Rietveld refinement is a common sequential step after obtaining a symmetrical x-ray diffraction pattern to determine lattice parameters, angles, strain, and the crystallite size of the sample.<sup>3,8,11</sup> Polycrystalline powders and films are best for this analysis because Rietveld refinement is a standardless, whole pattern fitting method that assumes random orientation of the crystallites.<sup>3,8,11</sup> Refinement is accomplished by minimizing the squared difference between the observed and calculated patterns.<sup>3</sup> Modeling the experimental pattern utilizing a known structure allows the calculated cell parameters to be slightly modified until the calculated pattern is similar to the experimental pattern. The program also improves the calculated diffraction pattern by varying the crystal properties such as particle size and strain. Once the calculated pattern is nearly identical to the experimental pattern and refinement no longer improves the pattern, quantitative phase analysis provides information such as the lattice parameters, angles, strain, and crystallite size of the sample.<sup>3,8,11</sup>

A x-ray diffraction symmetric scan of a ceria powder generated by bubbling oxygen into a cerium(III)-acetate bath was run. The experimental (red line), the calculated (green +), and difference (lower black line) patterns of the Rietveld refinement are shown in Figure 1. A difference pattern is the difference between the calculated and experimental diffraction patterns. The calculated lattice parameter of the powder is 0.5425 nm which is about 0.26% larger than the literature value of 0.5411 nm (JCPDS 34-0394). Based on the peak broadening, the average particle size and non-uniform strain were determined to be 6.2 nm and 0.7%. The weighted pattern residual error ( $R_{wp}$ ), an indication of the quality of the fit obtained by the Rietveld refinement, is 5.48%.

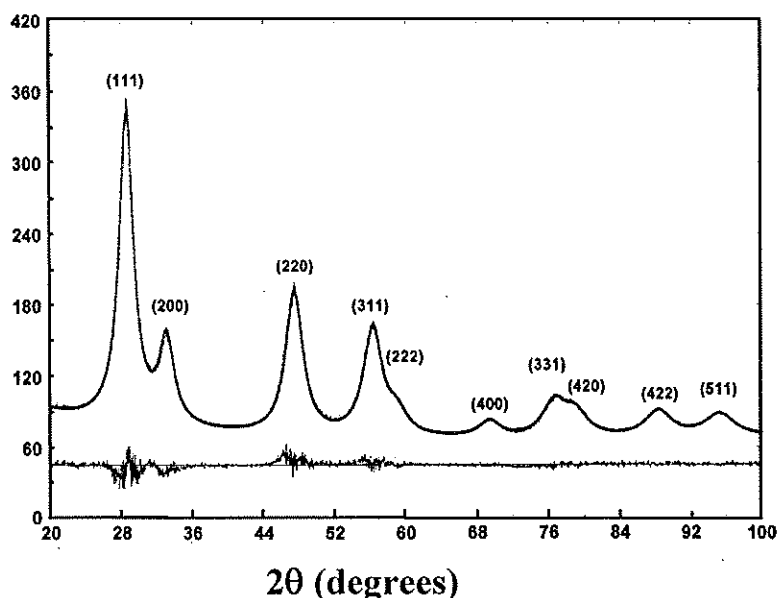


Figure 1. Rietveld analysis of a ceria powder generated by bubbling oxygen into a 0.4 M sodium acetate and 0.1 M cerium(III) acetate solution at 65 °C. The red line is the experimental x-ray diffraction pattern. The green pluses are the calculated x-ray diffraction pattern. The black line is the difference pattern between the two. Through the Rietveld refinement, the calculated lattice parameter of the ceria powder is 0.5425 nm with a particle size of 6.2 nm. (unpublished results)

**Vegard's Law.** The lattice parameters can be used as an indicator of composition. Usually, the unit cell expands if a small ion is being replaced by a bigger one and vice versa.<sup>1,3,7,12,13</sup> This shift can be seen in the XRD pattern in that if a smaller ion is substituted into the cell, then the d-spacing decreases and the peaks of the XRD pattern shift to larger values of  $2\theta$ . Vegard's law assumes that the changes in the unit cell parameters vary directly with composition which is controlled by the relative sizes of the ions substituting in the solid.<sup>1,3,7,12,13</sup> If a plot of the lattice parameter or d-spacing versus composition is linear, then Vegard's law is obeyed. Zen's law, a derivative of Vegard's

law, linearly interpolates composition versus the cell volume instead of the lattice parameter. Zen's law is beneficial for noncubic materials where the expansion or contraction of the unit cell with changing composition is not the same for all three axes. Vegard's or Zen's law is not obeyed when small ions like borides, carbides, and nitrides fit into the interstitial sites of lattices.<sup>3,7</sup> Slight divergences from linearity of these laws are not well understood since the observed departures are not consistent from system to system so as to develop trends or correlations to predict a positive or negative departure.<sup>1,7,12</sup> However, large departures from the laws have been contributed to a change in the crystal symmetry or a more complicated substitution mechanism.<sup>7,12</sup>

**X-ray Reflectivity.** Films, crystalline or amorphous, can be studied by x-ray reflectivity if the film and the substrate are smooth enough that interface roughness effects do not completely overwhelm the reflectivity signal. This method works best for films with thicknesses ranging 0.5 to 400 nm, a film roughness less than 20 nanometers, and a significant difference between the density of the film and the substrate.<sup>13</sup> A thicker film will have more fringes in the pattern than a thinner film will. As the film roughness increases, the intensity of the fringes decreases. The first fringe will occur at a higher  $2\theta$  value as the density difference between the film and substrate increases.

Based on these relationships, the thickness and density of the film can be determined using this method. From the fringes in the reflectance, the film thickness ( $t$ ) of the sample is calculated using a modified Bragg equation:

$$\sin^2\theta_i = \theta_c^2 + \frac{(n_i + \Delta n)^2 \lambda^2}{4t^2} \quad (6)$$

Here both the maxima and minima are used, with  $\theta_i$  the observed angle,  $\theta_c$  the critical angle for total external reflection,  $\lambda$  the x-ray wavelength,  $n_i$  an integer for the  $i^{\text{th}}$  fringe, and  $\Delta n = 0$  or  $1/2$  for minima and maxima respectively.<sup>13,14</sup> Plotting  $(n_i + \Delta n)^2$  versus  $\sin^2\theta_i$  yields the film thickness and critical angle.<sup>13,14</sup>

The density of the film can be determined from the critical angle, assuming negligible anomalous dispersion, by the following:

$$\theta_c^2 = \frac{N_A r_e \lambda^2 f}{\pi A} \rho \quad (7)$$

where  $N_A$  is Avogadro's number,  $r_e$  is the classical electron radius ( $2.8179 \times 10^{-13}$  cm),  $\lambda$  is the x-ray wavelength,  $f$  is the real part of the atomic scattering factor ( $\approx Z$ ),  $A$  is the average atomic mass, and  $\rho$  is the density.<sup>13,14</sup>

Figure 8A shows the x-ray reflectivity scan of a ceria film on a nickel Hastelloy alloy substrate. Figure 8B shows the plot of this data to determine the film thickness and the critical angle. Based on the slope of the line, the film thickness was calculated to be 39 nm. From the intercept, the density of this film was calculated to be  $4.48 \text{ g/cm}^3$  (~61% of the bulk density).<sup>14</sup>

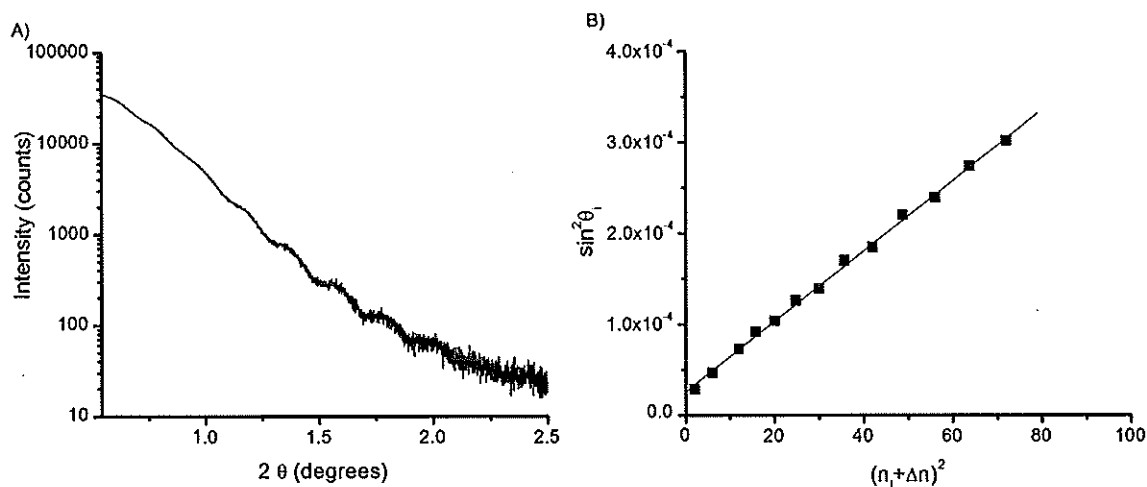


**Figure 8.** (A) X-ray reflectivity of a ceria film grown for 1000 s at +0.5 V vs. Ag/AgCl and 65 °C, showing a number of interference fringes. (B) Least-squares fit of the fringe numbers to determine film thickness (39 nm) and critical angle ( $\theta_c = 5 \times 10^{-3}$  rad, or  $2\theta_c = 0.573^\circ$ ) for this sample.<sup>14</sup>

**Epitaxial Films.** Epitaxy is the growth of a film on a crystalline substrate in which the film orientation is determined by the orientation of the substrate. One method to produce epitaxial films onto single crystalline conductive substrates is electrodeposition. The Switzer group has produced a variety of metal oxides such as  $\text{Fe}_3\text{O}_4$ ,<sup>15-16</sup>  $\text{Bi}_2\text{O}_3$ ,<sup>17,18</sup> and  $\text{ZnO}$ <sup>14,19</sup> on low index gold single crystals. They have also produced chiral epitaxial CuO films on single-crystal Au<sup>20-22</sup> and Cu.<sup>23</sup> Their most complete epitaxial studies have been  $\text{Cu}_2\text{O}$  on single-crystal Au,<sup>24-25</sup> Cu,<sup>26</sup> Si,<sup>27-29</sup> and InP.<sup>29-32</sup>

**2 $\theta$  Scans of Epitaxial Films.** Figure 2 shows two x-ray diffraction patterns of cuprous oxide (Cu<sub>2</sub>O) films on A) stainless steel and B) Au(001). In Figure 2A, a 2 $\theta$  pattern of a polycrystalline film shows all the peaks of the film, similar to the powder diffraction pattern of a material, because all possible orientations of the material are present. As in the powder diffraction pattern, the (111) is the most intense peak in the diffraction pattern. The ratio of the other orientations to this peak match the ratios found on the XRD card file of powder Cu<sub>2</sub>O showing that this film has no preferred orientation.

An epitaxial film will normally have only one orientation so it will only show a series of family planes in the x-ray diffraction pattern, as seen in Figure 2B. When the peaks are only associated with family planes or the family plane peaks are more intense than they should be in the powder patterns, these films are said to have a strong out-of-plane orientation or texture. In addition, an epitaxial film will typically grow with a minimal lattice mismatch. The lattice mismatch is calculated based on the XRD pattern of these films simply by dividing the difference between the lattice parameter (or d-spacing of a plane) of the film and the lattice parameter (or d-spacing of a plane) of substrate by the lattice parameter (or d-spacing of a plane) of the substrate. For example, the lattice mismatch of (002)Cu<sub>2</sub>O and (002)Au is  $\frac{(2.135 - 2.039)}{2.039} * 100 = 4.7\%$  whereas another orientation like (111)Cu<sub>2</sub>O on (002)Au would have a lattice mismatch of 20.9%. However, a strong out-of-plane texture with a low mismatch does not provide proof of an epitaxial film.

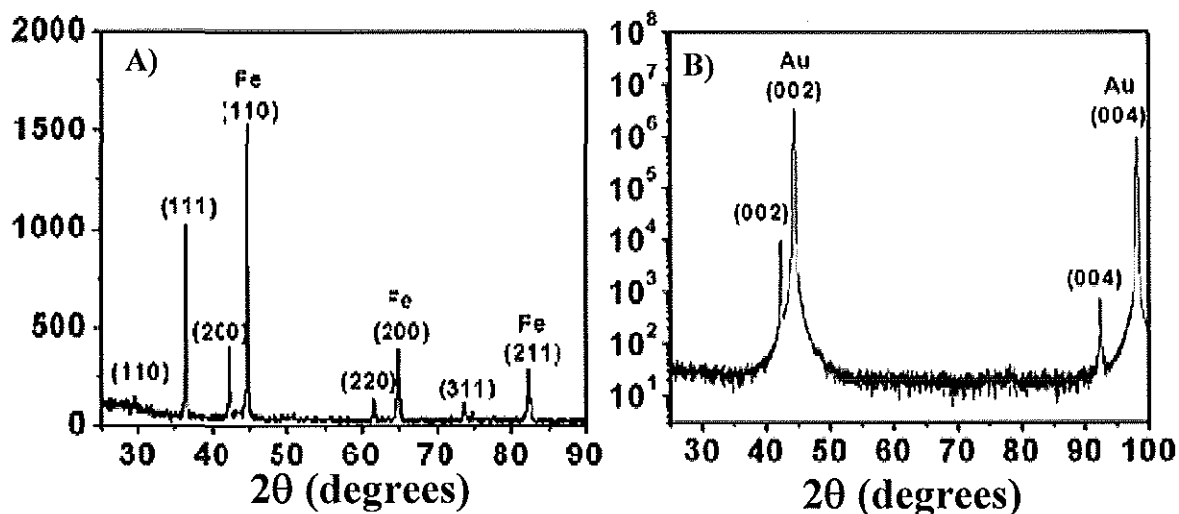


Figure 2: X-ray diffraction patterns of electrodeposited A) polycrystalline cuprous oxide film on stainless steel (Fe) and B) (001) oriented cuprous oxide film on a Au(001) single crystal.

**Pole Figures of Epitaxial Films.** An epitaxial film has out-of-plane and in-plane orientation. To determine the in-plane orientation distribution of the grains of the film, x-ray pole figures are run.<sup>1</sup> A pole figure probes reflections of planes that are oriented in-plane with respect to the sample normal while measuring the diffracted intensity as a function of sample tilt ( $\chi$ ) and rotation ( $\phi$ ).<sup>1,2</sup> To perform the pole figure analysis, the  $2\theta$  is set to the angle of the plane (reflection) of interest, normally the orientation with the highest intensity of a randomly oriented powder diffraction pattern of the material. The  $2\theta$  value is held constant. The sample is moved through a sequence of tilt angles,  $\chi$ , from  $0^\circ$  to  $90^\circ$ , as well as at each  $\chi$ , the sample is rotated azimuthally,  $\phi$ , from  $0^\circ$  to  $360^\circ$ . A peak results when Bragg's condition is met.

Figure 3 shows the morphologies and (011) pole figure results of three different scenarios of a cubic material such as  $\text{Cu}_2\text{O}$  deposited on a substrate. As seen in Figure 3A, a polycrystalline film has no out-of-plane or in-plane orientation. Each grain in the polycrystalline film has an orientation different than that of its neighbor resulting in a randomly distributed film.<sup>1,11,33</sup> A pole figure on this sample would have uniform intensity at all tilt and azimuthal angles (Figure 3D). Figure 3B and 3C show films with (001) out-of-plane orientation. In both cases, the grains have the same crystallographic orientation as its neighbor. Both would be characterized as having a nonrandom, preferred orientation.<sup>1,11</sup> However, the deposits of Figure 3B have multiple in-plane orientations known as a fiber texture while the deposits of Figure 3C are aligned in one in-plane orientation, an example of epitaxial growth.<sup>1,11,33</sup> A (001) fiber-textured film has a ring pattern pole figure at  $\chi = 45^\circ$  as seen in Figure 3E whereas an epitaxial film has a pole figure with four peaks at  $\chi = 45^\circ$  as seen in Figure 3F. The ring pattern in Figure 3E can be understood by using Figure 3F. Since the deposits in Figure 3B are rotated azimuthally with respect to one another, each aligned set would produce four peaks. Each set of four peaks are slightly shifted from each other. Therefore, a pole figure of a fiber-textured film is a product of multiple four peaks rotating azimuthally and converging together to form a ring.

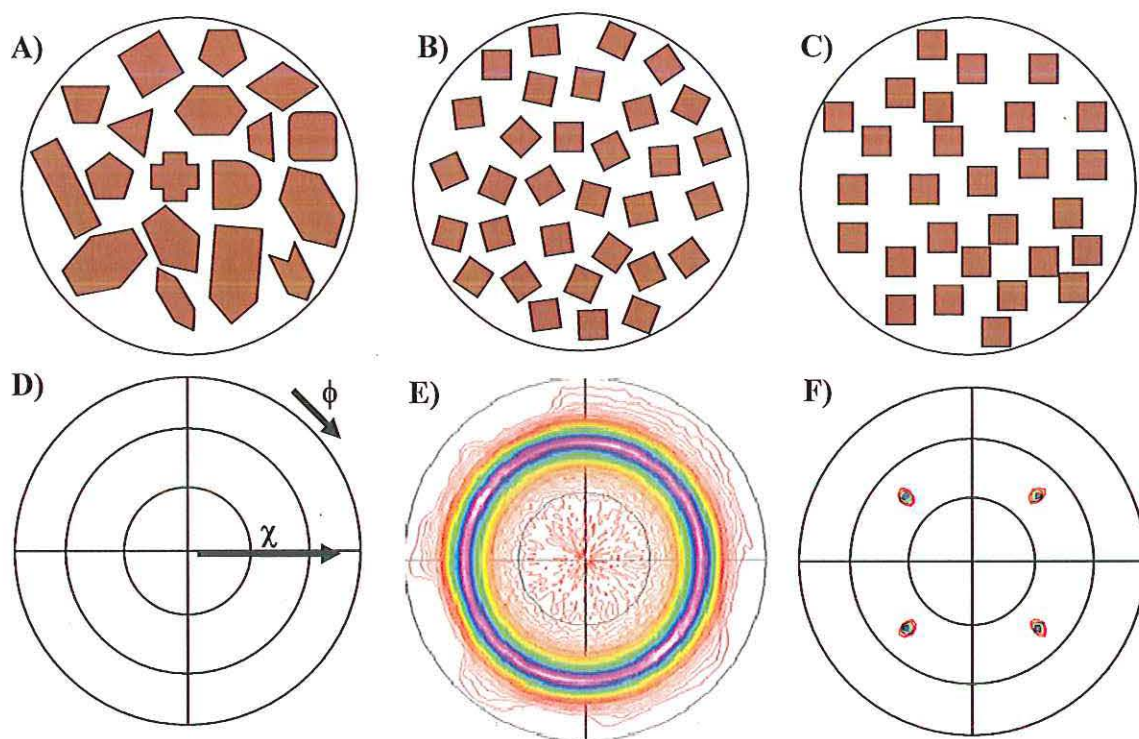


Figure 3: Illustrations of the cubic material cuprous oxide ( $\text{Cu}_2\text{O}$ ) as A) a polycrystalline film on stainless steel, B) a (001) fiber-textured film, on stainless steel and C) a (001) epitaxial film on Au(001). (011) Cuprous oxide pole figures of a D) polycrystalline, E) (001) fiber-textured, and F) (001) epitaxial films.

**Azimuthal scan.** An azimuthal scan can be considered a cross-section of a pole figure. An azimuthal scan is obtained when the measurement is carried out at a specific  $2\theta$  for only one specific tilt angle,  $\chi$ , and rotated azimuthally,  $\phi$ , from  $0^\circ$  to  $360^\circ$ . If the sample has an in-plane orientation, the azimuthal scan will show separated peaks at a specific tilt. If the sample has a fiber texture, the azimuthal scan will show equal intensity rather than peaks higher than the baseline at a specific tilt.

Pole figures and azimuthal scans are also performed on the substrate to determine the film alignment on the substrate, the number of domains, and the angles of separation of the domains.<sup>1</sup> The azimuthal scans of (011)Cu<sub>2</sub>O and (022)Au are shown in Figure 4. For Figure 4A, the 2 $\theta$  is set to the (011) 2 $\theta$  of Cu<sub>2</sub>O, 29.6°. For Figure 4B, the 2 $\theta$  is set to the (022) 2 $\theta$  of Au at 44.6°. By examining these scans, both show four equivalent reflections separated by 90° indicating the film and the substrate are both (001) oriented and have only one domain based on the symmetry of the (001) plane. Also, the peaks of the film are aligned with the peaks of the substrate. So, the film is not rotated on the substrate. Once this film and the substrate analyses are completed, the epitaxial relationships are determined.

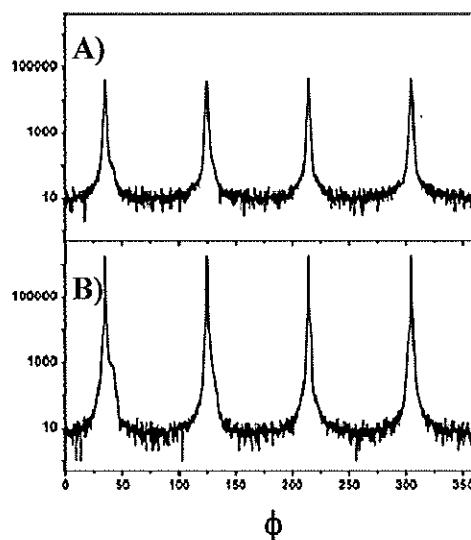


Figure 4: Azimuthal scans of an electrodeposited A) (001)Cu<sub>2</sub>O film on B) (001)Au at  $\chi = 45^\circ$ . For Figure 4A, the 2 $\theta$  is set to the (011) 2 $\theta$  of Cu<sub>2</sub>O, 29.6°. For Figure 4B, the 2 $\theta$  is set to the (022) 2 $\theta$  of Au at 44.6°. The film is epitaxial with one domain and is aligned on the substrate. (unpublished results)

**Stereographic projections.** An epitaxial relationship describes how the film is oriented relative to the substrate by finding a direction of the film that is parallel to a direction in the substrate.<sup>2,33</sup> To determine the epitaxial relationship, stereographic projections are often used.<sup>2,33</sup> A stereographic projection is a two-dimensional plot that shows the angular relationships of the crystal's faces and directions based on its crystallographic symmetry.<sup>1-3,33</sup> Simply, a stereographic projection is a way to represent a three-dimensional crystal on a two-dimensional page. So, a pole figure is similar to a stereographic projection with only specific reflections shown.<sup>1,2</sup>

Programs to produce stereographic projections are available such as Desktop Microscopist and CaRIne Crystallography for purchase or on the internet for free.<sup>33</sup> To determine the tilt angle between two planes, one representing the orientation of the film and the other the reflections being probed, the equations in Table 2 are used.<sup>1</sup> For a cubic system, a few calculated tilt angles are tabulated in Table 3.<sup>1</sup>

Table 2 where the angle  $\chi$  between the plane  $(h_1k_1l_1)$  with spacing  $d_1$  and the plane  $(h_2k_2l_2)$  with spacing  $d_2$ , utilizing this information and the lattice parameters:<sup>1</sup>

System	Tilt angle ( $\chi$ ) between two planes $(h_1k_1l_1)$ and $(h_2k_2l_2)$
Cubic	$\cos \chi = \frac{h_1h_2 + k_1k_2 + l_1l_2}{\sqrt{(h_1^2 + k_1^2 + l_1^2)(h_2^2 + k_2^2 + l_2^2)}}$
Tetragonal	$\cos \chi = \frac{\frac{h_1h_2 + k_1k_2}{a^2} + \frac{l_1l_2}{c^2}}{\sqrt{\left(\frac{h_1^2 + k_1^2 + l_1^2}{a^2 + b^2 + c^2}\right)\left(\frac{h_2^2 + k_2^2 + l_2^2}{a^2 + b^2 + c^2}\right)}}$
Orthorhombic	$\cos \chi = \frac{\frac{h_1h_2}{a^2} + \frac{k_1k_2}{b^2} + \frac{l_1l_2}{c^2}}{\sqrt{\left(\frac{h_1^2 + k_1^2 + l_1^2}{a^2 + b^2 + c^2}\right)\left(\frac{h_2^2 + k_2^2 + l_2^2}{a^2 + b^2 + c^2}\right)}}$
Hexagonal	$\cos \chi = \frac{h_1h_2 + k_1k_2 + \frac{1}{2}(h_1k_2 + h_2k_1) + \frac{3a^2}{4c^2}l_1l_2}{\sqrt{\left(h_1^2 + k_1^2 + h_1k_1 + \frac{3a^2}{4c^2}l_1^2\right)\left(h_2^2 + k_2^2 + h_2k_2 + \frac{3a^2}{4c^2}l_2^2\right)}}$
Rhombohedral	$\cos \chi = \frac{a^4d_1d_2}{V^2} \left[ \sin^2 \alpha (h_1h_2 + k_1k_2 + l_1l_2) + \right.$ $\left. (\cos^2 \alpha - \cos \alpha)(k_1l_2 + k_2l_1 + l_1h_2 + h_1k_2 + h_2k_1) \right]$ <p>where :</p> $V = a^3 \sqrt{1 - 3\cos^2 \alpha + 2\cos^3 \alpha}$
Monoclinic	$\cos \chi = \frac{d_1d_2}{\sin^2 \beta} \left[ \frac{h_1h_2}{a^2} + \frac{k_1k_2}{b^2} + \frac{l_1l_2}{c^2} - \frac{(l_1h_2 + l_2h_1)\cos \beta}{ac} \right]$
Triclinic	$\cos \chi = \frac{d_1d_2}{V^2} \left( S_{11}h_1h_2 + S_{22}k_1k_2 + S_{33}l_1l_2 + \right.$ $\left. S_{12}(h_1k_2 + h_2k_1) + S_{23}(k_1l_2 + k_2l_1) + S_{13}(h_1l_2 + h_2l_1) \right)$ <p>where :</p> $V = abc \sqrt{1 - \cos^2 \alpha - \cos^2 \beta - \cos^2 \gamma + 2\cos \alpha \cos \beta \cos \gamma}$ $S_{11} = b^2c^2 \sin^2 \alpha$ $S_{22} = a^2c^2 \sin^2 \beta$ $S_{33} = a^2b^2 \sin^2 \gamma$ $S_{12} = abc^2(\cos \alpha \cos \beta - \cos \gamma)$ $S_{23} = a^2bc(\cos \beta \cos \gamma - \cos \alpha)$ $S_{13} = ab^2c(\cos \gamma \cos \alpha - \cos \beta)$

Table 3. The interplanar angles in degrees between the plane  $(h_1k_1l_1)$  and the plane  $(h_2k_2l_2)$  of cubic systems used in Figure 5.<sup>1</sup>

$\{h_2k_2l_2\}$	$\{h_1k_1l_1\}$		
	$\{001\}$	$\{011\}$	$\{111\}$
$\{001\}$	0	45	54.7
	90	90	
$\{011\}$	45	0	35.3
	90	60	90
		90	
$\{111\}$	54.7	35.3	0
		90	70.5

The stereographic projections of cubic materials oriented  $[111]$ ,  $[011]$ , and  $[001]$  are shown in Figure 5, respectively, showing  $\{001\}$ ,  $\{011\}$ , and  $\{111\}$  reflections as generated by CaRIne Crystallography 3.1 software. However, pole figures are such that only one family of reflections can be probed at a time. So, normally for epitaxial studies, stereographic projects are produced to just show the reflections of interest. In Figure 6, the stereographic projects show the reflections of A)  $\{111\}$ , B)  $\{110\}$ , and  $\{100\}$  for an epitaxial  $(001)$  cubic film with one domain. The  $\chi$  values can be found in Table 3. In Figure 6, the  $[010]$  direction is pointed north and the  $[100]$  direction is pointed east for each stereographic projection.

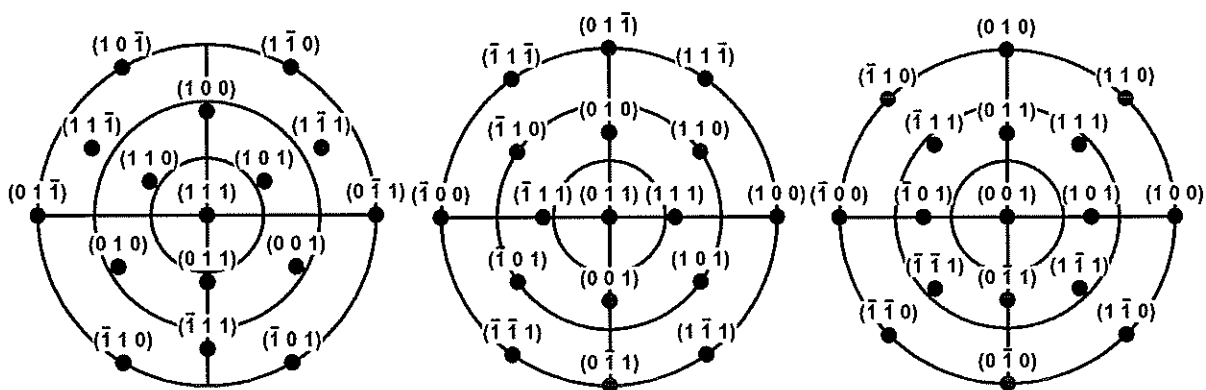


Figure 5. Stereographic projections of a cubic material with a A)  $[111]$ , B)  $[011]$ , and C)  $[001]$  orientation showing only  $\{111\}$ ,  $\{011\}$ , and  $\{001\}$  reflections.

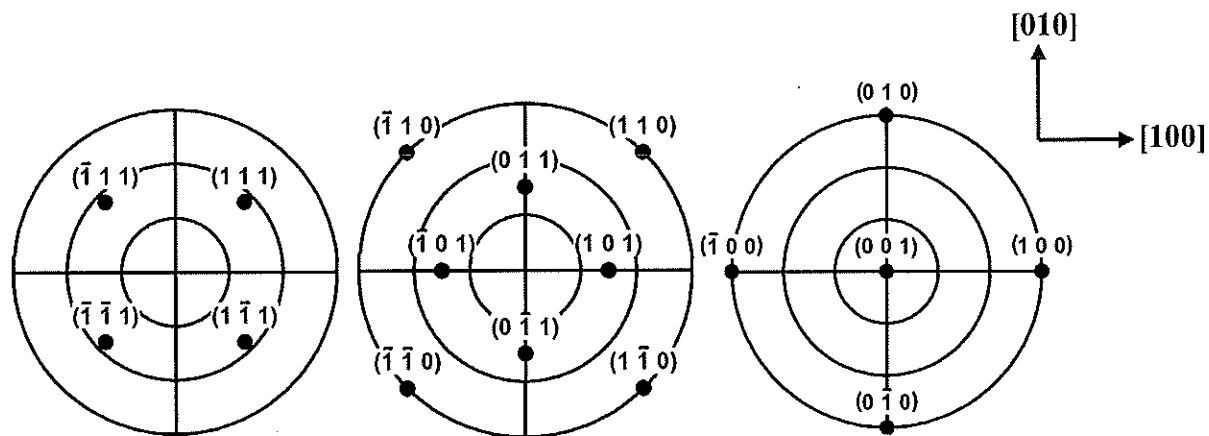


Figure 6. Stereographic projections for an epitaxial  $(001)$  oriented cubic film on  $\text{Au}(001)$  indicating the positions where A) the  $(111)$ -type, B) the  $(110)$ -type, and C) the  $(100)$ -type reflections that would be observed in the pole figures for a single domain film.

Cubic systems are unique in that their directions, indicated by brackets, are always normal to the planes (reflections). An epitaxial relationship describes how the film is oriented relative to the substrate by finding a direction of the film that is parallel to a direction in the substrate.<sup>2,33</sup> The pole figures of the reflections are dependent on one another because they are all related by the orientation of the sample. Regardless of the pole figures run, an epitaxial relationship can be determined. In Figure 6, the directions shown on the left are held constant for each of the stereographic projections.

In some instances multiple directions of the film can be parallel to multiple directions of the substrate. So, multiple epitaxial relationships that describe the film's orientation on the substrate exist. For example, the (001)Cu<sub>2</sub>O film on (001)Au shown in Figure 3F and 4 indicates that the film grows with one domain and is directly aligned with the substrate. Equivalent epitaxial relationships that describe how the film aligns on the substrate are Cu<sub>2</sub>O(001)[100]//Au(001)[100], Cu<sub>2</sub>O(001)[010]//Au(001)[010], Cu<sub>2</sub>O(001)[ $\bar{1}00$ ]//Au(001)[ $\bar{1}00$ ], Cu<sub>2</sub>O(001)[0 $\bar{1}0$ ]//Au(001)[0 $\bar{1}0$ ], Cu<sub>2</sub>O(001)[010]//Au(001)[100], Cu<sub>2</sub>O(001)[100]//Au(001)[010], and even Cu<sub>2</sub>O(001)[110]//Au(001)[110], Cu<sub>2</sub>O(001)[210]//Au(001)[210], and Cu<sub>2</sub>O(001)[520]//Au(001)[520]. By convention, the lowest index planes and directions are used for the epitaxial relationship. So, the reported epitaxial relationship would be Cu<sub>2</sub>O(001)[100]//Au(001)[100]. That is the Cu<sub>2</sub>O(001) and Au(001) planes are parallel and the Cu<sub>2</sub>O[100] and Au[100] in-plane directions are coincident.

**Rocking curves.** X-ray rocking curves measure the crystallographic quality (i.e. mosaic spread) of the films relative to the substrate. Mosaic spread is the misorientation of domains. In a perfect crystal, all the domains are aligned and no atomic dislocations are present (no mosaic spread). A large mosaic spread means poor crystal quality. For a rocking curve, the  $2\theta$  is set to a single diffraction peak, one of the family orientations present in the x-ray pattern of the epitaxial film. A rocking curve is performed by “rocking” the sample which brings each grain into Bragg’s condition.<sup>1</sup> The width of the rocking curve is a direct measurement of the range of orientation of the sample.<sup>1</sup> When the film is highly ordered, the full width at half maximum (FWHM) of the rocking curve peak is small. Rocking curves with broader peaks (bigger FWHM) have larger mosaic spreads. The rocking curves of the film and of the substrate are performed for mosaic spread comparison. This mosaic spreads of the film and the substrate are also seen in pole figures. The peaks in the pole figure become sharper and more intense when the film is more ordered.

**Superlattices.** Superlattices are characterized by XRD since the periodicity shows itself as satellites around the main Bragg peak. The fundamental reflection, main Bragg peak, is labeled as 0. The satellite peaks towards higher angles, to the right of the main Bragg peak, are labeled +1, +2, and so on whereas satellites are labeled -1, -2, at smaller angles. In a superlattice, the bilayer thickness is known as the modulation wavelength,  $\Lambda$ . The modulation wavelength,  $\Lambda$ , can be measured from the satellite spacing utilizing the following equation:

$$\Lambda = \frac{\lambda(L_1 - L_2)}{2(\sin \theta_1 - \sin \theta_2)} \quad (9)$$

Here,  $\lambda$  is the wavelength of the x-ray source (Cu  $K_\alpha$  1.5401 Å),  $L$  is the order of the satellite (i.e. 0, -1, or 2) and  $\theta$  is the diffraction angle of that reflection. As the  $\Lambda$  increases, the satellites move closer to the main Bragg peak. As the bilayers become thicker, eventually no satellites are seen and two separate peaks exist, one for each material of the bilayer.

## REFERENCES

1. B. D. Cullity, *Elements of X-ray Diffraction* (Addison-Wesley, Reading, 2<sup>nd</sup> ed., 1978).
2. C. Hammond, *The Basics of Crystallography and Diffraction* (Oxford University, New York, 2<sup>nd</sup> ed., 2001).
3. R. Jenkins, R. L. Snyder, *Introduction to X-ray Powder Diffraction* (Wiley, New York, 1996).
4. A. Guinier, *X-ray Diffraction in Crystals, Imperfect Crystals, and Amorphous Bodies* (Freeman, San Francisco, 1963).
5. J.-J. Rousseau, *Basic Crystallography* (Wiley, New York, 1998).
6. W. Borchardt-Ott, *Crystallography* (Springer, New York, 2<sup>nd</sup> ed., 1995).
7. A. R. West, *Solid State Chemistry and its Applications* (Wiley, New York, 1984).
8. H & M Analytical Services, Inc., (2001). *Literature* [online]. Available: [http://www.h- and m- analytical.com/literature.htm](http://www.h-and-m-analytical.com/literature.htm) [accessed 28 May 2008]
9. University of Cambridge, (2007). *X-ray Diffraction Techniques* [online]. Available : <http://www.doitpoms.ac.uk/tlplib/xray-diffraction/index.php> [accessed 28 May 2008]
10. R. J. Phillips. Ph.D. Dissertation from the University of Missouri-Rolla, 1995 pp. 215-231.
11. W. I. F. David, K. Shankland, L.B. McCusker, C. Baerlocher, *Structure Determination from Powder Diffraction Data* (Oxford University, New York, 2002).
12. W. D. Kingery, H. K. Bowen, D. R. Uhlmann, *Introduction to Ceramics* (Wiley, New York, 2<sup>nd</sup> ed., 1976).
13. T.C. Huang, R. Gilles, G. Will, *Thin Solid Films* **230**, 99 (1993).

14. E. A. Kulp, S. J. Limmer, E. W. Bohannan, J. A. Switzer, *Solid State Ionics* **178**, 749-757 (2007).
15. M. P. Nikiforov, A. A. Vertegel, M. G. Shumsky, J. A. Switzer, *Adv. Mater.* **12**, 1351-1353 (2000).
16. T. A. Sorenson, S. A. Morton, G. D. Waddill, J. A. Switzer, *J. Amer. Chem. Soc.*, **124**, 7604-7609 (2002).
17. J. A. Switzer, M. G. Shumsky, E. W. Bohannan, *Science*, **284**, 293-296 (1999).
18. E. W. Bohannan, C. C. Jaynes, M. G. Shumsky, J. K. Barton, J. A. Switzer, *Solid State Ionics*, **131**, 97-107 (2000).
19. R. Liu, A. A. Vertegel, E. W. Bohannan, T. A. Sorenson, J. A. Switzer, *Chem. Mater.* **13**, 508-512 (2001).
20. J. A. Switzer, H. M. Kothari, P. Poizot, S. Nakanishi, E. W. Bohannan, *Nature* **425**, 490-493 (2003).
21. H. M. Kothari, E. A. Kulp, S. Boonsalee, M. P. Nikiforov, E. W. Bohannan, P. Poizot, S. Nakanishi, J. A. Switzer, *Chem. Mater.* **16**, 4232-4244 (2004).
22. S. K. Sarkar, N. Burla, E. W. Bohannan, J. A. Switzer, *J. Am. Chem. Soc.* **129**, 8972-8973 (2007).
23. E. W. Bohannan, H. M. Kothari, I. M. Nicic, J. A. Switzer, *J. Am. Chem. Soc.* **126**, 488-489 (2004).
24. J. A. Switzer, M. G. Shumsky, E. W. Bohannan, *Chem. Mater.* **11**, 2289-2291 (1999).
25. J. A. Switzer, H. M. Kothari, E. W. Bohannan, *J. Phys. Chem. B* **106**, 4027-4031 (2000).
26. J. K. Barton, A. A. Vertegel, E. W. Bohannan, J. A. Switzer, *Chem. Mater.* **13**, 952-959 (2001).
27. J. A. Switzer, R. Liu, E. W. Bohannan, F. Ernst, *J. Phys. Chem. B* **106**, 12369-12372 (2002).

28. R. Liu, F. Oba, E. W. Bohannon, F. Ernst, J. A. Switzer, *Chem. Mater.* **15**, 4882-4885 (2003).
29. F. Oba, F. Ernst, Y. Yu, R. Liu, H. M. Kothari, J. A. Switzer, *J. Am. Ceram. Soc.* **88**, 253-270 (2005).
30. R. Liu, E. A. Kulp, E. W. Bohannon, F. Ernst, J. A. Switzer, *Chem. Mater.* **17**, 725-729 (2005).
31. R. Liu, F. Oba, E. W. Bohannon, F. Ernst, J. A. Switzer, *Chem. Mater.* **15**, 4882-4885 (2003).
32. R. Liu, E. W. Bohannon, J. A. Switzer, F. Oba, F. Ernst, *Appl. Phys. Lett.* **83**, 1944-1946 (2003).
33. D. B. Williams, C. B. Carter, *Transmission Electron Microscopy: A Textbook for Materials Science* (Plenum, New York, 1996).

## APPENDIX C

## ELECTROCHEMICAL BIOMINERALIZATION

## **Electrochemical Biomineralization: the Deposition of Calcite with Chiral Morphologies**

### **Supporting Information**

*Elizabeth A. Kulp and Jay A. Switzer\**

Department of Chemistry and Graduate Center for Materials Research, University of Missouri-Rolla, Rolla, Missouri 65409-1170, USA

[jswitzer@umr.edu](mailto:jswitzer@umr.edu)

#### **Electrochemical Deposition**

The calcium carbonate films were deposited at 30 °C using a constant potential of -1.1 V vs. Ag/AgCl for 1800-3600 s. The argon purged deposition solution consisted of 4.1 mM CaCl<sub>2</sub>\*2H<sub>2</sub>O and 7.1 mM NaHCO<sub>3</sub> with additive concentrations of 3.2 mM MgCl<sub>2</sub>, 2.5 mM of succinic acid, 2.0 mM of the enantiomer of tartaric acid, 2.2 mM of the enantiomer and racemic malic acid, or 4.5 mM of the enantiomer of aspartic acid. All of the films were deposited onto stainless steel substrates.

#### **Characterization Techniques**

Grazing incidence X-ray diffraction patterns were run on a high-resolution Philips X'Pert MRD diffractometer using CuK<sub>α</sub> source radiation with an X-ray mirror as the incident beam module and 0.18° parallel plate collimator as the diffracted beam module. A fixed incident angle of 1° was maintained. Stereographic projections were simulated for the calcite crystal structure using CaRIne 3.1 software. SEM images were obtained on

uncoated samples using a Hitachi S-4700 cold field-emission scanning electron microscope with an EDAX energy dispersive x-ray unit for elemental analysis.

### **Symmetry Aspects of Chirality for the Calcite Crystal Structure**

The chiral nature of calcite planes is easily visualized in stereographic projections. A stereographic projection is a two-dimensional plot that shows the angular relationships of the crystal's faces based on its crystallographic symmetry. As seen in Figures 1aS and 1bS, the stereographic projections of  $(10\bar{1}4)$  and  $(\bar{1}01\bar{4})$  are superimposable mirror images of each other. Therefore, these planes are achiral. However, the nonsuperimposable stereographic projections of the  $(11\bar{2}0)$  and  $(\bar{1}\bar{1}20)$  orientations and the  $(21\bar{3}1)$  and  $(\bar{2}\bar{1}3\bar{1})$  orientations of calcite show that they are enantiomers of each other (Figures 1cS, 1dS, 1eS, and 1fS, respectively).

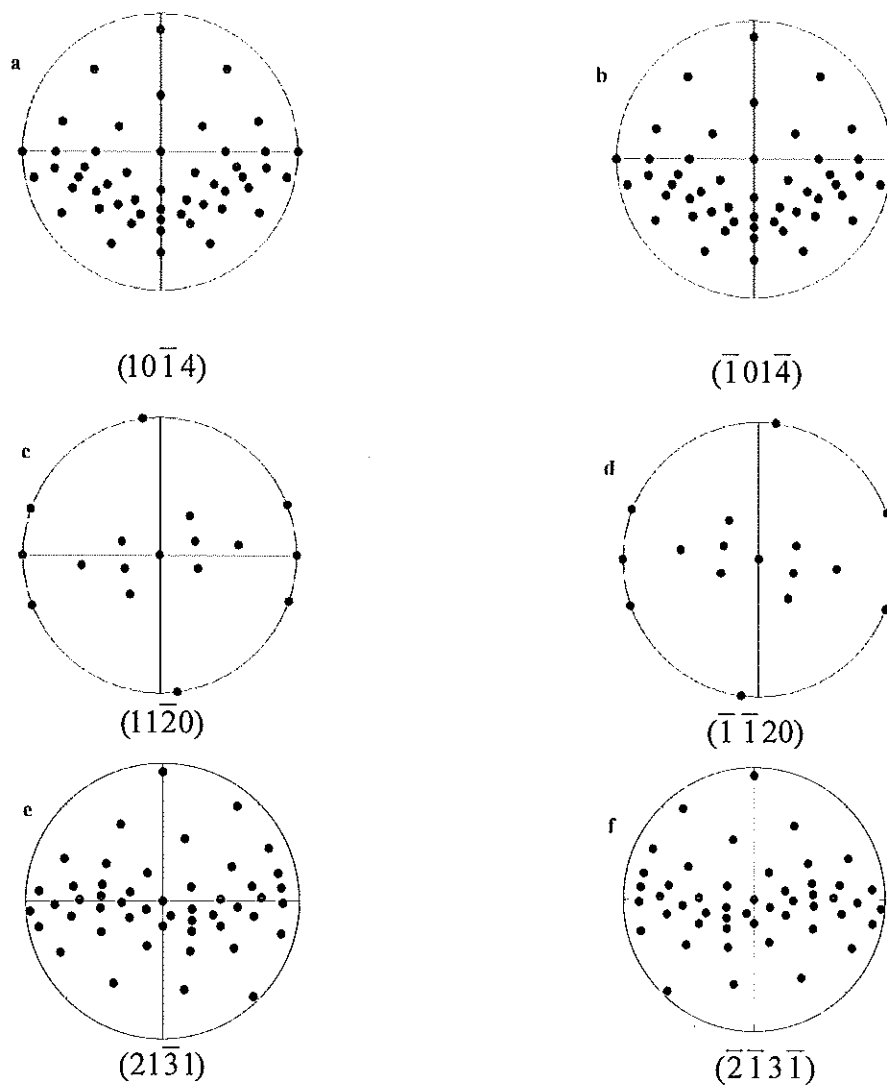
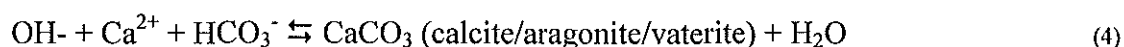
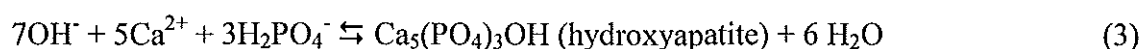
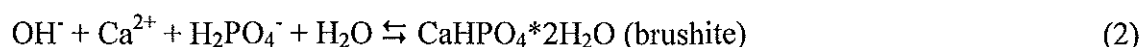


**Figure 1S** Stereographic projections of achiral and chiral orientations of calcite. The orientations (a)  $(10\bar{1}4)$  and (b)  $(\bar{1}01\bar{4})$  are achiral because the two stereographic projections have mirror symmetry and are superimposable. The orientations (c)  $(11\bar{2}0)$  and (d)  $(\bar{1}\bar{1}20)$  as well as (e)  $(21\bar{3}1)$  and (f)  $(\bar{2}\bar{1}3\bar{1})$  are chiral because the two stereographic projections lack mirror symmetry and are not superimposable.

### Electrochemical Biomineralization

The biominerals brushite, hydroxyapatite, calcite, and aragonite can then be electrodeposited by using the electrochemically generated base (Eq. 1) to react with  $\text{H}_2\text{PO}_4^-$  or  $\text{HCO}_3^-$  in solutions containing  $\text{Ca}^{2+}$  according to equation 2-4.



Brushite films with a (010) preferred orientation are deposited from a saturated solution of  $\text{Ca}(\text{H}_2\text{PO}_4)_2$  at 25°C using a cathodic current density of 10 mA/cm<sup>2</sup> for 8000 s. Hydroxyapatite is deposited from a saturated solution of  $\text{Ca}(\text{H}_2\text{PO}_4)_2$  containing 24 mM NaF and 1 M NaNO<sub>3</sub>. The solution is filtered and heated to 65°C. The film is electrodeposited using a cathodic current density of 6 mA/cm<sup>2</sup> for 1200 s. These solutions were purged with argon to eliminate side reactions such as the precipitation of calcium carbonates and the reduction of dissolved oxygen. Figure 1 shows SEM micrographs of A) brushite and B) hydroxyapatite electrodeposited on stainless steel.

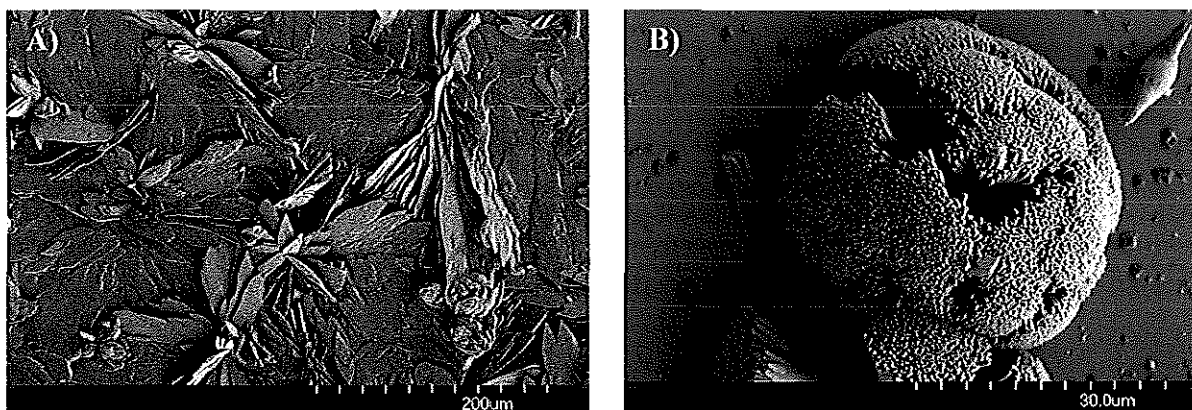


Figure 1. SEM images of electrodeposited calcium phosphates, A) brushite and B) hydroxyapatite on stainless steel substrates.

Calcium carbonate has three main polymorphs: calcite, aragonite, and vaterite. Calcite is trigonal whereas aragonite is orthorhombic and vaterite is hexagonal. Calcite is the most stable of the three polymorphs of calcium carbonates. Foreign cations such as  $Mg^{2+}$ ,  $Co^{2+}$ ,  $Cu^{2+}$ ,  $Sr^{2+}$ , and  $Pb^{2+}$  encourage aragonite formation, whereas  $Ba^{2+}$  favors vaterite formation while inhibiting calcite growth. To produce chiral morphologies of calcium carbonates, several enantiomers were studied in the presence and absence of magnesium.

Calcium carbonates are deposited from argon bubbled solutions of 600 ppm of calcium chloride, 600 ppm of sodium bicarbonate, 300 ppm of magnesium chloride, and 300 ppm of the enantiomer heated to 30°C. A constant potential of -1.1 V vs. Ag/AgCl was applied for 1800 s to deposit the calcium carbonates on stainless steel substrates. X-ray diffraction patterns were obtained for each film.

Electrodeposited calcite grows with rhombohedral morphologies, whereas aragonite tends to grow with rosette morphologies. Achiral rhombohedrons of calcite are deposited in the presence of most chiral amino acids and sugars. For example, Figure 2A

shows a SEM image of achiral morphologies of calcite grown in the presence of just L-alanine. The addition of magnesium to this solution produced achiral calcite and aragonite deposits (Figure 2B). The addition of dicarboxylic acids, including the amino acid aspartic acid, to the solution produced malformed rhombohedrons of calcite. The addition of magnesium to dicarboxylate solutions produced calcite with chiral morphologies. The morphology of the calcite deposits in the presence of just L-tartaric acid and in the presence of just L-tartaric acid and magnesium are shown in Figure 2C and 2D, respectively. As seen in Figure 2D, the deposits have barrel-like shape with facets on top. On the stainless steel substrates, the calcite deposits grow horizontally (Figure 2E) and vertically (Figure 2F). Regardless of their growth alignment on the substrate, the facets of this deposit are chiral.

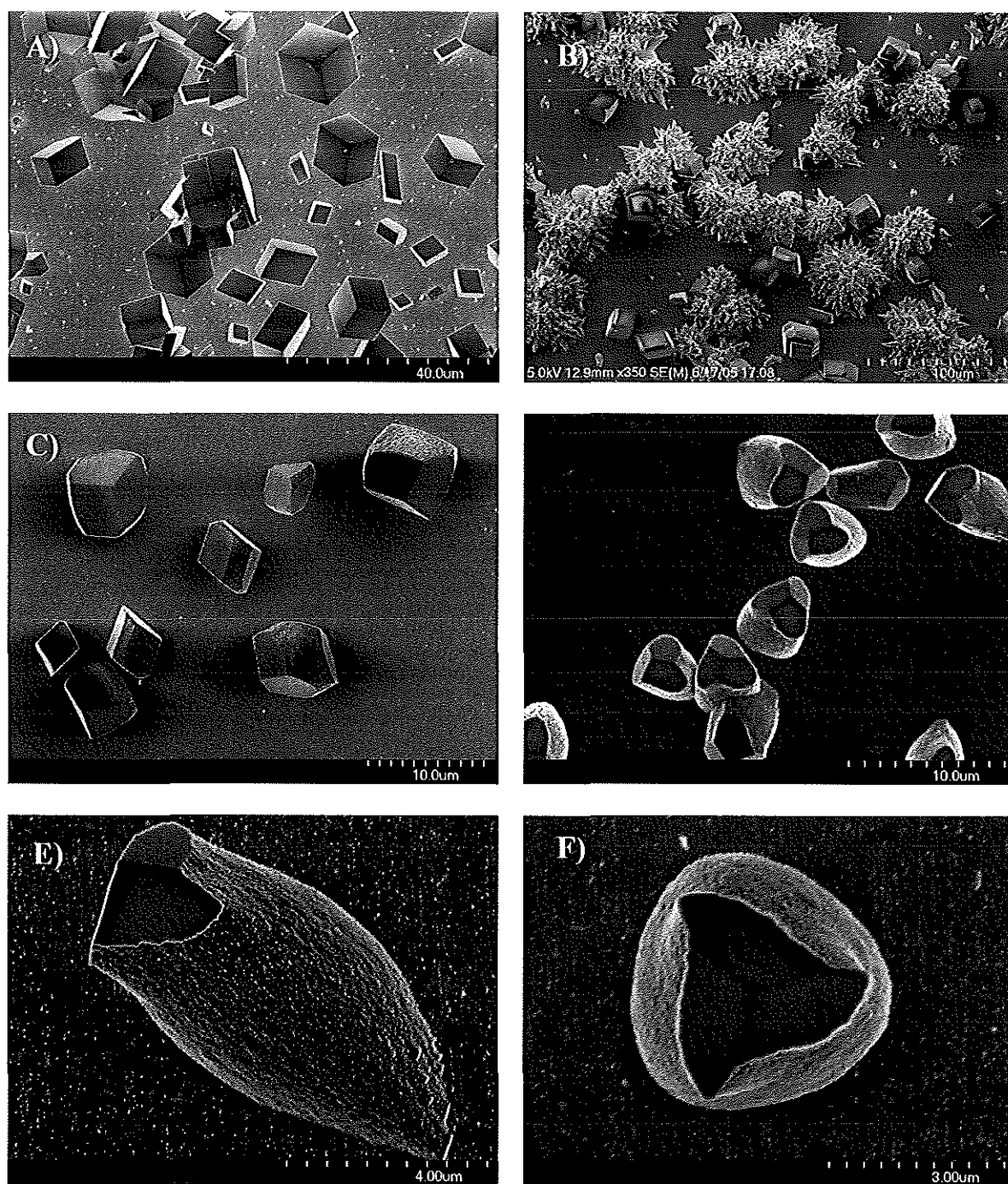


Figure 2. SEM images of calcium carbonates deposited on stainless steel substrates. The films were deposited from calcium bicarbonate solutions with additives such as A) L-alanine, B) magnesium and L-alanine, C) L-tartaric acid, and D) magnesium and L-tartaric acid. Films deposited in the presence of magnesium and L-tartaric acid have chiral morphologies. The calcite deposits grew E) horizontally and F) vertically.

As reported in Paper V, films grown in the presence of L-tartaric acid are nonsuperimposable mirror images of films grown in the presence of D-tartaric acid. Similar results have been seen in the SEM images of films grown in the presence of each enantiomer of malic acid and aspartic acid. Given that dicarboxylic acids have an effect on the morphology of the electrodeposited calcite, studies on the effect of maleic (cis-butenedioic acid) (Figure 3A) and fumaric (trans-butenedioic acid) acid (Figure 3B) in the presence of magnesium were performed. SEM images of these films in Figure 3 show that the same barrel-like morphology occurs. However, instead of a chiral morphology with three facets, multiple rhombohedral facets of calcite are present.

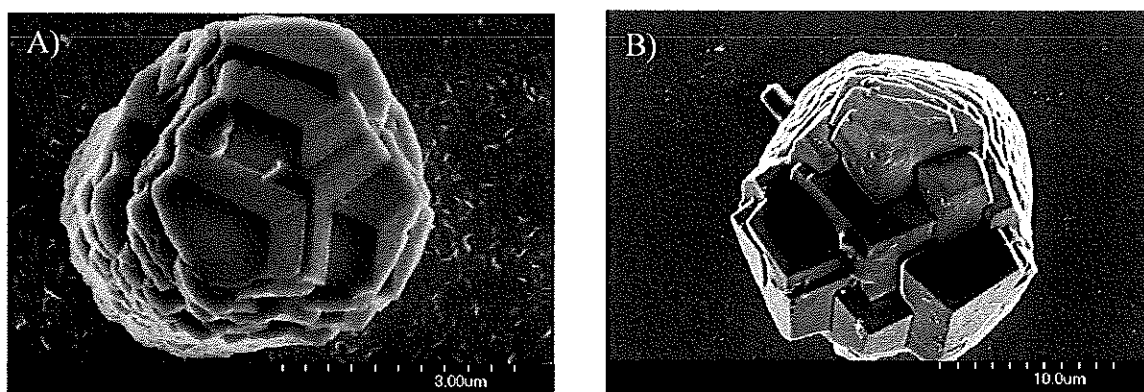


Figure 3. SEM images of calcite deposits grown from a calcium bicarbonate solution with magnesium and A) maleic acid (cis-butenedioic acid) or B) fumaric (trans-butenedioic acid) acid at 30°C. The films were deposited by applying a constant potential of -1.1 V vs. Ag/AgCl for 1800 s.

Calcium L-tartrate tetrahydrate and calcium D-tartrate tetrahydrate films are deposited from a saturated solution of  $\text{Ca}(\text{H}_2\text{PO}_4)_2$  with 50 mM L- or D-tartaric acid at  $30^\circ\text{C}$  using a cathodic current density of  $6 \text{ mA/cm}^2$  for 3600 s. Figure 4 shows SEM micrographs of A) calcium L-tartrate tetrahydrate and B) calcium D-tartrate tetrahydrate deposits electrodeposited on stainless steel. Although these deposits are superimposable images of each other, Addadi and Geva have shown that cells will preferentially grow on calcium L-tartrate tetrahydrate and not on calcium D-tartrate tetrahydrate.<sup>1</sup> Therefore, the chirality of the surface is just as important, if not more so, than a visible chiral morphology.

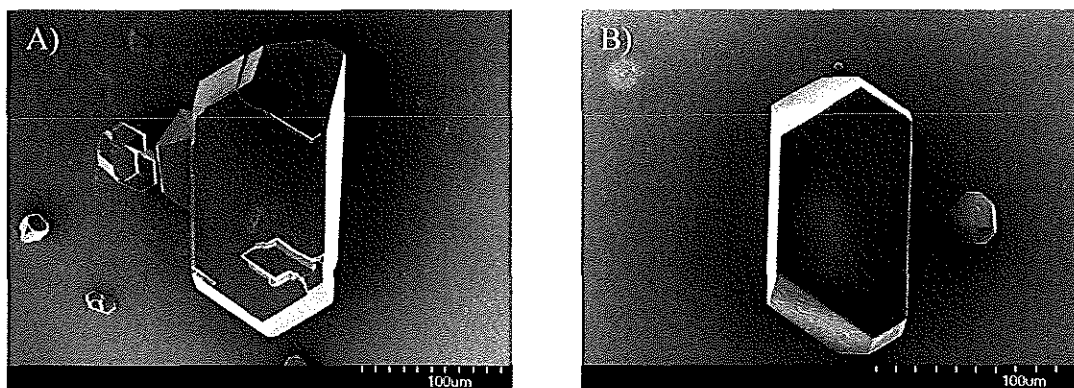


Figure 4. SEM images of A) calcium L-tartrate tetrahydrate and B) calcium D-tartrate tetrahydrate on stainless steel.

#### REFERENCE

1. L. Addadi and M. Geva, *Cryst. Eng. Comm.*, 2003, **5**, 140-146.

## VITA

Elizabeth Ann Kulp was born on February 7, 1978, in Jerseyville, IL, to Gerry Sam and Marion "Lotie" Kulp. She is the eldest of their seven children. She attended East Elementary, St. Francis Xavier School, and Jersey Community High School for her primary and secondary education. After receiving the honor of being the valedictorian of her 1996 high school class, she attended the University of Missouri-Rolla in Rolla, MO, to pursue her bachelor degree in Chemistry. She received her B.S. in Chemistry in May 2000 from the University of Missouri-Rolla with the baccalaureate honor of magna cum laude and a minor in Speech Leadership Communication. She continued her education towards a Ph.D. in Inorganic Chemistry at the University of Missouri-Rolla through a Chancellor's Fellowship. Her first graduate semester, she was a teaching assistant for Chemistry 1 recitations; she received an Outstanding Chemistry Teaching Assistant award for this work. At that time, she was researching under the guidance of Professor Jay A. Switzer who offered her a research assistantship after this first semester. Ms. Kulp's research has involved the electrodeposition and characterization of biomaterials and epitaxial metal oxides films. At the time of her defense, she has contributed to seven publications. She will receive her Ph.D. in May 2009 from the Missouri University of Science and Technology (formerly the University of Missouri-Rolla before January 1, 2008).

In addition, she has participated in the community's knowledge of chemistry through such programs as 2+2 (Girls Scout program), Primary Care Resource Initiative for Missouri /Missouri Area Health Education Centers (PRIMO/MAHEC) Chemistry Academy, Expanding Your Horizons (EYH), and Missouri Science Olympiad for the region. She was also a member and head of external fundraising of International Student Club and an evaluator for the university's Graduate Teaching Assistant (GTA) workshop. She was also a member of the Optimist Club of Rolla.